

Andrea Amaldi · Francois Tang *Editors*

# Proceedings of the 11th European Conference on Thermoelectrics

ECT 2013

 Springer

# Proceedings of the 11th European Conference on Thermoelectrics



Andrea Amaldi • Francois Tang  
Editors

# Proceedings of the 11th European Conference on Thermoelectrics

ECT 2013

 Springer



*Editors*

Andrea Amaldi  
Science and Applications Division  
European Space Agency  
Noordwijk, The Netherlands

Francois Tang  
Science and Applications Division  
European Space Agency  
Noordwijk, The Netherlands

ISBN 978-3-319-07331-6                      ISBN 978-3-319-07332-3 (eBook)  
DOI 10.1007/978-3-319-07332-3  
Springer Cham Heidelberg New York Dordrecht London

Library of Congress Control Number: 2014948549

© Springer International Publishing Switzerland 2014

This work is subject to copyright. All rights are reserved by the Publisher, whether the whole or part of the material is concerned, specifically the rights of translation, reprinting, reuse of illustrations, recitation, broadcasting, reproduction on microfilms or in any other physical way, and transmission or information storage and retrieval, electronic adaptation, computer software, or by similar or dissimilar methodology now known or hereafter developed. Exempted from this legal reservation are brief excerpts in connection with reviews or scholarly analysis or material supplied specifically for the purpose of being entered and executed on a computer system, for exclusive use by the purchaser of the work. Duplication of this publication or parts thereof is permitted only under the provisions of the Copyright Law of the Publisher's location, in its current version, and permission for use must always be obtained from Springer. Permissions for use may be obtained through RightsLink at the Copyright Clearance Center. Violations are liable to prosecution under the respective Copyright Law.

The use of general descriptive names, registered names, trademarks, service marks, etc. in this publication does not imply, even in the absence of a specific statement, that such names are exempt from the relevant protective laws and regulations and therefore free for general use.

While the advice and information in this book are believed to be true and accurate at the date of publication, neither the authors nor the editors nor the publisher can accept any legal responsibility for any errors or omissions that may be made. The publisher makes no warranty, express or implied, with respect to the material contained herein.

Printed on acid-free paper

Springer is part of Springer Science+Business Media ([www.springer.com](http://www.springer.com))

# Preface

The growing energy demands and the urgent necessity to curb greenhouse gas emissions have promoted the advancements of a broad range of possible solutions meant to mitigate the impact of our society on our environment. Among the different approaches to limit our footprint, thermoelectric materials have been positioned as a prime candidate to recover energy from heat that would otherwise be deemed wasted. The physics of thermoelectricity alone, namely the Seebeck effect, is unambiguously appealing. However, the engineering and commercial realities have been a major obstacle to the wider acceptance of thermoelectrics in practical applications. *Economically* viable generators have so far evaded the thermoelectric community.

The 11th European Conference on Thermoelectrics provided an international forum for discussion and a dissemination venue for thermoelectrics. Under the mandate of the European Thermoelectric Society, the event was organized by the European Space Agency at the European Science and Technology Centre (ESTEC) in Noordwijk, The Netherlands on November 18–20th, 2013. The Proceedings from the 11th European Conference on Thermoelectrics are a collection of 26 manuscripts that cover topics from material syntheses, the measurement of thermoelectric properties, and the design of modules and generators. The proceedings are being complemented by fully peer-reviewed manuscripts that will appear in a special issue of the *Journal of Electronic Materials*.

The large emphasis of these proceedings on the design of thermoelectric modules and generators reflects the need to grow thermoelectricity beyond investigations limited to the fundamental physical understanding and the material characterization. The future of thermoelectricity may lie in the discovery of new high-ZT material, but we believe that it resides as much, and perhaps even more, in the design of modules and generators where these materials can be best exploited.

We are thankful to all the participants and the authors who submitted manuscripts to the 2013 European Conference on Thermoelectrics. We hope that these proceedings correctly reflect the time and effort that each invested to achieve these results.

Noordwijk, The Netherlands

Andrea Amaldi  
Francois Tang



# Contents

<b>1</b>	<b>Effect of Structure and Microstructure on the Thermoelectric Properties of <math>\text{Yb}_{0.19}\text{Co}_4\text{Sb}_{12}</math> Alloy</b> .....	1
	A. Castellero, M. Ostorero, A. Ziggliotti, M. Brignone, and M. Baricco	
<b>2</b>	<b>Thermoelectric Properties of Hot-Pressed <math>\text{K}_2\text{Bi}_{8-x}\text{Sb}_x\text{Se}_{13}</math> Materials</b> .....	11
	T. Kyratsi and M. Ioannou	
<b>3</b>	<b>Effect of Open Die Pressing on the Chemical-Physical Properties of <math>\text{Zn}_4\text{Sb}_3</math> Compound</b> .....	19
	R. Carlini, C. Fanciulli, A. Castellero, F. Passaretti, M. Baricco, and G. Zanichchi	
<b>4</b>	<b>Phase Selection and Microstructure Refinement of Melt-Spun <math>\text{Zn}_4\text{Sb}_3</math>-Type Compound</b> .....	29
	R. Carlini, A. Castellero, C. Fanciulli, F. Passaretti, M. Baricco, and G. Zanichchi	
<b>5</b>	<b>The Role of Sodium-Rich Pretreatments in the Enhanced Sintering of Sodium Cobalt Oxide Thermoelectric Ceramics</b> .....	37
	E.M. Jakubczyk, C.L. Sansom, and R.A. Dorey	
<b>6</b>	<b>Novel Process for Metal Silicide Nanostructures Regarding Cheap and Large-Scale Material Synthesis</b> .....	43
	A. Schönecker, P.-Y. Pichon, J. König, M. Jäggle, M. den Heijer, and B. Kraaijveld	
<b>7</b>	<b>A Flexible Measurement System for the Characterization of Thermoelectric Materials</b> .....	53
	M. Schönhoff, F. Assion, and U. Hilleringmann	

<b>8</b>	<b>A Comparison of Thermoelectric Devices Evaluation Results Obtained with a Harman Method Based and a Porcupine Method Based <math>zT</math> Meters</b> .....	61
	A. De Marchi, V. Giaretto, S. Caron, A. Tona, and A. Muscio	
<b>9</b>	<b>Sintered Nano-Ag as Joining Material for Thermoelectric Modules</b> .....	71
	K. Brinkfeldt, J. Simon, K. Romanjek, S. Noel, M. Edwards, J. Räthel, M. Da Silva, and D. Andersson	
<b>10</b>	<b>Anodized Aluminum as Effective and Cheap Alternative Substrate for Thermoelectric Generators</b> .....	83
	F. Assion, V. Geneiß, M. Schönhoff, C. Hedayat, and U. Hilleringmann	
<b>11</b>	<b>Silica-Based Materials for Thermoelectric-Legs Embedding</b> .....	89
	A. Famengo, S. Boldrini, S. Battiston, S. Fiameni, A. Miozzo, M. Fabrizio, and S. Barison	
<b>12</b>	<b>Finite Element Approach for the Evaluation and Optimization of Silicide-Based TEG</b> .....	99
	A. Miozzo, S. Boldrini, S. Battiston, A. Famengo, S. Fiameni, T. Sakamoto, and S. Barison	
<b>13</b>	<b>Reliable Thermoelectric Generators for Space Missions</b> .....	109
	S.V. Novikov, E.Z. Parparov, and M.I. Fedorov	
<b>14</b>	<b>Challenges in Dimensioning of an Optimized Thermoelectric Generator for Waste Heat Recovery in Cars</b> .....	117
	M. Rauscher, T. Richter, F. Finsterwalder, and D. Schramm	
<b>15</b>	<b>Assessment of Thermoelectric Power Generation for Hybrid Electric Vehicles Based on Tracked Data</b> .....	129
	M. Morschel, B. Hesse, G. Bastian, and D. Schramm	
<b>16</b>	<b>Thermoelectric Generator for Low Temperature Applications</b> .....	137
	M. Follmer, B. Steiner, and D. Knospe	
<b>17</b>	<b>Waste Heat Recovery in Steelworks Using a Thermoelectric Generator</b> .....	143
	T. Kuroki, K. Kabeya, K. Makino, H. Kaibe, H. Hachiuma, and A. Fujibayashi	
<b>18</b>	<b>Thermoelectric Generator Power Converter System Configurations: A Review</b> .....	151
	E.A. Man, E. Schaltz, and L. Rosendahl	
<b>19</b>	<b>Transient Thermal Response of Heat Sinks and Its Implication on Power Control Strategies</b> .....	167
	N. Youn, Y.P. Kim, and D. Wee	

**20 Feasibility Study on Screen Printing as a Fabrication Technique for Low-Cost Thermoelectric Devices** ..... 177  
 I.A. Dimitriadou, A. Fulham, M.C. Robbins, K. Simpson,  
 R.A. Dorey, P. Jones, S. Bernadet, J. Laroche, S. Piles Guillem,  
 C. Potyrala, and J. Wood

**21 Improving Thermoelectric Cooling by Light Emission**..... 183  
 G. Min

**22 Simulation of Power Management Electronics and Energy Storage Unit for MEMS Thermoelectric Generator** ..... 189  
 L. Janak, Z. Hadas, Z. Ancik, and P. Kopecek

**23 Experimental Validation of a Multiphysics Model for the Optimization of Thermoelectric Generators**..... 197  
 C. Favarel, J.P. Bedecarrats, T. Kousksou, and D. Champier

**24 Electrical and Configuration Characterization of Thermoelectric Generator Modules**..... 205  
 M.A. Ashari, A.A. Abd. Rahman, and S. Sulaiman

**25 Modelica® Library for Dynamic Simulation of Thermoelectric Generators**..... 213  
 M. Nesarajah, L. Exel, and G. Frey

**26 Modeling and Design of Tubular Thermoelectric Generator Used for Waste Heat Recovery** ..... 219  
 H. Tjoa, B. Plochmann, and G. Fischerauer

**Index**..... 227



# Contributors

**Z. Ancik** Unis, a.s., Mechatronic & Embedded Systems, Brno, Czech Republic

**D. Andersson** Swerea IVF, Mölndal, Sweden

**M.A. Ashari** Department of Micro-Energy & Green Technology, Kuala Lumpur, Malaysia

**F. Assion** Sensor Technology Department, University of Paderborn, Paderborn, Germany

**M. Baricco** Dipartimento di Chimica and NIS, Università degli Studi di Torino, Torino, Italy

**S. Barison** Institute for Energetics and Interphases, National Research Council of Italy, Padova, Italy

**G. Bastian** Faculty of Technology and Bionics, Rhein-Waal University of Applied Sciences, Kleve, Germany

**S. Battiston** Institute for Energetics and Interphases, National Research Council of Italy, Padova, Italy

**J.P. Bedecarrats** Laboratoire de Thermique, Energétique et Procédés, Université Pau & Pays Adour, LaTEP – EA 1932, ENSGTI, PAU, France

**S. Bernadet** School of Applied Sciences, Cranfield University, Cranfield, Bedfordshire, UK

**S. Boldrini** Institute for Energetics and Interphases, National Research Council of Italy, Padova, Italy

**M. Brignone** Centro Ricerche FIAT, Orbassano, TO, Italy

**K. Brinkfeldt** Swerea IVF, Mölndal, Sweden



**R. Carlini** Dipartimento di Chimica e Chimica Industriale, Università di Genova, Genova, Italy

Unità di Ricerca di Genova, INSTM, Genova, Italy

**S. Caron** Dipartimento di Elettronica e Telecomunicazioni, Politecnico di Torino, Torino, Italy

**A. Castellero** Dipartimento di Chimica and NIS, Università degli Studi di Torino, Torino, Italy

**D. Champier** Laboratoire des Sciences de l'Ingénieur Appliquées à la Mécanique et au Génie Electrique (SIAME), Université Pau & Pays Adour, Pau Cedex, France

**I.A. Dimitriadou** European Thermodynamics Limited, Kibworth, Leicester, UK

**R.A. Dorey** University of Surrey, Guildford, Surrey, UK

**M. Edwards** Swerea IVF, Mölndal, Sweden

**L. Exel** Chair of Automation, Saarland University, Saarbrücken, Germany

**M. Fabrizio** Institute for Energetics and Interphases, National Research Council of Italy, Padova, Italy

**A. Famengo** Institute for Energetics and Interphases, National Research Council of Italy, Padova, Italy

**C. Fanciulli** Unità di Lecco, CNR, Istituto per l'Energetica e le Interfasi, Lecco, Italy

**C. Favarel** Laboratoire de Thermique, Energétique et Procédés, Université Pau & Pays Adour, LaTEP – EA 1932, ENSGTI, PAU, France

**M.I. Fedorov** Ioffe Physical-Technical Institute, St. Petersburg, Russia  
Saint-Petersburg National Research University of Information Technologies, Mechanics and Optics, St. Petersburg, Russia

**S. Fiameni** Institute for Energetics and Interphases, National Research Council of Italy, Padova, Italy

**F. Finsterwalder** Daimler AG, Ulm, Germany

**G. Fischerauer** University of Bayreuth, ZET, Chair of Metrology and Control Engineering, Bayreuth, Germany

**M. Follmer** Magna Powertrain – Engineering Center Steyr GmbH & Co KG, St. Valentin, Austria

**G. Frey** Chair of Automation, Saarland University, Saarbrücken, Germany

**A. Fujibayashi** Steel Research Laboratory, JFE Steel Corporation, Kawasaki, Kanagawa, Japan

Steel Research Laboratory, Environmental Process Research Department, JFE Steel Corporation, Kawasaki, Kanagawa, Japan

- A. Fulham** European Thermodynamics Limited, Kibworth, Leicester, UK
- V. Geneiß** Fraunhofer ENAS – Advanced System Engineering, Paderborn, Germany
- V. Giaretto** Dipartimento Energia, Politecnico di Torino, Torino, Italy  
Unità di Ricerca, Consorzio Nazionale Interuniversitario di Scienze fisiche della Materia (CNISM), Politecnico di Torino, Torino, Italy
- S. Piles Guillem** School of Applied Sciences, Cranfield University, Cranfield, Bedfordshire, UK
- H. Hachiuma** Thermo Generation Business Development Division, KELK Ltd., Hiratsuka, Kanagawa, Japan
- Z. Hadas** Faculty of Mechanical Engineering, Brno University of Technology, Brno, Czech Republic
- C. Hedayat** Fraunhofer ENAS – Advanced System Engineering, Paderborn, Germany
- M. den Heijer** RGS Development B.V., Oudkarspel, The Netherlands
- B. Hesse** University of Duisburg-Essen, Duisburg, Germany
- U. Hilleringmann** Sensor Technology Department, University of Paderborn, Paderborn, Germany  
Fraunhofer ENAS – Advanced System Engineering, Paderborn, Germany  
Institute of Electrical Engineering and Information Technology, University of Paderborn, Paderborn, Germany
- M. Ioannou** Department of Mechanical and Manufacturing Engineering, University of Cyprus, Nicosia, Cyprus
- M. Jäggle** Fraunhofer IPM, Institute for Physical Measurement Techniques, Freiburg, Germany
- E.M. Jakubczyk** School of Applied Sciences, Cranfield University, Cranfield, Bedfordshire, UK
- L. Janak** Faculty of Mechanical Engineering, Brno University of Technology, Brno, Czech Republic
- P. Jones** School of Applied Sciences, Cranfield University, Cranfield, Bedfordshire, UK
- K. Kabeya** Corporate Planning Department, JFE Steel Corporation, Chiyoda-ku, Tokyo, Japan
- H. Kaibe** Thermo Generation Business Development Division, KELK Ltd., Hiratsuka, Kanagawa, Japan

**Y.P. Kim** Department of Environmental Science and Engineering, Ewha Womans University, Seoul, Republic of Korea

**D. Knosp**e Magna Powertrain – Engineering Center Steyr GmbH & Co KG, St. Valentin, Austria

**J. König** Fraunhofer IPM, Institute for Physical Measurement Techniques, Freiburg, Germany

**P. Kopecek** Unis, a.s., Mechatronic & Embedded Systems, Brno, Czech Republic

**T. Kousksou** Laboratoire des Sciences de l'Ingénieur Appliquées à la Mécanique et au Génie Electrique (SIAME), Université Pau & Pays Adour, Pau Cedex, France

**B. Kraaijveld** RGS Development B.V., Oudkarspel, The Netherlands

**T. Kuroki** Steel Research Laboratory, Environmental Process Research Department, JFE Steel Corporation, Kawasaki, Kanagawa, Japan

**T. Kyratsi** Department of Mechanical and Manufacturing Engineering, University of Cyprus, Nicosia, Cyprus

**J. Laroche** School of Applied Sciences, Cranfield University, Cranfield, Bedfordshire, UK

**K. Makino** Thermo Generation Business Development Division, KELK Ltd., Hiratsuka, Kanagawa, Japan

**E.A. Man** Department of Energy Technology, Aalborg University, Aalborg, Denmark

**A. De Marchi** Dipartimento di Elettronica e Telecomunicazioni, Politecnico di Torino, Torino, Italy

Unità di Ricerca, Consorzio Nazionale Interuniversitario di Scienze fisiche della Materia (CNISM), Politecnico di Torino, Torino, Italy

**G. Min** School of Engineering, Cardiff University, Cardiff, UK

**A. Miozzo** Institute for Energetics and Interphases, National Research Council of Italy, Padova, Italy

**M. Morschel** Faculty of Technology and Bionics, Rhein-Waal University of Applied Sciences, Kleve, Germany

**A. Muscio** Dipartimento di Ingegneria “Enzo Ferrari”, Università di Modena e Reggio Emilia, Modena, Italy

**M. Nesarajah** Chair of Automation, Saarland University, Saarbrücken, Germany

**S. Noel** CEA, Grenoble Cedex 9, France

**S.V. Novikov** Ioffe Physical-Technical Institute, St. Petersburg, Russia

- M. Ostorero** Dipartimento di Chimica and NIS, Università degli Studi di Torino, Torino, Italy
- E.Z. Parparov** Ioffe Physical-Technical Institute, St. Petersburg, Russia
- F. Passaretti** Unità di Lecco, CNR, Istituto per l'Energetica e le Interfasi, Lecco, Italy
- P.-Y. Pichon** RGS Development B.V., Oudkarspel, The Netherlands
- B. Plochmann** University of Bayreuth, ZET, Chair of Functional Materials, Bayreuth, Germany
- C. Potyrala** School of Applied Sciences, Cranfield University, Cranfield, Bedfordshire, UK
- A.A. Abd. Rahman** Department of Micro-Energy & Green Technology, MIMOS Bhd., Kuala Lumpur, Malaysia
- J. Räthel** Fraunhofer IKTS, Dresden, Germany
- M. Rauscher** Daimler AG, Ulm, Germany
- T. Richter** Daimler AG, Ulm, Germany
- M.C. Robbins** European Thermodynamics Limited, Kibworth, Leicester, UK
- K. Romanjek** CEA, Grenoble Cedex 9, France
- L. Rosendahl** Department of Energy Technology, Aalborg University, Aalborg, Denmark
- T. Sakamoto** Department of Materials Science and Technology, Tokyo University of Science, Japan
- C.L. Sansom** School of Applied Sciences, Cranfield University, Cranfield, Bedfordshire, UK
- E. Schaltz** Department of Energy Technology, Aalborg University, Aalborg, Denmark
- A. Schönecker** RGS Development B.V., Oudkarspel, The Netherlands
- M. Schönhoff** Institute of Electrical Engineering and Information Technology, University of Paderborn, Paderborn, Germany
- D. Schramm** Universität Duisburg-Essen, Duisburg, Germany
- M. Da Silva** Swerea IVF, Mölndal, Sweden
- J. Simon** CEA, Grenoble Cedex 9, France
- K. Simpson** European Thermodynamics Limited, Kibworth, Leicester, UK

**B. Steiner** Magna Powertrain – Engineering Center Steyr GmbH & Co KG, St. Valentin, Austria

**S. Sulaiman** Department of Micro-Energy & Green Technology, MIMOS Bhd., Kuala Lumpur, Malaysia

**H. Tjoa** University of Bayreuth, ZET, Chair of Metrology and Control Engineering, Bayreuth, Germany

**A. Tona** Dipartimento di Elettronica e Telecomunicazioni, Politecnico di Torino, Torino, Italy

**D. Wee** Department of Environmental Science and Engineering, Ewha Womans University, Seoul, Republic of Korea

**J. Wood** School of Applied Sciences, Cranfield University, Cranfield, Bedfordshire, UK

**N. Youn** Department of Environmental Science and Engineering, Ewha Womans University, Seoul, Republic of Korea

**G. Zanicchi** Dipartimento di Chimica e Chimica Industriale, Università di Genova, Genova, Italy

Unità di Ricerca di Genova, INSTM, Genova, Italy

**A. Ziggotti** Centro Ricerche FIAT, Orbassano, TO, Italy

# About the Editors

**Andrea Amaldi** is an aeronautical engineer working at the Space Research and Technology Centre of the European Space Agency (ESA/ESTEC) in Noordwijk, The Netherlands. He works on materials and energy related projects and coordinates the EC-funded project ThermoMag on thermoelectricity R&D. He received his M.Sc. in Aeronautical Engineering from La Sapienza University of Rome in 1992 and in Materials Science from KU Leuven in 1995.

**Francois Tang** is currently a Research Fellow at the European Space Agency. His interests include the discovery of structural and functional light alloys, including thermoelectric materials, and additive manufacturing processes. He received his B.A.Sc. (2004) from the University of Ottawa and obtained his Ph.D. (2011) from McGill University in Mechanical Engineering where he studied the combustion of reactive dust mixtures.

# Chapter 1

## Effect of Structure and Microstructure on the Thermoelectric Properties of $\text{Yb}_{0.19}\text{Co}_4\text{Sb}_{12}$ Alloy

A. Castellero, M. Ostorero, A. Ziggotti, M. Brignone, and M. Baricco

**Abstract** In this work, we report the results of the synthesis and characterisation of the n-type  $\text{Yb}_{0.19}\text{Co}_4\text{Sb}_{12}$  thermoelectric alloy that is among the most promising materials for automotive applications with a value of ZT ranging around 1 at 600 K.

Sample preparation consisted of a sequence of three steps: (1) a solid/liquid reaction between the individual elements at 660 °C in a resistance furnace, (2) complete melting in an induction furnace, and (3) annealing at 730 °C in a resistance furnace for 0.75, 1.5, 3 and 6 h.

The unannealed samples consist of a mixture of Sb,  $\text{YbSb}_2$ , CoSb,  $\text{CoSb}_2$  and  $\text{CoSb}_3$ . Only a fraction (about 50 %) of the thermodynamically stable  $\text{CoSb}_3$ -type phase could be obtained by free cooling of the melt. This is due to the complex solidification path, involving two peritectic transformations, that does not allow the system to reach the equilibrium.

Annealing at 730 °C promotes the formation of the desired  $\text{CoSb}_3$ -type phase up to fractions ~98 % after 3–6 h.

Thermoelectric properties were measured between 300 and 500 K. Longer annealing time caused an increase of the absolute values of the Seebeck coefficient as a consequence of the higher fraction of the  $\text{Yb}_x\text{Co}_4\text{Sb}_{12}$  thermoelectric phase. In the case of electrical conductivity, no clear trend as a function of annealing time was observed.

**Keywords** Skutterudite • Processing • Thermoelectric material

---

A. Castellero (✉) • M. Ostorero • M. Baricco  
Dipartimento di Chimica and NIS, Università degli Studi di Torino,  
Via P. Giuria 7, 10125 Torino, Italy  
e-mail: [alberto.castellero@unito.it](mailto:alberto.castellero@unito.it)

A. Ziggotti • M. Brignone  
Centro Ricerche FIAT, Orbassano (TO), Italy

## Introduction

Filled skutterudites emerged as potential candidates for thermoelectric (TE) power generation in the 700–800 K temperature range [1]. In the case of n-type  $\text{CoSb}_3$ , a figure of merit (ZT) exceeding unity could be achieved with suitable Yb doping [2, 3]. Processing routes for obtaining the  $\text{CoSb}_3$  single phase consist of several steps and are often time and energy consuming. Alloying of the elements can be typically obtained by ball milling (BM) [3], by continuous reaction between solid Co and liquid Sb [4] or by direct melting of the pure elements [5, 6]. BM processing allows complete alloying in one step and the as-milled powders are ready for subsequent compaction. However, BM processing typically favours contamination and surface oxidation of the powder. On the other hand, samples prepared from the liquid are often not homogeneous from the microstructural point of view. In fact, a complex solidification path, involving two peritectic reactions, slows down the kinetics of phase transformations. Therefore, extremely long annealing time (up to 10 days) is currently used for promoting the formation of the  $\text{CoSb}_3$  single phase [6].

Attempts to shorten the synthesis were made by non-equilibrium techniques such as rapid solidification [7, 8], that also promotes nanostructuring and supersaturation of the phase with the dopant [7].

Despite the technological importance of controlling and optimising the synthesis of  $\text{CoSb}_3$  single phase, only few systematic studies have been carried out. For example, Kim et al. [9] performed isochronal annealing in vacuum of undoped  $\text{CoSb}_3$  at temperatures between 300 and 800 °C. Complete formation of the single phase was achieved after annealing at 400 °C for 24 h [9].

In this work,  $\text{Yb}_{0.19}\text{Co}_4\text{Sb}_{12}$  was synthesised with a sequence of three steps: (1) a solid/liquid reaction between the pure elements, (2) complete melting in an induction furnace, and (3) annealing at 730 °C. The effect of the annealing time on the evolution of phase structure and microstructure is studied and correlated to the thermoelectric properties. It is shown that annealing for 6 h at 730 °C promotes the formation of  $\text{Yb}_{0.1}\text{Co}_4\text{Sb}_{12}$  single phase. However, the samples are characterised by porosity (10–20 vol.%) that is detrimental for thermoelectric applications.

## Experimental

Samples with nominal composition  $\text{Yb}_{0.19}\text{Co}_4\text{Sb}_{12}$  (at.%) were prepared using elemental Co (Alfa Aesar, 99.8 % powder), Sb (Alfa Aesar, 99.999 % shot), and Yb (Aldrich, 99.9 % chip). A small excess of Sb (about 3 at.%) was added in order to compensate the loss of this element as a consequence of its evaporation during the thermal treatments. The elements were sealed in a BN-coated quartz crucible under an Ar atmosphere (6.1 kPa) and were heated at 660 °C for 2.5 h in a resistance furnace. The melting reaction was then completed in an induction furnace, under an Ar atmosphere. Finally, samples in bulk form (rods with diameter 9 mm and height 30 mm) were annealed at 730 °C for 0.75, 1.5, 3 and 6 h.



Structural analysis on ground powders obtained from the bulk samples was performed by X-ray diffraction (XRD) in transmission geometry (PANalytical X'Pert PRO, Cu K $\alpha$ ), using a rotating capillary. The experimental patterns were refined by Rietveld analysis using the MAUD software [10].

Microstructure and phase compositions were investigated by scanning electron microscopy (SEM) (Leica Stereoscan 420) equipped with an energy dispersive spectroscopy (EDS) microprobe (Oxford Instruments).

The density of the samples was measured with a pycnometer.

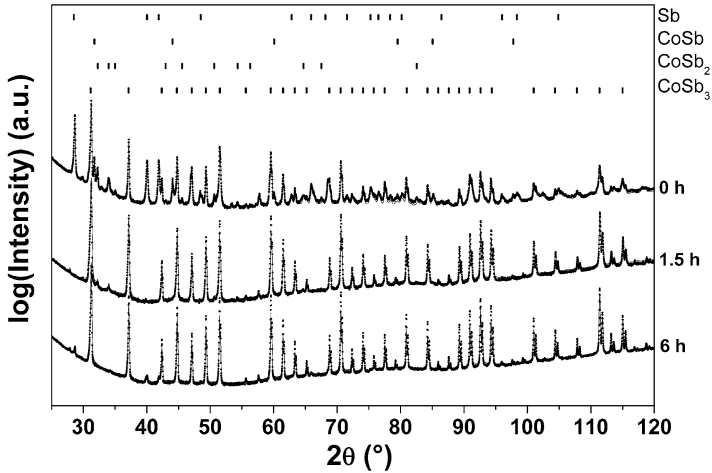
The electrical conductivity ( $\sigma$ ) was measured with the four-probe method. The Seebeck coefficient ( $\alpha$ ) was measured with a homemade apparatus where the sample is held between two plates. The whole sample holder can be inserted inside a vertical electrical furnace under an inert atmosphere. The temperature difference between the two plates during a heating ramp is maintained by heating the lower plate by Joule effect. Thermocouple wires were used to measure both the temperature of the plates and the potential difference generated by the sample. The Seebeck coefficient was obtained by the following equation:

$$\alpha = \alpha_{\text{wires}} - \frac{\Delta V}{\Delta T} \quad (1.1)$$

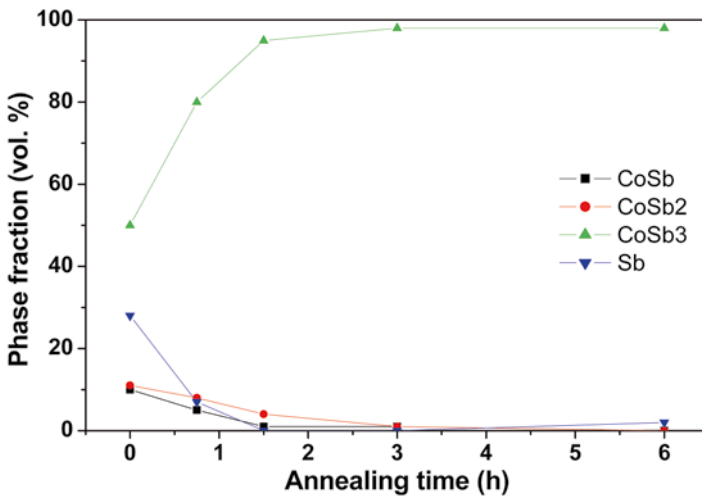
where  $\alpha_{\text{wires}}$  represents the Seebeck coefficient of the thermocouple wires,  $\Delta V$  is the measured potential difference and  $\Delta T$  is the measured temperature difference. All the measurements were performed in an Ar atmosphere in a temperature range between 25 and 300 °C.

## Results and Discussion

Figure 1.1 shows XRD patterns related to the phase evolution in the bulk samples after annealing at 730 °C for different times. The XRD pattern of the non-annealed sample clearly shows the crystallographic reflections of additional phases to CoSb<sub>3</sub> (i.e. Sb, CoSb and CoSb<sub>2</sub>). As expected, increasing the annealing time promotes the formation of the desired CoSb<sub>3</sub>-type phase. The evolution of the volume fraction of the various phases is shown in Fig. 1.2 as a function of annealing time. It can be seen that, after only 3–6 h of annealing, the formation of the CoSb<sub>3</sub>-type single phase is almost completed. Table 1.1 shows the values of the lattice parameter for the CoSb<sub>3</sub>-type phase after different annealing times, together with the values of  $R_w$  indicating the quality of the fit for the Rietveld refinement. The increase of the lattice parameter with annealing time indicates that the CoSb<sub>3</sub>-type phase progressively solubilises a larger amount of Yb. From the comparison of the lattice parameter for the sample annealed for 6 h ( $a=9.0462$  Å) with those reported in literature for undoped Co<sub>4</sub>Sb<sub>12</sub> ( $a=9.0347$  Å [11]) and Yb<sub>0.18</sub>Co<sub>4</sub>Sb<sub>12</sub> ( $a=9.0531$  Å [6]), we estimated that the maximum amount of Yb solubilised in Yb<sub>*x*</sub>Co<sub>4</sub>Sb<sub>12</sub> is  $x \sim 0.1$  indicating that the annealing is not enough for obtaining a complete dissolution (i.e. Yb<sub>0.19</sub>Co<sub>4</sub>Sb<sub>12</sub>).



**Fig. 1.1** X-ray diffraction patterns for  $\text{Yb}_1\text{Co}_4\text{Sb}_{12}$  for selected annealing times. *Scattered curves*: experimental patterns; *continuous curves*: fitted patterns



**Fig. 1.2** Evolution of the phase volume fraction as a function of annealing time

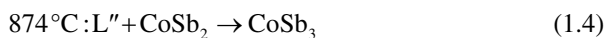
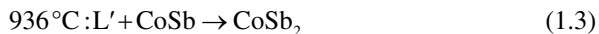
The microstructural evolution as a function of the annealing time is shown by the backscattered electron SEM images in Fig. 1.3. In the unannealed sample, Fig. 1.3a, large dendrites of the primary CoSb phase are surrounded by CoSb<sub>2</sub> and CoSb<sub>3</sub> phases, where CoSb, CoSb<sub>2</sub> and CoSb<sub>3</sub> are immersed in an Sb matrix. The inset of Fig. 1.3a shows a eutectic microstructure consisting of YbSb<sub>2</sub> and Sb, showing that the Yb atoms were not fully dissolved in the skutterudite structure. After 0.75 h of annealing, Fig. 1.3b, CoSb, CoSb<sub>2</sub> and Sb tend to disappear in favour of CoSb<sub>3</sub>, while a small fraction of the YbSb<sub>2</sub>/Sb eutectic is still present (see inset).

**Table 1.1** Values of the lattice parameter,  $a$ , of  $\text{Yb}_x\text{Co}_4\text{Sb}_{12}$  and  $R_w$  for the Rietveld refinement of the X-ray diffraction patterns at different annealing times

Annealing time (h)	Lattice parameter of $\text{Yb}_x\text{Co}_4\text{Sb}_{12}$ , $a$ (Å)	$R_w$ (%)
0	9.0403	2.5
0.45	9.0422	5.8
1.5	9.0428	5.4
3	9.0455	3.9
6	9.0462	6.1

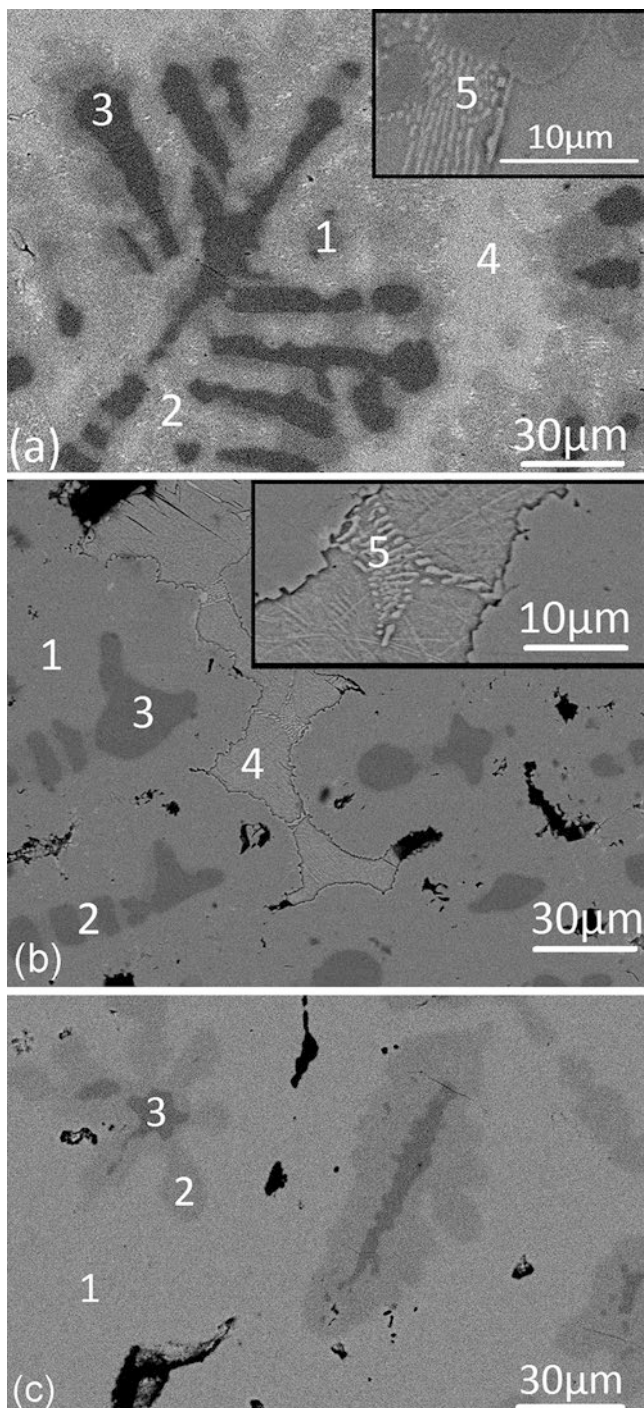
After 3 h of annealing, Fig. 1.3c, only residual traces of  $\text{CoSb}$  and  $\text{CoSb}_2$  are present, whereas the  $\text{YbSb}_2/\text{Sb}$  eutectic fully disappears. Finally, after 6 h of annealing, the microstructure shown in Fig. 1.3d becomes more homogeneous, with only a small fraction of  $\text{Sb}$  segregated at the grain boundaries of  $\text{CoSb}_3$ .

According to the  $\text{Co-Sb}$  equilibrium phase diagram [12], the sequence of reactions upon cooling is the following:



where  $\text{L}$ ,  $\text{L}'$  and  $\text{L}''$  represent the liquid phase with different compositions. The presence of significant amounts of  $\text{Sb}$ ,  $\text{CoSb}$  and  $\text{CoSb}_2$  in the unannealed sample indicates that the two peritectic reactions (1.3) and (1.4) were not completed during the uncontrolled cooling after induction melting, due to the need of long-range diffusion. The effect of annealing is to homogenise the microstructure progressively, favouring the formation of the expected  $\text{CoSb}_3$ -type phase. The presence of residual  $\text{Sb}$  in the sample annealed for 6 h indicates that the excess of  $\text{Sb}$  added at the beginning did not evaporate completely. All the samples show a significant amount of porosity (ranging between 10 and 20 vol.%) irrespective of the annealing time. The measured density ranges between 6.2 and 7.0  $\text{g}\cdot\text{cm}^{-3}$ , corresponding to 81–92 % of the theoretical density (7.60  $\text{g}\cdot\text{cm}^{-3}$ ). According to Geng et al. [5], the mechanism of the formation of porosity is the one explained below. During the peritectic reaction (1.3),  $\text{CoSb}_2$  dendrites form inside the network of primary dendrites of  $\text{CoSb}$  formed from reaction (1.2). As a consequence of the solidification contraction, empty volumes remain between the solid phases because the pores cannot be easily filled by the remaining liquid. Since the pore fraction does not show a trend with annealing time, it can be supposed that porosity is caused by the mechanism described by Geng et al. [5] rather than from the evaporation of  $\text{Sb}$ . This is also supported by the fact that the excess of  $\text{Sb}$  was not fully evaporated, as evidenced in Fig. 1.3d. Finally, pores tend to become more rounded when the annealing time increases as a consequence of the reduction of the surface area.

The results of the thermoelectric properties are reported in Fig. 1.4. The evolution of the Seebeck coefficient,  $\alpha$ , and of the electrical conductivity,  $\sigma$ , measured at different temperatures in function of the annealing time is reported in Fig. 1.4a, b, respectively.



**Fig. 1.3** SEM backscattered electron images of the microstructure evolution in  $\text{Yb}_5\text{Co}_4\text{Sb}_{12}$  at different annealing times: (a) 0 h, (b) 0.75 h, (c) 3 h, and (d) 6 h. The numbers in the micrographs indicate the corresponding phases: (1)  $\text{CoSb}_3$ , (2)  $\text{CoSb}_2$ , (3)  $\text{CoSb}$ , (4)  $\text{Sb}$ , (5)  $\text{YbSb}_2$

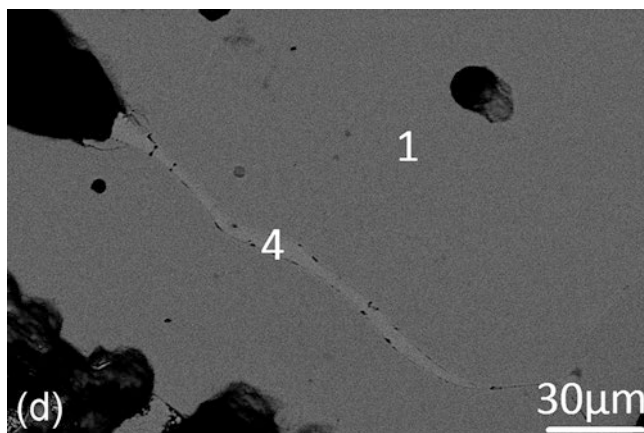
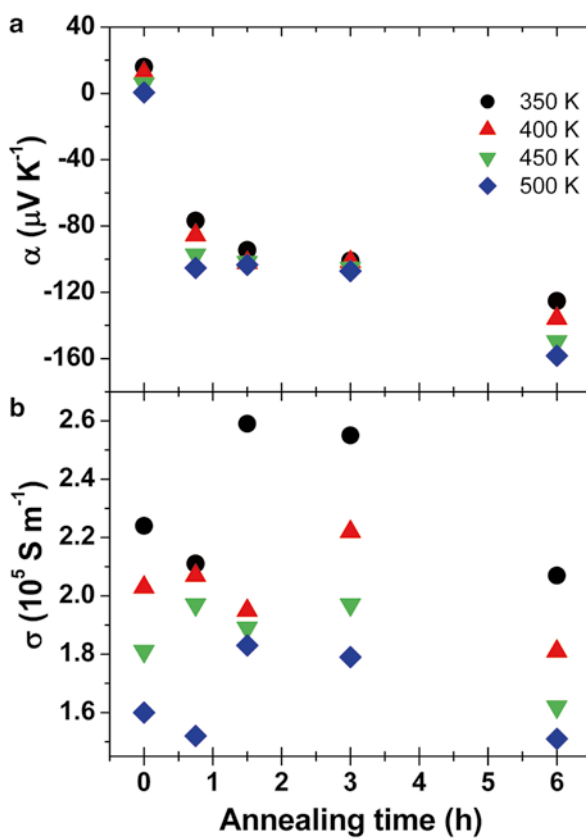


Fig. 1.3 (continued)

Fig. 1.4 Thermoelectric properties of  $\text{Yb}_x\text{Co}_4\text{Sb}_{12}$ . Seebeck coefficient (a) and electrical conductivity (b) as a function of annealing time



The Seebeck coefficient is initially positive and progressively becomes negative as the annealing proceeds. Values around  $-120$  and  $-160$   $\mu\text{V/K}$  at  $300$  K and  $500$  K, respectively, are reached after annealing for  $6$  h. This trend is due, on the one hand, to the progressive formation of the  $\text{CoSb}_3$ -type thermoelectric phase, and, on the other hand, to the doping of this phase with Yb, as shown by the progressive increase of the lattice parameter (Table 1.1). In fact, undoped  $\text{CoSb}_3$  has a p-type behaviour whereas Yb-doped  $\text{CoSb}_3$  has an n-type behaviour. After annealing for  $6$  h, the formation of the  $\text{CoSb}_3$ -type phase is almost completed, whereas the Seebeck coefficient does not reach a saturation value because  $\text{Yb}_x\text{Co}_4\text{Sb}_{12}$  is only partially doped with Yb, indicating that the solubilisation of Yb is a slower process with respect to the formation of the  $\text{CoSb}_3$ -type phase.

For each annealing time, the absolute value of the Seebeck coefficient becomes larger at higher temperature, revealing the typical behaviour of doped semiconductors. The magnitude of the Seebeck coefficient obtained for the sample annealed for  $6$  h is slightly lower than that reported in the literature for the Yb-doped  $\text{CoSb}_3$  single-phase compound. For example, values ranging from  $-130$  to  $-160$   $\mu\text{V/K}$  at  $300$  K, and from  $-170$  to  $-200$   $\mu\text{V/K}$  at  $500$  K have been reported [5, 7, 13, 14]. The difference between our results and those reported in the literature is likely due to the incomplete solubilisation of Yb ( $x \sim 0.1$ ) and the presence of a small fraction of Sb that shows metallic behaviour.

In the case of the electrical conductivity, there is not a clear trend as a function of annealing time. The significant scattering of the values is mainly due to the high porosity of the samples that affects the reliability of the resistivity measurements. The values obtained are slightly higher than those typically reported for this system (e.g. between  $8$  to  $15 \times 10^4$  S/m at  $300$  K [5, 7, 13, 14]). As expected, for each annealing time, the electrical conductivity decreases as the temperature increases, indicating a degenerated semiconductor behaviour due to the Yb doping.

Comparing the results of the thermoelectric properties (Fig. 1.4) with the structural and microstructural analyses of crystalline phases present in the samples as a function of annealing time (Figs. 1.1, 1.2, and 1.3), it appears clear that, with the proposed preparation process, short annealing times (i.e.  $3$ – $6$  h) might be sufficient to obtain a single-phase material. However, annealing for  $6$  h at  $730$  °C does not allow the complete solubilisation of Yb. Furthermore, the volume contraction upon solidification leads to undesired porosity ( $10$ – $20$  vol.%) and, consequently, to a relative density lower than  $92$  % with respect to the theoretical one. Thus, improvements are needed for optimising the preparation and annealing sequence in order to increase the final properties.

## Conclusions

In this work,  $\text{Yb}_{0.19}\text{Co}_4\text{Sb}_{12}$  alloy was prepared by a combination of liquid/solid reaction, induction melting and annealing. Samples with about  $98$  % of the desired  $\text{CoSb}_3$ -type phase were obtained after annealing for  $3$ – $6$  h. After annealing for  $6$  h, the samples have an effective composition of  $\text{Yb}_{0.1}\text{Co}_4\text{Sb}_{12}$  and show a

chemically homogeneous microstructure, apart from a small-fraction Sb in excess that segregated at the grain boundaries. All the samples show porosity ranging between 10 and 20 vol.%.

Concerning thermoelectric properties, on the one hand, the absolute value of the Seebeck coefficient progressively increases as a function of annealing time. Thermoelectric n-type behaviour reveals that the  $\text{CoSb}_3$ -type phase was successfully doped with Yb during the annealing. On the other hand, electrical conductivity does not show a clear trend with annealing because of the porosity of the samples that leads to a density 81–92 % of the theoretical one. It can be concluded that the processing route proposed in this work might be effective for preparing single-phase  $\text{CoSb}_3$ -based alloys for thermoelectric applications. However, improvements are needed for ensuring a higher density of the material and a complete solubilisation of Yb.

## References

1. Uher C (2001) Skutterudites: Prospective Novel Thermoelectrics. In: Tritt TM (ed) *Semiconductors and semimetals*, vol. 69, issue C. Academic Press, New York, p 139–253
2. Nolas GS, Kaeser M, Littleton RT, Tritt TM (2000) *Appl Phys Lett* 77:1855
3. Yang J, Hao Q, Wang H, Lan YC, He QY, Minnich A, Wang DZ, Harriman JA, Varki VM, Dresselhaus MS, Chen G, Ren ZF (2009) *Phys Rev B* 80:115329
4. Nolas GS, Cohn JL, Slack GA (1998) *Phys Rev B* 58:164
5. Geng HY, Ochi S, Guo JQ (2007) *Appl Phys Lett* 91:022106
6. Xiong Z, Chen X, Huang X, Bai S, Chen L (2010) *Acta Mater* 58:3995
7. Li H, Tang X, Zhang Q, Uher C (2008) *Appl Phys Lett* 93:252109
8. Yan YG, Wong-Ng W, Kaduk JA, Tan GJ, Xie WJ, Tang XF (2011) *Appl Phys Lett* 98:142106
9. Kim I-H, Choi G-S, Han MG, Kim J-S, Lee J-I, Ur S-C, Hong T-W, Lee Y-G, Ryu S-L (2004) *Mater Sci Forum* 917:449–452
10. <http://www.ing.unitn.it/~maud/>
11. Villars P, Calvert LD (eds) (1985) *Pearson's handbook of crystallographic data for intermetallic phases*, vol 2. American Society for Metals, Metals Park, OH, p 1825
12. Okamoto H (2000) *Phase diagram binary alloys*. American Society for Metals, Metals Park, OH
13. Li H, Tang X, Zhang Q (2009) *J Electron Mater* 38:1224
14. Li H, Tang X, Su X, Zhang Q, Uher C (2009) *J Phys D Appl Phys* 42:145409

# Chapter 2

## Thermoelectric Properties of Hot-Pressed $K_2Bi_{8-x}Sb_xSe_{13}$ Materials

T. Kyratsi and M. Ioannou

**Abstract** Alkali bismuth chalcogenides are promising for thermoelectric applications as suggested by previous works. The  $K_2Bi_8Se_{13}$  compounds were grown from melt as polycrystalline ingots or from Bridgman technique as highly oriented polycrystalline ingots. In this work, we apply powder techniques as a post-growth process on the  $K_2Bi_{8-x}Sb_xSe_{13}$  series and the effect of the sintering process and the Sb concentration on the thermoelectric properties of the series is discussed.

**Keywords** Sintering • Solid solutions • Structural disorder • Grain boundaries

### Introduction

Alkali bismuth chalcogenides attracted considerable attention in the last two decades as candidates for thermoelectrics due to their complex crystal and electronic structure [1]. The properties of  $K_2Bi_8Se_{13}$ -based compounds were studied in more detail as the most promising. The properties of materials grown from melt as polycrystalline ingots [2, 3] or from Bridgman technique as highly oriented polycrystalline ingots have been reported in several publications [4, 5]. Powder techniques were applied as post-growth methods through pressureless sintering [6, 7] and also, only recently, through hot pressing [8] on  $K_2Bi_8Se_{13-x}S_x$  series. The hot-pressed pellets had high density and performed ZT of about 0.5 at 800 K.

In this system, the formation of solid solutions has been extensively studied as a common strategy to minimize the thermal conductivity and there are several reports on substitution at the heavy metal sites, i.e.,  $K_2Bi_{8-x}Sb_xSe_{13}$  [4, 9], the chalcogenide sites, i.e.,  $K_2Bi_8Se_{13-x}S_x$  [10]; as well as the alkali metal sites, i.e.,  $K_{2-x}Rb_xBi_8Se_{13}$  [11].

---

T. Kyratsi (✉) • M. Ioannou

Department of Mechanical and Manufacturing Engineering, University of Cyprus,  
1678 Nicosia, Cyprus



Crystallographic studies show that the nonuniform partial substitution of Bi/Sb decreases the lattice thermal conductivity [12] but also significantly affects the electronic properties through changes in structural disorders [5].

In this work, we apply post-growth powder techniques on the Sb series and hot-pressed pellets of  $K_2Bi_{8-x}Sb_xSe_{13}$  ( $0 \leq x \leq 2.4$ ) are fabricated. The hot pressing conditions were selected based on the previously applied statistical design of experiments optimization approach [8]. The effect of the sintering process and the Sb concentration on the thermoelectric properties of the series is discussed. A comparison with different types of samples, prepared also by post-growth techniques (i.e., oriented polycrystalline ingots), is also presented.

## Experimental Section

Chemicals were used as obtained: potassium metal, rod, 99.5 % purity, Sigma Aldrich, and bismuth, antimony, and selenium metals, 99.999 % purity from Alfa Aesar and all manipulations during synthesis were carried out under a dry argon atmosphere in an MBraun glovebox. The  $K_2Bi_{8-x}Sb_xSe_{13}$  series was synthesized in the form of ingot as explained in the following: mixtures of elements were weighted according to the chemical formula of each member and were sealed in silica tube under pressure of  $<10^{-5}$  Torr. The mixtures were, then, heated to 850 °C over 12 h and kept there for 1 h, followed by cooling to 50 °C at a rate of  $-15$  °C/h. The ingots were broken in small pieces and ground using a mortar and pestle. Pellets were fabricated using a uniaxial hot-press system (HP20) from Thermal Technologies Inc. The sintering conditions were modified according to each member's melting point as discussed below.

The samples were examined by X-ray powder diffraction to assess phase purity. Powder patterns were obtained using a Rigaku Miniflex powder X-ray diffractometer with Ni-filtered Cu K $\alpha$  radiation operating at 30 kV and 15 mA. Seebeck coefficient and electrical conductivity measurements were carried out on the hot-pressed pellets simultaneously using a commercial ZEM-3 system from ULVAC-RIKO. A Netzsch LFA-457 system was used to measure thermal diffusivity and heat capacity. The diffusivity ( $D$ ), density ( $\rho$ ), and specific heat ( $C_p$ ) were measured and used to calculate the total thermal conductivity using the formula  $\kappa = D \times \rho \times C_p$ .

## Results and Discussion

### *Synthesis and Pellet Fabrication*

Selected members of  $K_2Bi_{8-x}Sb_xSe_{13}$  series were synthesized and hot pressed into pellets. The final products were single  $K_2Bi_8Se_{13}$  phase as concluded by powder X-ray diffraction (PXRD). The sintering conditions were selected based on the

**Table 2.1** Melting point ( $T_{MP}$ ) and sintering conditions (hot-pressing temperature ( $T_{HP}$ ), pressure ( $P$ ), and time at maximum temperature) of the  $K_2Bi_{8-x}Sb_xSe_{13}$  materials

$x$	$T_{MP}$ (°C)	$T_{HP}$ (°C)	$P$ (MPa)	Time (min)
0.0	700	540	80	90
0.8	687	530	80	90
1.6	675	520	80	90
2.4	654	505	80	90

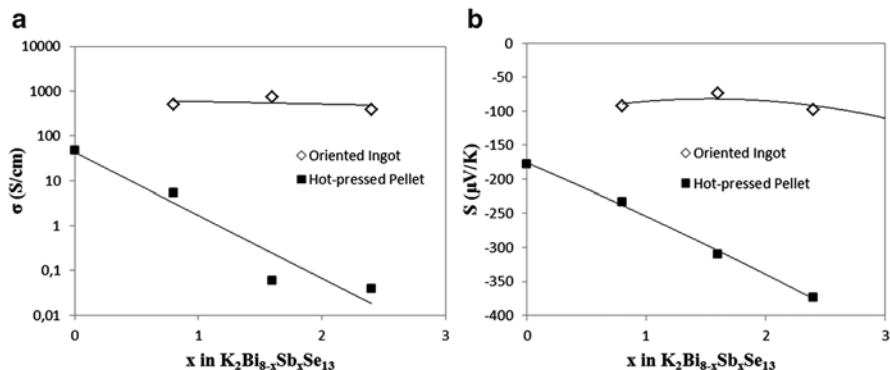
results of the previously reported optimization process [8]. However, the actual sintering temperatures had to be adjusted due to the different melting points of the Sb members. Table 2.1 shows the sintering conditions and melting points [4] for each stoichiometry. The relative densities of the hot-pressed pellets were between 94 and 98 %.

### *Electrical Conductivity and Seebeck Coefficient*

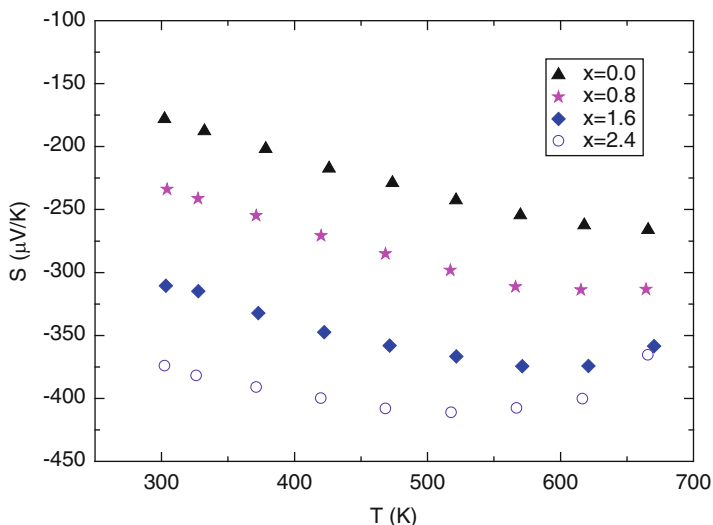
It is the first time that members of the  $K_2Bi_{8-x}Sb_xSe_{13}$  series are processed via powder techniques, i.e., grinding and sintering with hot pressing; therefore a comparison with the highly oriented ingots previously studied is attempted. Figure 2.1a shows that the electrical conductivity values of the members prepared as highly oriented polycrystalline ingots by Bridgman technique [5] are much higher than those reported here. Since the hot-pressed pellets include many grains and the boundaries significantly decrease the mobility of the carriers, such behavior was expected. In addition, the anisotropy of this system is well known and affects the thermoelectric properties along and perpendicular to the needle orientation (crystallographic  $b$ -axis). The electrical conductivity along the needle direction was found to be five times higher than the perpendicular one [4]. Therefore, the contribution of the different crystallographic directions is also involved here, although this does not seem to be the main mechanism here.

On the other hand, the Seebeck coefficient of the pressed pellets is higher, in absolute values, than the reported values for oriented ingots; see Fig. 2.1b. This suggests lower carrier concentration that could be explained by the fact that the post-growth processes were different; hot pressing is a solid-state process at lower temperatures while the oriented ingots were prepared after melting the materials at higher temperatures. The variation of the Seebeck coefficient due to anisotropy is less important as discussed in ref. [4].

According to previous work on polycrystalline oriented ingots [5], the behavior of the Bi-rich members is that of typical heavily doped semiconductors. For the hot-pressed pellets, this is also the case for the member  $x=0$ ; see Figs. 2.2 and 2.3. When Sb incorporates in the lattice the electron concentration decreases. At the same time, the temperature dependence of the electrical conductivity changes with Sb and this can also be attributed to the lower carrier concentration. The electrical



**Fig. 2.1** (a) Electrical conductivity and (b) Seebeck coefficient of  $\text{K}_2\text{Bi}_{8-x}\text{Sb}_x\text{Se}_{13}$  hot-pressed pellets in comparison to materials prepared as oriented ingots [5]



**Fig. 2.2** Temperature dependence of Seebeck coefficient of  $\text{K}_2\text{Bi}_{8-x}\text{Sb}_x\text{Se}_{13}$  hot-pressed pellets

conductivity in this temperature range changes from that of typical heavily doped semiconductors to intrinsic semiconducting region.

In order to better understand the properties, one should have a closer look on the crystal structure.  $\text{K}_2\text{Bi}_8\text{Se}_{13}$  material has a complex structure, as shown in Fig. 2.4, that includes two different interconnected types of Bi/Se building blocks and  $\text{K}^+$  atoms in tunnels. The two different Bi/Se blocks are connected to each other at special mixed-occupancy K/Bi sites that seem to be crucial in defining the electronic structure near the Fermi level and consequently the electronic properties. This is supported by ab initio density functional band structure calculations on this material [13].

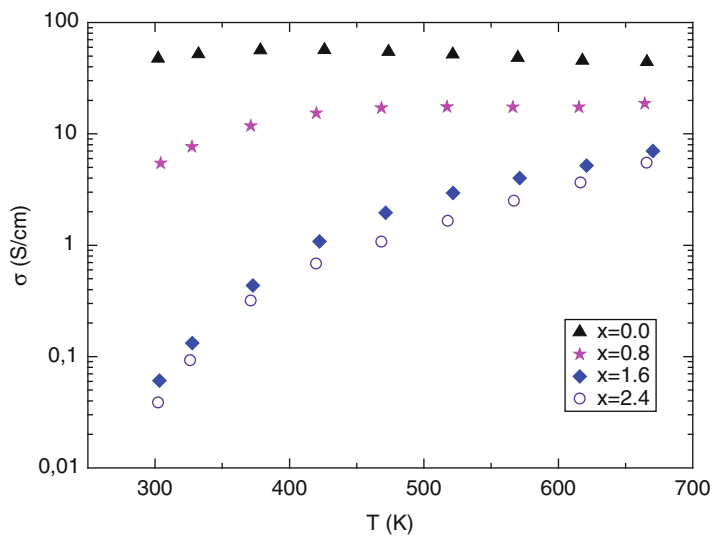


Fig. 2.3 Temperature dependence of Seebeck coefficient of  $K_2Bi_{8-x}Sb_xSe_{13}$  hot-pressed pellets

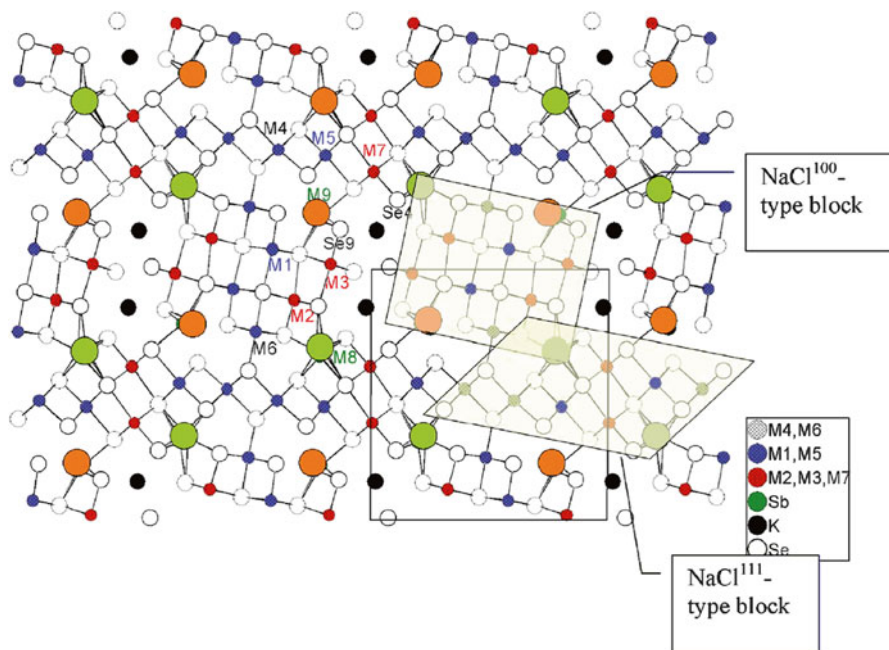


Fig. 2.4 Crystal structure of  $K_2Bi_8Se_{13}$  compound (from ref. [5])

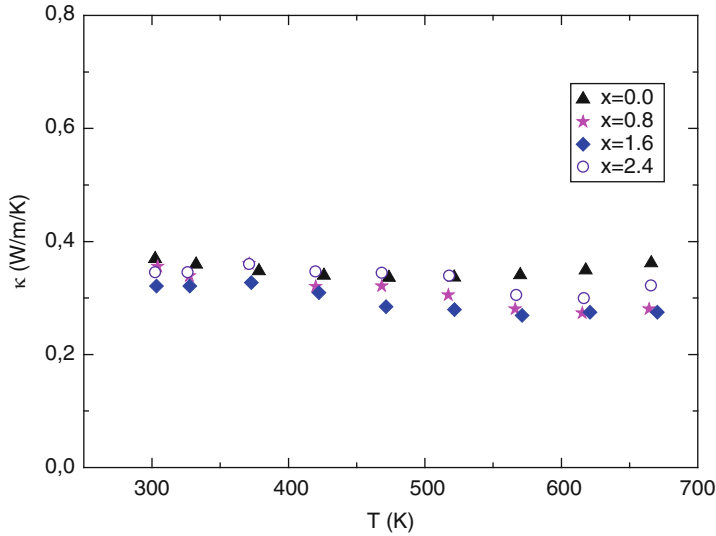
As discussed previously regarding the ingots [5], the incorporation of Sb affects the properties in two different ways, one related to these mixed-occupancy sites mentioned above. The band structure calculations on  $\text{K}_2\text{Bi}_8\text{Se}_{13}$  dealt with the mixed occupancy of the  $M/K$  sites  $M(8)$  and  $M(9)$  [13]. The occupancy of the  $M(8)$  and  $M(9)$  was once considered to exclusively contain either K or Bi atoms and according to band structure calculations this led to semimetallic behavior with  $E_g=0$ . In another case, a  $1 \times 2 \times 1$  supercell with ordered Bi and K distributions was involved and the band structure calculations showed a semiconductor with  $E_g=0.55$  eV, a value close to the experimental gap of 0.60 eV. When Sb is introduced in the lattice, it preferentially occupies the sites  $M(8)$  and  $M(9)$  (Fig. 2.4) until  $x$  reaches 1.5 or 1.7 [5]. At higher concentration, the additional Sb atoms show again a preferential substitution for the sites with distorted octahedral coordination environment which are proximal to the mixed sites  $M(8)$  and  $M(9)$  and these are  $M(2)$ ,  $M(3)$ ,  $M(7)$ ,  $M(1)$ , and  $M(5)$ ; see Fig. 2.4 [5]. Since the donors originate from the degree of order/disorder at the mixed-occupancy  $M/K$  sites, the gradual elimination of the disorder with the Sb incorporation reveals a more semiconducting character of the  $\text{K}_2\text{Bi}_{8-x}\text{Sb}_x\text{Se}_{13}$  materials. This is in agreement with our results in oriented ingots [5] as well as the hot-pressed pellets in this work.

On the other hand, there is a variation of the energy band gap of the compounds that affect the properties [4]. The energy gaps of the end members  $\text{K}_2\text{Bi}_8\text{Se}_{13}$  and  $\text{K}_2\text{Sb}_8\text{Se}_{13}$  are 0.59 eV and 0.78 eV respectively [2]. However, the gaps of the  $\text{K}_2\text{Bi}_{8-x}\text{Sb}_x\text{Se}_{13}$  series do not increase monotonously, as expected, but small amounts of Sb actually cause the  $E_g$  to slightly decrease and it actually increases only when Sb atoms replace 30 % of Bi atoms ( $x \approx 2.5$ ) [4].

In the case of the hot-pressed pellets, all the above phenomena are valid and can explain the variation in the properties with Sb concentration. The elimination of the structural disorder as well as the small changes in the energy gap are expected to affect the properties in the hot-pressed pellets in the same way as previously observed in oriented ingots. On the other hand, differences such as the lower doping level, can be understood in terms of the different type of the applied post-growth process (hot press as solid-state process vs. melting).

### ***Thermal Conductivity and Figure of Merit***

Thermal conductivity measurements of the members of the  $\text{K}_2\text{Bi}_{8-x}\text{Sb}_x\text{Se}_{13}$  series are shown in Fig. 2.5. The room-temperature values are between 0.30 and 0.6 W/m K which are very low compare to other thermoelectric materials. For  $x=0$  the thermal conductivity value is lower than that of 1.28 W/m K [2] that corresponds to highly oriented polycrystalline ingot, but it is similar to that of 0.3 W/m K, expected for pressed pellet [14] and these differences can be explained based on the anisotropy of these materials and the porosity as discussed elsewhere [14]. The lattice thermal conductivity seems to be the major contribution to the total thermal conductivity



**Fig. 2.5** Temperature dependence of thermal conductivity of  $K_2Bi_{8-x}Sb_xSe_{13}$  hot-pressed pellets

due to the low electrical conductivity values and correspond to values of 0.32–0.35 W/m K. These values are very similar to those of  $K_2Bi_8Se_{13-x}S_x$  pellets [8]. The figure of merit  $ZT$  was maximum for the  $x=0$  member reaching 0.58 at 673 K. For higher  $x$  values the maximum  $ZT$  decreased to 0.43, 0.22, and 0.15 for the members  $x=0.8$ , 1.6, and 2.4, respectively.

## Conclusions

In this work, hot-pressed pellets of the  $K_2Bi_{8-x}Sb_xSe_{13}$  series were prepared for the first time. The sintering conditions followed previous results based on statistical design of experiments approach and were modified based on the different melting point of the compounds. The pellets prepared by hot pressing presented different properties than those previously reported for oriented polycrystalline ingots and these can be understood based on the different post-growth processes applied in each case (solid-state process vs. melting). The electrical conductivities were significantly lower as expected due to the contribution of the grain boundaries, while the Seebeck coefficient measurements suggested lower doping level in these materials. Regarding the thermal conductivity, all members exhibited very low values due to the combination of the complex crystal structure of the materials and the powder processing. More work is in progress trying to modify the electronic properties as well as keep the benefit of this extremely low thermal conductivity.

**Acknowledgments** This work was co-funded by the European Regional Development Fund and the Republic of Cyprus through the Research Promotion Foundation (Infrastructure Project ANABAΘMISΗ/0308/17).

## References

1. Kanatzidis MG (2000) *Semiconduct Semimet* 69:51
2. Chung D-Y, Choi K-S, Iordanidis L, Schindler JL, Brazis PM, Kannewurf CR, Chen B, Hu S, Uher C, Kanatzidis MG (1997) *Chem Mater* 9:3060
3. Kyratsi T, Kika E, Hatzikraniotis E, Paraskevopoulos KM, Chrissafis K, Kanatzidis MG (2009) *J Alloys Compd* 474:351–357
4. Kyratsi T, Dyck JS, Chen W, Chung D-Y, Uher C, Paraskevopoulos KM, Kanatzidis MG (2002) *J Appl Phys* 92(2):965
5. Kyratsi T, Hatzikraniotis E, Paraskevopoulos KM, Malliakas CD, Dyck JS, Uher C, Kanatzidis MG (2006) *J Appl Phys* 100:123704
6. Tsiappos A, Kyratsi Th, Kanatzidis MG (2006) *Proceedings of 25th international conference on thermoelectrics, IEEE*, pp. 516–519
7. Tsiappos A, Kyratsi Th, Hatzikraniotis E, Paraskevopoulos KM, Kanatzidis MG (2007) *Proceedings of 5th European Conference on Thermoelectrics, Ukraine*
8. Kyratsi T, Ioannou M (2013) *J Electron Mater* 42:1604
9. Kyratsi T, Chung D-Y, Kanatzidis MG (2002) *J Alloy Comp* 338:36–42
10. Kyratsi T, Kanatzidis MG, Anorg Z (2003) *Allg Chem* 629(12):2222–2228
11. Kyratsi T, Chung D-Y, Ireland JR, Kannewurf CR, Kanatzidis MG (2003) *Chem Mater* 15:3035–3340
12. Kyratsi T, Hatzikraniotis E, Paraskevopoulos KM, Dyck JS, Shin HK, Uher C, Kanatzidis MG (2004) *J Appl Phys* 95(8):4140
13. Bilc D, Mahanti SD, Kyratsi T, Chung D-Y, Larson P, Kanatzidis MG (2005) *Phys Rev B* 71(8):085116
14. Kyratsi T, Hatzikraniotis E, Ioannou M, Chung DY, Tsiaoussis I (2011) *J Appl Phys* 110:033713
15. Chung D-Y, Iordanidis L, Choi K-S, Kanatzidis MG (1998) *Bull Kor Chem Soc* 19:1281–1293
16. Kanatzidis MG (ed) (2003) *New thermoelectric materials workshop chemistry, physics and materials science of thermoelectric materials: beyond bismuth telluride, fundamental materials science series*. Kluwer Academic/Plenum, New York

# Chapter 3

## Effect of Open Die Pressing on the Chemical-Physical Properties of $\text{Zn}_4\text{Sb}_3$ Compound

R. Carlini, C. Fanciulli, A. Castellero, F. Passaretti, M. Baricco,  
and G. Zanicchi

**Abstract** Recently, semiconducting intermetallic compounds, belonging to the Zintl phases, have attracted much attention due to their unexpectedly low thermal conductivity, which leads to improved thermoelectric properties. The glass-like thermal conductivity of  $\text{Zn}_4\text{Sb}_3$ , originated in the framework Zn position of its structure, makes this compound one of the most studied phases in the thermoelectric field. The reduction of grain size obtained by the melt spinning process can lead to an improvement of figure of the Merit-ZT but, unluckily, is associated with an increase of material brittleness.

As a prosecution of a previous work, melt-spun samples and powders obtained by a solid-phase synthesis of  $\text{Zn}_4\text{Sb}_3$  were sintered by Open Die Pressing (ODP) process: with this technique, already used for sintering of nano-powder of chalcogenides, bulk samples with high density and compactness were produced.

Chemical physical properties and the stability of the pure phase  $\text{Zn}_4\text{Sb}_3$  are investigated after ODP process. All samples were studied in terms of crystal structure, phase composition, thermal stability, mechanical resistance and thermoelectric properties. Preliminary results show the formation of ZnSb phase into the  $\text{Zn}_4\text{Sb}_3$

---

R. Carlini • G. Zanicchi

Dipartimento di Chimica e Chimica Industriale, Università di Genova,  
Via Dodecaneso 31, 16146 Genova, Italy

Unità di Ricerca di Genova, INSTM, Via Dodecaneso 31, 16146 Genova, Italy

C. Fanciulli (✉) • F. Passaretti

Unità di Lecco, CNR, Istituto per l'Energetica e le Interfasi,  
Corso Promessi Sposi 29, 23900 Lecco, Italy  
e-mail: [c.fanciulli@ieni.cnr.it](mailto:c.fanciulli@ieni.cnr.it)

A. Castellero • M. Baricco

Dipartimento di Chimica and NIS, Università degli Studi di Torino,  
via P. Giuria 7, 10125 Torino, Italy



matrix after both melt spinning and ODP processes: the effects of time and temperature parameters of ODP process on ZnSb phase formation have also been investigated and thermoelectric properties have been compared for the different conditions.

**Keywords** Zn<sub>4</sub>Sb<sub>3</sub> • Thermoelectric materials • Mechanical processing • Rapid solidification

## Introduction

Efficient thermoelectric devices for technological applications require the development of new materials that combine high thermoelectric performance, low cost and chemical stability, in order to make them suitable for different operating conditions [1, 2]. The challenge of thermoelectric materials research is to find compounds with high ZT, in particular in the intermediate- and high-temperature range, in order to improve their capability in wasted heat recovery. The *glass-like* thermal conductivity of some compounds belonging to the Zintl phases makes this class one of the most studied in the thermoelectric field [3]. Particularly the Zn<sub>4</sub>Sb<sub>3</sub>, originating its good thermoelectric performance from its disordered structure, is one of the most studied intermetallic due to its very low thermal conductivity. Unfortunately, the Zn<sub>4</sub>Sb<sub>3</sub>, as the main intermetallic compound, presents a very high brittleness [4]. This behaviour is a heavy obstacle for its application in thermoelectric modules.

Here a new approach, aimed to obtain an improvement of the Zn<sub>4</sub>Sb<sub>3</sub> mechanical performance, is proposed. The intermetallic, obtained through a simple route, has been processed using Open Die Pressing (ODP) technique [5] starting from both ground bulk material and Melt-Spun (MS) material. ODP has already been successfully applied for fast chalcogenide powder sintering, the main feature of the process being the low temperature involved and the short time required for sintering. Both these factors contribute in preserving a fine structure in the final sample. In this work the results of an investigation carried out on the effects of ODP on microstructural, mechanical, thermal and thermoelectric properties are presented.

## Experimental

The intermetallic binary compounds Zn<sub>4</sub>Sb<sub>3</sub> were synthesised as bulk samples. A stoichiometric ratio of pure commercial elements (purity 99.999 %), sealed in silica vials under Ar flow, were heated at 750 °C in a muffle furnace, annealed at this temperature for 10 h and spontaneously cooled for 5 h. The material produced was processed following two different paths. In the former the ingot was ground and the powders obtained ODP processed into a Fe sheath. In the latter the material was melt spun [6] and the ribbons obtained were sintered via ODP process again using a Fe sheath as mechanical support for the compaction. The sintering process was

performed at 285 and 290 °C with a sintering time varying from 2 to 10 min. Following both the procedures described, densifications between 98.5 and 99 % of the theoretical value reported in literature [7] were obtained.

A Scanning Electron Microscope (SEM) equipped with Energy-Dispersive X-ray spectroscope (EDX)—EVO 40 (Carl Zeiss) with Pentafet Link (Oxford Instruments)—was used to examine microstructures and determine phase composition. X-ray diffraction (XRD) analysis was used to investigate the phase crystal structures and the lattice parameters. The measurements were performed on bulk or powdered samples using a vertical diffractometer (PANalytical X'Pert Pro model). XRD measurements were also performed at different temperatures, in order to evaluate possible effects on the phase stability in the samples. Data refinement was carried out using Rietveld method by Full Proof Suite software. To evaluate the analytical sample composition, an ICP-AES analysis (Inductively Coupled Plasma-Atomic Electronic Spectroscopy) was performed to support XRD and EDX analyses.

Thermal stability of the samples was investigated by differential scanning calorimetry (DSC) using a power compensation Perkin Elmer Diamond DSC.

Electrical conductivity of the processed samples was measured as a function of the temperature using Van Der Pauw method between 300 and 700 K. In the same range measurements of the Seebeck coefficient have been performed using an MMR Technology system, in order to evaluate the power factor.

## Results and Discussions

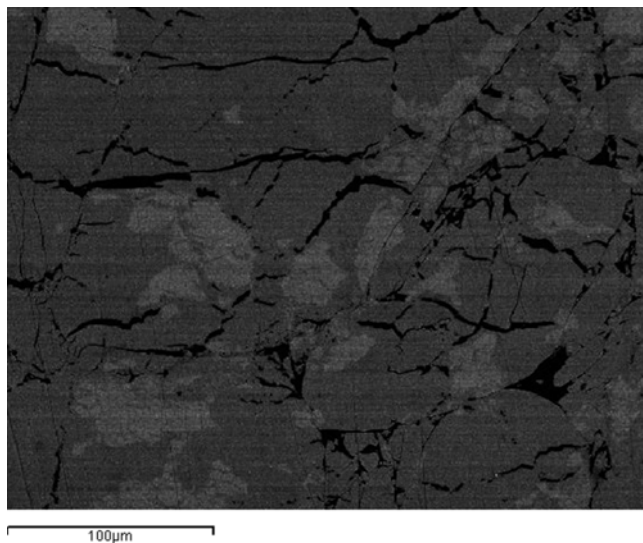
In Table 3.1 the results of ICP analyses are reported. A change in Zn content at different steps of sample preparation was observed: starting from stoichiometric 4:3 Zn–Sb ratio for as-cast sample, a reduction of this ratio to 1.25 was found after ODP process. This result is consistent and explains the results of other characterizations.

Indeed SEM investigations showed the presence of ZnSb phase into the  $Zn_4Sb_3$  matrix as displayed in Fig. 3.1. The little solubility field of this secondary phase is consistent with the phase diagram [8] considering the Zn content in each sample characterised.

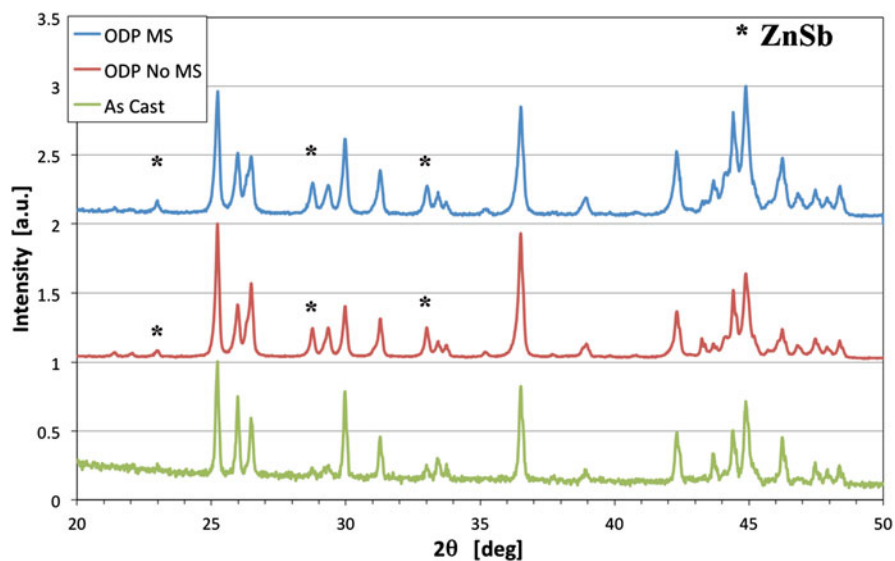
Normalised XRD patterns are reported in Fig. 3.2: Rietveld refinement allowed to obtain lattice parameters, atomic positions and atomic occupancies in the  $\beta$ - $Zn_4Sb_3$ . Results of the analyses were in accordance with cell parameters reported in literature [9, 10], giving lattice parameters  $a$  and  $c$ , 1.2228 nm and 1.2424 nm,

**Table 3.1** Results of ICP analyses performed on different samples

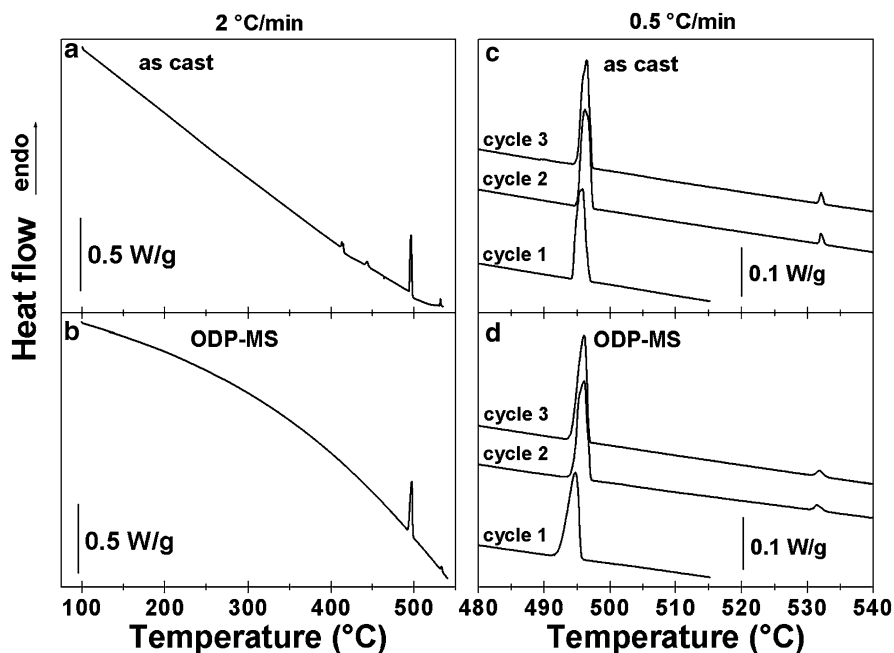
Sample	Zn (ppm)	Sb (ppm)	Zn:Sb ratio	Zn at. %
$Zn_4Sb_3$ (th)	–	–	1.33333	57.1
As-cast	10.9	7.85	1.3410	57.3
Melt spun	7.58	5.63	1.3830	58.0
ODP no MS	70.2	47.2	1.2520	55.5
ODP MS	62.3	39.6	1.1836	54.1



**Fig. 3.1** SEM image of ODP sample. The darker phase corresponds to  $Zn_4Sb_3$  matrix, the lighter one to ZnSb secondary phase



**Fig. 3.2** XRD patterns of, starting from the *bottom*, as-cast material, ODP-processed powders and ODP-processed MS ribbons

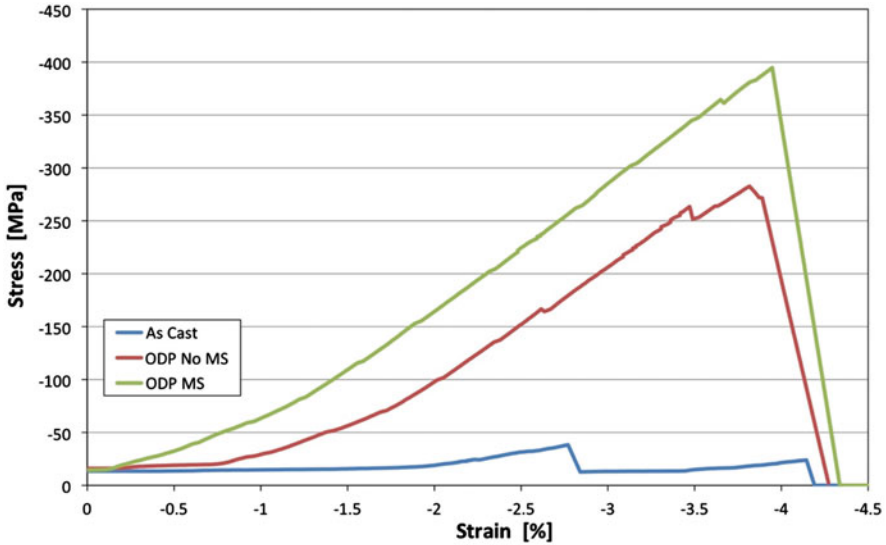


**Fig. 3.3** Calorimetric analyses of as-cast (a) and ODP samples (b) in the range of 100–550 °C. Both measurements were performed at 2 °C/min. Thermal cycling of the same samples is reported in (c) and (d), respectively, in the range of 480–540 °C: slower rates were used (0.5 °C/min)

respectively. The ODP process resulted to have no significant effect on structural properties of the starting compounds. The two phases already seen with previous analyses were observed: peaks due to the presence of a little amount, estimated in the range of 3–4 %, of ZnSb were identified. XRD performed up to 285 °C displayed no phase evolution in the range of temperatures proper of ODP processing performed on the material.

Calorimetric analyses were performed on the samples up to 550 °C. In order to study the effects of ODP, the starting (Fig. 3.3a, c) and processed (Fig. 3.3b, d) materials were tested.

In the case of the bulk sample, the DSC trace, Fig. 3.3a, shows upon heating a sequence of four endothermic signals: between 409 and 411 °C, around 440, 493, and 532 °C. Each peak can be associated to a corresponding invariant reaction proposed in the equilibrium-phase diagram [8]. However, the two signals at lower temperature (409–411 and 440 °C) are not compatible with the nominal and measured composition, suggesting that the sample is not fully homogeneous. The result can be related to the presence of regions richer in Zn due to local fluctuation of the chemical composition. The two signals at lower temperature disappear in a second DSC heating cycle (not shown here) indicating that the sample became chemically homogeneous after the completion of the first DSC cycle. Repeated heating cycles at 0.5 °C/min on the same sample, Fig. 3.3c, show the reproducibility of the signals at 493 and 532 °C.



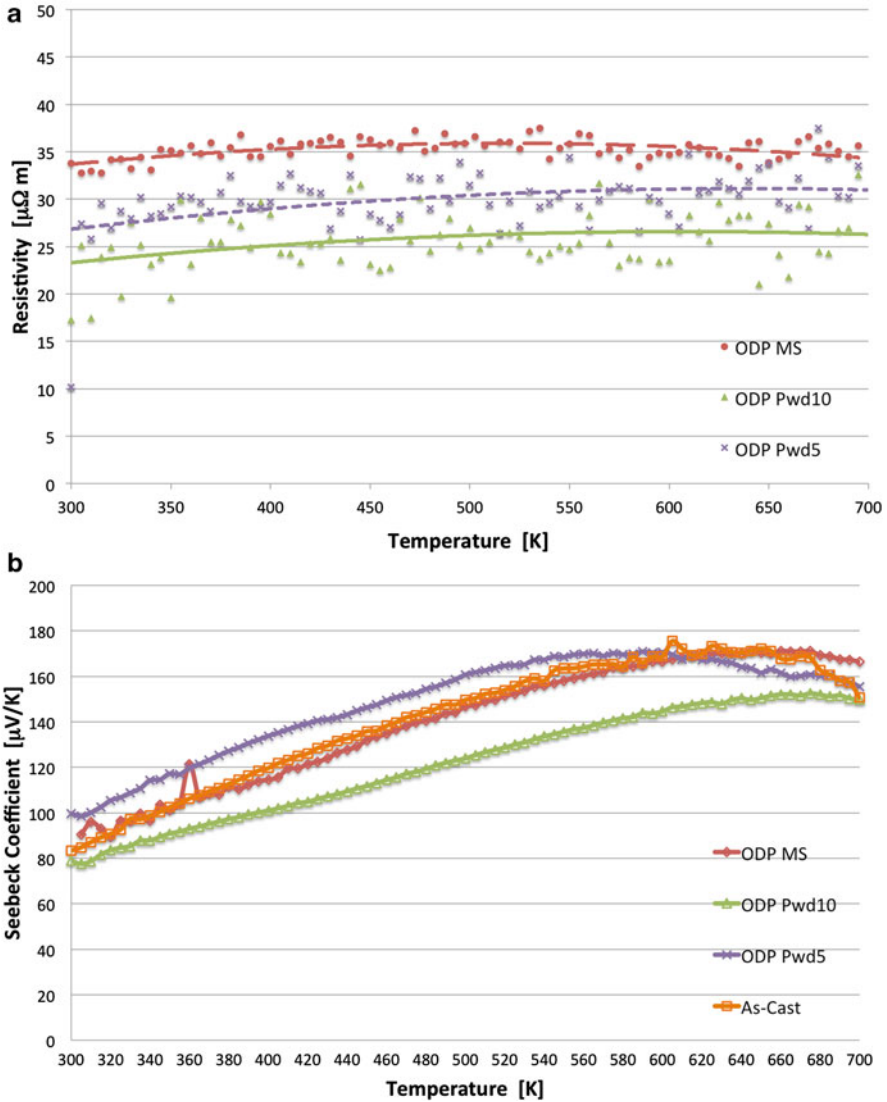
**Fig. 3.4** Stress–strain plots in compressive configuration of as-cast, ODP from powders and ODP from MS samples. Sintered material overcomes the limits due to the brittleness of as-cast one

In the case of the ODP sample, the DSC trace, Fig. 3.3b, shows the two expected endothermic signals at 493 and 532 °C, indicating that after ODP processing the sample is already in the equilibrium conditions. Repeated heating cycles at 0.5 °C/min on the same sample show again the reproducibility of the signals at 493 and 532 °C, Fig. 3.3d.

Comparing the DSC traces at 0.5 °C/min, it can be observed that the signal around 532 °C is slightly broader in the ODP sample with respect to the bulk sample. This difference is due to the small variation of composition between the two samples (see Table 3.1) that slightly modify the equilibrium between the phases.

The mechanical behaviour of the samples obtained following the different routes was investigated by stress–strain tests performed in compression in a mechanical test machine (MTS 2/M) at room temperature. Compressive setup was chosen because it better reproduces the most common operating conditions for a material into a basic device (module). Data are reported in Fig. 3.4: the curves correspond to as-cast, ODP of powders and ODP of MS materials. All the samples, as expected, displayed a fragile behaviour with fragile fractures at high strains. The value of fracture load showed a large increase after ODP processing the material: both ODP samples, MS and not, display a maximum load at least eight times greater than the one for original material. MS sample reached the highest value, consistently with the refined structure of starting material. This result suggests that processing the starting material could be helpful in order to overcome the technological limits in the usage of the material represented by its brittleness.

In order to evaluate the effective influence of the ODP process on obtained samples, measurements of electrical resistivity and Seebeck coefficient were carried



**Fig. 3.5** Thermoelectric properties for as-cast and ODP-processed samples. Resistivity (a) and Seebeck coefficient (b) were measured from 300 to 700 K

out. Results reported in Fig. 3.5 are related to as-cast sample, ODP samples obtained from powders with 5-min and 10-min sintering time (named Pwd5 and Pwd10, respectively) and ODP sample from MS material sintered for 5 min. All the ODP samples were processed and sintered at 285 °C.

The resistivity of ODP-MS samples resulted to be just a bit greater than the one of powdered samples. This effect can be associated to the finer structure of the

sintered material. As expected, a longer sintering time resulted in lower resistivity. The values obtained for as-cast material, here not reported, resulted to be afflicted by the large granularity of the samples obtained from the billet.

The values of the Seebeck coefficient resulted to be lower than the best ones reported in literature: this could be due to the presence of a mix of phases into the final material. As reported in literature the presence of pure Zn and/or ZnSb phase affects the Seebeck value depending on the content of the secondary phases [11, 12]: compared to the pure phase of as-cast sample, the results seem to be similar in all cases.

As a result we can deduce that ODP processing does not clearly affect thermoelectric behaviour of the material: an improvement should be expected in the reduction of thermal conductivity, especially in melt-spun materials, due to the fast sintering process and the low temperatures involved in the ODP process but, up to now, thermal conductivity measurements are still in progress.

## Conclusions

Open Die Pressing process was successfully used for the first time to sinter  $Zn_4Sb_3$  compound. The bulk obtained resulted to be fully dense with a sintering time of 5 min at 285 °C: these conditions were such to preserve the microstructure of the sample. Effects of the process have been investigated on melt-spun ribbons, obtaining again good results in terms of densification and thermoelectric properties.

The main result presented in this work is the high improvement in mechanical behaviour of the material after ODP processing: preserving thermoelectric properties of the material, we were able to increase the mechanical resistance of the bulk up to 11 times as respect to the starting as-cast bulk.

Looking for thermoelectric property optimization, further developments are needed in order to reduce the presence of secondary phases in the final material. Moreover, a further refinement of starting powders or a grain refinement of melt-spun ribbons could represent a way to improve mechanical and thermoelectric performances of the ODP-processed samples.

**Acknowledgements** The authors would like to thank Dr. Gianluca Fiore for the support in the preparation of the rapidly solidified samples by melt spinning, Dr. Francesco Soggia for the ICP-AES analyses, and Dr. Elena Villa and Enrico Bassani for their support in ODP processing and mechanical characterizations.

## References

1. Takeuchi T (2012) Thermoelectrics and its energy harvesting. In: Rowe DM (ed) *Materials, preparation and characterization in thermoelectrics*. CRC, Boca Raton, FL, 7.1–7.27
2. Mahan G, Sales B, Sharp J (1997) *Phys Today* 50:42
3. Kauzlarich SM, Brown SR, Snyder GJ (2007) *Dalton Trans.* 2099

4. Ueno K, Yamamoto A, Noguchi T, Inoue T, Sodeoka S, Obara H (2005) *J Alloys Compd* 388:118
5. Ceresara S, Fanciulli C, Passaretti F, Vasilevskiy D (2012) *J Electron Mater* 42:1529
6. Baricco M, Bosco E et al (2004) *Int J Mater Prod Technol* 20:358
7. Pedersen BL, Birkedal H, Iversen BB (2006) *J Appl Phys* 89:242108
8. Okamoto H (2000) Phase diagram binary alloys. Materials Park, OH, USA
9. Mozharivskiy YA, Pecharsky AO, Bud'ko SL, Miller GJ (2004) *Chem Mater* 16:1580
10. Carlini R, Marré D, Pallecchi I, Ricciardi R, Zanicchi G (2014) *Intermetallics* 45:60
11. Zhang LT, Tsutsui M, Ito K, Yamaguchi M (2003) *J Alloys Compd* 358:252
12. Cadavid D, Rodriguez JE (2008) *Physica B* 403:3976



# Chapter 4

## Phase Selection and Microstructure Refinement of Melt-Spun $\text{Zn}_4\text{Sb}_3$ -Type Compound

R. Carlini, A. Castellero, C. Fanciulli, F. Passaretti,  
M. Baricco, and G. Zanicchi

**Abstract** The  $\text{Zn}_4\text{Sb}_3$  phase is considered one of the most interesting compounds for thermoelectric applications in the intermediate temperature range (400–600 K) because of its very low thermal conductivity. Typical processing routes of this material for technological applications require several steps, in order to obtain a homogeneous single phase with fine microstructure.

In this work, melt spinning was used as an intermediate processing step for improving the structural homogenization and microstructure refinement of  $\text{Zn}_4\text{Sb}_3$ . The effect of rapid solidification on the phase stability and microstructure was investigated.

Melt-spun samples show, on the one hand, other crystalline phases in addition to the expected  $\text{Zn}_4\text{Sb}_3$ -type phase, probably because the high cooling rate did not allow the system to reach the thermodynamic equilibrium. On the other hand, rapid solidification induced a remarkable decrease of crystallite size down to the nanoscale, as estimated by the peak broadening in the X-ray diffraction patterns and shown by scanning electron micrographs. Additionally, the presence of an irreversible exothermic peak in the differential scanning calorimetry (DSC) trace can be likely related to the crystallization of a small amount of amorphous phase, formed as a result of the high cooling rate that could not be detected by XRD.

---

R. Carlini • G. Zanicchi

Dipartimento di Chimica e Chimica Industriale, Università di Genova,  
Via Dodecaneso 31, 16146 Genova, Italy

Unità di Ricerca di Genova, INSTM, Via Dodecaneso 31, 16146 Genova, Italy

A. Castellero (✉) • M. Baricco

Dipartimento di Chimica and NIS, Università degli Studi di Torino,  
Via P. Giuria 7, 10125 Torino, Italy  
e-mail: [alberto.castellero@unito.it](mailto:alberto.castellero@unito.it)

C. Fanciulli • F. Passaretti

Unità di Lecco, CNR, Istituto per l'Energetica e le Interfasi,  
Corso Promessi Sposi 29, 23900 Lecco, Italy

The results suggest that melt-spun flakes can be used as a starting material in the subsequent compaction steps.

**Keywords**  $Zn_4Sb_3$  • Thermoelectric material • Rapid solidification • Processing

## Introduction

Today an enormous amount of unused waste heat could be converted to electricity by using thermoelectric solid-state devices [1]. Research in the thermoelectric field covers a lot of different materials such as intermetallics, composites, and nanomaterials [1, 2]. Thermoelectric efficiency of these materials can be improved by doping, nanostructuring, or nonequilibrium synthesis routes [1, 3]. Up to now, intermetallics are the most studied materials for thermoelectric applications due to their stability and mechanical properties in thermoelectric devices.

The intermetallic  $Zn_4Sb_3$  compound has raised great interest due to its glass-like thermal conductivity and consequently due to its good thermoelectric performance in the intermediate temperature range (400–600 K) [2]. Several studies were carried out on this compound to evaluate the influence of different processing routes on its efficiency [4–7]. Processing of this material for technological applications requires several steps, in order to obtain a fully dense homogeneous single phase with fine microstructure [1]. In fact, it is well known that phonon contribution to thermal conductivity can be significantly depressed by a very high density of grain boundaries, leading to an increase of the figure of merit ZT.

Among non-equilibrium processing techniques, melt spinning allows fast quenching, promoting the formation of amorphous or metastable phases, together with a significant grain size refinement [8]. Furthermore, the short processing time required strongly reduces contamination due to the working atmosphere. Such a technique could be effective in producing starting materials suitable for further processing, in view of an efficiency increase of thermoelectric properties.

In this chapter, the effect of melt spinning on the microstructural, structural, and thermal properties of  $Zn_4Sb_3$  intermetallic compound is investigated in view of thermoelectric applications.

## Experimental

Bulk samples of the intermetallic binary compound  $Zn_4Sb_3$  were synthesized with a simple preparation route. Stoichiometric quantities of zinc and antimony (purity 99.99 mass %) sealed in silica vials under Ar flow were heated up to 750 °C in a muffle furnace, annealed at this temperature for 10 h and, finally, spontaneously cooled.

Rapidly solidified samples of  $Zn_4Sb_3$  were obtained with a melt-spinning (MS) apparatus by Edmund Bühler GmbH. The bulk alloy was induction melted in a BN crucible and ejected by an Ar overpressure (0.2 bar) on a copper wheel rotating at 20 m/s.

Chemical analyses of the bulk and melt-spun samples were performed by Induction Coupled Plasma-Atomic Electron Spectroscopy (ICP-AES) analyses. The ICP-AES system used was an axially viewed Varian (Springvale, Australia) Vista PRO.

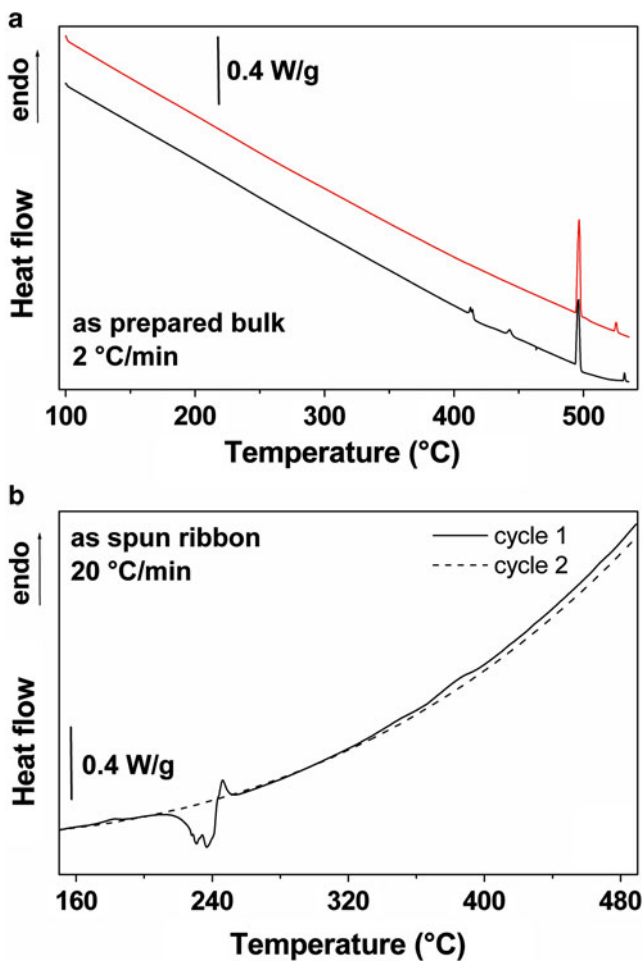
The microstructure and the composition of the samples before and after melt spinning were investigated by scanning electron microscopy (SEM) and energy-dispersive X-ray spectroscopy (EDXS), using an SEM EVO 40 by Carl Zeiss. Structural characterization was performed by X-ray diffraction (XRD). The measurements were performed on bulk or powdered samples in the angular range of 10–100°, with a step of 0.002°, using a PANalytical X'Pert Pro model diffractometer with  $Cu\ k_\alpha$  radiation. XRD measurements were also performed using an environmental chamber in order to study the structural evolution of as-spun samples as a function of temperature. Refinement of the XRD pattern was performed using Rietveld method by Full Prof Suite software in order to determine the lattice parameters and the relative phase fractions.

Thermal stability of the samples was investigated by differential scanning calorimetry (DSC) using a power compensation Perkin Elmer Diamond DSC.

## Results and Discussion

X-ray diffraction analyses of the bulk samples show only the reflections of the  $\epsilon$ - $Zn_4Sb_3$  equilibrium phase (not shown here), in accordance with the chemical composition measured by ICP ( $Zn_{57.3}Sb_{42.7}$  at.%) and the equilibrium-phase diagram [9]. The first DSC heating cycle of the bulk sample, Fig. 4.1a, shows a sequence of four endothermic signals between 409–411, ~440, ~493, and 532 °C. The sequence of endothermic peaks can be explained by the invariant reactions proposed in the equilibrium-phase diagram. However, the two signals at lower temperature (409–411 °C and 440 °C) are not compatible with the nominal and measured compositions, suggesting that the sample is not fully homogeneous, and can be related to the presence of a small amount of Zn-rich regions due to local fluctuation of the chemical composition. In the second DSC heating cycle, the first two low-temperature peaks disappear, while those at higher temperature are reproduced, indicating that after the first DSC heating cycle the sample results chemically homogeneous.

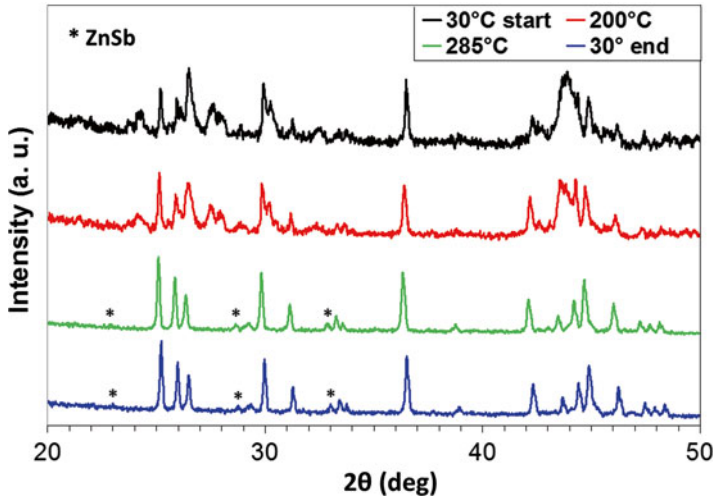
The XRD pattern of the as-spun sample (pattern at 30 °C start, in Fig. 4.2) shows the presence of the equilibrium-phase  $\epsilon$ - $Zn_4Sb_3$  and additional phases that could not be indexed. On the basis of the phase diagram, it is likely that some high-temperature phase has been retained as a consequence of the rapid quenching. The broadening of the reflections suggests that a highly defective microstructure was produced by



**Fig. 4.1** DSC traces of the bulk sample at 2 °C/min (black curve: first cycle; red curve: second cycle), (a), and the as-spun sample at 20 °C/min, (b)

rapid solidification. Furthermore, the low intensity of the pattern and the relative high value of baseline at low angle reflections suggest the presence of amorphous phases consistent with the rapid solidification proper of the melt spinning process. The values obtained for the lattice parameters of the rhombohedral cell ( $R_{-3c}$ ) are in agreement ( $a = 1.2228$  nm,  $c = 1.2424$  nm) with those reported in the literature for the  $\epsilon$ - $Zn_4Sb_3$  phase [10, 11].

The microstructure of the as-spun sample is shown by the SEM micrographs in Fig. 4.3. The as-spun sample reveals a cross section  $\sim 2$ – $10$   $\mu\text{m}$  thick (Fig. 4.3a), and a fine microstructure constituted by small elongated particles (about  $2 \times 6$   $\mu\text{m}^2$ ) (Fig. 4.3b), which are separated by small pores.

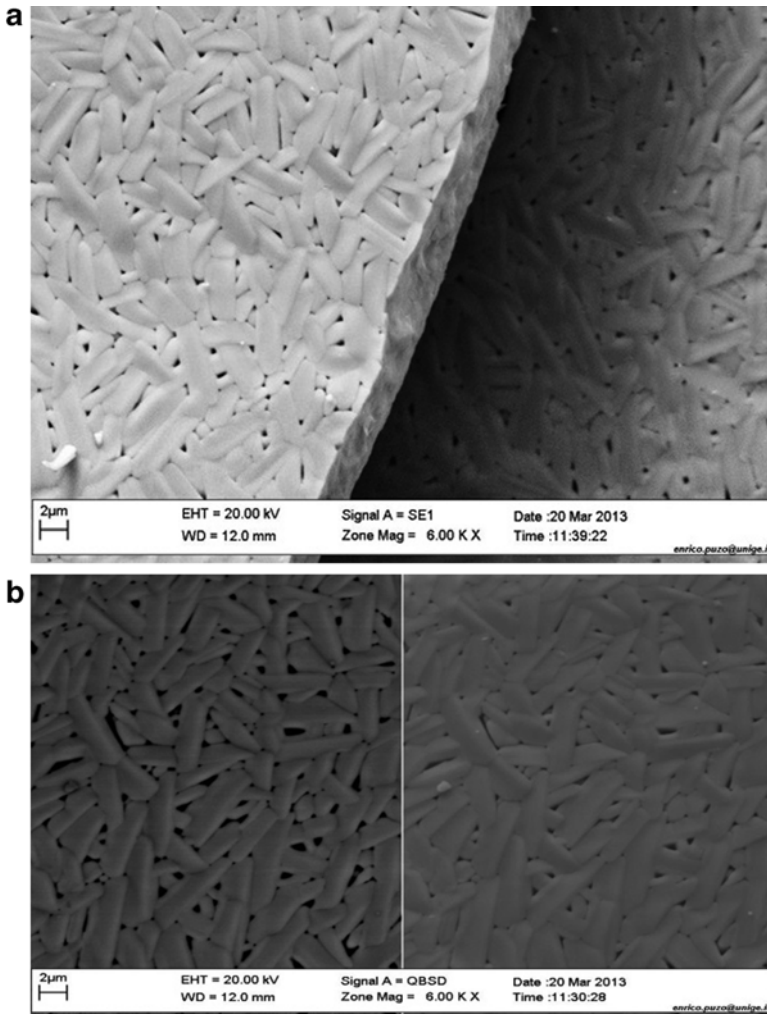


**Fig. 4.2** X-ray diffraction pattern of the as-spun ribbon as a function of temperature: 30 °C (start), 200, 285, and 30 °C (end)

The DSC measurements of the as-spun sample (Fig. 4.1b), show the disappearance of two irreversible exothermic signals between 200 and 260 °C during the second heating cycle. Such signals are compatible with the presence of amorphous or other metastable phases that irreversibly transform to more stable phases.

The structural evolution of the spun samples as a function of temperature is shown in Fig. 4.2. The XRD pattern at 200 °C does not show any significant variation with respect to the one measured at 30 °C (start). At 285 °C the pattern clearly shows the disappearance of the peaks related to secondary metastable phases and the appearance of some peak related to the phase ZnSb (oP16-CdSb) as indicated by the star in Fig. 4.2. Furthermore, the signal/baseline ratio tends to become higher after annealing at 285 °C and the profile of the crystallographic reflections becomes sharper indicating the occurrence of a recrystallization process and the disappearance of an amorphous phase responsible for the low intensities observed in the pattern of the as-spun sample. Finally, the XRD pattern at 30 °C (end) after the thermal cycle confirms the presence of the same phases formed at 285 °C indicating that the structural transformation into the equilibrium phases ZnSb and  $\epsilon$ -Zn<sub>4</sub>Sb<sub>3</sub> is irreversible and compatible with the transformation observed by DSC.

On the basis of the results obtained, it can be concluded that rapid solidification is a suitable technique for producing in a controlled way (i.e., no contamination, short processing time) microstructurally refined  $\epsilon$ -Zn<sub>4</sub>Sb<sub>3</sub>, that can be successfully used in the subsequent compaction step [12].



**Fig. 4.3** (a) Secondary electron SEM micrograph showing the cross section of the as-spun sample. (b) SEM micrograph showing the texture of the as-spun sample, constituted by small elongated particles divided by submicrometric pores. *Left image*: Secondary electron detector. *Right image*: Backscattered electron detector

## Conclusions

Melt spinning was used as an intermediate technique in the processing sequence for the preparation of thermoelectric  $\text{Zn}_4\text{Sb}_3$ .

Rapid solidification leads to a nonequilibrium solidification path with the possible formation of amorphous and metastable phases, together with the desired  $\epsilon\text{-Zn}_4\text{Sb}_3$  equilibrium phase. The broadening of the XRD patterns indicates the presence of a

highly defective microstructure. From the morphological point of view, the as-spun samples are characterized by thin foils (2–10  $\mu\text{m}$ ) constituted by an agglomeration of small elongated particles (around 2  $\mu\text{m}$  wide and 6  $\mu\text{m}$  long).

Irreversible transformations of the metastable phases in the as-spun sample were evidenced by DSC measurements and XRD analysis upon heating, showing the formation of the ZnSb and  $\epsilon\text{-Zn}_4\text{Sb}_3$  equilibrium phases after thermal cycling up to 285 °C.

**Acknowledgements** The authors would like to thank Dr. Gianluca Fiore for the support in the preparation of the rapidly solidified samples by melt spinning, Dr. Francesco Soggia for the ICP-AES analyses, and Dr. Elena Villa and Enrico Bassani for their support in open die processing and mechanical characterizations.

## References

1. Rowe DM (2006) *Thermoelectrics Handbook: macro to nano*. CRC, Boca Raton, FL
2. Snyder GJ, Toberer ES (2008) *Nat Mater* 7:105–114
3. Nolas GS, Sharp J, Goldsmid HJ (2001) *Thermoelectrics: basic principles and materials development*, vol 45. Springer, Berlin
4. Pan L, Qin XY, Liu M, Liu F (2010) *J Alloys Compd* 489:228–232
5. Toberer ES, Rauwel P, Gariel S, Taftø J, Snyder GJ (2010) *J Mater Chem* 20:9877–9885
6. Liu F, Qin XY, Xin HX (2007) *J Phys D Appl Phys* 40(24):7811–7816
7. Stiewe C, Dasgupta T, Bottcher L, Pedersen B, Muller E, Iversen B (2010) *J Electron Mater* 39(9):1976–1980
8. Baricco M, Bosco E, Olivetti E, Palumbo M, Rizzi P, Stantero A, Battezzati L (2004) *Int J Mater Prod Technol* 20:358
9. Okamoto H (2000) *Phase diagram binary alloys*. ASM International, Materials Park, OH
10. Carlini R, Marré D, Pallecchi I, Ricciardi R, Zanicchi G (2014) *Intermet* 45:60–64
11. Mozharivskiy YA, Pecharsky AO, Bud'ko SL, Miller GJ (2004) *Chem Mater* 16:1580–1589
12. Fanciulli C, Carlini R, Castellero A, Passaretti F, Baricco M, Zanicchi G (2013) Submitted to the 11th European Conference on Thermoelectrics, 18–20 November 2013. Noordwijk, The Netherlands

# Chapter 5

## The Role of Sodium-Rich Pretreatments in the Enhanced Sintering of Sodium Cobalt Oxide Thermoelectric Ceramics

E.M. Jakubczyk, C.L. Sansom, and R.A. Dorey

**Abstract** Oxide-based thermoelectric materials are of growing interest for high-temperature operation and as a route to eliminate elements, such as Te and Pb, that pose issues of safety, sustainability and security of supply.  $\text{NaCo}_2\text{O}_4$  bulk ceramic materials were prepared from powders synthesized using a solid state reaction (SSR) process. The effects of different Na-enriching pretreatments were evaluated with respect to microstructural evolution and thermoelectric and electric behaviours of the samples. Such modifications were found to be a critical factor affecting the microstructure of the bulk ceramic materials. Both premixing the powder and infiltrating a Na-rich precursor solution into the material prior to sintering were found to improve the density by up to 10 %, increase the electrical resistivity and help to compensate for Na losses at high sintering temperatures. A Seebeck coefficient and resistivity of 17  $\mu\text{V/K}$  and 2.85  $\text{m}\Omega\cdot\text{m}$ , respectively, were recorded around room temperature.

**Keywords** Sodium cobalt oxide • Thermoelectric oxide • SSR synthesis • Production modification • Electrical properties • Structural changes

---

E.M. Jakubczyk • C.L. Sansom  
School of Applied Sciences, Cranfield University, Cranfield, Bedfordshire, MK43 0AL, UK  
e-mail: [e.m.jakubczyk@cranfield.ac.uk](mailto:e.m.jakubczyk@cranfield.ac.uk); [c.l.sansom@cranfield.ac.uk](mailto:c.l.sansom@cranfield.ac.uk)

R.A. Dorey (✉)  
University of Surrey, Guildford, Surrey, GU2 7XH, UK  
e-mail: [r.dorey@surrey.ac.uk](mailto:r.dorey@surrey.ac.uk)



## Introduction

The increasing level of interest in thermoelectric materials is driven not only by the search for materials with increased thermoelectric efficiency close to room temperature but also materials which can be used for applications at higher temperatures where generation efficiencies are higher. Layered cobaltites exhibit a large Seebeck coefficient, small resistivity and thermal conductivity making them attractive for such thermoelectric applications.

A number of proposals for the synthesis  $\text{Na}_x\text{Co}_2\text{O}_4$  have been reported in literature including: solid state reaction (SSR) [1], auto-ignition followed by the airflow shatter process [2], the citric acid complexing (CAC) [3,4], reactive template grain growth (RTGG) [5], polymerized complex (PC) method [6], sol gel (SG) method [7]. To produce usable thermoelectric materials those powders need to be shaped and sintered to produce homogeneous bulk materials. Such sintering requires high temperatures to bring about densification. However the use of high temperatures has a deleterious effect on composition due to the volatile nature of Na. Here, a number of sodium-rich pretreatments are proposed to both compensate for Na loss and reduce the high temperature.

## Experimental

The sodium cobalt oxide powder was produced by a mixed oxide synthesis route whereby the reagent powders  $\text{Co}_3\text{O}_4$  (99.9 %) and  $\text{Na}_2\text{CO}_3$  (99.9 %), in a Na:Co atomic ratio of 1:2, were ball milled in propan-2-ol for 24 h using  $\text{ZrO}_2$  milling media. The resulting slurries were dried in an oven at 75 °C for 12 h. The mixed powders were then calcined at 850 °C for 12 h in air to yield  $\text{NaCo}_2\text{O}_4$ . Besides the  $\text{NaCo}_2\text{O}_4$  phase, the calcined powder also contains small amounts of residual initial reactants. Three routes to incorporate a NaOH sintering aid were evaluated as detailed in Table 5.1.

All pellets were uniaxially pressed using a pressure of 13 MPa and sintered at 950 or 1,000 °C for 1, 2, 6, and 12 h. The sintered samples were examined using X-ray diffraction (XRD) at room temperature. The microstructure of the as-sintered samples was examined using a scanning electron microscope (SEM) and energy dispersive X-ray spectroscopy (EDX). The density was determined from the measured weight and dimensions of the prepared pellets. The Seebeck coefficient was determined by applying a temperature differential across the sintered pellets and measuring the resultant voltage. In all tests the temperature of the hot side was controlled by means of a custom hot plate mounted above the sample. The temperature differential was maintained through the use of a cooled metal plate on the cold side of the sample. Temperature differences of between 10 and 30 °C were applied with this method with no significant difference in results observed. The thermal conductivity was measured using a heat flux method, using

**Table 5.1** Processing stages, and details of Na pretreatments, used in the preparation of  $\text{NaCo}_2\text{O}_4$  pellets

Preparation procedures	Sample			
	Solid state reaction (SSR)	Infiltrated (INF)	Mixed (M)	Ball milled (BM)
Ball mill: $\text{Na}_2\text{CO}_3 + \text{Co}_3\text{O}_4$ (1:2 mol ratio) for 24 h, calcinated at 850 °C for 12 h	x	x	x	x
Ball milled process (24 h) in propan-2-ol and dry at 75 °C	x	x	x	
Ball mill (24 h) in NaOH aqueous solution <sup>a</sup> and dry at 80–90 °C				x
Mix SSR powder with NaOH aqueous solution <sup>a</sup> and dry			x	
Press into pellet	x	x	x	x
Infiltrate the surface of pellets with NaOH aqueous solution <sup>a</sup> and dry at 80–90 °C		x		
Sintered at 950–1,000 °C for 1–12 h	x	x	x	x

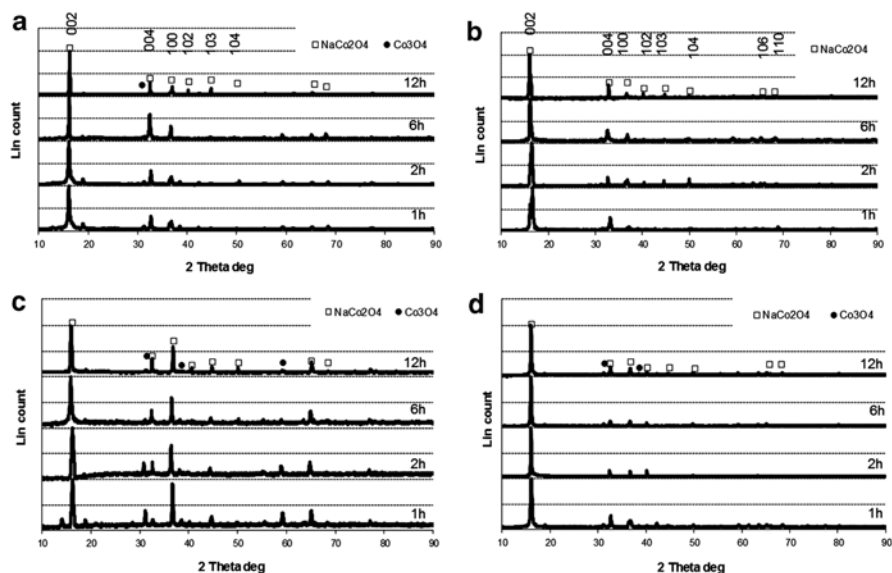
<sup>a</sup>2 wt% (relative to the  $\text{NaCo}_2\text{O}_4$  powder mass) of NaOH dissolved in distilled water

a low-temperature differential (40–80 °C), where the sample was sandwiched between two glass samples of known thermal conductivity and the temperature recorded at each interface.

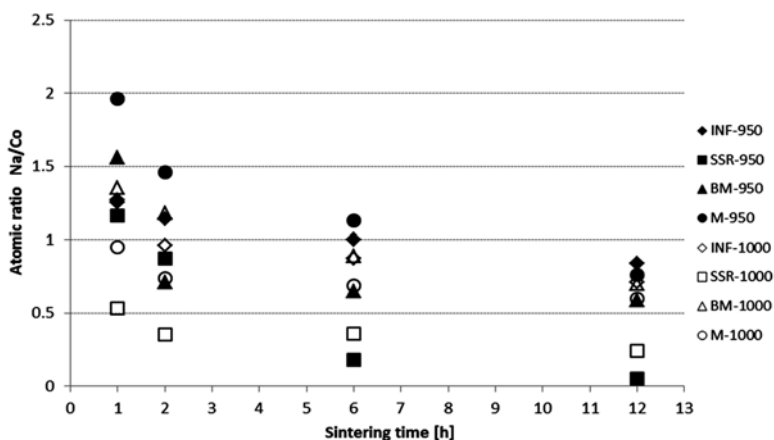
## Result and Discussion

The XRD patterns of the pellets sintered at 950 °C for different lengths of time are shown in Fig. 5.1. All of the prepared pellets contained  $\text{NaCo}_2\text{O}_4$  (JCPDF no. 27 0682) in addition to residual  $\text{Co}_3\text{O}_4$ . A reduction in  $\text{Co}_3\text{O}_4$  content was observed with increasing sintering time. Additionally, the amount of  $\text{Co}_3\text{O}_4$  was lower in samples subjected to Na pretreatments. The Na:Co ratio, as determined by EDX, of the materials sintered under different conditions is shown in Fig. 5.2. All samples showed high purity. Additionally, it can be noted that the most consistent composition is shown by the infiltrated (INF) pellets. However, both EDX and XRD analysis indicate loss of sodium with increasing temperature and sintering time for all samples. The observed co-occurrence of decreases in  $\text{Co}_3\text{O}_4$  and Na is explained by the homogenisation through atomic diffusion consuming  $\text{Co}_3\text{O}_4$  and simultaneous loss of Na from the system leading to the formation of low sodium Na-Co oxide phases.

The ceramic samples pretreated with additional sodium show a measured density close to the theoretical density 4.5 g/cm<sup>3</sup> in particular after sintering at the higher (1,000 °C) temperature. The samples showed an increased density with increased sintering temperature and processing time, especially evident at higher sintering temperature (Fig. 5.3).

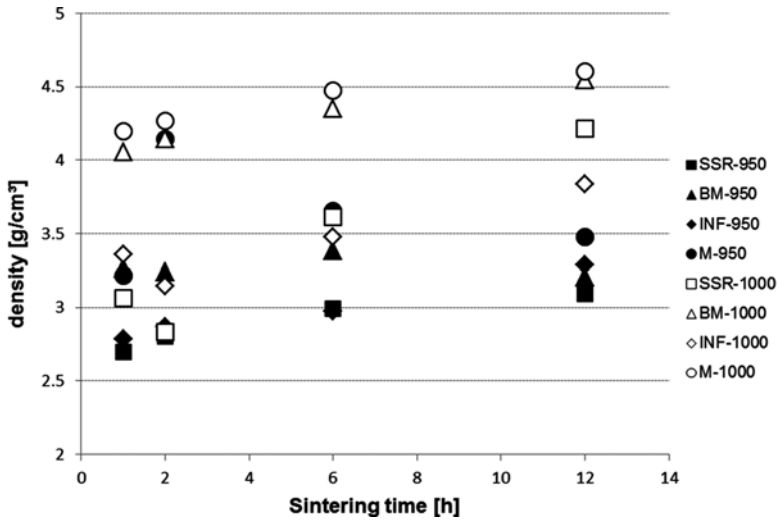


**Figure 5.1** XRD patterns of pellets sintered at 950 °C for a 1, 2, 6 and 12 h respectively: (a) solid state reaction, (b) infiltrated, (c) ball milled, (d) mixed



**Figure 5.2** Variation in Na/Co atomic ratio as a function of sintering time, sintering temperature and NaOH pretreatment

The results shown in Table 5.2 indicate that the thermal conductivity was slightly affected by sintering temperature. No detectable variation in thermal conductivity was observed with changes in sintering time. Despite increases in density, corresponding increases in thermal conductivity were not observed due to a simultaneous loss of Na from the system due to volatilisation at elevated sintering temperatures.



**Figure 5.3** Evolution of density as a function of sintering time, temperature and NaOH pretreatment

**Table 5.2** Dependence of thermal conductivity of pellets on sintering temperature and Na pretreatment

Sample	Average $\kappa$ [W/m K] ( $\pm 0.1$ )	
	Sintered at 950 °C	Sintered at 1,000 °C
SSR	1.51	1.76
BM	1.24	1.21
INF	1.24	1.22
M	1.39	1.32

All samples were sintered for 12 h

**Table 5.3** Average voltage output, Seebeck coefficient and electrical conductivity of untreated and pretreated  $\text{NaCo}_x\text{O}_y$  pellets sintered for 12 h

	Average sample temperature (°C)	Voltage output range (mV)	Average Seebeck coefficient ( $\mu\text{V/K}$ ) ( $\pm 0.5$ )	Average electrical resistivity ( $\text{m}\Omega\cdot\text{m}$ ) ( $\pm 0.2$ )
SSR	41.4	0.17–0.48	17.8	2.85
BM	41.6	0.24–0.63	23.2	4.49
INF	41.6	0.23–0.66	22.0	3.39
M	41.5	0.23–0.57	19.7	2.97

Within experimental errors no differences in results for samples produced at 950 and 1,000 °C could be observed

The study shows that the pretreatment of samples affects the thermoelectric properties to a large degree with the Seebeck coefficient increasing with sodium pretreatment (Table 5.3). For each sample type, all data was within experimental error and no effect of temperature could be discerned. Moreover, all materials produced a positive Seebeck coefficient that confirms a p-type behaviour. Values of Seebeck coefficient recorded in this work are similar to those found in the literature [1].

With the solid-state reaction (SSR) material considered as the reference material, three microstructural changes can be considered to have led to the observed changes in electrical and thermal properties: (1) increases in density leading to increased thermal and electrical conductivities; (2) increases in grain size leading to increased conductivities; (3) the formation of a second phase at the grain boundaries predominantly affecting thermal conductivity. This is manifested in each of the samples such that:

- Ball milled (BM)—Enhanced densification and grain growth offset against formation of grain boundary phase result in decreased electrical and thermal conduction.
- Infiltrated (INF)—Minimal changes in microstructure relative to SSR with slight grain boundary disruption results in a decrease in thermal conductivity.
- Mixed (M)—The densification, without grain growth, and the formation of a second phase at the grain boundaries results in decreased thermal conductivity but no changes in electrical conductivity.

## Conclusion

Thermoelectric ceramics were successfully prepared using three different Na-rich pretreatments. The results suggested that the Na-rich pretreatment methods played an important role in enhancing the thermoelectric behaviour of bulk ceramics. The infiltration pretreatment of the sodium cobalt oxide samples resulted in enhanced stability of the chemical composition, while BM also better maintains the correct stoichiometry. All NaOH pretreatments resulted in enhancements in uniformity of shape and reduced porosity.

**Acknowledgment** This work was supported by EC project MATS - Multipurpose Applications by Thermodynamic Solar (Project No. FP7-ENERGY-2010-2,268219).

## References

1. Seetawan T, Amornkitbamrung V, Burinprakhon T, Maensiri S, Tongbai P, Kurosaki K, Muta H, Uno M, Yamanaka S (2006) *J Alloy Compd* 416:291
2. Pramanick AK, Das PK (2006) *Int J Heat Mass Transf* 49:1420
3. Terasaki I (2003) *Phys B Condens Matter* 328:63
4. Katsuyama S, Kishida A, Ito M (2006) *J Alloy Compd* 414:215
5. Tajima S, Tani T, Isobe S, Koumoto K (2001) *Mater Sci Eng B Solid* 86:20
6. Seetawan T, Amornkitbamrung V, Burinprakhon T, Maensiri S, Kurosaki K, Muta H, Uno M, Yamanaka S (2006) *J Alloy Compd* 414:293
7. Ma F, Ou Y, Yang Y, Liu Y, Xie S, Li J-F, Cao G, Proksch R, Li J (2010) *J Phys Chem C* 114:22038

# Chapter 6

## Novel Process for Metal Silicide Nanostructures Regarding Cheap and Large-Scale Material Synthesis

A. Schönecker, P.-Y. Pichon, J. König, M. Jägler, M. den Heijer, and B. Kraaijveld

**Abstract** Thermoelectric power generation presents a promising and attractive way to utilize waste heat and to generate electricity in remote locations. Thanks to continuing technology development an outlook of converting a significant amount of waste energy comes within reach. The class of structured metal silicide materials ( $\text{MgSi}_2$ ,  $\text{Mn}_{11}\text{Si}_{19}$ ,  $\text{CrSi}_2$ ) is considered a class of sustainable and cost-effective candidates for thermoelectric applications. An important way to improve the effectiveness of these materials is by nanostructuring. Nanostructured metal silicides can be obtained by using a rapid solidification technology, ribbon growth on substrate (RGS), where a mixture of liquid metal and silicon melt is solidified under controlled conditions by cooling on a solid, reusable substrate. This technology allows for low-cost and high-throughput synthesis of silicide materials with controllable structures in the nano- and micrometer range. Crystallizing materials from the melt allows for an easy way to add dopants or alloy with different metals. Controlling the structure and composition offers the opportunity of optimizing the thermoelectric properties of silicides. This paper describes the current status of development and validation process for higher manganese silicides and chromium silicides as demonstrators, as well as future perspectives for TE applications.

**Keywords** Thermoelectric material • Higher manganese silicides • Metal silicides • Eutectic • Nanostructuring

---

A. Schönecker (✉) • P.-Y. Pichon • M. den Heijer • B. Kraaijveld  
RGS Development B.V., P.O. Box 40, 1724ZG Oudkarspel, The Netherlands  
e-mail: [Schonecker@rgsdevelopment.nl](mailto:Schonecker@rgsdevelopment.nl)

J. König • M. Jägler  
Fraunhofer IPM, Institute for Physical Measurement Techniques,  
Heidenhofstr. 8, 79110 Freiburg, Germany

## Introduction

Thermoelectric conversion of thermal energy into electricity has been a well-known technology for many years; however, the production of mid-temperature thermoelectric systems has always been limited in volume to special applications or niche markets. Recently, there are a couple of factors that make it very likely that thermoelectric are on the verge of becoming a widespread commodity technology. The expectation is that with the increase in conversion efficiency that has been realized by development of new classes of nanostructured thermoelectric materials, the technology is now ready for widespread use [1]. However, in order to enable large-scale market development, not only does the conversion efficiency and the figure of merit but also factors like, the availability of raw materials, the cost of materials and systems, environmental aspects, and large-scale manufacturing capability become areas of importance.

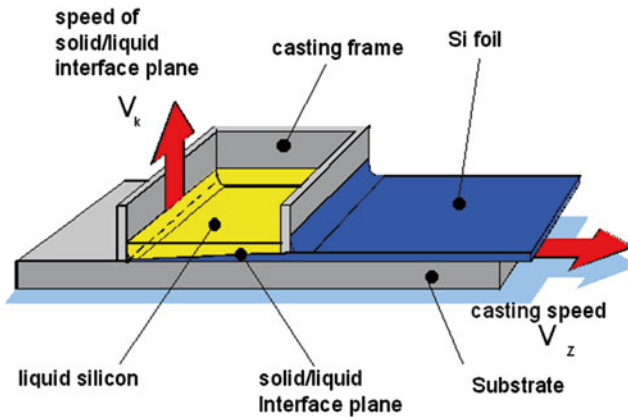
Weighing all factors, the family of metal silicide materials, such as higher manganese silicides, magnesium silicide, and others have a high potential in enabling this widespread market development [2]. Silicon is one of the most abundant materials on Earth. Metal silicides show a very promising figure of merits [3], are environmentally benign, and potentially of very low cost. Furthermore, many metal silicides are resistant to corrosion and stable even under high temperature. Beyond the well-known higher manganese silicides, iron silicide, and magnesium silicide, there is a large potential for further excellent material combinations in this group. Additionally, the ability to provide nano- and microstructured material composition of silicon in combination with metal silicides allows for the tuning of electron and phonon properties beyond the silicide in itself.

This paper demonstrates the state of the art of the ribbon growth on substrate (RGS) process providing a low-cost manufacturing method for the development, optimization, and industrial-scale production of structured metal silicide materials for thermoelectric applications.

## Structured Metal Silicide Manufacturing

### *The RGS Technology*

The RGS technology has been developed to provide a cost-efficient alternative to the silicon wafer manufacturing process in the field of photovoltaic solar energy. The concept of the process is to combine a high-speed silicon crystallization process with sufficient control to allow for wafer qualities that enable state-of-the-art solar cell efficiencies. The unique feature of the process is the controlled crystallization by cooling on a solid material, the substrate (see Fig. 6.1). After crystallization, the produced sheet can be removed and the substrate is reused for the next crystallization. This concept combines a high production rate with excellent crystallization



**Fig. 6.1** Principle of the RGS—Ribbon Growth on Substrate wafering process

**Table 6.1** Example of RGS manufacturing costs for silicon wafers (note that input material and casting costs are subject to the material used; further processing steps such as ball milling and spark plasma sintering are not considered)

RGS Si casting	Input Si material costs (€/kg)	Nominal throughput [kg/h]	Output Si material costs (€/kg)
	10–20	40–60	40–75

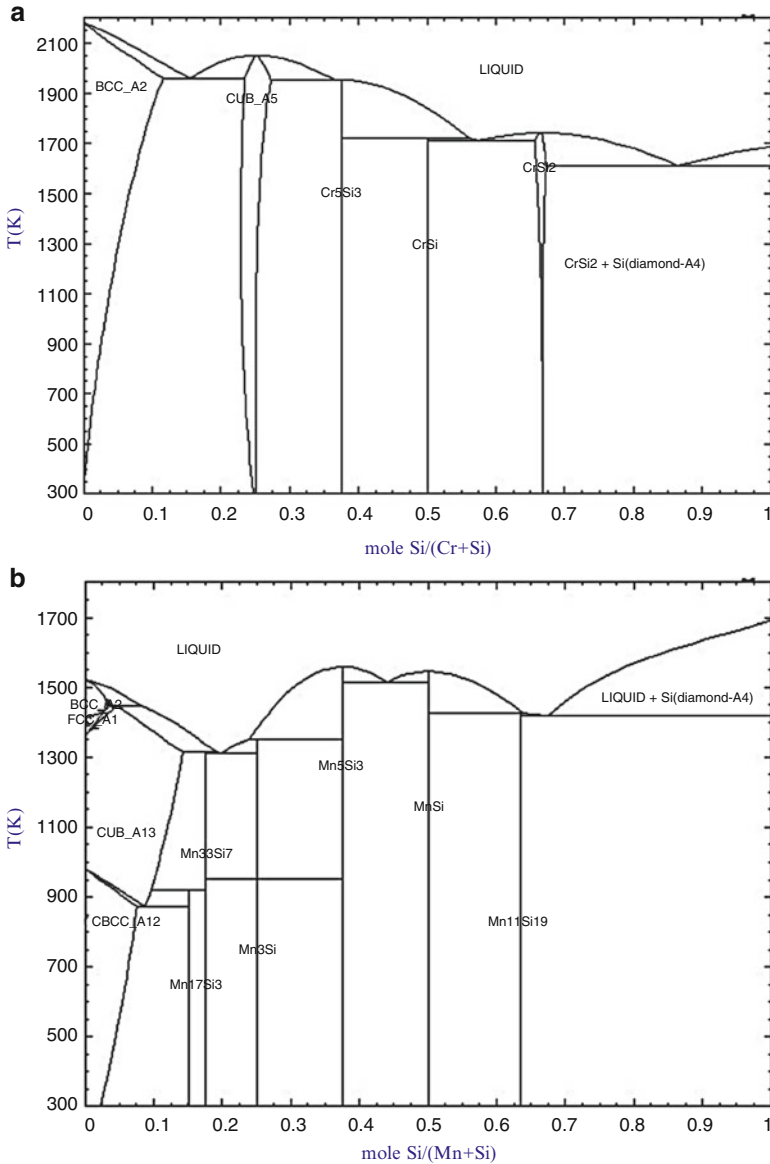
control that allows for tuning of the crystallization velocity over a wide range, without influencing the material output rate. In a well-control environment, this process also has the capability to produce other materials from a liquid silicon melt, such as metal silicides and structured metal silicides.

Being developed for solar wafer manufacturing, the process has been optimized for low manufacturing costs and a high throughput of material. The product typically is a sheet of silicon, or metal silicide composite with a nominal dimension of  $156 \times 156 \text{ mm}^2$  and an adjustable thickness between 0.1 and 1 mm. The material can be further processed by etching or mechanical processing such as ball milling. Table 6.1 summarizes a typical output volume, costs assuming the manufacturing of a Si sheet based upon solar grade silicon.

## Structured CrSi-Si Eutectic Material

The characteristics of metal silicides grown from the liquid state by rapid solidification in contact with a substrate are mainly controlled by the following parameters: melt composition, crystal growth velocity, under-cooling, nucleation affinity with the substrate material, and substrate parameters such as the choice of material and

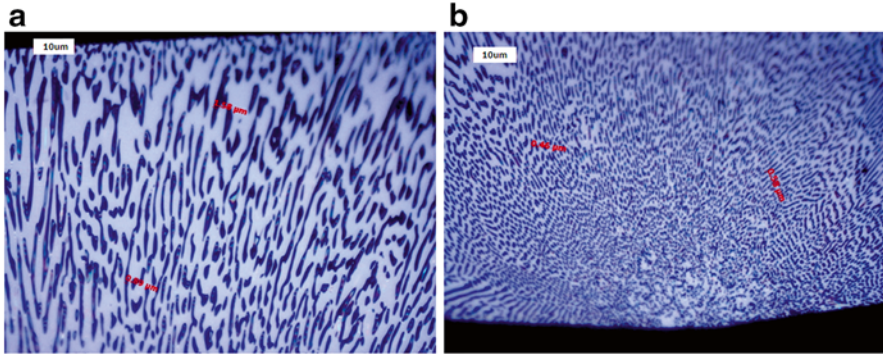




**Fig. 6.2** Binary phase diagrams of the Cr-Si (a) and Mn-Si (b) systems [3]

surface geometry. Controlling these parameters allows for the design of specific material properties according to the application requirements.

As an example, the growth of a CrSi<sub>2</sub>-Si structured sheet is described in the following. In the Cr-Si phase diagram (see Fig. 6.2a), a eutectic point exists in the silicon-rich side of the diagram around 85 at. % Si. Assuming a thermodynamic equilibrium, the eutectic composition, cooled down to crystallize into a solid sheet,



**Fig. 6.3** Cross sections of the  $\text{CrSi}_2$ -Si (Table 6.2—C1) material after removal of the  $\text{CrSi}_2$  by wet chemical etching in the fast growing volume (**b**), the typical structure geometry is  $\sim 500$  nm. In the slow growing region (**a**), the geometry is  $\sim 1,500$  nm

will solidify into two solid phases  $\text{CrSi}_2$  and Si. These eutectic systems are well known and the growth of the phase structure is described by Jackson et al. and Trivedi et al. [4, 5]. According to these models, the phases show typical rod-like or lamellar patterns with a geometrical dimension that is controlled by the crystallization velocity, the diffusivity of the components in the melt, and the interface energies between the different phases.

The model predicts a dependence of the microstructure scale (lamellar spacing  $L$ ) with the solidification velocity  $v$  according to:

$$L = \frac{k}{v^2} \quad (6.1)$$

with  $k$  being a constant depending on the material properties only.

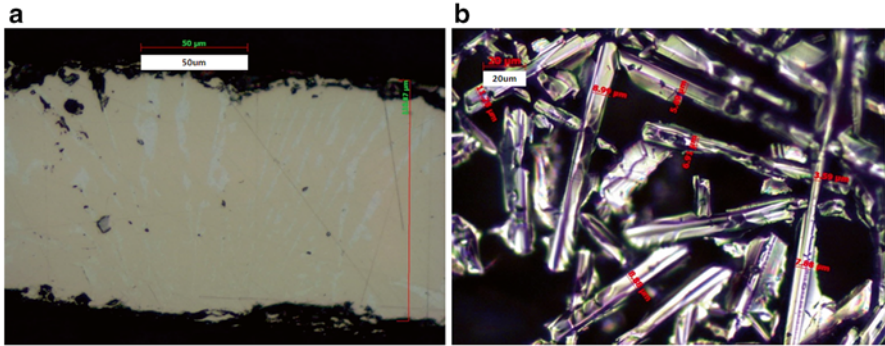
Figure 6.3 shows microscope pictures of a cross section of  $\text{CrSi}_2$ -Si eutectic material, at two different crystallization velocities. The faster crystallization velocity (Fig. 6.3b) results in a microstructure scale of  $\sim 500$  nm, while at the slower crystal growth velocity (Fig. 6.3a), the microstructure scale is  $\sim 1,500$  nm. Depending upon the growth velocity, the structure size can thus be determined. By controlling the crystallization velocity via the substrate in the RGS process, the micro-/nanostructure can be adjusted.

## Structured Higher Manganese Silicide Material

Higher manganese silicides are generally of great interest as potential candidates for highly efficient thermoelectric materials [6]. However, the phase diagram for Mn-Si compositions shows some relevant differences compared to the  $\text{CrSi}_2$ -Si system (Fig. 6.2b). The most obvious difference is the position of the eutectic point, which

**Table 6.2** Material descriptions and their different compositions

Code	Description	Overall composition (at. %)		Phase composition (wt. %)	
C1	CrSi <sub>2</sub> -Si	Si=85	Cr=15	Si=52	CrSi <sub>2</sub> =48
C2	CrSi <sub>2</sub>	Si=67	Cr=33	Si=0	CrSi <sub>2</sub> =100
M1	MnSi <sub>1.74</sub> -Si	Si=67	Mn=33	Si=7	MnSi <sub>1.74</sub> =9
M2	MnSi <sub>1.74</sub>	Si=63	Mn=37	Si=0	MnSi <sub>1.74</sub> =100



**Fig. 6.4** Cross section of (a) Mn<sub>11</sub>Si<sub>19</sub>-Si eutectic sheet (Table 6.2, M1) and (b) the silicon phase after etching away Mn<sub>11</sub>Si<sub>19</sub>. The *light grey needle* like areas correspond with the Si phase, the slightly *darker* areas are the Mn<sub>11</sub>Si<sub>19</sub> phase

is much closer to the Mn<sub>11</sub>Si<sub>19</sub> phase. When such a eutectic melt is crystallized, the Mn<sub>11</sub>Si<sub>19</sub> phase has higher volume ratio compared to the silicon phase. Furthermore, the Mn<sub>11</sub>Si<sub>19</sub> phase is not “well defined” as there is a number of Mn-Si ratios around this point [7].

In order to produce such a material, tests were done using the eutectic composition (see Table 6.2, M1) and the exact Mn<sub>11</sub>Si<sub>19</sub> composition (Table 6.2, M2) without additional silicon. Prior to melting, the Mn surface was etched to remove any oxide layer and the melting and crystallization process was done in an argon environment to prevent oxide formation during the process itself.

In the case of eutectic growth of two phases with atomically rough growth interface, the growth morphology typically forms lamellar or rod like structures (CrSi<sub>2</sub>-Si). When a phase grows with an atomically smooth interface, the morphology is more complex due to faceting of one phase (Mn<sub>11</sub>Si<sub>19</sub>-Si). This explains the differences between the structure of CrSi<sub>2</sub>-Si (Fig. 6.3) and the morphology of the Mn<sub>11</sub>Si<sub>19</sub>-Si sample (Fig. 6.4) with the strongly faceted silicon crystal phase (Fig. 6.4b). It is well known that pure silicon solidifies into faceted crystals [8], because it has an atomically smooth interface. As is also known, the addition of solute can roughen the growth interface of silicon [9]. Although we do not have the thermodynamic data to evaluate the interface roughness of Si in the case of these eutectics as in Taylor et al. [9], the strongly directional silicon crystal structures in the case of the Mn<sub>11</sub>Si<sub>19</sub>-Si eutectic are likely caused by faceting of the silicon–melt

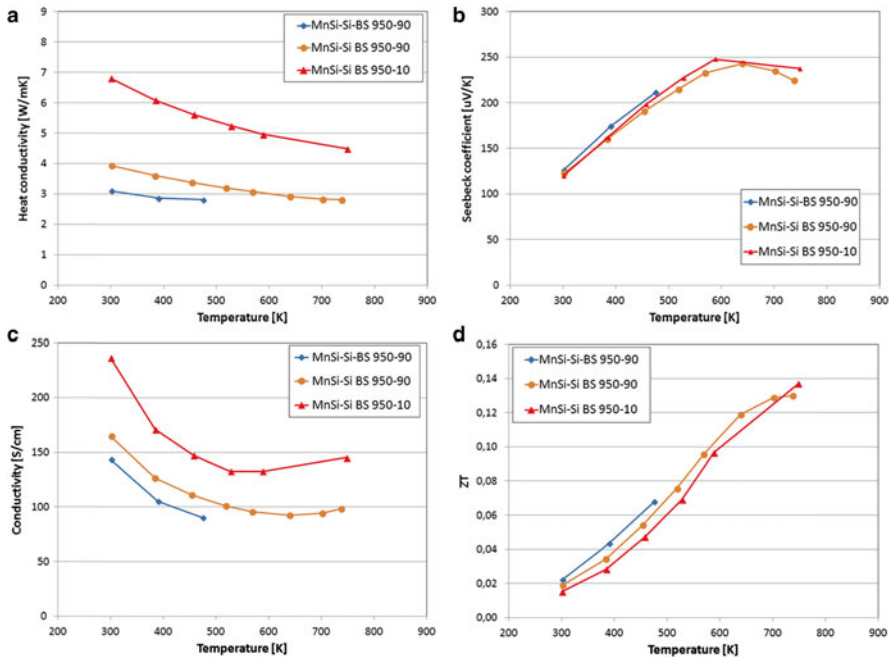
interface during growth. The lamellar morphology of the  $\text{CrSi}_2\text{-Si}$  shows that the silicon–melt interface is rough in this case. After the results of the thermoelectric property measurements are available, process tuning can be used to change material composition and structural properties to further optimize the material properties.

## Thermoelectric Properties of $\text{Mn}_{11}\text{Si}_{19}\text{-Si}$ and $\text{CrSi}_2\text{-Si}$

The first sample grown by the RGS process was ball-milled and sintered into 1-mm diameter, 1-mm high legs using spark plasma sintering technology. In order to optimize the sintering process, temperature and sinter duration were varied. Figure 6.5 shows the thermoelectric properties of the samples sintered for 10 and 90 min, respectively, at 950 °C.

Measurements of the thermoelectric properties of the other samples are still ongoing. Table 6.3 shows the preliminary measurements of a  $\text{CrSi}_2\text{-Si}$  sample.

Although not all samples have been characterized yet, the results above indicate the potential of  $\text{Mn}_{11}\text{Si}_{19}\text{-Si}$  as industrially useful thermoelectric material. The Seebeck coefficient and thermal conductivity of  $\text{Mn}_{11}\text{Si}_{19}\text{-Si}$  are very promising.



**Fig. 6.5** (a) Heat conductivity, (b) Seebeck coefficient, (c) electrical conductivity, and (d) calculated ZT of  $\text{Mn}_{11}\text{Si}_{19}\text{-Si}$  samples after ball milling and spark plasma sintering. The samples were sintered at 950 °C for 90 min (MnSi-Si BS 950-90) and 10 min. (MnSi-Si BS 950-10)

**Table 6.3** Initial characterization results of a  $\text{Mn}_{11}\text{Si}_{19}\text{-Si}$  sample and a  $\text{CrSi}_2\text{-Si}$  sample after ball milling and sintering at 950 °C for 90 min

Sample	Electrical Conductivity [S/cm]	Seebeck coefficient [mV/K]	Thermal conductivity [W/m K]	ZT	Temperature [K]
CrSi-Si 950-10	1.8	360	36.2	0.00019	299
	4.9	255	24.8	0.00060	473
	16.1	195	18.5	0.00213	647
	43.2	139	15.0	0.00456	821

However, the electrical conductivity should further be improved by adding a dopant to the melt during the RGS process for example. The  $\text{CrSi}_2\text{-Si}$  sample exhibits a low electrical conductivity and relatively high thermal conductivity. As a consequence, the figure of merit ( $ZT$ ) is almost two orders of magnitude lower than for  $\text{Mn}_{11}\text{Si}_{19}\text{-Si}$ . Due to the lower band gap of  $\text{CrSi}_2\text{-Si}$ , it is generally believed that such a material is unlikely candidate for high figure of merit. However, structuring  $\text{CrSi}_2\text{-Si}$  and changing its composition have not been investigated so far.

## Conclusions and Outlook

Although the application of the low-cost, high-throughput RGS technology to thermoelectric materials has only started quite recently, preliminary results on test materials and the ability to tune the material to the desired properties strongly indicate that this technology can be an ideal base for the development, optimization, and market introduction of metal silicides for thermoelectric power generation.

In order to develop these materials in the short term, it is necessary to gain a deeper understanding of the material properties, especially in a multi-phase material. As the number of combinations of possible material compositions and structures is very large, a technology roadmap is needed to develop a strategy for material optimization. Interesting areas with respect to that are: phonon transport properties at metal silicide–silicon at phase boundaries; microscopic crystal characterization with respect to the electron mobility and the conductivity in a two-phase material. The addition of doping materials to change the conductivity type and optimize the carrier concentration have to be known as well as the impact of phases and doping on the band structure.

With the application of the RGS crystallization process in combination with metal-silicon melts, a low-cost, industrialized process is available for large-scale manufacturing of thermoelectric materials. This process allows the structural and chemical composition control over a wide parameter range. It is further expected that these materials show good thermal stability due to their typical production temperature exceeding 1,000 °C.

Combining the know-how of the thermoelectric community on material development (technology roadmap) with a market introduction plan, the availability of the

RGS technology provides the opportunity to rapidly produce metal silicide–silicon based systems and test them with respect to their thermoelectrical properties.

Consequently the combination of the promising class of metal silicide materials with the low-cost, high-throughput RGS manufacturing process can be the enabler to reduce the cost of thermoelectrical power generation and to open the market for large-scale application.

**Acknowledgements** Fraunhofer IPM acknowledges the financial support from the ThermoMag Project, which is co-funded by the European Commission in the 7th Framework Programme (contract NMP4-SL-2011-263207), by the European Space Agency and by the individual partner organizations.

## References

1. Observatory Nanobriefing (2011) [www.nanopinion.eu/sites/default/files/observatorynano\\_briefing\\_no.17\\_thermoelectricity\\_for\\_energy\\_harvesting.pdf](http://www.nanopinion.eu/sites/default/files/observatorynano_briefing_no.17_thermoelectricity_for_energy_harvesting.pdf). Accessed 11 Nov 2013
2. Fedorov MI (2009) *J Thermoelectricity* 2:51
3. [www.factsage.com](http://www.factsage.com). Accessed 11 Nov 2013
4. Jackson KA, Hunt JD (1966) *T Metall Soc AIME* 236:1129
5. Trivedi R, Magnin P, Kurz W (1987) *Acta Metall Mater* 35(4):971
6. Takashi I (2010) *Trans JWRI* 39(2):276
7. Miyazaki Y, Igarashi D, Hayashi K, Kajitani T (2008) *Phys Rev B* 78:214104
8. Aoyama T, Takamura Y, Kuribayashi K (1999) *Metall Mater A* 30A:133
9. Taylor MR, Fidler RS, Smith RW (1971) *Mater Trans* 2:1793

# Chapter 7

## A Flexible Measurement System for the Characterization of Thermoelectric Materials

M. Schönhoff, F. Assion, and U. Hilleringmann

**Abstract** The figure of merit needs to be determined to rate the quality of thermoelectric materials (TM). Therefore, it is necessary to measure all involved parameters—the Seebeck coefficient ( $S$ ), the thermal conductivity ( $\lambda$ ), and the electrical conductivity ( $\sigma$ ).

Hence, a concept of a measurement system was developed to perform a quick and global characterization of TM by the use of two different sample mounts. The maximum measurement temperature was planned to be at least 600 °C. The first mount contains a four-point measurement system to determine the electrical conductivity. The second one generates a heat flow which could be metered by measuring temperatures at six specified points. In combination with the recorded voltage at two points on the sample,  $S$  and  $\lambda$  can be calculated at the same time.

Because of the strong dependence between contact resistance and contact pressure, the measurement system was designed to keep the pressure constant for a high reproducibility and a small error margin. All measuring points like the commercial spring-mounted pogo-pins and the thermocouples (TC), which are integrated spring-mounted in a special designed capsule, have small variances.

Experiments could show that the divergence of the force from the mounting cylinder to the sample is constant and not dependent on the air pressure. Thus, the accuracy of the measurement device was improved by increasing the contact pressure.

**Keywords** Measurement device • Characterization • Contact resistance • Measuring error

---

M. Schönhoff (✉) • U. Hilleringmann  
Institute of Electrical Engineering and Information Technology,  
University of Paderborn, 33098 Paderborn, Germany  
e-mail: [schoenhoff@sensorik.upb.de](mailto:schoenhoff@sensorik.upb.de)

F. Assion  
Sensor Technology Department, University of Paderborn, Paderborn, Germany

## Introduction

Thermoelectric generators (TEG) can be used to harvest electric power from waste heat [1]. Hence, there are a great number of possible applications and a big potential for TEGs. However, due to their low efficiency, they are currently not widely used yet.

Proper characterization of thermoelectric materials (TM) is necessary to analyze new materials and improve them [2]. Their efficiency is given by the figure of merit:

$$ZT = \frac{S^2 \times \sigma}{\lambda} \times T \quad (7.1)$$

where  $S$  is the Seebeck coefficient,  $\lambda$  is the thermal conductivity, and  $\sigma$  is the electrical conductivity [3]. Nowadays, there are different measurement systems to characterize each of these parameters separately, but there is no commercial device which can be used to determine all the three parameters. However, even these measurement devices are very expensive and/or very complex [4]. In addition to this, the characterization of TE materials could be difficult, when different sample dimensions are required for the various measurement systems.

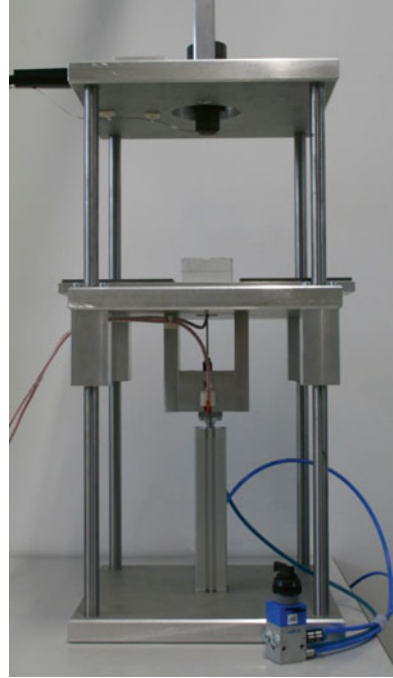
## Experiment

For characterizing TM a pneumatic measurement system was built with the basic objective to acquire and minimize errors caused by thermal and electrical contact resistance. These contact resistivities are strongly dependent on the contact pressure [5, 6]. Initial experiments have shown that the output power of a silicon based TEG can be enhanced by almost 600 % just by increasing the contact pressure from the heat source to the TEG. This gives an idea about how important a constant and reproducible pressure is for high accuracy measurement systems. Thereby, the use of a pneumatic system gives a great advantage, because the pressure is constant and it does not change with thermal expansion of the sample. Present measurement devices generate the contact pressure with a screw system or a spring. By the use of a screw system the measurement setup is absolutely fixed. Thus, the contact pressure increases during measurement caused by thermal expansion of the sample. This effect can be reduced by using a spring but it does not vanish though. Hence, a pneumatic system is a promising new approach.

The frame of the measurement device consists of two massive aluminum platforms with dimensions of  $300 \times 300 \times 30$  mm and four shafts between them with a length of 720 mm each. The heat source is fixed at the upper platform. A third platform with the same dimensions is mounted in the middle applying ball bearings, as Fig. 7.1 depicts. It can be lifted up by a pneumatic cylinder whose force can be controlled by used compressed air pressure, and defines the resulting contact pressure



**Fig. 7.1** Full measurement device

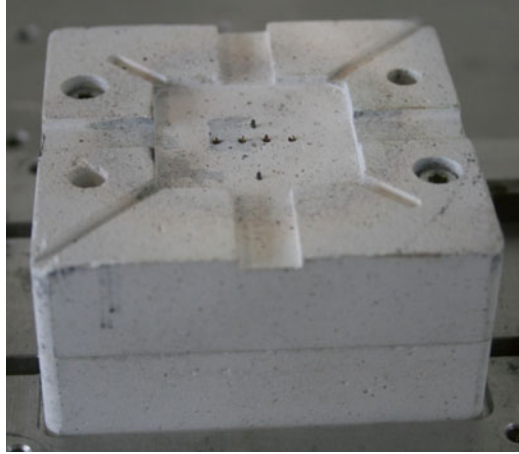


between the sample and the heat source. This variability offers the possibility to analyze the effect of different contact pressures on TEGs.

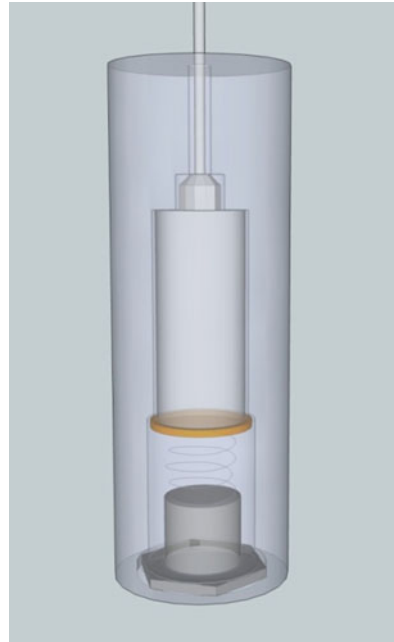
The moveable platform represents the base for two different sample mounts. The first one is used to determine  $\sigma$  by a four-point collinear probe method [7]. This kind of four-point measurement is deliberately used, instead of the common van der Pauw method, because it is easier and faster for samples with fixed dimensions. Nowadays, it is not difficult to ensure reproducible dimensions and it is necessary for later manufacturing of TEGs anyway. For this measurement four spring-mounted pogo-pins are arranged in a row and embedded into MONOLUX 800 as shown in Fig. 7.2.

MONOLUX 800 from Promat consists of a calcium silicate alloy which is stable up to 1,000 °C and has an extremely low thermal conductivity, less than 0.5 W/m K [8]. The commercial spring-mounted pogo-pins ensure a constant contact pressure of averaged 280 cN during the four-point measurement [9]. Furthermore, two N-type TCs are integrated in this mount to record the temperature of the sample. To ensure a constant contact pressure, the TCs are spring-mounted by integrating them in new developed special capsules. In this capsule a spring is pressed against the TC as illustrated in Fig. 7.3. A tube made of stainless steel is welded to the capsule to guide, protect, and support the TC. Without this guidance the TCs would just deform and not spring back which would eliminate the repeatability.

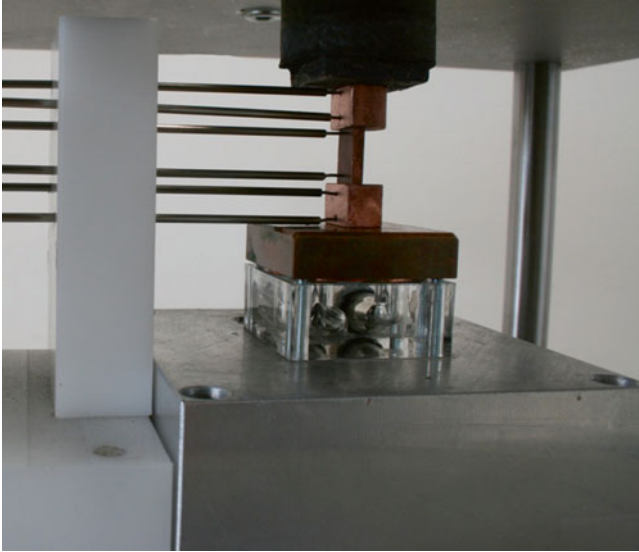
**Fig. 7.2** Four-point measurement system integrated in MONOLUX 800



**Fig. 7.3** Cross section view of developed capsule for thermocouples



The second mount includes a water cooler to establish a heat sink. It is attached to a cover to easily fix it above the four-point measurement mount. The device could be used for a TEG function test as well as for determining  $\lambda$  and  $S$ . For characterizing the material, a sample is mounted between two copper blocks. One is mounted above and the other one below the sample. Two TCs are connected to each copper block to determine the thermal flow which is ideally equal to the one through the sample.



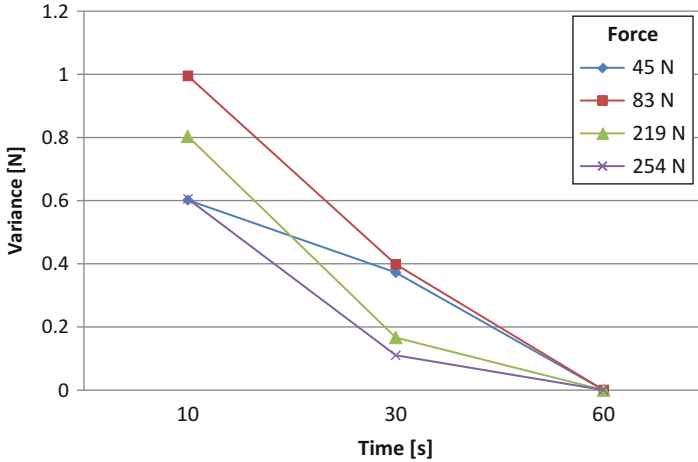
**Fig. 7.4** Full setup for determination of  $S$  and  $\lambda$

Heat losses can be quantified by comparing the measured thermal flow above and under the sample.  $\lambda$  can be calculated by considering the dimensions of the sample. At the same time, two further TCs are pressed against the sample. They are used to measure the temperature difference and the voltage between these two points which enables to calculate  $S$  [10]. The full setup is shown in Fig. 7.4.

All three parameters can be determined at one sample without changing the sample dimension for each characterization. The simultaneous measuring of  $\lambda$  and  $S$  is an additional advantage regarding the needed measurement time. With the help of a data logger all necessary parameters can be recorded and sent to a computer. Both measurement setups get thermally insulated by covers made out of MONOLUX 800. The material properties enable a precisely fitting cover with a high reproducible thermal insulation, which can be easily mounted and removed. These are advantages in contrast to, for example, powder or wool which are sometimes used for thermal insulation.

## Discussion

The spring-mounted pogo-pins have a force variation of  $\pm 20\%$  from minimum to maximum spring compression [8]. This high value shows how difficult it is to ensure a constant contact pressure, even in a commercial product. Because of the fixed position in the first mount, the spring compression should always be the same.



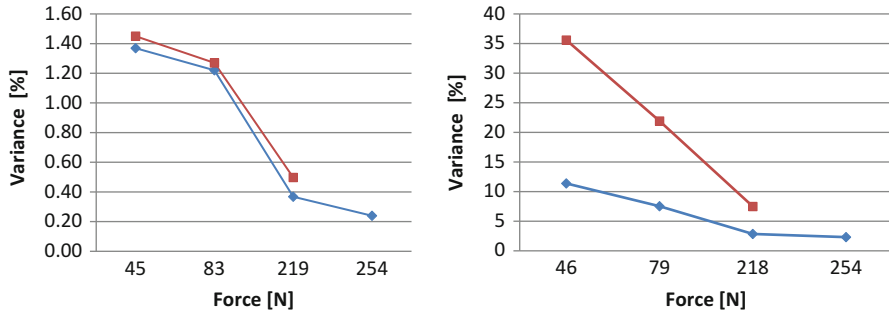
**Fig. 7.5** Pressure variance referred to the final pressure after 60 s dependent on time and force

Hence, the force variation should also be smaller than  $\pm 20\%$ . Analyzes have proven that the averaged contact force of the spring-mounted TC is 3.81 N with a deviation of  $\pm 6.5\%$  from minimum to maximum spring compression. During measurements the effectively occurring deviation should be even smaller, because of the identical spring compression.

In a next step the reproducibility of the force between the sample and the heat source was investigated by use of a ring load cell. To evaluate how exact the same pressure can be achieved, four different fixed pressure settings were applied and repeated for ten times. Each time the pressure was measured after 10, 30, and 60 s to determine pressure variations in time. The results are shown in Fig. 7.5.

The variance is referred to the final pressure after 60 s. After this time no further deviations have been observed. The time needed to reach the final force is longer than expected. It can be assumed that the damping rings, which are integrated in the cylinder, lead to this delay. On the other hand, the variance is already small with a maximum of 1 N after 10 s and it gets even smaller by increasing the pressure in the cylinder. Hence, a maximum variance of 1.3 % is good enough for an exact measurement.

Furthermore, it was noticed that jiggling also highly affects the contact pressure. After 60 s, when the force is rather constant, the pressure could have been increased by 35 % by concussions. The absolute difference of this effect is constant with 16.76 N and not dependent on the force of the cylinder. Therefore, we assumed friction in the ball bearings to be responsible for this effect. When building the measurement device we tried to improve the guidance by using extensions under the moveable



**Fig. 7.6** Compared percentage variance of 4 (blue) and 8 (red) installed ball bearings dependent on the generated force of the cylinder. *Left:* Variance dependent on time after 10, 30, and 60 s. *Right:* Variance caused by concussion after 60 s

platform to assemble one more ball bearing on each tube. So the extensions were removed, which reduced the number of ball bearings from 8 to 4. This caused a cut-back of the absolute force from 16.76 to 5.85 N. Figure 7.6 compares the variance of the force to the ring load cell for four and eight ball bearings. In the left figure the variance dependent on the time is shown. In the right figure the variance caused by concussion is shown. Both figures show that the error is bigger when more bearings are used.

Especially the error for low pressures with the use of eight ball bearings is huge and affirms the assumption, that friction is responsible for this effect. The combination of low pressure and high friction requires too much power which the cylinder cannot supply.

## Conclusions

A measurement device with high reproducible thermal and electrical contact pressure was successfully built up. It was shown that the error is constant and probably caused by friction. Measurement results revealed that the accuracy for characterizing TM could be improved by using higher contact pressure and minimized friction. For results with high accuracy, it is necessary to give the pneumatic cylinder 60 s to build up the pressure, even though the error is after 10 s already smaller than 1.3 %. After 1 min the cylinder builds up the final pressure and holds it constant.

**Acknowledgments** The author would like to thank the German Federal Ministry of Education and Research (BMBF) for funding the Project HOTGAMS (03X3547A) and PROMAT GmbH for providing free samples of different insulation materials.

## References

1. Rowe DM (2000) Handbook of thermoelectrics. CRC, Boca Raton, FL. ISBN 0-8493-0146-7
2. Tritt TM (2001) Recent trends in thermoelectric materials research 1. Academic, San Diego, CA. ISBN 0-12-752178-X
3. Zlatic V, Hewson AC (2008) Properties and applications of thermoelectric materials. Springer, Dordrecht. ISBN 978-90-481-2891-4
4. Ferre L, Lin L (2013) Thermal conductivity measurement methods for SiGe thermoelectric materials. J Electron Mater. doi:[10.1007/s11664-013-2505-3](https://doi.org/10.1007/s11664-013-2505-3)
5. Braunovic M, Konchits VV, Myshkin NK (2007) Electrical contact. CRC, Boca Raton, FL. ISBN 157444-727-0
6. Kelleher MD, Shah RK, Sreenivasan KR, Joshi Y (1993) Experimental heat transfer, fluid mechanics and thermodynamics. Elsevier, Amsterdam. ISBN 0-444-81619-4
7. Schroder DK (2006) Semiconductor material and device characterization. Wiley, Hoboken, NJ. ISBN 0-471-73906-5
8. Datasheet of MONOLUX 800, Promat. [http://www.promat.de/twd/default.aspx?PageName=PROMATECT\\_L\\_PROMALUX\\_V\\_MONOLUX&CL=DE-en](http://www.promat.de/twd/default.aspx?PageName=PROMATECT_L_PROMALUX_V_MONOLUX&CL=DE-en). Accessed 27 Oct 2013
9. Datasheet of pogo-pins, Serie 100N, Tekon. <http://www.tekon-prueftechnik.de/page/deutsch/pdf/federkontaktstifte.pdf>. Accessed 27 Oct 2013
10. Kanatzidis MG, Mahanti SD, Hogan TP (2003) Chemistry, physics and materials science of thermoelectric materials. Kluwer Academic, New York. ISBN 0-306-47738-6

# Chapter 8

## A Comparison of Thermoelectric Devices Evaluation Results Obtained with a Harman Method Based and a Porcupine Method Based $zT$ Meters

A. De Marchi, V. Giaretto, S. Caron, A. Tona, and A. Muscio

**Abstract** This paper compares the results obtained for the series resistance  $R$  and the dimensionless figure of merit  $zT$  of a variety of different thermoelectric devices with two instruments based on alternative approaches: a commercial  $zT$  meter (DX 3065) manufactured by RMT and based on the Harman method, and a prototype realized at the Politecnico di Torino and based on the porcupine method. All devices were evaluated with both instruments at three different temperatures (20, 25, and 30 °C) in a climatic chamber, and results were compared. As expected from the theoretical analysis, the porcupine method consistently returned lower  $R$  values than those obtained by the Harman approach. Values obtained for  $zT$  with the two instruments are instead much more aligned, which is unexpected if thermoelectric effects

---

A. De Marchi (✉)

Dipartimento di Elettronica e Telecomunicazioni, Politecnico di Torino,  
C.so Duca degli Abruzzi, 24, 10129 Torino, Italy

Unità di Ricerca, Consorzio Nazionale Interuniversitario di Scienze fisiche della Materia (CNISM), Politecnico di Torino, C.so Duca degli Abruzzi, 24, 10129 Torino, Italy  
e-mail: [andrea.demarchi@polito.it](mailto:andrea.demarchi@polito.it)

V. Giaretto

Dipartimento Energia, Politecnico di Torino,  
C.so Duca degli Abruzzi, 24, 10129 Torino, Italy

Unità di Ricerca, Consorzio Nazionale Interuniversitario di Scienze fisiche della Materia (CNISM), Politecnico di Torino, C.so Duca degli Abruzzi, 24, 10129 Torino, Italy

S. Caron • A. Tona

Dipartimento di Elettronica e Telecomunicazioni, Politecnico di Torino,  
C.so Duca degli Abruzzi, 24, 10129 Torino, Italy

A. Muscio

Dipartimento di Ingegneria “Enzo Ferrari”, Università di Modena e Reggio Emilia,  
Via Vignolesse 905, 41125 Modena, Italy

are assumed to be correctly accounted for. A discussion of these results is presented, with comments on extrapolations which are introduced in both approaches in order to infer relevant quantities.

**Keywords** Thermoelectricity • Figure of merit •  $zT$  meter • Porcupine diagram • Harman method

## Introduction

Measuring the dimensionless figure of merit  $zT$  of thermoelectric devices requires a strategy to separate the voltage observed across the sample into Seebeck and ohmic contributions. Both time domain and frequency domain approaches have been used to that aim. The former yields methods [1, 2] which historically go under the name of Harman, who was the first to propose it back in the fifties; the latter leads to the porcupine method [3], which is named after the shape of the device's impedance diagram in the complex plane.

A novel  $zT$  meter has been recently developed as a variation on the concept of the Vector Impedance Meter to implement such frequency domain approach, and preliminary results obtained with a prototype instrument based on a high resolution Digital Phase Meter and Digitally Controlled Attenuators were presented [4] to the international community.

In this paper, a comparison is carried out between results obtained with a second generation prototype of the porcupine  $zT$  meter and with a commercial time domain (Harman type) instrument [5] produced by RMT (model DX 3065). In both cases, measurements of  $zT$  and  $R$  (the ohmic series resistance) were performed on a number of thermoelectric devices in a temperature controlled chamber at 20, 25, and 30 °C in order to avoid environmental disturbances and get a good estimate of temperature coefficients of the measured quantities.

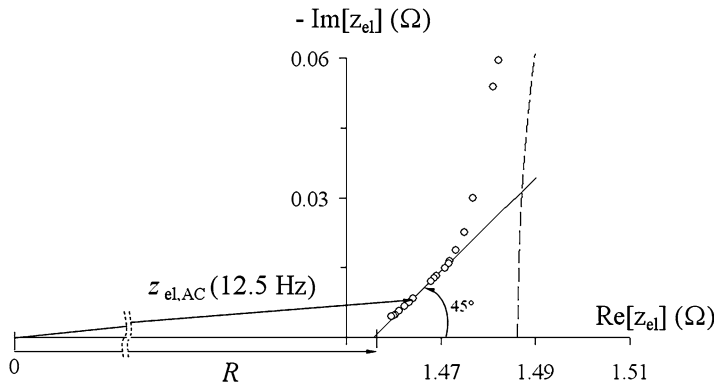
Values of  $R$  measured with the porcupine meter turned out to be consistently lower than the so-called AC resistance  $R_{AC}$  returned by the Harman based  $zT$  meter. The difference between the two is discussed below, and turns out to be greater than expected from the comparative analysis of the two methods, as it has previously been [3] spelled out and is recalled in the next section.

In partial contradiction, instead,  $zT$  values obtained from the porcupine meter were not significantly different from those returned by the commercial Harman type meter. A discussion of possible reasons for this discrepancy is also proposed below.

## Comparison of the Two Methods

Both considered Time Domain and Frequency Domain methods are first quickly illustrated here as implemented in the two instruments at hand. One is based on the study of the Time Domain response to strategically designed excitation current





**Fig. 8.1** Strategy used in the porcupine method in order to estimate the ohmic resistance  $R$  from electrical impedance measurements. The snout slopes at  $45^\circ$  at high frequencies, and  $R$  is taken to be its intercept on the real axis. The dashed line shows the circle that approximates the porcupine body at low frequencies. The indicated 12.5 Hz impedance point is highlighted because such is the frequency  $f_{AC}$  that was used for measurements of  $R_{AC}$  with the RMT meter

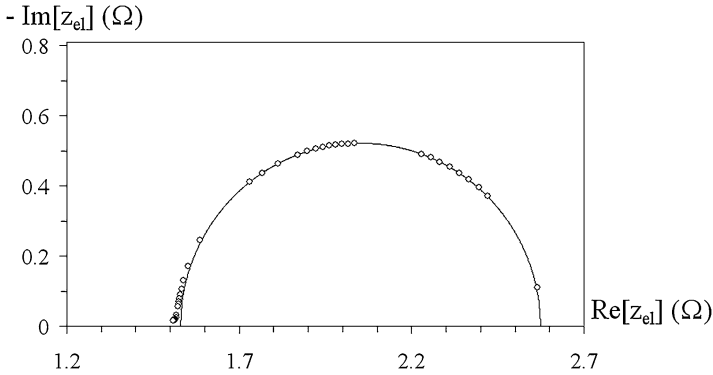
steps; the other on the study of the device's electrical impedance in the complex plane. A more complete description of both can be easily found in the open literature together with the underlying theory [3–5].

In both cases the dimensionless figure of merit  $zT$  is obtained from the ratio between resistances exhibited by the device in DC, where the developed voltage includes the Seebeck effect, and at very high frequency, where it is expected to asymptotically approach the ohmic resistance  $R$ . Such ratio is clearly equal to  $zT + 1$ . Neither condition is experimentally viable in practice, as one is sensitive to boundary conditions and the other would in principle require operation at infinite frequency. Extrapolations are therefore necessary at both ends. The two approaches differ in the way such extrapolations are made and such resistances are estimated.

The former, in fact, identifies  $R$  with  $R_{AC}$ , measured by switching directions of the injected current [5] at some frequency  $f_{AC}$ , assumed high enough to avoid the onset of thermal effects in the device. No extrapolation is made. The latter instead, as shown in Fig. 8.1, which reports data for a device of the test group, finds  $R$  by extrapolation as the point of the real axis where the complex impedance porcupine diagram can be expected to finally land on it at very high frequency. The extrapolation is based on the a priori knowledge [3] that the “snout” of the porcupine slopes down at an asymptotic angle of  $45^\circ$  due to diffusion effects that are overlooked in the Harman approach.

Also shown in Fig. 8.1 is the electrical impedance  $z_{elAC}$  measured at 12.5 Hz, which is equal to the  $f_{AC}$  value used in this work for the measurement of  $R_{AC}$  with the commercial Time Domain  $zT$  meter. Clearly  $|z_{elAC}|$  is always greater than  $R$ , but  $R_{AC}$  is a different thing yet because it is not measured in sine wave regime. Further discussion on this point will be given in the next section.

In order to estimate the DC resistance value, instead, the Time Domain approach extrapolates to steady state the step response, by assuming that it is shaped like an



**Fig. 8.2** Typical agreement between measured electrical impedance along the porcupine's body and the circle used to extrapolate it at low frequencies

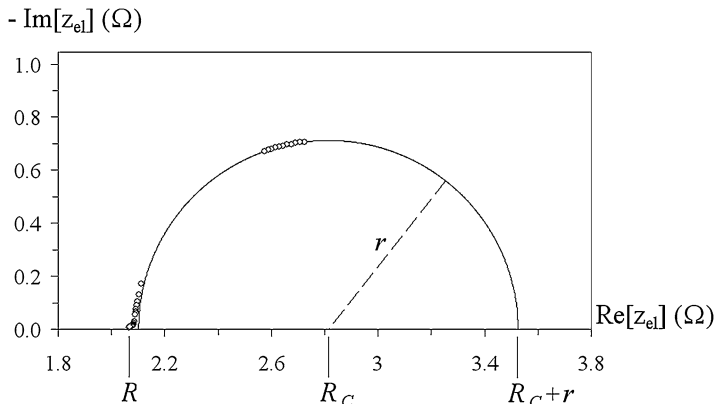
asymptotic exponential [5], in order to identify an asymptotic voltage, and then divides the latter by the injected current. No provision is made for the possibility that diffusion effects may invalidate the assumption on the shape of the transient by making the lumped parameters model inadequate.

The Frequency Domain approach, in turn, extrapolates the porcupine impedance diagram down to very low frequencies, from the frequency range where it can be easily measured, on the assumption that it lays on a circle [3]. This procedure is valid in principle inasmuch as the lumped parameters model can be considered adequate down in that region. How valid it is in practice can be judged by inspection from the agreement shown in Fig. 8.2 between such extrapolating circle and the measured impedance points for one of the devices tested in this work. The result is typical.

Different optimization procedures can be devised to identify such circle from a limited number of experimental data, and one possible approach was illustrated in ref. 4. In the present work, the approach was taken to use a number of impedance data closely spaced in frequency in a range slightly above the thermal pole, and best fit to them a circle centered on the real axis. The DC resistance is then found as the resistance  $R_C$  of the circle center plus its radius  $r$ , as shown in Fig. 8.3.

The Type A uncertainty of results clearly depends on that associated with the individual impedance points used for the least square fit, which in turn depends on signal level (that is on injected current and number of pairs in the device) and on the number of averages chosen for the single data point. In the course of the evaluation of the modules considered in this work, which all had more than 60 pairs, an rms injected current of about 5 mA and averages of more than 20 samples were adequate to obtain statistical contributions to an uncertainty of the order of 0.5 % for  $zT$  and smaller yet for  $R$ .

Further comments will be given in the next section on the validity of the lumped parameters model and on extrapolations made in the two approaches in order to estimate the DC resistance.



**Fig. 8.3** Strategy used for the low frequency extrapolation based on a limited number of measured impedance points just above the thermal pole. The estimated circle center  $R_C$  and radius  $r$  are shown

### Results and Discussions

Values of series ohmic resistance and figure of merit obtained with the two  $zT$  meters on four different devices at three different temperatures are reported in Table 8.1. All measurements were carried out in an environmental chamber with less than 0.3 K uncertainty, and enough time was allowed after changing temperature settings for reaching adequate uniformity in the chamber and inside the containers hosting the modules under test.

Series resistance results obtained with the porcupine meter are reported in Table 8.1 with 1 m $\Omega$  resolution because they are considered accurate better than 2 m $\Omega$  on the basis of the observed reproducibility (Type A contribution) and the absence of reasons to think that the adopted model is faulty at that level (Type B contribution). The reference resistor of the instrument [3, 4] is a 1 ppm/K Vishay<sup>®</sup> unit accurate to better than  $10^{-4}$ , which does not introduce uncertainty at the 1 m $\Omega$  level. Since a four terminal structure is used in this meter, the leads' resistance is not included. The most important cause of  $R$  result variability in porcupine measurements, incidentally, may well have been the 0.3 K instability of the chamber temperature, which is expected to introduce variations of about 0.15 % on the actual resistance value through the temperature coefficient, typically measured at the level of 0.5 %/K. All other results are reported in Table 8.1 with three significant digits.

Both  $zT$  and  $z$  results are reported for the RMT meter because, in spite of the fact that it actually measures  $zT$ , only  $z$  values are presented to the user, as calculated from  $zT$  by the embedded software. The ambient temperature  $T_a$  used for this is measured with a dedicated probe inside the sample holder. The  $z$  column shows therefore displayed experimental results, while data in the  $zT$  column are obtained by multiplying those by the measured  $T_a$ , as given by the meter itself. Type A uncertainties associated with quoted  $R$  and  $z$  results may well be dominated at the  $1\sigma$  level

**Table 8.1** Results obtained with both meters for  $R$  and  $zT$ 

Device trade name	Test temperature (°C)	Harman			Porcupine		Relative deviation	
		$R_{AC}$ ( $\Omega$ )	$z$ (1,000/K)	$zT$	$R$ ( $\Omega$ )	$zT$	$\Delta R/R$ (%)	$\Delta zT/zT$ (%)
Sirec TEC1-12704	20	1.56	2.42	0.709	1.460	0.707	+6.8	+0.3
	25	1.61	2.43	0.725	1.494	0.723	+7.8	+0.3
	30	1.64	2.43	0.737	1.531	0.737	+7.1	0.0
Sirec TEC1-12705	20	1.88	2.38	0.698	1.753	0.683	+7.2	+2.2
	25	1.94	2.36	0.704	1.800	0.693	+7.8	+1.6
	30	2.00	2.35	0.712	1.845	0.700	+8.4	+1.7
Sirec TEC1-12706	20	2.20	2.41	0.706	2.068	0.706	+6.4	0.0
	25	2.28	2.42	0.722	2.118	0.715	+7.6	+1.0
	30	2.36	2.41	0.731	2.174	0.725	+8.3	+1.2
RMT	20	1.03	2.21	0.648	0.933	0.634	+10.4	+2.2
IMDL06-050-03t	25	1.07	2.18	0.650	0.956	0.640	+11.9	+1.6
	30	1.09	2.19	0.664	0.982	0.645	+11.0	+2.8

Quoted  $zT$  values for the RMT meter are obtained by multiplying displayed  $z$  results times  $T_s$ . Relative deviations of  $R$  and  $zT$  are the Harman result minus the porcupine result divided by the latter. Shown discrepancies suggest the existence of undetected errors and Type B contributions as a consequence

of 5 m $\Omega$  for the resistance and of  $5 \times 10^{-6}$  for  $z$  by the second decimal digit truncation operated by the instrument. A trustable evaluation of Type B uncertainties appears much more difficult.

Uncertainties associated to results obtained with the porcupine meter were judged to be dominated by Type A contributions for both  $R$  and  $zT$ , at the level of less than 2 m $\Omega$  for the former and less than 0.004 for the latter. These estimates were based on repeatability of results in the presence of noise in impedance data. Uncertainties in radius and center of the porcupine body's approximating circle, whose estimate is needed for the calculation of uncertainty on  $zT$ , were determined with the well known sensitivity matrix technique in the context of the best fit least square routine. No evidence was found of model inadequacy at these levels.

Nevertheless, it can be noticed in looking at Table 8.1 that discrepancies exist, between ohmic resistance results obtained with the two methods, which are much greater than the quoted uncertainty, a clear sign that the used model is inadequate in at least one of the two approaches, leading to grossly underestimated Type B uncertainty.

Besides the irrelevant leads' resistance, which is included by the Harman meter, one cause for such discrepancy could certainly be thought to be the fact that the frequency at which  $R_{AC}$  is measured in the Harman meter is far from infinite, which in sine wave regime would lead to the operation point and the ohmic resistance evaluation error shown in Fig. 8.1. In fact, there is no reason why the meter should not measure  $R_{AC}$  in sine wave regime and reduce the error to the indicated level: in practice a fraction of the snout length, which in the case of Fig. 8.1 amounts to about 1 % on  $R$ . As it turns out, instead, the meter produces estimates of  $R$  which appear

**Table 8.2** Results obtained with Harman and porcupine meters for the temperature coefficients (TC) of  $R$  and  $zT$ 

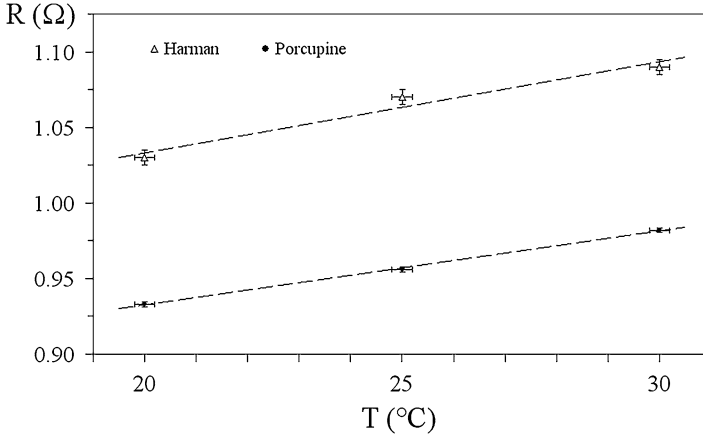
Device trade name	Harman		Porcupine	
	$TC_R$ (mK) <sup>-1</sup>	$TC_{zT}$ (mK) <sup>-1</sup>	$TC_R$ (mK) <sup>-1</sup>	$TC_{zT}$ (mK) <sup>-1</sup>
Sirec TEC1-12704	5.00±0.20	3.9±0.2	5.11±0.08	4.2±0.3
Sirec TEC1-12705	6.20±0.15	2.0±0.2	5.11±0.06	2.5±0.2
Sirec TEC1-12706	7.00±0.15	3.5±0.2	5.00±0.05	2.7±0.3
RMT 1MDL06-050-03t	5.64±0.30	2.4±0.2	5.1±0.1	1.7±0.3

Indicated uncertainties are Type A contributions only

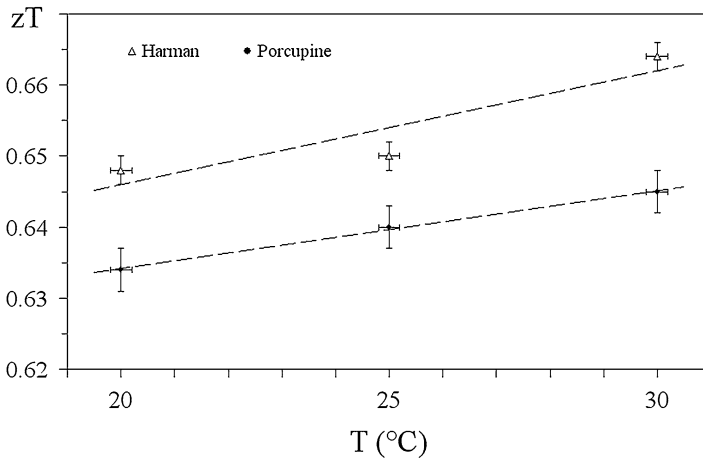
to be biased by up to 12 % toward higher values for the tested devices, as shown in Table 8.1. Such a huge deviation appears to be probably caused by the step response of the device, which starts with an ideally infinite slope due to diffusion, so that no frequency is high enough to avoid thermal effects and allow to correctly isolate the ohmic voltage drop in the thermoelectric device if a square wave regime is adopted. A dedicated study would be needed to determine if this effect does indeed explain observed discrepancies, but this goes beyond the scope of this paper.

On the other hand, also the evaluation of the asymptotic value of the developed voltage that is made in the Harman approach is not immune from diffusion effects and may be altered by their existence. In fact, since the step response is not an asymptotic exponential, albeit less and less so as time elapses, a systematic error is generated when trying to estimate the asymptotic value by best fitting to experimental data a canonical RC type exponential response. Such an error is always positive, and its size depends on the time position along the response curve where the fit is attempted. Although this too needs closer consideration, it seems reasonable to think that errors incurred in this way by the Harman meter in the evaluation of the asymptotic voltage may just happen to be similar to the errors made in the evaluation of  $R$ , so that they roughly compensate them when  $zT$  is calculated from the ratio between asymptotic and AC developed voltages. It is suggested here that this might be the reason why  $zT$  values yielded by the two meters are so similar, while resistance results are instead so different. The relative deviation between  $R$  and  $zT$  evaluations obtained with the two meters is shown in percentage in Table 8.1 as the Harman result minus the porcupine result, divided by the latter.

The temperature coefficients (TC) of both  $R$  and  $zT$  are reported in Table 8.2 as calculated with a linear regression from results yielded by both meters. It can be noticed that, although in some cases they fail to agree within  $2\sigma$ , TC estimates obtained with the two approaches are not substantially different, at least in the face of the huge discrepancy found in the estimate of series ohmic resistance. This fact can be taken as an indication that whatever systematic errors do exist in either method do not change significantly with temperature and are therefore mostly in common mode in slope calculations. However, it should be pointed out here that resistance TCs measured with the porcupine meter all turned out very close to one another for the tested devices, as one might expect from the fact that they all employ



**Fig. 8.4** Temperature dependence of  $R$  as estimated for the RMT module (model 1MDL06-050-03t) with the two instruments. Plotted uncertainty intervals are  $1\sigma$  Type A contributions



**Fig. 8.5** Temperature dependence of  $zT$  as estimated for the RMT module (model 1MDL06-050-03t) with the two instruments. Plotted uncertainty intervals are  $1\sigma$  Type A contributions

the same thermoelectric material ( $\text{Bi}_2\text{Te}_3$ ), while TC values measured with the Harman type meter do not; a clear indication that errors and Type B uncertainties are probably to be looked for in that part of the comparison.

In Figs. 8.4 and 8.5, a typical example of temperature dependence of  $R$  and  $zT$  is shown, as measured with the two meters on the RMT-1MDL06-050-03t module. It can be seen that the mean distance of data points from best fit regression straight lines is smaller than the indicated Type A uncertainty of data points themselves in the case of the porcupine meter, which suggests noise whiteness and lack of undetected systematic errors at the quoted level of uncertainty. In fact their variations

would likely show departure from whiteness if they existed. The same cannot be stated for temperature dependence plots of the Harman meter data, where the mean distance of data points from regression straight lines is greater than the indicated Type A uncertainty, suggesting the existence of Type B contributions.

## Conclusions

In this paper, results obtained for the ohmic resistance  $R$  and the dimensionless figure of merit  $zT$  of a number of thermoelectric devices with a second generation prototype  $zT$  meter based on the porcupine method are compared with results obtained for the same devices by a commercial  $zT$  meter based on a variation of the Harman method. Each device was measured with both meters at three different temperatures in an environmental chamber. The ohmic resistance measured with the porcupine meter was consistently smaller than the value returned by the Harman meter, while figure of merit results were much more aligned. Type A uncertainties were estimated from the variability of measured data and their mean deviations from the linear regression line in plots of their temperature variations, and turned out to be typically  $<0.2\%$  for  $R$  and  $<0.5\%$  for  $zT$  with the porcupine meter, and about  $0.5\%$  for  $R$  and  $<0.3\%$  for  $zT$  with the Harman type meter, limited in the latter case by truncation of displayed measurement results. Temperature coefficients of the series resistance were estimated with better than 2 and 5 % Type A uncertainty with the porcupine and the Harman meter respectively. Similarly,  $zT$  temperature coefficients were determined with Type A uncertainty of the order of 10 % with both meters. Disagreements between results obtained with the two methods for  $R$  and  $zT$  could not be completely explained by published models, which is a clear sign that, at least in one of the two approaches, not all systematic errors have been detected yet, and residual Type B uncertainty contributions at the 10 % level should be considered to exist. It was argued that the model adopted in the Frequency Domain approach should be expected to grant accuracy at least at the percent level, and speculations were made on the directions in which further research should be done in order to compose such discrepancies.

## References

1. Harman TC (1958) *J Appl Phys* 29:1373
2. Harman TC, Cahn JH, Logan MJ (1959) *J Appl Phys* 30:1351
3. De Marchi A, Giaretto V (2011) *Rev Sci Instrum* 82:034901. doi:[10.1063/1.3558696](https://doi.org/10.1063/1.3558696)
4. De Marchi A, Giaretto V, Caron S, Tona A (2013) *J Electron Mater* 42(9):2067. doi:[10.1007/s11664-013-2530-2](https://doi.org/10.1007/s11664-013-2530-2)
5. Gromov G, Kondratiev D, Rogov A, Yershova L (2001) Proceedings of the 6th European workshop on thermoelectricity of the European Thermoelectric Society, Freiburg im Breisgau, p 1

# Chapter 9

## Sintered Nano-Ag as Joining Material for Thermoelectric Modules

K. Brinkfeldt, J. Simon, K. Romanjek, S. Noel, M. Edwards, J. Räthel, M. Da Silva, and D. Andersson

**Abstract** The use of sintered silver particles as an alternative to other types of joining materials for the electrical connection between thermoelectric materials and the substrate in thermoelectric modules (TEM) has been investigated. Sintered silver particles have recently gained attention in the field of power electronics due to the high thermal and electrical conductivity of the material. The nanosilver paste used in this work has originally been developed for use as a die attach material, where these properties are important. The sintering process involved a thermal treatment at 310 °C, under a 15 kg mechanical load, in a nitrogen atmosphere. Sample TEMs with sintered silver connections were tested both mechanically and electrically. Initial results showed that the TEMs performed well during thermal gradient tests with the hot side heated from 50 °C to 550 °C and the cold side kept at 20 °C. This performance also indicates that the nano-Ag joints have good contact resistance. The resistivity of the sintered silver joints were measured at room temperature to  $\rho = 15 \mu\Omega \text{ m}$  (average value of Ti/Au plated thermoelectric legs). Shear force tests of the sintered thermo electrical leg material showed that the joints are brittle when W metallized AlN substrates were used and these have an average shear strength of  $3.3 \pm 1.9 \text{ MPa}$ . On Cu metallized AlN substrates, ductile fracture behavior was observed and an average shear strength of  $2.4 \pm 1.4 \text{ MPa}$  was measured.

**Keywords** Thermoelectric modules • Joining material • Contact resistance • Shear force • Nanosilver

---

K. Brinkfeldt (✉) • M. Edwards • M. Da Silva • D. Andersson  
Swerea IVF, Argongatan 30, 431-53 Mölndal, Sweden  
e-mail: [klas.brinkfeldt@swerea.se](mailto:klas.brinkfeldt@swerea.se)

J. Simon • K. Romanjek • S. Noel  
CEA, 17 rue des Martyrs, 38054 Grenoble Cedex 9, France

J. Räthel  
Fraunhofer IKTS, Winterbergstrasse 28, 01277 Dresden, Germany



## Introduction

Thermoelectric (TE) materials rely on the Seebeck effect to transform heat energy to electric power. Due to their simple, reliable operation without moving parts they have been deployed as part of the power generation in space applications for several decades [1–3]. They are also under investigation as waste heat recovery devices in industrial and automotive applications [4–6].

Though the efficiency of the TEM depends largely on the properties of the TE-material itself, the properties of the interface and electrode materials are also important. If the joining and current-carrying materials do not have high thermal and electrical conductivities, the efficiency is decreased due to resistive losses. The interface materials are also critical from a reliability perspective. As applications of TE-modules (TEMs) involve high temperature gradients, thermal cycling, or both, difficulties arise due to the coefficient of thermal expansion (CTE) mismatches between the constituent materials, resulting in significant stresses and strains, which ultimately could cause fracture in the interface.

Others have recently reported on the use of Ag–Cu brazing methods to join  $\text{CoSb}_3$  and Cu [7].  $\text{CoSb}_3$ -based skutterudite materials have also been joined with Mo or Mo–Cu electrodes by spark plasma sintering using Ti or Ag–Cu foils [8–10]. Kadhim et al. have used Ag-paste/Cu plate/Ag-paste as electrodes for Bi–Sb–Se–Te and Bi–Se–Te TE-materials [11]. They conclude that the contact resistance  $R_c$  is mostly attributed to the boundary resistance and the contribution of the Ag–Cu–Ag electrodes is very small. The details of the Ag paste were not reported.

Recently, sintered nano-Ag particles have been introduced as a die attach material in the field of power electronics [12]. The material consists of nanoscale particles in an organic solvent/binder. The small particle size enables a sintering temperature in the order of 250–310 °C depending on if the surface material is Ag or Au, while the resulting joint is pure Ag with a melting temperature,  $T_m=961$  °C. Chen et al. reported that nano-Ag can have similar or improved mechanical properties compared to solder joints [13]. This, combined with the high thermal and electrical conductivity of Ag, low processing temperature and high  $T_m$ , makes the material very attractive to power electronics die attach applications, which also makes it attractive to use in TEMs.

In this work we have evaluated nano-Ag as the joining material in small, proof of concept TEMs consisting of four SiGe TE-legs joined to ceramic substrate metallizations of different materials. In “Method” section, the fabrication of samples, including the SiGe TEMs and special samples used for contact resistance ( $R_c$ ) measurements, are described. Two different metallizations schemes for the SiGe TE-legs were investigated with respect to contact resistance: Ti/Au and  $\text{MoSi}_2/\text{Ti}/\text{Ag}$ . “Method” section also describes the measurement setups for the electrical and mechanical tests. “Result” section describes the results of the  $R_c$  measurements, mechanical test, and performance of the TEMs during thermal gradient tests with  $\Delta T$  ranging from 30–530 °C.

## Method

### *Sample Manufacturing Process*

The TE material used in all of the measurements in this work was a polycrystalline Silicon–Germanium alloy (80 % Si and 20 % Ge) made by spark plasma sintering, with mechanical synthesis of the initial powder [14]. The material is completely dense and has a submicron scale grain size. The N-type dopant is Phosphorous and P-type is Boron.

The TE-material was sintered into pellets, which were then metallized on top and bottom. Two different metallizations: (a) thin Ti/Au and (b) MoSi<sub>2</sub>/Ti/Ag were used, and the pellets were then diced into 4×4×5 mm<sup>3</sup> TE-legs. For metallization (b), MoSi<sub>2</sub> was included as a barrier material. The use of silicides as diffusion barrier materials has shown good results in thin film applications at very high temperatures [15–17]. The MoSi<sub>2</sub> layer was created by sputtering a thin Mo layer followed by a thin Si layer and this was repeated 60 times to create a film of the desired thickness. The sputtering times were calibrated, so that the ratio of Mo atoms to Si atoms was as close as possible to 0.5. This layered sputtering step was followed by an annealing step at 900 °C for 3 h. After annealing, the resulting MoSi<sub>2</sub> layer was ≈90 nm thick. Finally, the MoSi<sub>2</sub> layer was covered with a Ti/Ag capping layer (Ag thickness ≈2 μm).

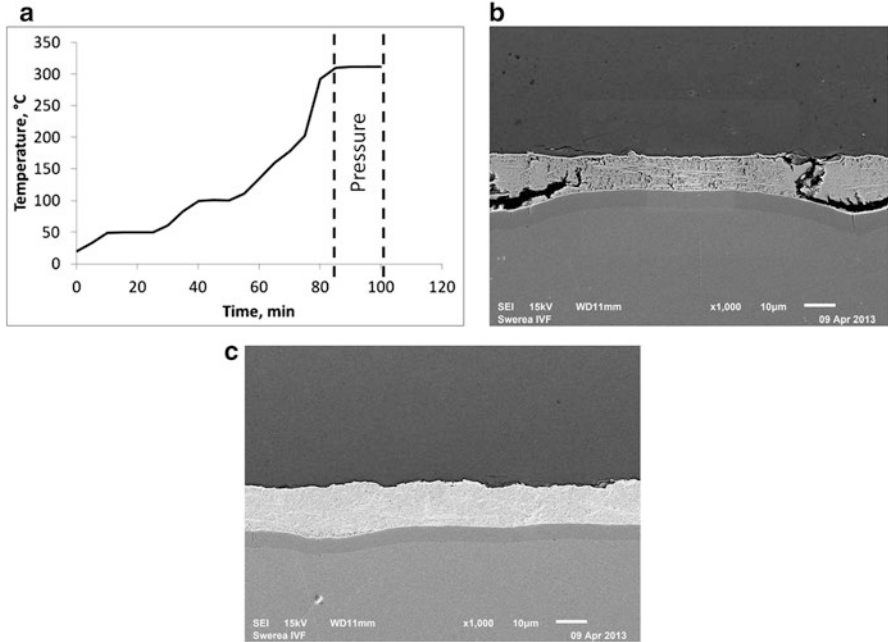
The TE-legs (two P-type and two N-type) were then sintered to cold and hot side substrates to form proof of concept TEMs. The types of metallizations used on the different TEM substrates are listed in Table 9.1.

The nano-Ag material used to sinter the TE-legs to the substrate metallizations was nanoTach paste from NBE-Tech, Virginia. Nano-Ag was selected due to its high thermal and electrical conductivity, as well as its low Young’s modulus compared to Cu.

The process to make the connection involved screen-printing of the nano-Ag paste onto both hot and cold side substrate metallizations, the TE-legs were then attached to the hot and cold side metallizations, which was followed by a sintering process in a furnace at 310 °C with or without pressure applied at the peak temperature. The peak temperature (and pressure, when used) was maintained for 20 min. The resultant joining interface is able to operate at much higher temperatures, which

**Table 9.1** Substrates and metallizations used in the TEMs

Substrate	Material	Metallization
AlN/Cu Cold side	AlN	300 μm Cu/0.1 μm Au/10 μm nano-Ag/300 μm Ag
AlN/Cu Hot side	AlN	300 μm Cu/0.1 μm Au
AlN/W Cold side	AlN	16 μm porous W/10 μm Ni/0.1 μm Au/10 μm nano-Ag/300 μm bulk Ag
AlN/W Hot side	AlN	16 μm porous W/10 μm Ni/0.1 μm Au



**Fig. 9.1** (a) Measured temperature profile for nano-Ag sintering process. (b) and (c) SEM images of the cross section of SiGe leg material sintered to a Cu surface. The image (c) shows the resulting interface with pressure applied during the final processing step

are theoretically near the melting temperature of Ag at  $T_m = 961$  °C, if the joint itself is not required to withstand mechanical loads.

Figure 9.1 shows the measured temperature profile for the nano-Ag sintering process in a  $N_2$  atmosphere. If the bond surfaces are large, then an additional mechanical pressure during the final temperature step is required. Since the TE-leg surface area is  $4 \times 4$  mm<sup>2</sup>, which is close to the limit, tests with and without mechanical pressure have been made. Figure 9.1 also shows comparative cross sections of SiGe TE-legs sintered to a Cu surface using nano-Ag paste. The sample in Fig. 9.1c has been sintered with a mechanical load of 15 kg applied during the final sintering step. This load corresponds to a pressure of  $\approx 2$ –3 MPa on the sintered interfaces. This process was followed by a slow, passive cooling period for several hours. When the temperature decreased below 70 °C, the furnace was opened and the remainder of the cooling was done in air.

### *Electrical Measurement Setup*

A 4-point resistance (R4P) measurement method was used to find the total resistance of the TEM. A known current was forced through the TEM and the voltage was measured between the input and output. The resistance through the TEM was

then calculated using Ohm's law. The measurements were done at room temperature and the device is assumed to be passive (zero heat flux through the device). In order to limit the Peltier effect, which appears when a current is forced through a TEM, currents were limited to  $-100\text{ mA}$ – $100\text{ mA}$  and the  $U(I)$  characteristics were measured for less than 1 s.

The measurement principle used to determine the contact resistance ( $R_c$ ) of the nano-Ag interface was similar. Special samples were prepared for this measurement. Two TE-legs, consisting of the same N- or P-type material, were attached directly to each other using the nano-Ag sintering process. Current was then forced between the top and the bottom of the TE-leg/joint/TE-leg stack and the voltage was measured on either side of the joint. The resistance through the stack was then calculated using Ohm's law. In order to extract  $R_c$ , the resistance ( $R_{TE}$ ) of a pure TE leg with the same geometry as the stack was measured in the same way.  $R_c$  was then determined using the following formula:

$$R_c = R_{TE/joint/TE} - R_{TE}. \quad (9.1)$$

The measurement was done at room temperature assuming there was no heat flux flowing through the material stack.

## ***Mechanical Testing***

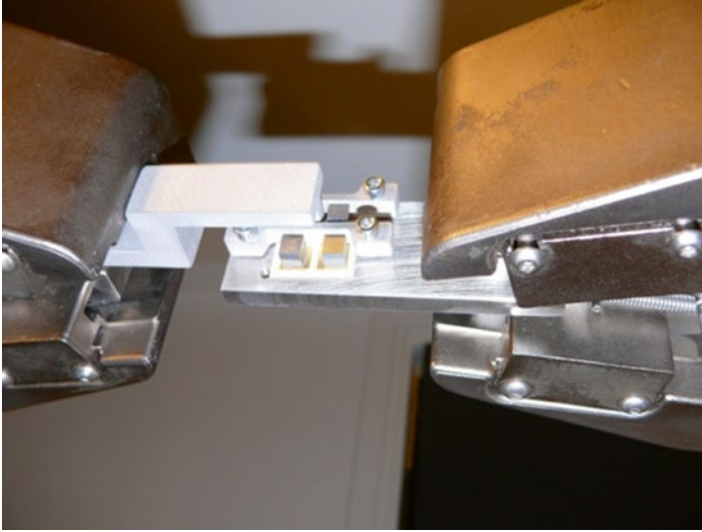
Sample TE-legs of both N- and P-type material with Ti/Au metallization were sintered to both AlN/Cu and AlN/W substrates. The metallizations were identical to the hot side substrate metallization shown in Table 9.1.

The substrates were then mounted on a plate, which in turn was attached to one of the clamps in a MTS 20/M rig. On the other clamp, a hook was attached. The hook was placed on the surface of the TE-leg, as close to the substrate as possible without touching the surface. The clamps were then separated at a velocity of 1 mm/min and the force was recorded. Figure 9.2 shows a photograph of a substrate holding four TE-legs attached to the rig.

## **Results**

### ***$R_c$ Measurement Results***

Table 9.2 shows the results from the R4P measurements of the joined TE-legs. The resistance through the stack ( $R_{TE/joint/TE}$ ), resistivity ( $\rho$ ), electrical conductivity ( $\sigma$ ), and the resistance of the nano-Ag joints ( $R_c$ ) are all derived from Equation 1. In addition, the TE-material properties were measured on TE-legs coming from the



**Fig. 9.2** A photograph of the shear test setup used in the MTS 20/M rig. A sample substrate with four TE-legs is mounted in the rig

same or similar pellets. In detail, the AA608P and AA786N material, both with Ti/Au metallization, showed low values of  $R_c$ . In one of the measurements, the stack became misaligned during the final pressure step of the sintering process (marked by \* in Table 9.2) and should not be considered representative of the results. The measured  $R_{TE/joint/TE}$  values were very high and dispersed for the AA637P and AA787N material stacks. The measured values were in the order of 300 times higher than  $R_{TE}$ , which results in the high  $R_c$  values derived.

### ***Shear Test Results***

Figure 9.3 shows shear diagrams for the AlN/Cu and AlN/W samples. For the AlN/Cu substrates, only two N-type material samples were tested successfully. The tests indicate a brittle fracture mechanism for the AlN/W, whilst the AlN/Cu samples experience some ductile behavior prior to fracture. Average shear strengths of  $2.4 \pm 1.4$  MPa for the AlN/Cu substrate samples and  $3.3 \pm 1.9$  MPa for the AlN/W substrate samples were obtained. For both substrate types, the results were largely dispersed.

An analysis of the fracture surfaces was done, which is shown in Fig. 9.4. It showed that the fracture surface contained mostly Ag for the AlN/Cu N2 sample while the AlN/W P1 sample fracture surface also included significant amounts of other elements. Au, Si, and Ge were easily identified in the spectrum.

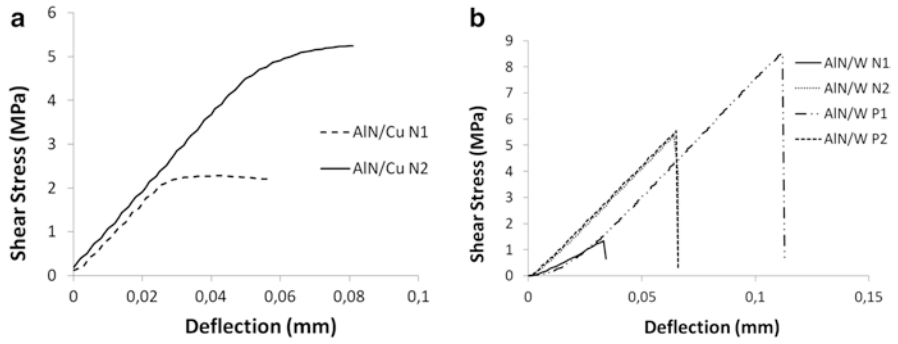
**Table 9.2** Results of the  $R_c$  measurements

SiGe legs with Nano-Ag			R4P Measurements			
TE material designation	Type	Metallization	$R_{TE/joint/TE}$ m $\Omega$	$\rho$ ( $\mu\Omega\cdot\text{m}$ )	$\sigma$ (S/m)	$R_c$ ( $\Omega\cdot\text{m}^2$ )
AA608	P	Ti/Au	2.5	12.4	80,336	-3.50E-10
			2.9	14.3	69,844	4.40E-09
			2.4	11.8	85,023	-2.10E-09
TE-material only (same pellet)				12.6	79,463	
AA637	P	MoSi <sub>2</sub> /Ti/Ag	566.3	2780.3	360	7.10E-06
			18.3	89.9	11,123	2.00E-07
			576.8	2831.9	353	7.20E-06
TE-material only (similar pellet)				10.3	96,874	
AA786	N	Ti/Au	3.6	17.5	57,136	2.00E-09
			3.4	16.7	59,826	2.10E-09
			<i>5.1*</i>	<i>25.1*</i>	<i>39,858*</i>	<i>2.10E-08*</i>
TE-material only (similar pellet)				16.7	59,857	
AA787	N	MoSi <sub>2</sub> /Ti/Ag	906.9	4452.5	225	1.10E-05
			688.8	3381.9	296	8.60E-06
			568.7	2792.1	358	7.10E-06
TE-material only (similar pellet)				16.7	59,857	

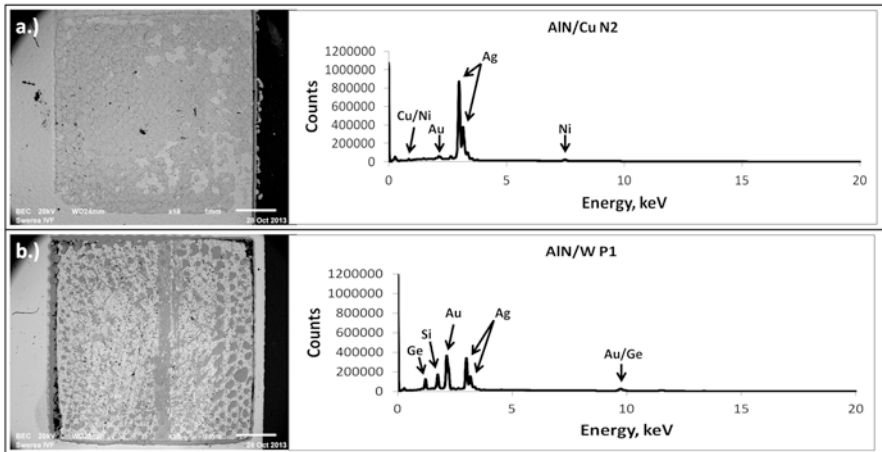
### TEM Performance

AlN/Cu and AlN/W TEMs were tested on four probe setup to determine internal resistance at room temperature. The results are shown in Table 9.3. The TEMs built using AlN/W substrates had an internal resistance 2–3 times higher than the AlN/Cu samples.

Samples A1 and A2 in Table 9.3 subsequently failed during wiring, due to a faulty pressure application during the final sintering step, so they could not be used further in the performance tests. The AlN/W TEMs were tested under the following conditions:



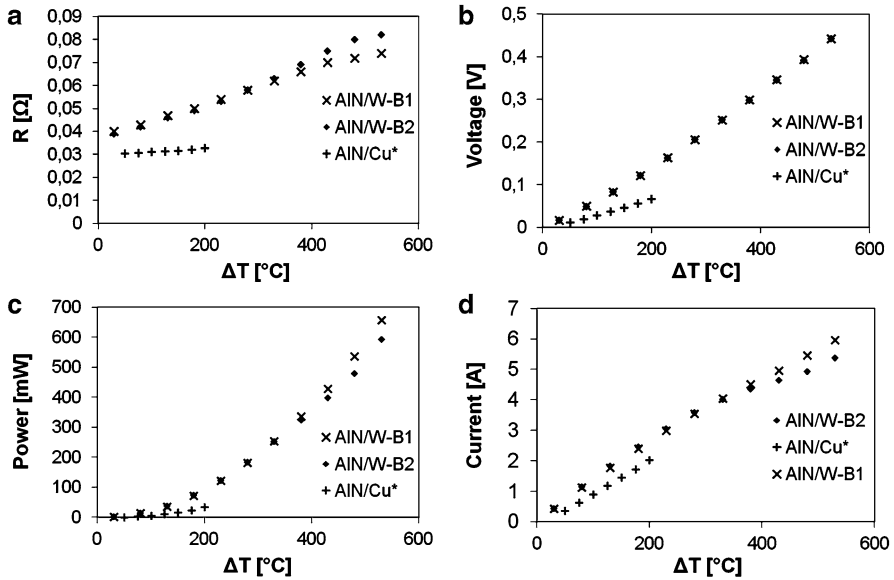
**Fig. 9.3** Shear stress as a function of the actual movement of the shear tool. (a) Shows the results from the AIN/Cu substrates and (b) the results from the AIN/W substrates



**Fig. 9.4** SEM image and EDX spectral response of the shear test fracture surfaces of (a) AIN/Cu N2 and (b) AIN/W P1 samples

**Table 9.3** Results of TEM resistance measurements

TEM	R4P (mΩ)
AIN/Cu—A1	11
AIN/Cu—A2	16
AIN/W—B1	32
AIN/W—B2	31



**Fig. 9.5** Electrical results of the AlN/W TEMs. The figure shows (a) internal resistance, (b) open circuit voltage, (c) maximum power, and (d) current of the tested TEM

$T$  cold: 20  $^{\circ}\text{C}$   
 $T$  hot: 50–550  $^{\circ}\text{C}$   
 Pressure: 10 mBar

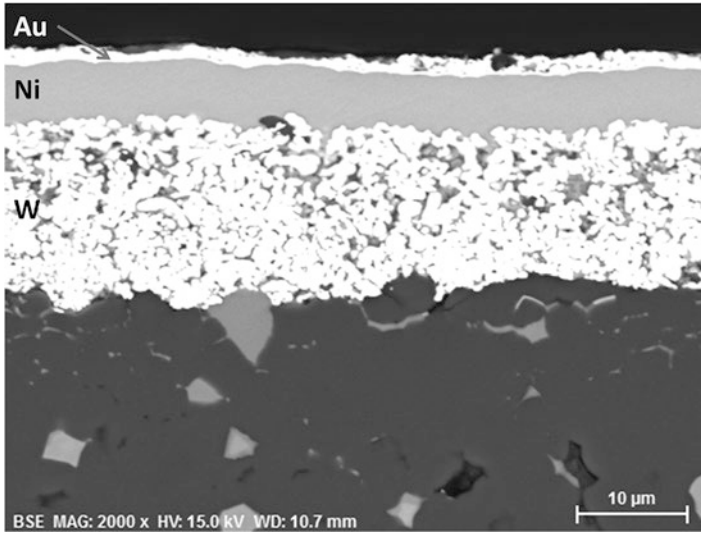
Figure 9.5 shows the electrical property measurements of the tested AlN/W TEMs. Measurements of current and power for AlN/Cu TEMs previously tested to 200  $^{\circ}\text{C}$  (denoted AlN/Cu\*) have been included in Fig. 9.5 for comparison. A different connection technique was applied to the AlN/Cu\* samples, with a 300  $\mu\text{m}$  diameter Ag wires used to electrically connect the devices instead of the 300  $\mu\text{m}$  thick Ag plates. The AlN/W devices tested resulted in higher values for all measurements except internal resistance, when compared to the AlN/Cu\* devices.

## Discussion of Results

The poor contact resistance from the  $\text{MoSi}_2/\text{Ag}$  metallization stack could be the result of inadequate cleaning of the SiGe surface prior to sputtering. There was also some discoloration on the surface following the 900  $^{\circ}\text{C}$  anneal of unknown origin that could be linked to this. The future process will include Ar-plasma etch prior to the sputtering and a different furnace will be used for annealing.

In the shear tests, the AlN/W samples all displayed brittle behavior, whilst the AlN/Cu samples experienced some ductile behavior prior to fracture. This could be





**Fig. 9.6** Cross section SEM image of the AlN/W substrate metallization

an effect of the more ductile Cu (300  $\mu\text{m}$ ) compared to the W/Ni/Au metal stack (30  $\mu\text{m}$ ) on the substrate on which the TE-leg was attached. The analysis of the fracture surfaces in Fig. 9.4 showed almost exclusively Ag on the AlN/Cu fracture surface, while the AlN/W substrate also contained Au, Si, and Ge. This means that the fracture is located in the nano-Ag joint for the AlN/Cu substrates and in the interface between the SiGe TE-leg and the nano-Ag for the AlN/W substrate. Further analysis and better statistics are required.

The complete internal resistance of the AlN/Cu modules was almost 3 times lower than that of the AlN/W modules. This is mostly a result of the metallization thickness on the hot side substrates. The thickness of the AlN/Cu is 10 times thicker than for the AlN/W. Cu is also a better electrical conductor than W/Ni. This difference exists on both parts of metallization between the TE-legs and the hot side metallization which the current passes through. Additionally, as shown on the cross section image of the AlN/W substrate metallization in Fig. 9.6, the W layer is very porous, which increases the resistance further and it can be assumed that this layer has 60–80 % of the electrical conductivity of bulk W.

Figure 9.1 shows that the use of pressure in the sintering process significantly improves the density of the nano-Ag layer. Apart from mechanical consequences, this would also affect the electrical resistance. The AlN/Cu TEMs that failed after the internal resistance measurement could be expected to have even lower internal resistance when processed correctly.

The electrical results of the tested AlN/W TEMs are shown in Fig. 9.5. The internal resistance of sample B2 increases more than that for B1 with respect to temperature. The open circuit voltage is almost identical for both samples throughout the

entire temperature range. The AlN/W-B1 exhibits a slightly higher power output at higher temperatures, which is a result of the slightly higher current, which in turn results from a lower internal resistance for temperatures above 300 °C.

In spite of the lower performance of the AlN/Cu\* sample, this version of the device still has a lower resistance than both AlN/W samples. This indicates that much improved results should be expected from the AlN/Cu versions with the new generation of TE-material when the correct pressure process is applied on these type of samples.

## Conclusions

Results show that the use of nano-Ag sintered joints between TE-material and electrodes is possible, but the low and dispersed shear stress tolerance indicates there is room for improvement in the sintering process. The contact resistance of the nano-Ag layer was low in the case where the TE-leg metallization was Ti/Au. The low contact resistance was also reflected in the complete TEM measurements of the AlN/Cu substrate. The AlN/W TEMs show promising results, but they suffer from high internal resistance due to the thin metallization on the hot side substrates.

**Acknowledgement** This work was supported by the FP7 EU-project NEAT under grant agreement NMP4-SL-2011-263440.

## References

1. Mondt, J. F., & Ambrus, J. H. (1984). Thermoelectric and thermionic conversion technology. NASA Conference Publication, 301–307.
2. Bennett, G. L., Lombardo, J. J., Hemler, R. J., Silverman, G., Whitmore, C. W., Amos, W. R., et al., (2008). The general-purpose heat source radioisotope thermoelectric generator: A truly general-purpose space RTG. AIP Conference Proceedings, 969: 663–671.
3. Ravi V, Firdosy S, Caillat T, Brandon E, Van Der Walde K, Maricic L et al (2009) J Electron Mater 38(7):1433–1442
4. Crane D, Lagrandeur J, Jovovic V, Ranalli M, Adldinger M, Poliquin E et al (2013) J Electron Mater 42(7):1582–1591
5. Schock H, Brereton G, Case E, D'Angelo J, Hogan T, Lyle M, et al (2013) J. Energy Resour. Technol. 135; JERT-11-1087; doi:[10.1115/1.4023097](https://doi.org/10.1115/1.4023097)
6. Roy G, Matagne E, Jacques PJ (2013) J Electron Mater 42(7):1781–1788
7. Wojciechowski KT, Zybala R, Mania R (2011) Microelectron Reliab 51:1198–1202
8. Fan J, Chen L, Bai S, Shi X (2004) Mater Lett 58:3876–3878
9. Zhao D, Li X, He L, Jiang W, Chen L (2009) Intermetallics 17:136–141
10. Zhao D, Tian C, Tang S, Liu Y, Jiang L, Chen L (2010) Mater Sci Semiconductor Process 13:221–224
11. Kadhim A, Hmood A, Abu Hassan H (2013) Mater Lett 97:24–26
12. Bai JG, Zhang ZZ, Calata JN, Lu G-Q (2004) IEEE Trans Compon Pack Technol. doi:[10.1109/TCAPT.2005.853167](https://doi.org/10.1109/TCAPT.2005.853167)

13. Chen G, Cao Y, Mei Y, Han D, Lu G-Q, Chen X (2012) *IEEE Trans Compon Pack Manufact Technol* 2(11):1759–67
14. Bernard-Granger G, Leforestier J, Navone C, Soulier M, Boidot M, Deniau B, et al (2013) “Microstructure–thermoelectrical properties relationships for a n-type polycrystalline Si<sub>1-x</sub>Gex alloy sintered by SPS” Presented at the European-Materials Research Society Spring Meeting, May 27–30.
15. Inoue T, Koike K (1978) *Appl Phys Lett* 33:826
16. Cvitkovic R, Ivey DG, Stiles J (1995) *J Mater Sci* 30(21):5415–5426
17. Mochizuki T, Kashiwagi M (1980) *J Electrochem Soc* 127:1128

# Chapter 10

## Anodized Aluminum as Effective and Cheap Alternative Substrate for Thermoelectric Generators

F. Assion, V. Geneiß, M. Schönhoff, C. Hedayat, and U. Hilleringmann

**Abstract** The wide usage of thermoelectric generators (TEG) is still blocked by very high product costs. This paper presents anodized aluminum (Al) as an effective and cheap alternative for ceramics like alumina ( $\text{Al}_2\text{O}_3$ ) or aluminum nitride (AlN). Al has a significantly higher thermal conductivity as both named ceramics. In addition, the lower thermal stability of Al is still high enough to work with bismuth telluride based modules, which are most common. To show the advantages of the changed substrate, finite element method (FEM) simulations were performed. These simulations show that by changing the cold side substrate material the temperature drop across the substrate is reduced by 60 K. This correlates to a theoretical power gain of more than 20 %. Furthermore, Al can be shaped much easier than a ceramic material. The biggest advantage is obviously the price. Anodized Al is around twenty times cheaper than  $\text{Al}_2\text{O}_3$ . To demonstrate the easy fabrication of the proposed substrate, samples were prepared only with widely used processes like those used for conventional printed circuit boards.

**Keywords**  $\text{Al}_2\text{O}_3$  • Substrate • Anodized Al • Costs • TEG

---

F. Assion (✉)

Sensor Technology Department, University of Paderborn, 33098 Paderborn, Germany  
e-mail: [assion@sensorik.upb.de](mailto:assion@sensorik.upb.de)

M. Schönhoff

Institute of Electrical Engineering and Information Technology,  
University of Paderborn, Paderborn, Germany

V. Geneiß • C. Hedayat

Fraunhofer ENAS – Advanced System Engineering, 33098 Paderborn, Germany

U. Hilleringmann

Fraunhofer ENAS – Advanced System Engineering, 33098 Paderborn, Germany

Sensor Technology Department, University of Paderborn, 33098 Paderborn, Germany

## Introduction

The wide usage of thermoelectric generators (TEG) is still blocked by very high product costs. Almost all commercially produced TEGs nowadays are mounted on ceramics like alumina ( $\text{Al}_2\text{O}_3$ ) or aluminum nitride (AlN). On the one hand, these materials have a very high thermal stability and a rather good thermal conductivity, which makes them interesting for thermoelectric applications. On the other hand, they are very expensive and their thermal conductivity actually drops with rising temperatures. Furthermore, the maximal working temperature of thermoelectric (TE) materials used nowadays is rather low so the high thermal stability might not really be needed. This paper is not the first one calling the use of expansive ceramic substrates into question [1] by looking at requested cost–performance ratios of around one Euro per watt for TEGs.

Anodized aluminum (Al) could be an effective and cheap alternative for ceramics used nowadays. For good module efficiency, the thermal resistance of a TEG substrate must be as low as possible. Al has a significantly higher thermal conductivity as both named ceramics (see Fig. 10.1).

In addition, the lower thermal stability of Al is still high enough to work with bismuth telluride ( $\text{Bi}_2\text{Te}_3$ ) based modules that are most widely spread.  $\text{Bi}_2\text{Te}_3$  based modules have a maximum working temperature of around 300 °C.

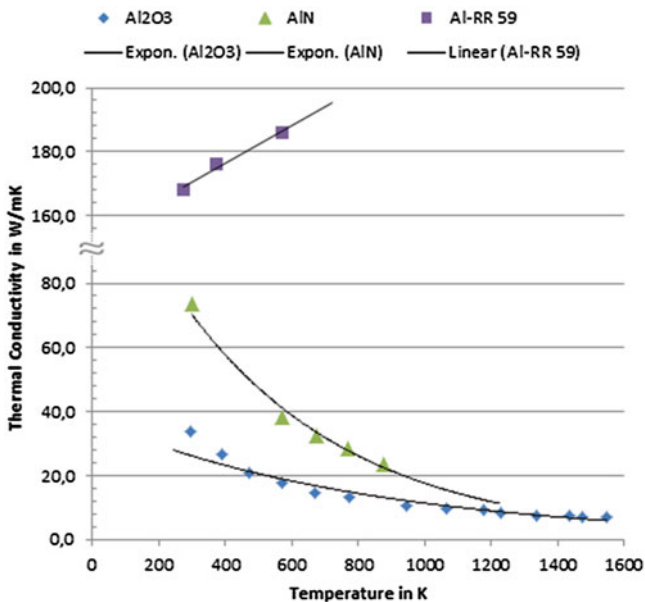


Fig. 10.1 Thermal conductivity of  $\text{Al}_2\text{O}_3$ , AlN, and Al vs. temperature [2–4]

## Experiment and Results

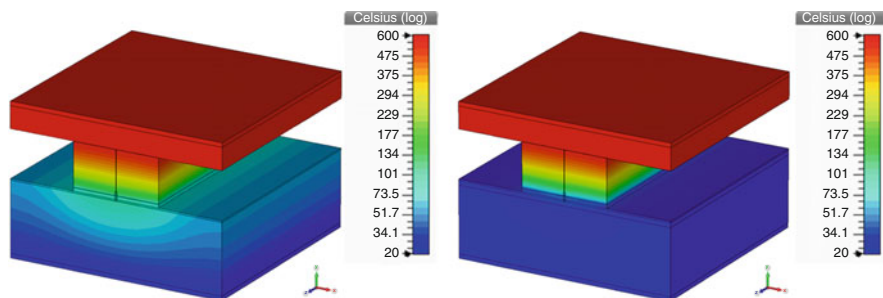
To show the advantages of the substrate change finite element method (FEM), simulations were performed with the CST Studio Suite. All material properties are given in Table 10.1. In the simulation, a theoretical silicon/germanium (SiGe) TEG was analyzed. The TEG was placed between a 20 °C cold side and a 600 °C hot side. Caused by the rather high thermal conductivity ( $\kappa=4.0\text{--}5.9\text{ W/m K}$  [5]) of the SiGe material, the thermocouples are short ( $l=1\text{ mm}$ ). Shorter thermocouples lead to a better cost–performance ratio and therefore reduce the overall costs of TEG systems [6]. The hot side substrate is a 0.5 mm thick  $\text{Al}_2\text{O}_3$ . The cold side mounting material has for mechanical reasons a thickness of 1.6 mm.

In Fig. 10.2, the simulation results of two different substrates are shown. The temperature distribution reveals the losses inside the particular mounting substrate. On the left picture the substrate is a commercially used <92 % pure  $\text{Al}_2\text{O}_3$  ceramic with a thermal conductivity of  $\kappa=14\text{--}24\text{ W/mK}$  [8, 9]. With this substrate, the thermocouple cold side temperature is 99 °C, which means nearly 80 K temperature difference, are lost. By using an anodized Al substrate (1.5 mm Al + 0.1 mm  $\text{Al}_2\text{O}_3$ ), the thermocouple cold side temperature decreases to 39 °C (compare Fig. 10.2, right).

This means that by changing the cold side substrate material the effective temperature difference across the thermocouples increases by 60 K, which is a relative increase of more than 11 %. Moreover, since the temperature difference is squared to get the output power this equals a theoretical power gain of 23 %. Even by consideration that this is a theoretical example and that the output power gain also

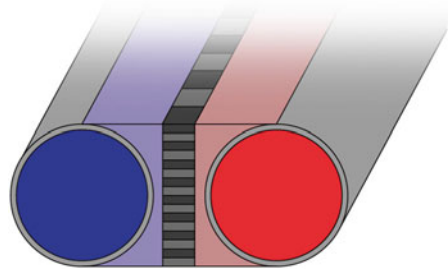
**Table 10.1** Material properties of the simulation model

Material	SiGe	Al	$\text{Al}_2\text{O}_3$	References
Density in $\text{g/cm}^3$	3.009	2.7	3.6	[5, 7, 8]
Therm. conductivity in $\text{W/mK}$	4.0–5.9	237	14–24	[5, 7–9]
Specific heat in $\text{J/kgC}$	770	900	850–1,050	[5, 7, 8]



**Fig. 10.2** FEM-simulations of thermocouples with  $\text{Al}_2\text{O}_3$  (left) and anodized Al (right) substrate (log scale)

**Fig. 10.3** A theoretical round shaped TEG between two pipes



**Table 10.2** Prices for different materials

Material	Price	Reference
AlN	70 €/cm <sup>3</sup>	[11]
Al <sub>2</sub> O <sub>3</sub>	1.3 €/cm <sup>3</sup>	[12]
Al (anodized)	0.06 €/cm <sup>3</sup>	[13]

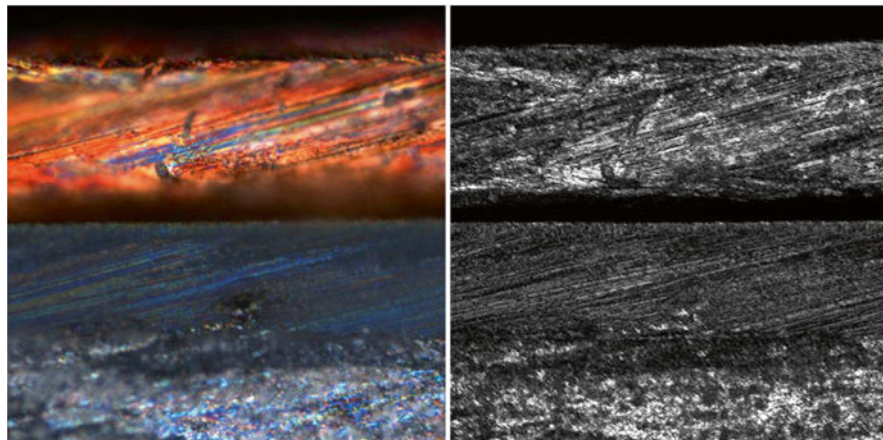
causes a higher needed input power, the message is clear. High thermal conductive substrates lead to higher output powers. Earlier simulations have already shown this trend [10].

In addition, there are still two more things to be mentioned by comparing anodized Al vs. Al<sub>2</sub>O<sub>3</sub> and AlN. Al can be shaped much easier than a ceramic material which could be used for a further reduction of the thermal resistance by more detailed substrate shapes. Even round shapes can easily be processed and, due to the high thermal conductivity of Al, the added thermal resistance is rather small (compare Fig. 10.3).

The biggest advantage is obviously the price. Anodized Al is around twenty times cheaper than Al<sub>2</sub>O<sub>3</sub> and even a thousand times cheaper than AlN (see Table 10.2). Depending on the substrate's share of total costs, the cost reduction can be in the region of several single percentages.

To demonstrate the actual behavior of the proposed new TEG substrate, several samples have been prepared. Figure 10.4 shows two pictures of the same sample. The left one is taken with a light microscope at a 50-times magnification. For the other one a confocal laser scanning microscope (CLSM) was used. In the shown pictures the Al<sub>2</sub>O<sub>3</sub>-layer in the middle has a thickness of about 36 μm. It was grown in sulfuric acid at room temperature with a current density of 20 mA/cm<sup>2</sup>. Tests have shown that layers with a minimum of 12 μm are thick enough to insulate the top copper (Cu) layer from the lower Al-substrate. However, to ensure mechanical stability the Al<sub>2</sub>O<sub>3</sub> has to be a little thicker. Even though for thermal reasons the Al<sub>2</sub>O<sub>3</sub>-layer should be as thin as possible.

On top of the Al<sub>2</sub>O<sub>3</sub> is a 45 μm thick Cu-layer which shall be used to connect the single thermocouples to a complete TEG. It was grown by a simple galvanic step in Cu(II) sulfate with a current density of 28 mA/cm<sup>2</sup> onto a thin sputtered titanium start layer. The start layer was deposited by magnetron sputtering in argon at a pressure of 2.4 Pa and 2 kW DC power. The gap between the metal and the insulation



**Fig. 10.4** Cross section view of anodized Al with Cu metallization—light microscope (*left*)/CLSM (*right*)

accrued during the sample preparation. Exchanging the titanium with titanium nitride will enhance the adhesion and will thereby enhance the mechanical stability. To structure this layer conventional printed circuit board processes can be used.

## Conclusions

It was shown that anodized aluminum is a cheap alternative for ceramics used nowadays. In special cases, anodized aluminum will actually enhance the output power of the device. In the simulated example, the exchange of the substrate revealed a power gain of over 20 %. Even though this is a constructed case, the consequences are distinct. It was also demonstrated that the substrate can be made very easily with widely used processes like those used for usual printed circuit board. In the end, anodized aluminum is at least one order of magnitude cheaper than usually used ceramics.

**Acknowledgments** The author would like to thank the German Federal Ministry of Education and Research (BMBF) for funding the Project HOTGAMS (03X3547A).

## References

1. Semeniuk VA (2013) A comparison of performance characteristics of multi-stage thermoelectric coolers based on different ceramic substrates; ICT 2013; Kobe, Japan; D3\_05; July, 2013
2. Rohde M, Schulz B (1990) The effect of the exposure to different irradiation sources on the thermal conductivity of  $\text{Al}_2\text{O}_3$ . *J Nucl Mater* 173(3):289–293
3. Barrett Jackson T, Virkar AV, More KL, Dinwiddie RB Jr, Cutler RA (1997) High-thermal-conductivity aluminum nitride ceramics: The effect of thermodynamic, kinetic, and microstructural factors. *J Am Ceram Soc* 80(6):1421–1435



4. Morrell R (2005) Tables of physical & chemical constants (16th edition 1995). 2.3.7 Thermal conductivities. Kaye & Laby Online. Version 1.0. [http://www.kayelaby.npl.co.uk/general\\_physics/2\\_3/2\\_3\\_7.html](http://www.kayelaby.npl.co.uk/general_physics/2_3/2_3_7.html)
5. Bhandari CM, Rowe DM (1980) Silicon–germanium alloys as high-temperature thermoelectric materials. *Contemp Phys* 21(3):219–242
6. Yazawa K, Shakouri A (2012) Scalable cost/performance analysis for thermoelectric waste heat recovery systems. *J Electr Mater* 41(6):1845–1850
7. Goodfellow.com: Properties of aluminum; 26.10.2013
8. Rohde M, Schulz B (1990) Thermal Conductivity of irradiated and nonirradiated fusion ceramics. In: *Thermal Conductivity*, vol 21. Plenum, New York, pp 509–519
9. Informationszentrum Technische Keramik: Aluminiumoxid 92%; [http://www.keramik-rs.de/ksuche/k\\_detail.asp?w\\_id=06](http://www.keramik-rs.de/ksuche/k_detail.asp?w_id=06). 30 Sept 2013
10. Assion F, Fischer C, Schönhoff M, Hilleringmann U, Hedayat C (2013) Designing output-power-optimized thermoelectric generators via analytic and finite element method modelling. In *Proceedings of the 2013 IEEE ICIT*, Cape Town; ISBN: 978-1-4673-4568-2; pp 695–699
11. Goodfellow.com; Article No. 662-250-90; 25 Jul 2013
12. Quick-Ohm.de; Article No. 5061-00490; 02 Aug 2013
13. Alu-Verkauf.de; Article AlMg1elox; 25.07.2013

# Chapter 11

## Silica-Based Materials for Thermoelectric-Legs Embedding

A. Famengo, S. Boldrini, S. Battiston, S. Fiameni, A. Miozzo, M. Fabrizio, and S. Barison

**Abstract** Sol-gel chemistry was used to synthesize low-density  $\text{SiO}_2$  aerogel for matrix embedding of silicide-based ( $\text{Mg}_2\text{Si}$  and  $\text{MnSi}_{(2-x)}$ ) thermoelectric legs. In thermoelectric (TE) modules, the heat conduction in air and the convective and radiative contribution to the heat transfer play an important role in the reduction of the efficiency of the module. Silica aerogels are known for the lowest thermal conductivity of any non-evacuated solid. With this in mind, silica-based aerogel materials were employed to fill the void spaces between the thermoelectric legs of a module. In order to do this, different synthesis procedures were taken into account to produce suitable silica materials. It is important that the silica can be easily cast into place, avoiding mechanical cracks of the matrix. Silica aerogel typically requires a supercritical drying step to remove the pore fluid from the  $\text{SiO}_2$  gel, avoiding the collapse of the pores. This procedure is not practical for TE-legs embedding and it is dangerous, expensive, and time-consuming. It is known that replacing the  $-\text{OH}$  groups with organic hydrophobic substituents in the  $\text{SiO}_2$  pores prevents the pore-shrinkage and the sintering of the matrix during solvent evaporation step. This allows synthesizing relatively light materials at low temperature and ambient pressure, with no need of supercritical drying of the gel. The obtained aerogels were characterized by thermogravimetric analysis and differential scanning calorimetry to evaluate the stability of the material and the chemical modification with increasing temperature. The thermal expansion of the silica was evaluated by means of dilatometry. Finally, the thermal diffusivity was measured with the laser flash method.

---

A. Famengo (✉) • S. Boldrini • S. Battiston • S. Fiameni • A. Miozzo  
M. Fabrizio • S. Barison  
Institute for Energetics and Interphases, National Research Council of Italy,  
Corso Stati Uniti 4, 35127 Padova, Italy  
e-mail: [a.famengo@ieni.cnr.it](mailto:a.famengo@ieni.cnr.it)

## Introduction

Thermoelectric devices are built up from thermoelectric legs made by conventional thermoelectric materials such as  $\text{Bi}_2\text{Te}_3$  and  $\text{PbTe}$ , and less conventional  $\text{Mg}_2\text{Si}$  and  $\text{MnSi}_{(2-x)}$  (higher manganese silicide, HMS) linked together by means of metal contacts. The thermoelectric legs are contacted electrically to obtain an electrical series configuration and a thermally parallel configuration, in order to keep all the legs on the same side at the same temperature. Embedding the legs in a chemically and electrical inert matrix could enhance the TE module performance by improving thermal insulation between the hot and the cold side. Furthermore, the matrix could act as a sublimation barrier, especially for materials where metallic elements tend to sublime into corrosive vapors [1]. Metal vapors can condense far from the material leg, creating problems such as thermal and/or electrical short circuits and consequently they can reduce the efficiency and the life of the module.

$\text{SiO}_2$  is an appealing candidate for TE module embedding because it is inert in the whole temperature range exploited for TE generation with several materials, such as skutterudites, TAGS,  $\text{PbTe}$ , and silicides. The most important feature is the versatility of  $\text{SiO}_2$  towards the formation of different nano- and microstructures with a high degree of porosity. For this reason, the lightest solids ever obtained are silica aerogels.

Module encapsulation on silica aerogel has already been exploited by Salvador et al. [2] and Sakamoto et al. [1]. However, obtaining silica aerogel suitable for high temperature thermoelectric applications is not straightforward. Wet chemistry like sol-gel reactions of silane precursor is used to synthesize porous  $\text{SiO}_2$  networks. The silica backbone created upon gelation of the silane precursor undergoes tensional stresses and it is sensitive to cracks. During the drying process necessary to obtain the  $\text{SiO}_2$  matrix, the solvent evaporates from the pores and the latter tends to collapse because of the capillary forces, causing severe shrinkage of the structure. Two possible techniques are commonly exploited to reduce pore collapse: drying the aerogel in an autoclave under supercritical conditions, avoiding the formation of the liquid solid meniscus, and the functionalization of  $\text{Si-OH}$  groups of the pores with organic hydrophobic groups.  $\text{Si-CH}_3$  groups are not reactive and they keep the pores “open.” Furthermore, the solvent inside the pores (usually alcohols) is replaced by nonpolar hexane (or other linear alkanes) which has a low surface tension, reducing the shrinkage during the drying step even at ambient pressure.

In this work, low-density silica was synthesized via ambient pressure drying with the aim to embed thermoelectric legs made of  $\text{Mg}_2\text{Si}$  and  $\text{MnSi}_{(2-x)}$ . Three samples named HMDZ\_1 (from the Si precursor HMDZ-hexamethyldisilazane), MTMS\_1 and MTMS\_2 (from the Si precursor MTMS-methyltrimethoxysilane) are discussed here. Ambient pressure drying was preferred to autoclave drying because it is more versatile. In principle, all the synthetic steps could be carried out directly on the mold where the thermoelectric legs are placed.

The thermal behavior of the silica synthesized was investigated up to 600 °C, considering that the operating temperature of  $\text{Mg}_2\text{Si}$  and  $\text{MnSi}_{(2-x)}$  is in the range 500–600 °C. The thermal diffusivity was evaluated for the sample showing adequate thermal behavior.

## Experimental Procedure

HMDZ\_1 was synthesized according to Wei et al. [3] modifying the synthesis procedure using hexamethyldisilazane (HMDZ) in place of trimethylchlorosilane (TMCS).

MTMS\_1 was synthesized following the procedure reported by Xu et al. [4] with minor modifications.

MTMS\_2 was obtained by reaction of methyltrimethoxysilane (MTMS) with an aqueous solution of oxalic acid (0.01 M) in methyl alcohol (MeOH) with  $\text{MeOH:MTMS}=26$  and  $\text{oxalic acid:MTMS}=0.004$  molar ratios. The system was stirred at room temperature for 1 h and then an aqueous solution of  $\text{NH}_3$  (2.75 M) was added to the reaction mixture, keeping a molar ratio of  $\text{NH}_3\text{:MTMS}=0.20$ . After 1 h of stirring, the sol was poured into polyethylene molds and let to gel overnight. Residual MeOH was removed and the alcogels were aged in ethylic alcohol (EtOH) for 6 h at 60 °C. After aging, EtOH was removed washing the material several times with n-hexane and the materials were dried at 50 °C for 24 h. The samples were thermal treated at 100 °C for 1.5 h followed by 150 °C for 1.5 and finally they were kept at 200 °C for 1 h.

Thermogravimetric analysis were performed on a TA SDT Q600 TGA/DSC analyzer for the three samples under dry air (100 mL/min) using an alumina crucible.

Dilatometry measurements were recorded on a Netzsch DIL 402 PC dilatometer under an Ar atmosphere (90 mL/min) for sample HMDZ\_1 cut as a 7.6-mm bar.

Thermal treatment on MTMS\_1 and MTMS\_2 was performed on a homemade apparatus with a flux of air of 200 mL/min in a Nabertherm P330 tubular furnace.

The thermal diffusivity was measured via laser flash method by means of a Netzsch Microflash LFA457, using a powder sample holder with an internal graphite coating.

## Results and Discussion

Three types of  $\text{SiO}_2$  matrices were synthesized with the idea of embedding the n- $\text{Mg}_2\text{Si}$  and p-HMS (Higher Manganese Silicide) legs of a thermoelectric module. The matrix should be light and should act as thermal and electrical insulation barriers between the legs and between the hot and cold sides of the module. Among the large variety of organosilane precursors, tetraethoxysilane (TEOS) and methyltrimethoxysilane (MTMS) were chosen for their availability and fast hydrolysis and

condensation time [5]. It must be pointed out that sol-gel chemistry is very complex and the reactivity of the precursors does not depend only on their chemical nature but also on the applied reaction conditions [6, 7]. The solutions of the precursors are liquids of low viscosity before gelation time so it is possible to cast the SiO<sub>2</sub> matrix on modules of the desired shape.

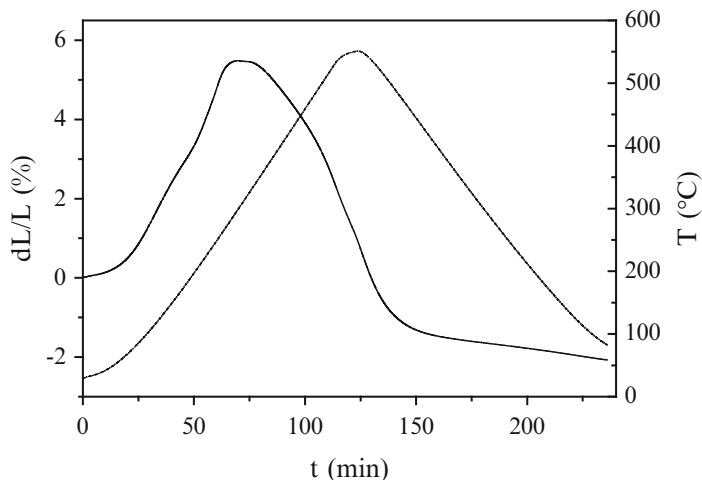
In order to obtain silica materials with low densities, two main synthetic paths were followed. The first was the formation of hydrophilic alcogels via acidic hydrolysis (HCl) of TEOS and then condensation of the polysiloxane species with aqueous NH<sub>3</sub>, as previously reported by Wei et al. [3]. The as-obtained gels underwent silylation with hexamethylsilazane (HMDZ), less hazardous than trimethylchlorosilane (TMCS) usually employed. The silylation process changes the liquid-solid contact angle and reduces the capillary liquid tension avoiding cracking of the network during the drying process. Furthermore, it passivates the pore surface, limiting the condensation of –Si–OH groups that leads to shrinkage of the gel [7]. After silylation, the gels were kept several days in hexane and then air dried to obtain a relative low-density hydrophobic silica (0.3 g/cm<sup>3</sup>), indicated here as HMDZ\_1.

In the second synthetic route, MTMS was used as the precursor because of the presence of the nonpolar CH<sub>3</sub>–Si on the silane molecule. This avoids the silylation step reducing the processing time and costs. Two procedures were followed with MTMS. In the first, reported by Xu et al. [4], MTMS was hydrolyzed in MeOH with an aqueous solution of oxalic acid and then aqueous ammonia was added to obtain the alcogel. The gel was aged and dried replacing MeOH with EtOH, followed by thermal treatments at 50, 100, 150, and 200 °C. The aerogel so obtained (density 0.102 g/cm<sup>3</sup>) was named MTMS\_1.

It must be said that, for this reaction, toxic MeOH was replaced by EtOH first as the solvent. Unfortunately, any attempts to carry out the synthesis with MTMS in ethanol led to cracked transparent xerogel granules.

In the second synthesis procedure, a solution of aqueous ammonia was added after the hydrolysis of MTMS with oxalic acid in MeOH, working with a high content of water. It has been observed that adding F<sup>-</sup> ions (within the NH<sub>3</sub> solution), which generally decreases the gelation time of the silica [8], did not considerably change the gelation time in this case. The excess of water should favor the acidic hydrolysis of MTMS, while the condensation process is enhanced by the high pH (9–10) of the solution after the addition of NH<sub>3</sub>.

The silica matrix was aged in ethanol, washed several times with ethanol and then n-hexane, and then dried. Thermal treatments at 50, 100, 150, and 200 °C were performed. Hydrophobic and light silica was obtained, indicated here as MTMS\_2 (density 0.09 g/cm<sup>3</sup>). As to the macroscopic scale, HMDZ\_1 appeared as a semi-transparent solid while MTMS\_1 and MTMS\_2 were opaque. MTMS\_1 retained its shape when small deformations were applied and it was quite easy to cut into slices without breaking the material. MTMS\_2 appeared as a highly compressed powder, and after compression, it became powdery. However, it was possible to cut it into pieces of all shapes and thickness.



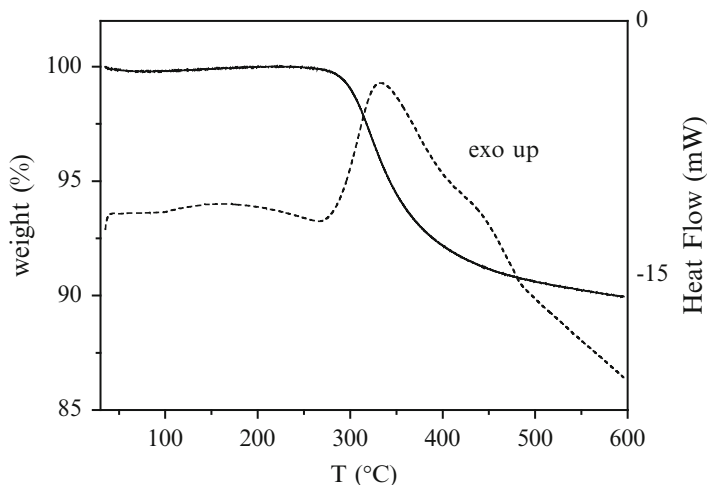
**Fig. 11.1** Percentage of one-dimensional expansion  $dL/L$  versus time (*dash*) and temperature versus time (*solid*) for sample HMDZ\_1

To understand the mechanical behavior of the  $\text{SiO}_2$  materials synthesized, thermal expansion measurements from RT to 600 °C, the operative range for  $\text{Mg}_2\text{Si}$  and HMS thermoelectric materials, were performed on sample HMDZ\_1 under an Ar atmosphere. The expansion ( $dL$ ) curve versus time and temperature ramp is displayed in Fig. 11.1.

In the range 30–250 °C the relative expansion was not perfectly linear: the system expanded linearly up to 150 °C, a small decrease of the slope  $dL/L$  versus  $t$  was observed until 200 °C and then it increased up to 250 °C, from where the expansion became constant up to 330 °C. After 330 °C, HMDZ\_1 underwent shrinking while heating up to 600 °C. After 600 °C, the cooling segments started and the shrinkage continued. This behavior could be explained by thermogravimetric (TGA) and differential scanning calorimetry (DSC) analyses (Fig. 11.2) performed in air: an important weight loss for HMDZ\_1 occurred from 250 to 600 °C. This corresponds to the oxidation of the organic  $-\text{CH}_3$  groups present on the surface of the pores. After oxidation, the pores  $-\text{CH}_3$  groups, which could not react, were replaced by  $-\text{OH}$  polar groups that could condense to give  $\text{Si-O-Si}$  new bonds, leading to pore collapse and consequently to material shrinkage.

Even if the dilatometry was performed under an argon flux of 100 mL/min, small amounts of oxygen impurities could cause the oxidation of methyl groups of the pores. It is important to consider that also under inert atmosphere chemical reaction, like pyrolysis of the methyl groups, could occur in the temperature range considered, leading to the rearrangement of the microstructure and possible shrinkage.

The HMDZ\_1  $dL/L$  curve reached the origin at 550 °C and the shrinkage continued linear until 475 °C. At this point, the slope of the curve decreased and remained constant up to 80 °C (below this temperature the dilatometer is no more able to control the cooling rate). From the DSC signal (Fig. 11.2) it can be observed that the



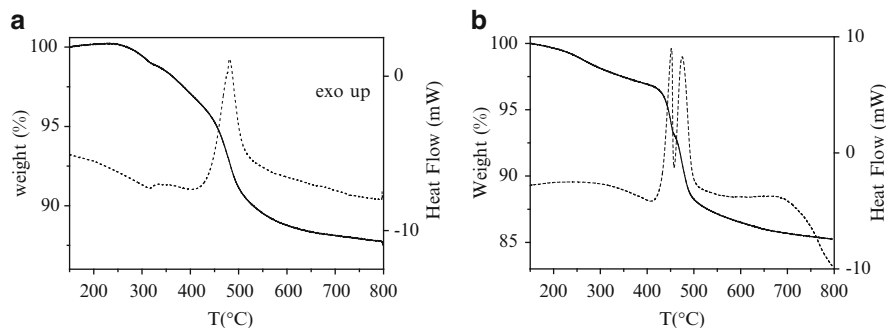
**Fig. 11.2** TGA (solid) and DSC (dash) curves for HMDZ\_1 (heating rate: 5 °C/min, air: 100 mL/min)

main peak at 350 °C had a shoulder at 450 °C that corresponds to the oxidation of secondary methyl groups, located on a different site of the silica network. This could affect the thermal expansion of the material.

After the thermal expansion measurement, HMDZ\_1 showed several cracks that propagated during the measurement. This could be due to the collapse of pores during oxidation of  $-\text{CH}_3$  groups and, probably, the silica network was not strong enough to resist the thermal stresses. On the basis of this consideration, and as observed by Sakamoto et al. [1], more “elastic” and deformable matrices are required in order to embed parallelepiped TE modules because the edges could act as stress intensifier causing the propagation of cracks. MTMS, with a methyl group bound directly to Si could lead to elastic and compressible aerogel materials, as reported by Xu et al. [4].

For MTMS\_1 and MTMS\_2, the thermal expansion curves were not recorded because it was not possible to determine the origin of the dilatometer measuring bar. Because the typical operating temperatures of the  $\text{Mg}_2\text{Si}/\text{HMS}$  TE modules are between 500 and 600 °C, a thermal treatment was performed under air (200 mL/min) from RT to 600 °C (heating/cooling ramp 5 °C/min, 120 min at 600 °C) on both samples to check the presence of cracks and their integrity. MTMS\_1 broke up into powdery pieces after the thermal treatment and it was not possible to measure its density. On the other hand, MTMS\_2 retained its shape with a linear shrinkage of 10 %. The thermal treated MTMS\_2 has a density of 0.11 g/cm<sup>3</sup>.

Thermogravimetric and differential scanning calorimetry analyses of MTMS\_1 and MTMS\_2 in air are shown in Fig. 11.3. In the case of MTMS\_1, a sharp exothermic peak was present at 481 °C corresponding to the main weight loss in the TGA curve. These are related to the oxidation of  $\text{CH}_3$  groups present in the Si-O-Si backbone. At 350 °C, a broad and less intense exothermic peak was present together



**Fig. 11.3** DSC (*dash*) and TGA (*solid*) curves for MTMS\_1 (a) and MTMS\_2 (b) recorded with a heating rate of 3 °C/min in air (100 mL/min)

with a weight loss starting at 250 °C. This could be attributed to the oxidation of surface functional  $\text{CH}_3$  groups but also to the evaporation and oxidation of residual organic solvent that could be trapped inside the silica matrix. It has to be noted that after the analysis, the residual sample appeared as powder after the thermal treatment at 600 °C.

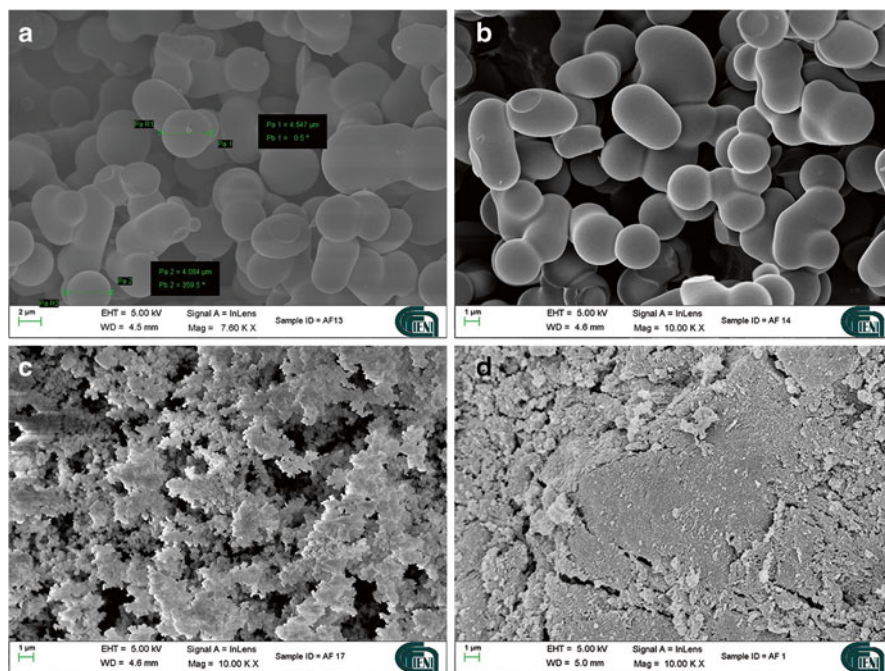
For MTMS\_2, a slight weight loss was present in the range 150–350 °C as observed for MTMS\_1, but, in this region, the DSC signal is smooth. This could be an indication of the residual solvent evaporation, trapped into the silica matrix. The oxidation of organic  $\text{CH}_3$  occurred from 400 °C. Two sharp and well-resolved exothermic peaks at 451 and 475 °C are an indication of two different sites for  $\text{Si}-\text{CH}_3$  groups in the silica network, leading to site-affected oxidation enthalpy.

MTMS\_1 and MTMS\_2 showed similar thermal behaviors but the former one cracked upon heating at 600 °C. The density of MTMS after the thermal treatment was 0.21 g/cm<sup>3</sup> and the matrix linearly shrunk by 18 % of the original length. The thermal behavior could be better understood considering the microstructure of the samples.

Secondary electron field emission (FE)—scanning electron microscope (SEM) micrographs for MTMS\_2 before and after thermal treatment are displayed in Fig. 11.4. For comparison, also HMDZ\_1 and MTMS\_1 (before thermal treatment) are shown.

The microstructure of MTMS\_2 seems to not be affected by the thermal treatment and it consists of micrometer-rounded silica particles attached to each other to form opened chain structures and leaving void opened spaces. This is consistent with the Ostwald ripening mechanism for silica formation, by which small particles re-dissolve and larger particles grow from the condensation of the dissolved ones. This mechanism is favored mainly in aqueous systems [5]. In this case, MTMS\_2 was synthesized in the presence of a large excess of water. It has to be pointed out also that the sizes of the microspheres are highly homogeneous. By comparison, MTMS\_1 showed compact agglomerates of grains of the order of 100 nm forming micrometer sized open spaces, as previously reported [4]. HMDZ\_1 had similar globular structures as for MTMS\_1 but smaller voids and pores (less than 200 nm)



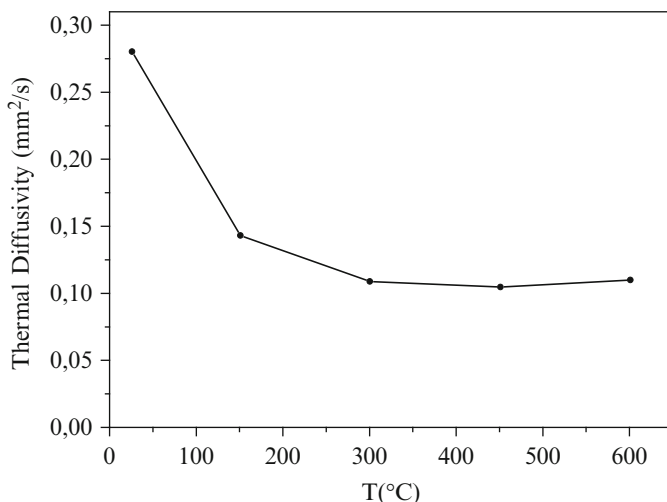


**Fig. 11.4** Secondary electron SEM micrographs for MTMS\_2 before (a) and after (b) thermal treatment at 600 °C; MTMS\_1 (c) and HMDZ\_1 (d)

around the agglomerates. The chained structures of MTMS\_2 are probably held together via electrostatic forces and this could be the reason that, on macroscopic scale, this material appeared as pressed powder, retaining its shape. The chain agglomerations of silica microspheres and the presence of void spaces made MTMS\_2 retain its shape upon thermal treatment. It is reasonable to consider that the chains can be rearranged during heating in the void spaces without breaking. Furthermore, the organic products of combustion have enough space to escape from the silica structure preserving the network. On the other hand, HMDZ\_1 and MTMS\_1 networks could be damaged because of the retention of organic products on the pores, which are less accessible to gases such oxygen or air.

The thermal diffusivity of MTMS\_2 after thermal treatment at 600 °C was measured via the laser flash method. Thermal-treated MTMS\_2 was chosen because the typical silicide TE module working temperature is in the range of 500–600 °C, and no organic groups are present in the SiO<sub>2</sub> matrix at these temperatures.

The measurement was carried out under an Ar atmosphere to avoid the oxidation of the graphite layer needed for the measurement. As it can be observed in Fig. 11.5, the thermal diffusivity decreased with temperature reaching a minimum value of 0.1047 mm<sup>2</sup>/s at 450 °C and then slightly increased at 600 °C (0.1099 mm<sup>2</sup>/s). It was not possible to evaluate the thermal conductivity because the value of the density ( $\rho$ ), that should be used for this calculation, is not the measured one. In fact,



**Fig. 11.5** Thermal diffusivity of MTMS\_2 as function of the temperature

MTMS\_2 was slightly pressed inside the sample holder here used and the density remained uncertain.

Furthermore, to the best of author knowledge, in the literature, thermal conductivity measurements on silica aerogel and light xerogel are usually performed via the hot-disc or the hot wire techniques [3], and the values are restricted to room temperature, so it is not possible to make a comparison in the temperature range here considered (25–600 °C). On this basis, only thermal diffusivity values are reported in Fig. 11.5. From a qualitative point of view, considering the low density of MTMS\_2 together with an intrinsic low specific heat for silica, it is reasonable to expect values of thermal conductivity of the order of few mW/mK, as previously reported [3, 9].

## Conclusions

Three types of SiO<sub>2</sub> matrices were considered with the aim of embedding Mg<sub>2</sub>Si/HMS thermoelectric modules. HMDZ\_1 and MTMS\_1 were synthesized as already reported [3, 4] with minor variations of the synthesis procedure. MTMS\_2 was synthesized according to the procedure here reported, adding more water to enhance the gelation step and to reduce gelation time and to obtain more elastic SiO<sub>2</sub> network. The SiO<sub>2</sub> was made hydrophobic to reduce shrinkage during the ambient pressure-drying of the gel, in order to obtain low-density and highly porous materials. These characteristics are required to avoid much weight increase after embedding TE modules, made of light Mg<sub>2</sub>Si and MnSi<sub>(2-x)</sub> and to control the thermal conductivity.

**Acknowledgments** The authors are grateful to Dr Stefano Fasolin for dilatometry measurement. This work has been funded by the Italian National Research Council—Italian Ministry of Economic Development Agreement “Ricerca di sistema elettrico nazionale.”

## References

1. Sakamoto J, Caillat T, Fleurial JP, Jones S, Paik JA. <http://trsnew.jpl.nasa.gov/dspace/>
2. Salvador JR, Cho JY, Ye Z, Moczygemba JE, Thompson AJ, Sharp JW, König JD, Maloney R, Thompson T, Sakamoto J, Wang H, Wereszczak AA, Meisner GP (2013) *J Electr Mater* 42(7):1389–1399
3. Wei TY, Chang TF, Lu SY (2007) *J Am Cer Soc* 90(7):2003–2007
4. Xu B, Cai JY, Finn N, Cai Z (2012) *Microporous Mesoporous Mater* 148:145–151
5. Husing N, Schubert U (2005) *Synthesis Inorg Mater*, Chapter 4, Wiley VCL, New York, NY
6. Gurav JL, Jung IK, Park HH, Kang ES, Nadargi DY (2010) *J Nanomat* 1–11. <http://dx.doi.org/10.1155/2010/409310>
7. Schmidt HJ (1988) *Non Cryst Sol* 100:51–64
8. Brinker CJ, Scherrer GW (1990) *Sol-gel science. The physics and chemistry of sol-gel processing*, Chapter 3. Academic, Boston, MA
9. Gurav JL, Venkateswara Rao A, Nadargi DY (2009) *J Sol-Gel Sci Technol* 50:275–280

# Chapter 12

## Finite Element Approach for the Evaluation and Optimization of Silicide-Based TEG

A. Miozzo, S. Boldrini, S. Battiston, A. Famengo, S. Fiameni, T. Sakamoto, and S. Barison

**Abstract** Numerical modelling represents an effective tool for designing and evaluating the performances of thermoelectric power generators (TEG). In particular, the finite element (FE) method allows performing multiphysics simulation, that is coupling different physical phenomena, such as heat transfer, thermoelectric effects, and Joule heating. In this work, FE modeling is at first used to reproduce the results of the open circuit voltage and output power measurements on an undoped  $\text{Mg}_2\text{Si}$  TE-chip under large temperature differences. Furthermore, the conversion efficiency of a 16-chip TEG module has been calculated with different ratios of the cross sections of the n-type (Bi-doped  $\text{Mg}_2\text{Si}$ ) and the p-type (higher manganese silicide, HMS) legs. In both analyses, the thermal and electrical conductivities and Seebeck coefficient are given, as input, in function of temperature. The effects of thermal and electrical contact resistances were taken into account, by introducing thin thermally/electrically resistive layers in the numerical model.

---

A. Miozzo (✉) • S. Boldrini • S. Battiston • A. Famengo  
S. Fiameni • S. Barison  
Institute for Energetics and Interphases, National Research Council of Italy,  
Corso Stati Uniti 4, 35127 Padua, Italy  
e-mail: [alvise.miozzo@ieni.cnr.it](mailto:alvise.miozzo@ieni.cnr.it)

T. Sakamoto  
Department of Materials Science and Technology, Tokyo University of Science, Japan

## Introduction

Evaluating the performances of thermoelectric devices is usually a hard task to achieve, since it involves the solution of the coupled field equations of the thermoelectric effects on three-dimensional domains (thermoelectric chips). No analytical solution normally can be found even with simplified geometries and, for this reason, numerical strategies must be implemented. Numerical methods generally employed are based on the discretization of the domains, in order to convert the continuous operator problem (differential equations) to a discrete problem (iterative solution of linear systems) that leads to the evaluation of the values of temperature and electric potential on the nodes linking the adjacent subdomains. In this work, the finite element method was used to solve the coupled thermal-electrical equations of the thermoelectric effect; other numerical procedures available are the finite difference method and the finite volume method [1].

The thermoelectric effect is governed by the equations of heat flow and continuity of electric charge [1, 2]:

$$\rho C \frac{\partial T}{\partial t} + \nabla \cdot \mathbf{q} = Q \quad (12.1)$$

$$\nabla \cdot \mathbf{J} = \frac{\partial \rho_c}{\partial t} \quad (12.2)$$

where  $T$  is the temperature [K],  $\rho$  is the density [kg/m<sup>3</sup>],  $C$  is the specific heat [J kg<sup>-1</sup> K<sup>-1</sup>],  $\mathbf{q}$  is the heat flux vector [W/m<sup>2</sup>],  $Q$  is the heat generation rate per unit volume [W/m<sup>3</sup>],  $\mathbf{J}$  is the electric current density vector [A/m<sup>2</sup>], and  $\rho_c$  is the space charge density [A/m<sup>3</sup>]. In Eqs. (12.1) and (12.2),  $\mathbf{q}$  and  $\mathbf{j}$  are given by the thermoelectric constitutive equations:

$$\mathbf{q} = P\mathbf{J} - k\nabla T \quad (12.3)$$

$$\mathbf{J} = \sigma(\mathbf{E} - \alpha\nabla T) = \sigma(-\nabla V - \alpha\nabla T) \quad (12.4)$$

where  $P$  is the Peltier coefficient [V],  $k$  the thermal conductivity [W m<sup>-1</sup> K<sup>-1</sup>],  $\sigma$  the electrical conductivity [S/m],  $\mathbf{E}$  the electric field intensity vector [V/m],  $V$  the electrical potential [V], and  $\alpha$  is the Seebeck coefficient [V/K]. Furthermore, the internal heat source, including the Joule heating contribution, is defined by:

$$Q = \mathbf{J} \cdot \mathbf{E} \quad (12.5)$$

For steady-state analyses Eqs. (12.1) and (12.2) become:

$$\nabla \cdot (-k\nabla T + P(-\sigma\nabla V - \sigma\alpha\nabla T)) = (-\sigma\nabla V - \sigma\alpha\nabla T) \cdot (-\nabla V) \quad (12.6)$$

$$\nabla \cdot (-\sigma \nabla V - \sigma \alpha \nabla T) = 0 \quad (12.7)$$

The aim is to calculate the distribution of temperature  $T$  and electric potential  $V$  on the thermoelectric material (domain). Joule heating in Eq. (12.7) makes the problem nonlinear [3]; furthermore, the temperature dependency of material properties  $k$ ,  $\sigma$ ,  $\alpha$  must be taken into account.

The thermoelectric effect, described by Eqs. (12.1) and (12.2), is a coupled problem and in general, in the applications such as evaluation of thermoelectric generators (TEG) with different operating conditions, Eqs. (12.1) and (12.2) need to be considered together with further equations governing other involved physics. Therefore, a multiphysics approach can be considered as a suitable strategy for modelling thermoelectric devices and the finite element method can be easily used to implement multiphysics simulation.

## FE Analysis

The finite element version of Eqs. (12.6) and (12.7) was implemented through the *Physics Builder Interface* of *COMSOL Multiphysics* [4] in the weak form of the problem [5, 6]:

$$\int_{\Omega} (\nabla \cdot \mathbf{q}) w_T \partial \Omega = \int_{\Omega} Q w_T \partial \Omega \quad (12.8)$$

$$\int_{\Omega} (\nabla \cdot \mathbf{J}) w_V \partial \Omega = 0, \quad (12.9)$$

where  $w_T$  and  $w_V$  are  $H^1(\Omega)$  Sobolev weight functions.

Equations (12.8) and (12.9) are solved on the discretized domain (mesh) [2] where:

$$T = \mathbf{N} \cdot \mathbf{T}_e \quad (12.10)$$

$$V = \mathbf{N} \cdot \mathbf{V}_e \quad (12.11)$$

where  $\mathbf{T}_e$  and  $\mathbf{V}_e$  are the values of  $T$  and  $V$  on the nodes of the mesh, and  $\mathbf{N}$  the shape functions that approximate the shape of the distribution of temperature and electric potential within the finite elements. In this work, the FEM procedure is used to perform analyses on (a) single TE chips (height  $h=6-15$  mm) and on (b) an embedded in air 16-leg TEG (legs height  $h=10$  mm), calculating the temperature and electric potential distributions using Eqs. (12.10) and (12.11) in the chips, in the connecting Cu elements, and in the fluid (the domains). The thermoelectric materials are assumed to be isotropic, considering  $k$ ,  $\sigma$  and  $\alpha$  as scalar quantities instead of  $3 \times 3$  matrices  $[k]$ ,  $[\sigma]$ ,  $[\alpha]$  [2]; the temperature dependency of these properties is taken

into account. In the finite element approximation of Eqs. (12.10) and (12.11), quadratic Lagrange elements are used. The resulting mesh was almost coarse with a maximum size of the elements varying from 0.6 mm up to 2.0 mm; finer meshes did not lead to a significantly higher accuracy in the results.

In order to consider thermal and electrical resistances, boundary features have been implemented. This is useful to avoid the introduction of thin geometric domains, which would force the mesh to be, locally, extremely fine. For the thermal contact resistance, heat flux across the resistive boundary is defined by [4]:

$$-\mathbf{n}_d \cdot (-k_d \nabla T_d) = -k_s \frac{T_u - T_d}{d_s} \quad (12.12)$$

$$-\mathbf{n}_u \cdot (-k_u \nabla T_u) = -k_s \frac{T_d - T_u}{d_s} \quad (12.13)$$

where  $T$  is the temperature, u and d subscripts stand for upside and downside of the contact surface [4], and  $k_s$  and  $d_s$ , thermal conductivity and thickness of an equivalent thin domain, are defined through the thermal contact resistivity  $R_t = d_s/k_s$  [ $\text{m}^2 \text{K/W}$ ]. In the same way, for the electrical contact resistance, the current density across the boundary is defined by [4]:

$$\mathbf{n} \cdot \mathbf{J}_d = \frac{1}{\rho_s} (V_u - V_s) \quad (12.14)$$

$$\mathbf{n} \cdot \mathbf{J}_u = \frac{1}{\rho_s} (V_s - V_u) \quad (12.15)$$

where  $V$  is the electric potential and  $\rho_s$  is the electrical resistivity of the contact surface.

## Results of the FE Analysis on Silicide-Based TEG

Finite element analyses were performed on a single chip and a 16-chip thermoelectric generator. In the first case, the analysis was carried out to verify the conformity of numerical results with open-circuit voltage and output power data measurements, reported in Iida, Sakamoto et al. [7]. In the second case, the goal is to find out the efficiency of a thermoelectric module, embedded in dry air, with different values of the cross-section ratio of the p-type HMS legs and the n-type Bi-doped  $\text{Mg}_2\text{Si}$  legs. This latter analysis led to the identification of an optimal geometrical configuration, which can improve the results obtained through a simplified analytical method based on the mean values for  $k$ ,  $\sigma$  and  $\alpha$  [8].

### ***Steady-State Analysis of a Single Undoped Mg<sub>2</sub>Si Chip***

FEM simulation was performed on a parallelepiped-shaped sample with cross-section area  $2\text{ mm} \times 2\text{ mm}$  and height varying from 6.0 to 15.0 mm, for  $\Delta T = 500\text{ K}$  (cold side  $T_c = 373\text{ K}$ , hot side  $T_h = 873\text{ K}$ ). The results of the numerical analysis were compared to those obtained by Iida, Sakamoto et al. in [7]. In Fig. 12.1a, b the values of measured thermal and electrical conductivities and Seebeck coefficient are plotted [7].

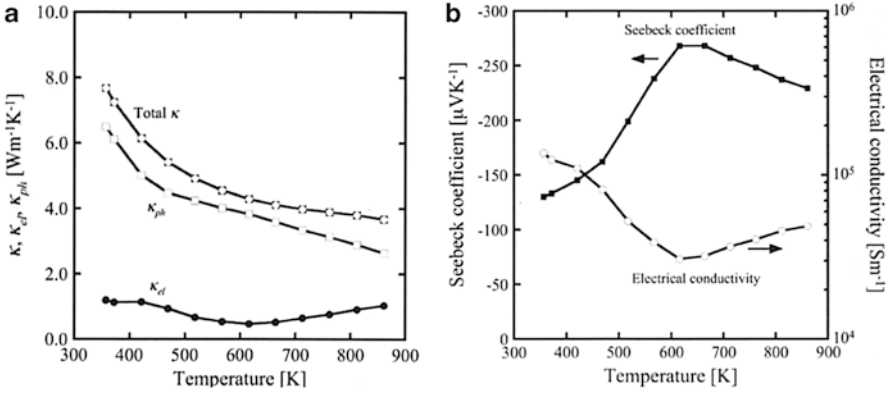
Thermal contact resistivity values were taken into account on both the cold and the hot side; reference values were considered  $0.3195 \times 10^{-4}\text{ m}^2\text{ K/W}$  at the cold side and  $0.8241 \times 10^{-4}\text{ m}^2\text{ K/W}$  at the hot side, being at both sides  $d_s = 0.10\text{ mm}$ , corresponding to a feasible value of roughness of the contact layer [9]. Steady-state FE analysis was developed on a geometrical model with the same cross-section area and with different height values from 6.0 to 15 mm for the thermoelectric domain; on the bottom and the top two 1.0 mm thick Cu layer were considered. Boundary conditions were defined at the lower and upper faces, forcing temperature values to be 373 and 873 K respectively. The temperature distribution on the Mg<sub>2</sub>Si and Cu domains is reported in Fig. 12.2.

Open-circuit voltage and output power were also calculated; Fig. 12.3 shows the leg height dependency of open-circuit voltage to be compared with experimental measurements reported in Iida et al. [7]. Numerical analysis yields an open-circuit voltage value  $V_{oc} = 102.6\text{ mV}$  with  $h = 7.5\text{ mm}$ , whereas measured value for the same height is  $V_{oc} = 101.1\text{ mV}$ . Numerically evaluated maximum output power density for  $h = 7.5\text{ mm}$  is  $1.58\text{ W/cm}^2$  whereas the measured value is  $1.42\text{ W/cm}^2$ . The higher difference between measured and calculated values of power density may be related to the fact that no electrical contact resistance has been defined. The electrical contact resistance would affect output power with no effect on the open-circuit voltage. The output power density calculated with FEM procedure is plotted on Fig. 12.4 as function of the electric current.

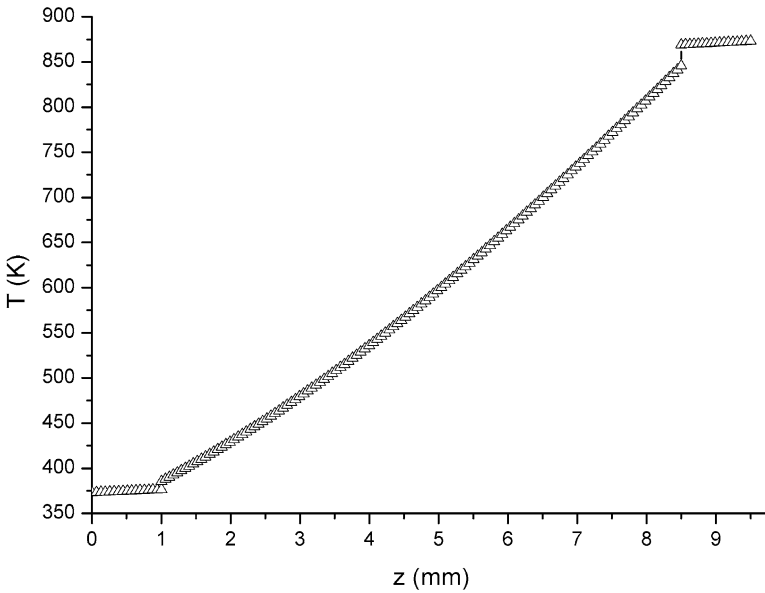
### ***Steady-State Analysis of a 16-Chips Thermoelectric Generator (TEG)***

A finite element analysis has been carried out on a 16-element thermoelectric module with HMS p-type legs and Bi-doped Mg<sub>2</sub>Si n-type legs with different values of cross-sectional ratios  $A_p/A_n$  and with  $\Delta T = 500\text{ K}$ . The thermoelectric legs were considered to be embedded in a medium with the temperature dependent thermal properties of the dry air. For the n-type legs (1 % Bi-doped Mg<sub>2</sub>Si) the values of the thermal and electrical resistivities and Seebeck coefficient were taken as reported in Fiameni et al. in [10]; p-type legs were characterized with the properties of higher manganese silicide reported in Famengo et al. in [11]. The n-type legs were considered with a fixed  $4.0 \times 4.0\text{ mm}^2$  cross section, whereas for the p-type leg was

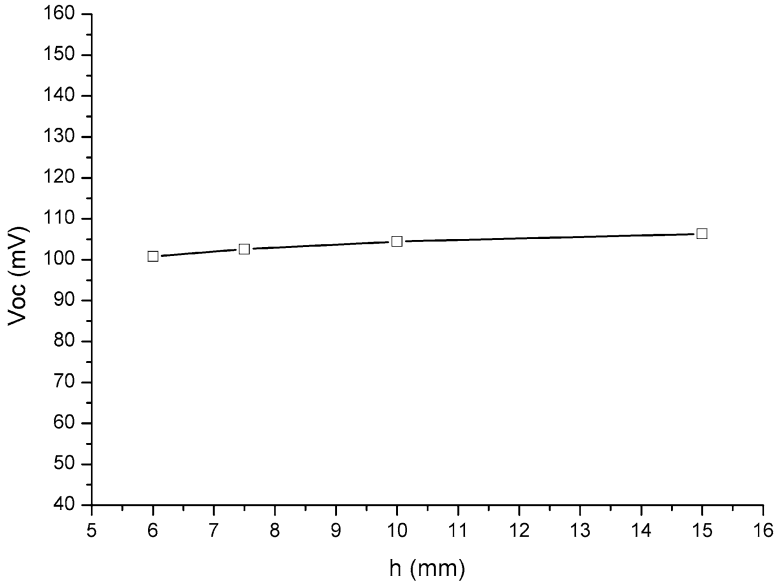




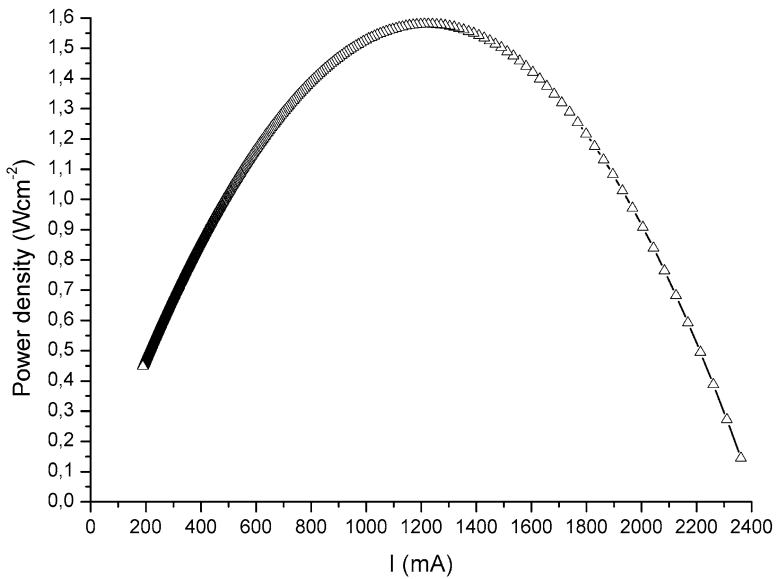
**Fig. 12.1** (a) Temperature dependence of the thermal conductivity of the undoped Mg<sub>2</sub>Si sample over the temperature range from 300 to 860 K (Iida, Sakamoto et al. [7]). (b) Temperature dependence of the electrical conductivity and the Seebeck coefficient of the undoped Mg<sub>2</sub>Si sample (Iida, Sakamoto et al. [7])



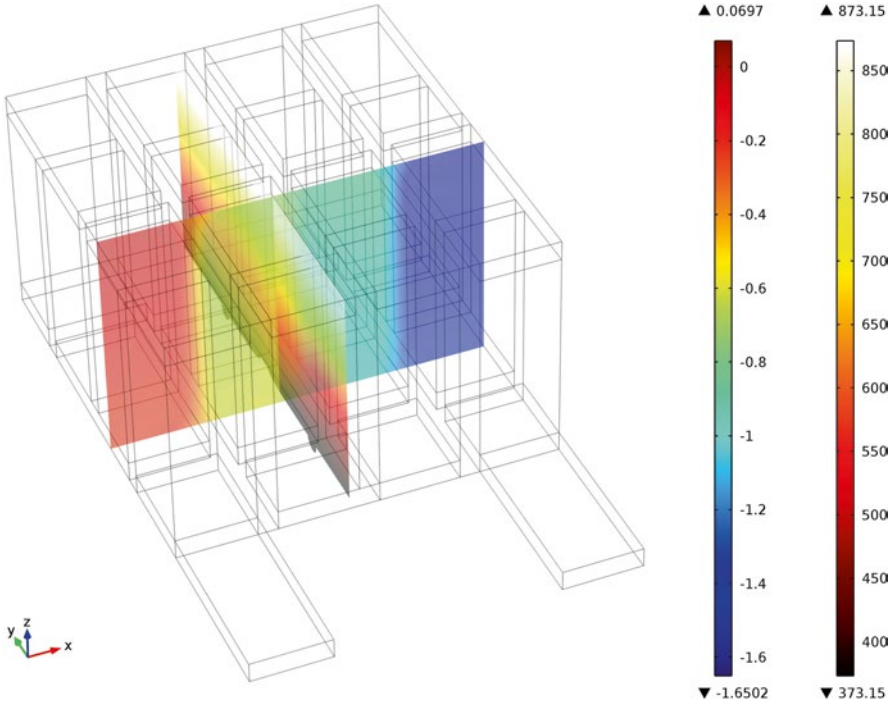
**Fig. 12.2** Temperature distribution on the Mg<sub>2</sub>Si chip with the bottom and top Cu layers, height of the TE chip  $h=7.5$  mm plotted as a function of  $z$ -coordinate: discontinuities occur where thermal contact resistivity conditions are defined



**Fig. 12.3** Numerically evaluated open-circuit voltage for different values of the height of the  $2 \times 2 \text{ mm}^2$   $\text{Mg}_2\text{Si}$  chip; the numerically evaluated open-circuit voltage with  $h=7.5$  mm is  $V_{oc,num} = 102.6$  mV whereas the measured value [7] is 101.1 mV



**Fig. 12.4** Numerically evaluated power density [ $\text{W}/\text{cm}^2$ ] as function of current intensity [mA]. The maximum value of power density is  $1.58 \text{ W}/\text{cm}^2$  for load resistance  $42 \text{ m}\Omega$



**Fig. 12.5** Distribution of temperature  $T$  [K] ( $yz$  plane) and electric potential  $V$  [V] ( $zx$  plane) on the thermoelectric, connection and fluid domains for cross-sectional ratio  $A_p/A_n=1.25$

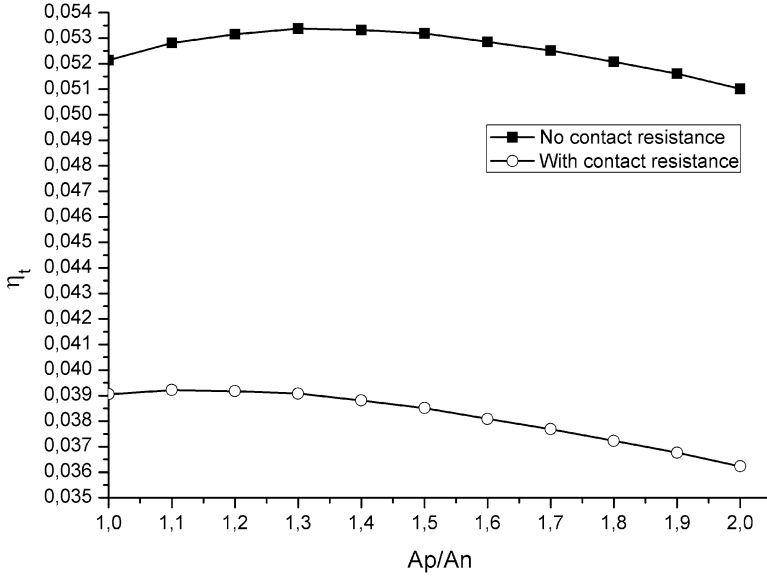
considered  $A_p=4.0 \times L_{yp}$  mm<sup>2</sup> with  $L_{yp}$  varying from 4.0 to 8.0 mm ( $1.0 \leq A_p/A_n \leq 2.0$ ); for all legs, the height was taken  $h=10$  mm.

In Fig. 12.5, the distributions of the temperature ( $yz$ -plane) and the electric potential ( $zx$ -plane) on the thermoelectric, the connecting Cu element and the fluid domains are shown for cross-sectional ratio  $A_p/A_n=1.25$ . At first, no thermal/electrical contact resistances have been defined for the interfaces; the cross-sectional ratio dependence of conversion efficiency has been investigated.

With  $1.0 \leq A_p/A_n \leq 2.0$ , the internal resistance of the thermoelectric legs varies from 0.1821 to 0.2561  $\Omega$ . The FE analysis shows that for a load resistance  $R_{load}$  equal to the mean value  $R_{int,m} \approx 0.21$   $\Omega$ , the optimum value of the cross-sectional ratio for the conversion efficiency is  $(A_p/A_n)_{opt,eff} \approx 1.30$ . The maximum value for conversion efficiency with no electrical contact resistance was found to be  $\eta_{l,max} = 5.33$  %. The optimum value for  $A_p/A_n$  can be compared with the result obtained with mean values for the thermoelectric properties [8]:

$$\Psi^* = \sqrt{\lambda_n \rho_p / \lambda_p \rho_n} \quad (12.16)$$

Taking the mean values for thermal conductivity and the electrical resistivity for the n,p-legs:



**Fig. 12.6** Conversion efficiency as function of cross-sectional ratio  $A_p/A_n$  ( $1.0 \leq A_p/A_n \leq 2.0$ ),  $R_{\text{load}} = R_{\text{int,m}} = 0.21 \Omega$ , (a) without and (b) with electrical contact resistance taken into account

$\lambda_{n,\text{mean}} = 3.36 \text{ Wm}^{-1} \text{ K}^{-1}$ ;  $\rho_{n,\text{mean}} = 2.172 \times 10^{-5} \Omega\text{m}$ ;  $\lambda_{p,\text{mean}} = 2.91 \text{ Wm}^{-1} \text{ K}^{-1}$ ;  $\rho_{p,\text{mean}} = 2.940 \times 10^{-5} \Omega\text{m}$ ; Eq. (12.16) yields  $\Psi^* = 1.25$ .

Defining internal boundary conditions, introducing electrical contact resistance on the interface between thermoelectric legs and the metallic connections on the cool side, using as reference value  $\rho_{\text{int}} = 12 \times 10^{-4} \Omega \text{ cm}^2$ , the optimum value of  $(A_p/A_n)$ , for  $R_{\text{load}} = R_{\text{int,m}} = 0.21 \Omega$  shifts to  $(A_p/A_n)_{\text{opt,eff}}^* \approx 1.15$ , as shown in Fig. 12.6, whereas  $(A_p/A_n)_{\text{opt,eff}}^* = 1.30$  for  $R_{\text{load}} = R_{\text{int,m}} = 0.18 \Omega$ . The maximum value of conversion efficiency itself decreases: for  $R_{\text{load}} = R_{\text{int,m}} = 0.21 \Omega$ , the maximum value was found to be  $\eta_{t,\text{max}}^* \approx 3.9 \%$ .

## Conclusions

Numerical investigations on the performances of uni-leg and multi-leg silicide-based thermoelectric generators have been carried out using the finite element method. The numerical solution of the thermoelectric coupled field equations has been based on experimental measured properties in all analyses, and on measured data for open-circuit voltage and output power in the case of the uni-leg TEG. The task to match measured data led to the implementation of boundary features to reproduce the effect of thermal and electrical contact resistances; the temperature dependence of the thermoelectric properties was taken into account. The numerical analyses have been performed on a single undoped  $\text{Mg}_2\text{Si}$  leg [7]

and on a 16-element thermoelectric module, with Bi-doped  $\text{Mg}_2\text{Si}$  n-type legs and HMS p-type legs. In the first case, numerical results fit the available experimental data for the evaluation of the open-circuit voltage with the definition of thermal contact resistance conditions on the interfaces between the metallic and the thermoelectric elements. On the other hand, a closer agreement was expected in the case of the output power; this can reasonably be related to the fact that no electrical contact resistance was taken into account. In the second case, the numerical evaluation of the conversion efficiency, with different ratios of cross-sectional areas for the n, p-type legs, was performed without and with electrical contact resistance defined at the cool side. On the first analysis, the best geometrical configuration was found to be  $(A_p/A_n)_{\text{opt,eff}} \approx 1.30$ , whereas the calculation with mean (temperature independent) thermoelectric properties yielded  $(A_p/A_n)_{\text{opt,eff}}^* \approx 1.25$ . The calculated maximum value for the efficiency with no electrical resistance taken into account dramatically decreases from 5.33 to 3.91 %; in the second analysis, the optimum configuration is found to be  $A_p/A_n)_{\text{opt,eff}}^* \approx 1.15$ .

**Acknowledgements** This work has been funded by the Italian National Research Council—Italian Ministry of Economic Development Agreement “Ricerca di sistema elettrico nazionale.”

## References

1. Hogan TP, Shih T (2005) *Thermoelectrics handbook: macro to nano*. CRC, Boca Raton, FL, p 12, 1
2. Antonova EE, Looman DC (2005) *Thermoelectrics, 2005. ICT 2005 24th International Conference on*, 215–218, 19–23, doi: [10.1109/ICT.2005.1519922](https://doi.org/10.1109/ICT.2005.1519922)
3. Holst MJ, Larson MG, Målvist A, Sönderlund R (2010) BIT Numer Math 50:781
4. COMSOL Multiphysics Documentation, Release 4.3 (2012)
5. Attouch H, Buttazzo G, Michaille G (2006) Variational analysis in sobolev and BV spaces: applications to PDEs and optimization. SIAM, Philadelphia, PA, pp 67–73
6. Zienkiewicz OC, Taylor RL (2000) *The finite element method*. Butterworth-Heinemann, Oxford, p 42
7. Iida T, Sakamoto T, Naoki F, Honda Y, Tada M, Taguchi Y, Mito Y, Taguchi H, Takanashi Y (2011) *Thin Solid Films* 519:8528
8. Cobble MH (1995) In: Rowe D (ed) *Thermoelectrics handbook*. CRC, Boca Raton, FL, p 489
9. Sakamoto T, Iida T, Taguchi Y, Sekiguchi T, Hirayama N, Nishio K, Takanashi Y. *J Electron Mater*, doi: [10.1007/s11664-014-3165-7](https://doi.org/10.1007/s11664-014-3165-7)
10. Famengo A, Battiston S, Saleemi M, Boldrini S, Fiameni S, Agresti F, Toprak M.S, Barison S, Fabrizio M (2013) *J Electron Mater*, 42(7):2020–2024
11. Fiameni S, Famengo A, Agresti F, Boldrini S, Battiston S, Saleemi M, Johnsson M, Toprak M.S, Fabrizio M (2014) *J Electron Mater*, doi: [10.1007/s11664-014-3048-y](https://doi.org/10.1007/s11664-014-3048-y)

# Chapter 13

## Reliable Thermoelectric Generators for Space Missions

S.V. Novikov, E.Z. Parparov, and M.I. Fedorov

**Abstract** Different solar elements are being used in space researches, but these cannot be efficient power supply devices for the space vehicles that are far from the Sun, the main reason being the low intensity of the solar radiation. Thermoelectric (TE) generators are devices that can successfully work in deep space. Thermoelectric power is determined by the physicochemical properties of the thermoelectric material and the temperature gradient applied.

**Keywords** Space applications • Thermoelectric generators • Tellurides

### History

Snapshot (USA, 1965) and Kosmos-367 (USSR, 1970) were the first spacecrafts with a thermoelectric power supply. The nuclear reactor was the heat source [1]. However, such types of spacecrafts were forbidden because of the risk of radioactive contamination in the case of a launch failure.

The Radioisotope Thermoelectric Generator (RTG) is another type of power supply for the spacecrafts, where radioactive isotopes ( $\text{Po}^{210}$ ,  $\text{Cs}^{137}$ ,  $\text{Cm}^{242}$ , etc.) are used as the heat source. The Voyager 1 and Voyager 2 spacecrafts were launched by NASA in 1977 and are still successfully operating. They are also the furthest man-made objects from the Earth. The power supply devices on board of these spacecrafts

---

S.V. Novikov (✉) • E.Z. Parparov  
Ioffe Physical-Technical Institute, St. Petersburg, Russia  
e-mail: [S.Novikov@mail.ioffe.ru](mailto:S.Novikov@mail.ioffe.ru)

M.I. Fedorov  
Ioffe Physical-Technical Institute, St. Petersburg, Russia

Saint-Petersburg National Research University of Information Technologies,  
Mechanics and Optics, St. Petersburg, Russia



**Fig. 13.1** The thermoelectric battery for RTG “Life.” Temperature gradient 320–850 K, efficiency 10 %

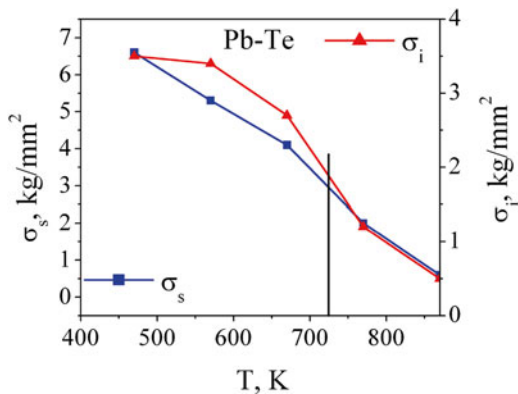
**Fig. 13.2** The thermoelectric battery for RTG “Visit.” Temperature gradient 520–720 K, efficiency 4.5 %



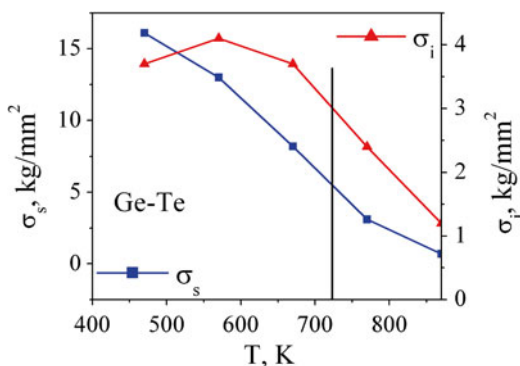
are RTGs [2]. The famous Mars Science Laboratory mission rover “Curiosity” was launched in 2011 and has RTGs as the main power supply device on board.

The Ioffe Physical-Technical Institute RAS is very experienced in the thermoelectric area. Various types of thermoelectric devices have been developed, constructed, and tested. Among these devices were the thermoelectric batteries for space missions. The RTG “Life” was developed for electrical and thermal life support (Fig. 13.1). It was made using low (Bi-Sb-Se-Te)- and middle (Pb-Te-Ge-Sn)-temperature TE materials. The RTG “Visit” was developed as an emergency power supply device for Mars mission (Fig. 13.2). It was manufactured using middle (Pb-Te-Ge-Sn)-temperature TE materials. These thermoelectric batteries were exposed to cyclic thermal, environmental, cantilevered, vibration, percussion, and other loadings during testing. The test time lasted 8,500–20,000 h, and all parameters maintained the initial values.

**Fig. 13.3** Temperature dependences of ultimate compression strength  $\sigma_s$  and ultimate bending strength  $\sigma_i$  for the PbTe compound



**Fig. 13.4** Temperature dependences of ultimate compression strength  $\sigma_s$  and ultimate bending strength  $\sigma_i$  for the GeTe compound



## Present Time

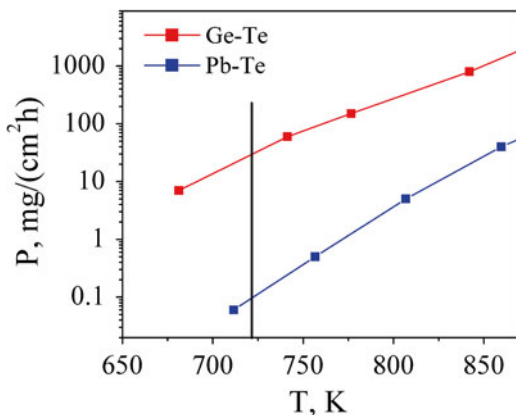
At present, high-efficiency, long-life, and reliable thermoelectric generators are developed at Ioffe Physical-Technical Institute RAS. Pb-Te-Ge-Sn compounds are one of the most efficient thermoelectric middle-temperature materials [3] in the temperature gradient 420–870 K. One of the most efficient thermoelectric low-temperature materials are Bi-Te-Se-Sb compounds. Their working temperature gradient is 300–520 K. The lifetime of such devices essentially depends on the temperature of the hot junction during working conditions. For this reason, devices' lifetime with low-temperature compounds is  $\sim 200,000$  h, while with middle-temperature compounds is only  $\sim 20,000$  h.

The maximum allowable temperature of the middle-temperature materials is about 870 K, dictated by the consequences of high chemical activity, low mechanical strength (Figs. 13.3 and 13.4), strong vaporization (Fig. 13.5), and in the absence of a reliable anti-sublimation protection.

It is important to notice that Cr-Si, Fe-Si, Mn-Si, Mg-Si-Sn, and other emerging compounds are studied too [4–6]. However, little is known about their long-term stability under thermal conditions, and therefore we will not address here the possibility of using them for space applications.



**Fig. 13.5** Temperature dependences of vapor tension for the PbTe and the GeTe compounds



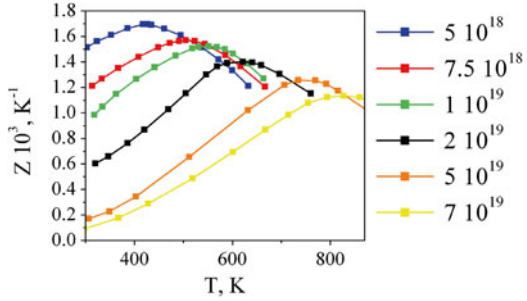
Space applications require the highest reliability of every device, meaning that special attention must be paid to the stability of the thermoelectric materials.

In our opinion, it is necessary to find the optimal temperature conditions of the Pb-Te-Ge-Sn compounds for the long life of thermoelectric generators. This is really important because they have high chemical activity, high vapor tension, and low mechanical strength at high temperature. This is particularly important in case of Ge-Te compounds. These optimal conditions can be obtained by a temperature decrease of 150–200 K. The reasons for this are the higher physicochemical stability and mechanical strength of the materials at 670–720 K compared to a temperature of 870 K (Figs. 13.3 and 13.4). Thereby, working at lower temperatures can significantly increase the reliability of the thermoelectric generators. In addition, it gives the possibility to use other switch materials for the cold junctions. Figure 13.5 shows that the temperature decrease of 700 K leads to lower vapor tension that can help to almost remove the sublimation and hence to ensure the long working time. Moreover, lower temperatures lead to a reduction in physicochemical activity of the switch materials and a reduction in the diffusion processes in the area of the junctions.

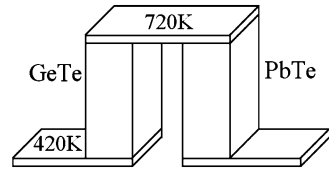
One of the most significant problems is to achieve the highest thermoelectric efficiency in the new working temperature range. Thereby, not only the hot temperature but also the cold temperature can be decreased, which partly compensates for the temperature gradient reduction. Efficiency of n-PbTe compounds can be enhanced in the new temperature range by changing the charge carriers' concentration (Fig. 13.6), so that reduction in the temperature gradient can be partly compensated as well. Unfortunately, Ge-Te compounds do not have such features.

A very important and complex task is the junction of the thermoelectric legs. This technology for the new temperature range was developed on the basis of the technology for the high temperature gradient. This method can be applied for different types of materials (pressed, extruded, crystalline). It gives the possibility of manufacturing separate legs with the optimal technology and achieve high efficiency for every leg, for the thermoelements and ultimately for the thermoelectric generators. The thermoelectric technology designed for the temperature gradient 420–720 K consists of several stages (Fig. 13.7): (1) Thermoelectric leg manufacture.

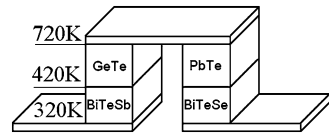
**Fig. 13.6** Temperature dependences of thermoelectric figure of merit (Z) for the Pb-Te compounds with different concentration of the charge carriers



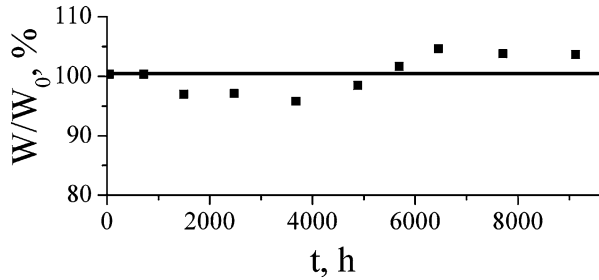
**Fig. 13.7** The thermoelement based on the p-GeTe-n-PbTe compounds



**Fig. 13.8** The multistage thermoelement for the wide temperature range



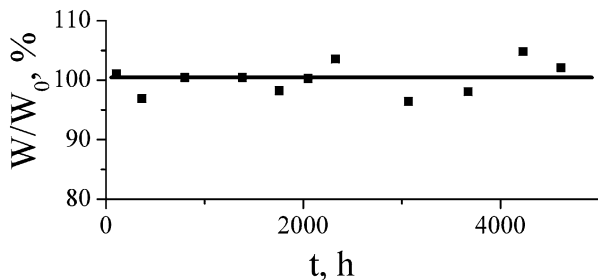
**Fig. 13.9** Testing of the thermoelement (PbTe-GeTe) during 9,200 h



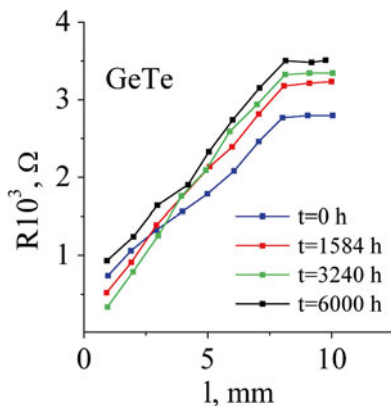
Optimal technology is used for every leg for high efficiency. (2) Hot junctions. (3) Cold junctions. (4) Assembly of thermoelectric batteries.

It is possible to construct multistage thermoelements based on middle-temperature (Ge-Te, Pb-Te) and low-temperature (Bi-Te-Se-Sb) materials (Fig. 13.8). Representative properties of the single thermoelement are 130 mWt and efficiency of 6.5 % (cross-section of the legs 5×5 mm<sup>2</sup>). Thermoelements were tested during 9,200 h in the temperature gradient 420–720 K and were subjected to different thermal cycles (Fig. 13.9). After this life test, the electric power was nearly the same. Similar results were obtained for the thermoelectric battery, which consisted of four thermoelements (Fig. 13.10). Visible intermediate resistances of the junctions were still absent respectively after 1,584, 3,240, and 6,000 h at 720 K (Figs. 13.11 and 13.12).

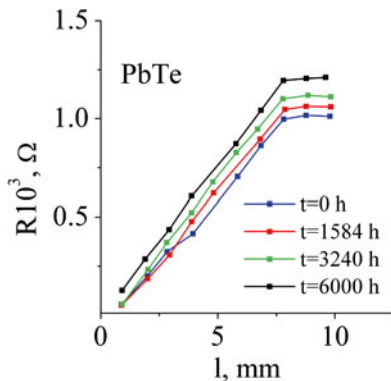
**Fig. 13.10** Testing of the thermoelectric battery during 5,000 h



**Fig. 13.11** Intermediate resistances of the junctions Ge-Te compound



**Fig. 13.12** Intermediate resistances of the junctions Pb-Te compound



## Conclusions

In this study, we have shown that our thermoelements have a lifetime of 10,000 h. We optimized the temperature conditions, the material properties, and the junction technology for a new temperature gradient. The efficiency of the thermoelements decreased because of the new temperature gradient, but its reliability was significantly increased.

**Fig. 13.13** The thermoelements for different heat flows



**Fig. 13.14** The thermoelectric multistage battery (four thermoelements)



Highly efficient and reliable thermoelements were developed, constructed, and tested in this work (Figs. 13.13 and 13.14). Such thermoelements have stood the test of time under different stresses and hence can be used in thermoelectric generators for space exploration.

## References

1. Andryushin IA, AK Chernyshev, Yudin Y (2003) The taming of the nucleus. Pages of history of nuclear weapons and nuclear infrastructure of the USSR, Sarov, p 481. ISBN/ISSN: 5-7493-0621-6
2. <http://voyager.jpl.nasa.gov>
3. El-Genk M, Saber HH, Sakamoto J, Caillat T (2003) Life tests of skutterudites thermoelectric unicouples (MAR-03). Twenty-second international conference on thermoelectrics. Proceedings of ICT'03, IEEE, New York, pp 417–420
4. Zaitsev VK, Fedorov MI, Gurieva EA, Eremin IS, Konstantinov PP, Samunin AY, Vedernikov MV (2006) Phys Rev B 74:045207
5. Novikov S, Burkov A, Schumann J (2013) J Alloy Comp 557:239
6. Samunin A, Zaitsev V, Konstantinov P, Fedorov M, Isachenko G, Burkov A, Novikov S, Gurieva E (2013) J Electron Mater 42(7):1676

# Chapter 14

## Challenges in Dimensioning of an Optimized Thermoelectric Generator for Waste Heat Recovery in Cars

M. Rauscher, T. Richter, F. Finsterwalder, and D. Schramm

**Abstract** An exhaust system in a car has to face and withstand a lot of different operating conditions and so does a thermoelectric generator (TEG) integrated in the exhaust system. In addition, the TEG has to transform heat into electricity at the highest possible efficiency in order to save fuel. This results in several challenges with regard to the design and the dimensioning of the TEG.

One lever to improve the efficiency of a TEG is the optimization of the thermal resistance of the thermoelectric material. This paper shows performance data of TE modules made of identical material and active area but of different thickness. These modules have been measured under thermostatic conditions, i.e., fixed surface temperatures. Subsequently the different TE modules have been tested in a hot air test bench. Here, the consequences of the different thermal resistances can be shown. Furthermore the measurements highlight the influence of the electric load on the thermal resistance of the module entailing different surface temperatures of the modules and different heat transfer rates.

Along with the experimental tests, numeric optimization of the thermal resistances of the TE modules has been carried out in order to achieve the maximum electrical power output. The optimum module thermal resistance significantly depends on whether the power output of the modules is optimized individually or if the power generation of TEG is optimized as a whole.

**Keywords** Thermoelectric generator • Waste heat recovery • Thermal resistance • Optimization

---

M. Rauscher (✉) • T. Richter • F. Finsterwalder  
Daimler AG, Ulm, Germany  
e-mail: [matthias.rauscher@daimler.com](mailto:matthias.rauscher@daimler.com)

D. Schramm  
Universität Duisburg-Essen, 47057 Duisburg, Germany

## List of Symbols

$A$	Module surface
$A_{\text{tem}}$	Surface of thermoelectric material in a module
$P_x$	Electric power output in segment $x$ (W)
$\dot{Q}_x$	Heat flow rate into the thermoelectric material in segment $x$ (W)
$R_x^{\text{hs}}$	Thermal resistance from the exhaust gas to the thermoelectric material in segment $x$ ( $\text{K m}^2\text{W}^{-1}$ )
$R_x^{\text{tem}}$	Thermal resistance of the thermoelectric module in segment $x$ ( $\text{K m}^2\text{W}^{-1}$ )
$R_x^{\text{cs}}$	Thermal resistance from the thermoelectric material to the coolant in segment $x$ ( $\text{K m}^2\text{W}^{-1}$ )
$T_x^{\text{g}}$	Temperature of the exhaust gas in segment $x$ (K)
$T_x^{\text{c}}$	Temperature of the coolant in segment $x$ (K)
$T_x^{\text{tem,hs}}$	Temperature at the hot side of the thermoelectric material in segment $x$ (T)
$T_x^{\text{tem,cs}}$	Temperature at the cold side of the thermoelectric material in segment $x$ (T)
$T_{\text{CS,HS}}$	Positions of temperature measurements at the cold side and the hot side of the thermoelectric module
$T_{\text{HS}1,2,3}$	Positions of temperature measurements in the cube of the hot side
$T_{\text{CS}1,2,3}$	Positions of temperature measurements in the cube of the cold side
$\eta_x$	Efficiency of the thermoelectric material in segment $x$

## Introduction

The limitation of crude oil, the rising petrol price during the last years, as well as legislation requires a drastic reduction of vehicle fuel consumption. State-of-the-art vehicles with modern combustion engines still produce more waste heat than they convert into mechanical energy [1]. An important field of research is therefore the recovery of waste heat, for example using thermoelectric materials. In this regard, the exhaust gas is particularly attractive due to its generally high energy content at elevated temperatures, although this varies strongly over a drive cycle turning the dimensioning and the design of the TEG in a demanding exercise. Small packaging and minimized weight and costs are further targets of the automotive industry. Within these boundaries the TEG must work at the highest possible performance.

As a consequence the module design has to be adapted to the heat exchanger, e.g., by changing the height or the surface area of the thermoelements (legs) of the modules. An increase of the leg height leads to a higher thermal resistance of the module and therefore to a reduced heat flux and a higher efficiency within a TEG. The same effect is obtained when the surface area is reduced in the direction of the heat flux in a leg. For this purpose a small demonstrator TEG has been built. This TEG is not intended to be used in a car, but allows getting insight into the behavior of different module designs.

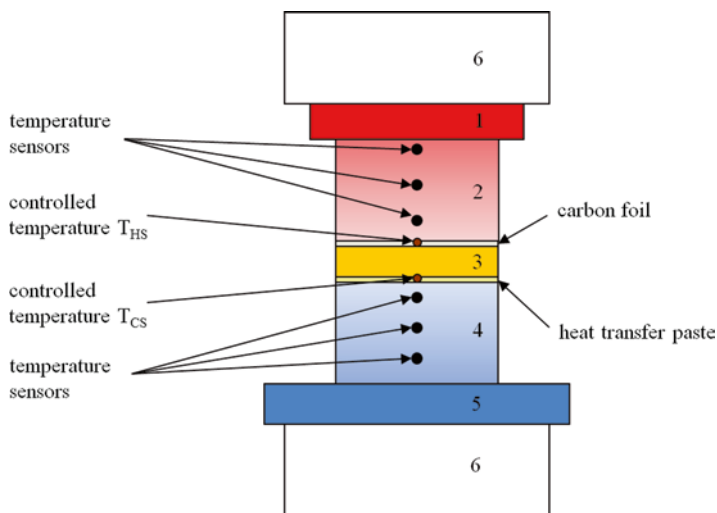
### Test Bench Results

Two thermoelectric modules of the same contact area, identical thermoelectric material (bismuth telluride) but different height of the legs (see Table 14.1), have been tested under thermostatic conditions in a module test bench at different hot and cold side temperatures.

The different module designs result in a different thermoelectric behavior of the modules. The higher number of legs in module A leads to a higher open voltage compared to module B at the same surface temperature. Simultaneously, the electrical resistance of module A is higher owing to the number of legs, which are electrically in series, and the higher geometric factor (ratio of leg length to leg footprint). Due to the same ratio of thermoelectrically active surface compared to the module surface, but the higher geometric factor, module A has a smaller thermal resistance, which results in a higher heat flux through the module compared to module B. Figure 14.1 shows the test setup of both modules at the module test bench.

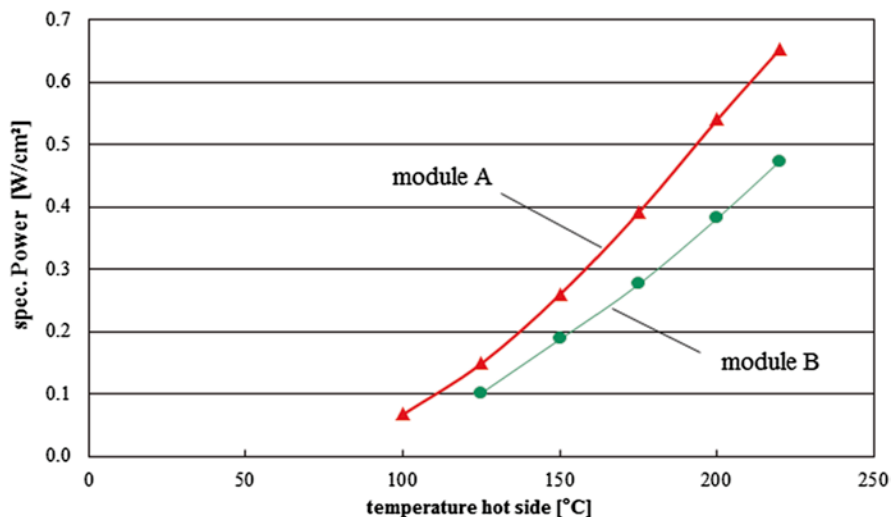
**Table 14.1** Module basic data

	Module surface (cm <sup>2</sup> )	Ratio: $A_{\text{leg}}/A$	Geometric factor of the legs (mm <sup>-1</sup> )
Module A	16	ca. 0.5	0.83
Module B	16	ca. 0.5	0.75



**Fig. 14.1** Test bench Setup: Module test bench (1) Cooling plate, (2) aluminum cube, (3) thermo-electric module, (4) copper cube, (5) heating plate, (6) isolating stone





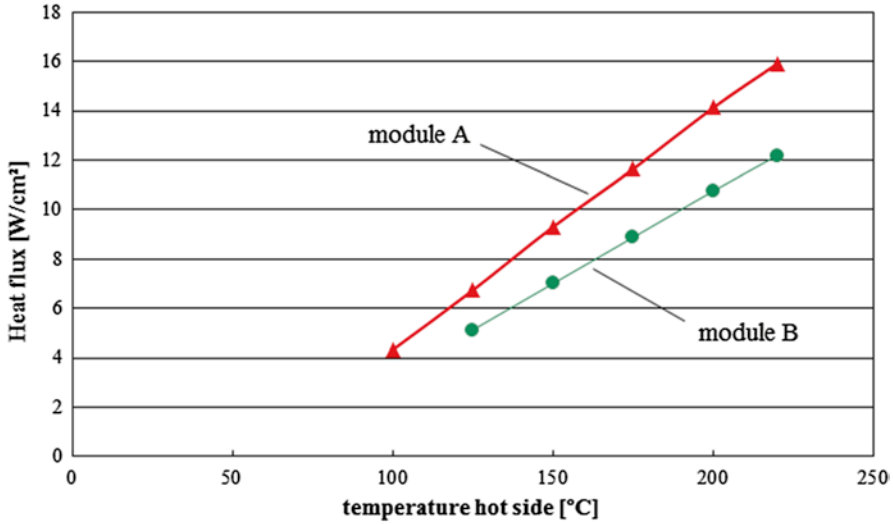
**Fig. 14.2** Electrical power output of module A and B at fixed surface temperatures (the cold side temperature was 50 °C)

The applied contact pressure was 10 bars. The electrical contacts have been connected to an electrical load. To measure the maximal power output, the current of the electric load was successively increased until the electrical power output reached its maximum. The temperatures on the hot and cold side of the module have been readjusted during the measuring procedure. Figure 14.2 illustrates the power output in the maximum power point of the two modules for a cold side temperature of 50 °C and various hot side temperatures in the range of 100–220 °C.

Over the range of hot side temperatures the maximum electric power output of module A is around 1.33 times higher than the maximum electrical power output of module B. This is due to the decreased thermal resistance of module A as a consequence of the reduced leg height.

Figure 14.3 shows the heat flux into the modules in the maximum power point. The heat flux has been calculated using the measured temperature differences, the surface of the cube, and the known thermal conductivity of the copper cube shown in Fig. 14.1. At the same operating temperatures the heat flux into module A is also ca. 1.33 higher than the heat flow rate into module B. Again, this is a result of the reduced thermal resistance of module A.

Obviously, the efficiency is nearly the same, as one would expect from modules made of identical materials and layer composition.



**Fig. 14.3** Test results for heat flux of module A and B for fixed surface temperatures (the cold side temperature was 50 °C)

## Hot Air Test Bench Results

The previously described thermoelectric modules (type A and B) have been integrated in a heat exchanger of which the setup is shown in Fig. 14.4.

The TEG has one gas channel and two channels for the coolant. The TE modules are inserted between the gas and the liquid side: three modules of type A on the upper half of the heat exchanger and three modules of type B on the lower half. Two thermocouples (inserted in pockets punched into the graphite foils) have been positioned on each module, one on the hot and one on the cold side.

The TEG has been tested under steady-state conditions. The gas (dry air) inlet temperature was 320 °C and the coolant (water glycol mixture) temperature was 40 °C.

Table 14.2 shows the surface temperatures module A1 and B1 at open electrical circuit. Due to the higher thermal resistance of module B1, the temperature difference between hot and cold side is larger for B1 than for A1.

The electric power output of the modules has been determined using a variable electronic load. As in the test setup in the module test bench, the electronic load increases the electrical current from zero to maximum within 4 min. The maximum power point has been tracked for all modules individually.

Figure 14.5 illustrates the surface temperature and the electric current while changing the electric current from zero to its maximum. In this case, the load has only been applied to module B1. The temperature on the hot side of B1 decreases with increasing current, while the corresponding temperature on the cold side increases. The reason is that the heat transport of the module B1 has changed because of the Peltier, Joule, and

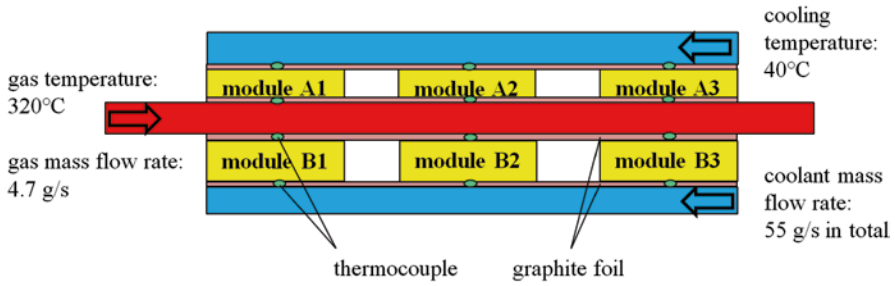


Fig. 14.4 Schematic of the TEG demonstrator unit (side view)

Table 14.2 Module surface temperatures

	Measured surface temperature hot side (°C)	Measured surface temperature cold side (°C)	Temperature difference (K)
Module A1	197	118	79
Module B1	211	111	100
Module A2	168	101	67
Module B2	178	100	78

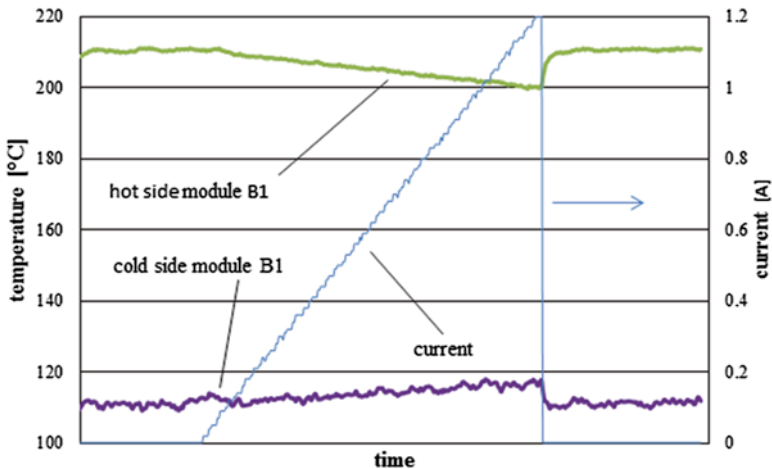


Fig. 14.5 Dependence of the surface temperature of module B1 on the electric load

Thomsen effect. When the electric load is removed, the surface temperatures of the module return to their initial values.

The maximum power outputs of modules B exceed the corresponding maximum power of the neighboring modules A by the factor of 1.22–1.53, depending on their position in the TEG. This is in contrast to the power outputs measured under fixed

surface temperatures (see Fig. 14.2), where the type B modules have shown inferior performance. Here, the type B modules (integrated in the heat exchanger) have a higher temperature gradient between the hot and the cold side as a result of the higher thermal resistance of the module. This leads to an increased efficiency (electrical output power divided by ingoing heat flux) of the module. In this case, the higher efficiency of the module overcompensates the reduced heat flow across the module (due to the higher thermal resistance) resulting in an overall superior maximum electrical power output.

### Numerical Optimization of the Thermal Module Resistance for Maximum Power Output

As can be seen from the previous results the thermal resistance is a key parameter with regard to the electrical power output. Its optimization plays a vital role in the design process of an automotive TEG. The following section describes a numerical approach for the optimization of the thermal resistance to get the highest yield of electrical power.

The optimum thermal resistance, determined by the aspect ratio of the legs of the module, can be determined relatively easily for a single module with no lateral temperature gradient using thermoelectric equations [2, 3]. However, the calculation becomes much more complicated when lateral temperature gradients occur within the TEG (usually consisting of several module segments, see Fig. 14.6) along the flow direction of the hot and cold media [4]. As a result, the efficiency as well as the local power generation varies.

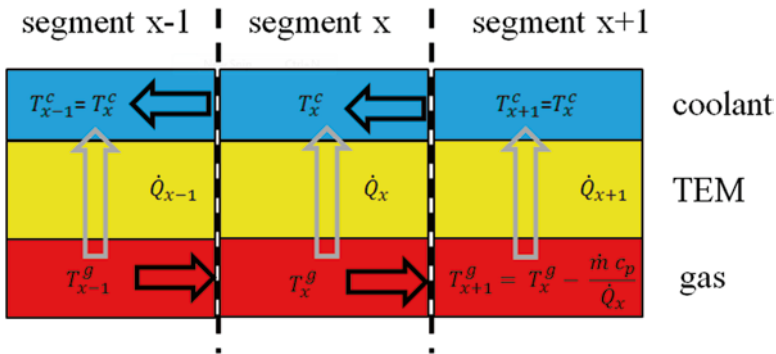


Fig. 14.6 Schematic model of the TEG

For this case, we assume that the identical material (PbTe) is used in every segment of the TEG and we suppose a constant heat transfer coefficient ( $R_x^{\text{hs}}$ ,  $R_x^{\text{cs}}$ ) for both gas and coolant side. The module segments are considered discretely, so we assume there is no electrical interaction between the segments.

The heat flow rate of each of the segments (see Fig. 14.6) of the TEG has been calculated by using Eq. (14.1).

$$\dot{Q}_x = A \frac{1}{R_x^{\text{hs}} + R_x^{\text{tem}} + R_x^{\text{cs}}} (T_x^{\text{g}} - T_x^{\text{c}}) \quad (14.1)$$

$$T_{x+1}^{\text{g}} = T_x^{\text{g}} - \frac{\dot{m}_{\text{g}} \cdot c_{\text{p}}}{\dot{Q}_x} \quad (14.2)$$

The temperature of the coolant is set to a constant value. This simplification is done because of the much higher mass flow and heat capacity compared to the gas, so that the warming of the coolant can be neglected.

The temperatures  $T_x^{\text{tem,cs}}$  and  $T_x^{\text{tem,hs}}$  can be calculated from the ratio of the thermal resistances in each segment. For the calculation of the electric power output the following equations [5] were used.

$$\eta_x = \frac{\sqrt{1 + ZT_x} - 1}{\sqrt{1 + ZT_x} + \frac{T_x^{\text{tem,cs}}}{T_x^{\text{tem,hs}}}} \cdot \frac{T_x^{\text{tem,hs}} - T_x^{\text{tem,cs}}}{T_x^{\text{tem,hs}}} \quad (14.3)$$

$$P_x = \eta_x \cdot \dot{Q}_x \quad (14.4)$$

Equation (14.3) assumes that the electric current in a segment is adapted in the way that the thermoelectric material works at maximum efficiency.

For the calculation of the temperature-dependent  $ZT_x$  value the average temperature of the thermoelectric material in the segment has been used. This simplification can still be employed with an acceptable degree of accuracy [5].

Three different optimization methods of the thermal resistance  $R^{\text{tem}}$  of the modules have been employed:

1. Maximization of the electric power output of *every single* segment:  
The thermal resistance  $R^{\text{tem}}$  of each individual segment is adapted in the way that the maximum electrical power of the segment is generated using the locally available waste heat energy. The calculation is started with the segment nearest to the gas inlet.
2. Maximization of the electric power output of the *complete TEG*:  
The thermal resistance  $R^{\text{tem}}$  of each individual segment is adapted in a way that the added electrical power output of all segments becomes a maximum.
3. Maximization of the electric power output of the *complete TEG*:  
The thermal resistances  $R^{\text{tem}}$  of all segments are equal and adapted in a way that the added electrical power output of all segments becomes a maximum.

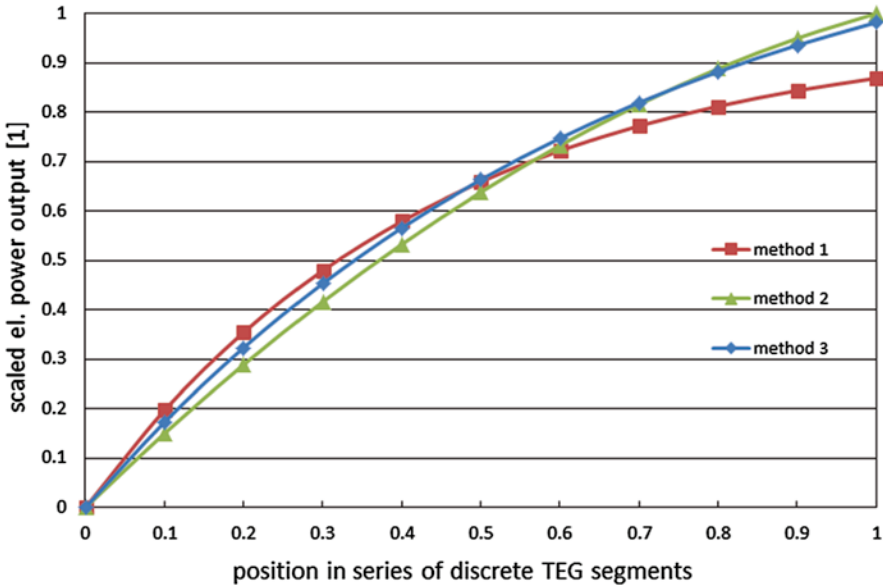


Fig. 14.7 Cumulated electrical power output as a function of the scaled length of the TEG

For all three methods, the optimal thermal resistances were calculated using an iterative algorithm (Generalized Reduced Gradient [6]). The results of the different methods of electrical power optimization along the TEG are shown in Fig. 14.7. The y-axis is normalized to the electrical power output of method 2.

Within the first half of the TEG, the optimization method 1 gives the highest electric power output. The reason is that the TEG optimized by method 1 cools down the exhaust gas relatively strongly at the inlet (maximum electrical power generation of each segment), so that the remaining amount of heat for the downstream segments is relatively low. Therefore the first segments produce much electrical power at relatively low efficiency at the expense of the following segments. The decline in power generation of each segment is more pronounced than in the other cases where the power drop is less steep.

The thermoelectric segments of the TEG optimized by method 2 have got a much higher thermal resistance in the inlet area. Therefore the heat flow is reduced and the electric power output is lower despite the higher efficiency. Hence, the available gas temperature and energy for the downstream segments is higher. This entails a superior power output in the remaining segments in comparison to method 1. Apparently, the overall power output of the TEG optimized according to method 2 is higher than that when using method 1 (in this operating point the gain in power amounts to approximately 13 %).

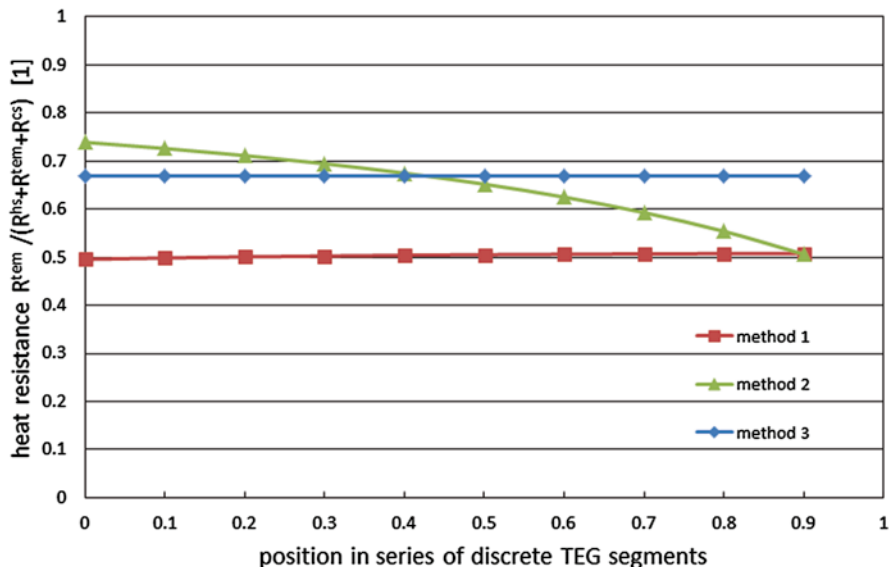


Fig. 14.8 Segment heat resistance along the TEG for different optimization methods

Optimization method 3 implies identical module resistances along the TEG (see Fig. 14.8). The optimized resistance throughout the TEG is clearly higher than the resistances resulting from method 1, which show only very little variation. Compared to method 2, the resistance at the beginning of the TEG is lower, whereas the resistance at the outlet of the TEG is higher.

In total, electric power output for method 3 is only 2 % lower than for method 2 despite the additional boundary condition of constant resistance.

Note that the calculations refer only to one operating point, which is however typical for the curve progression. Changes of the operating parameters lead to changes in the absolute values of the optimized thermal resistances but the general trend, i.e., the strongly digressive power output along the TEG when using method 1, remains. In all chosen boundary conditions for the exhaust gas mass flow or temperature, method 1 leads to the lowest average thermal resistance compared to the other methods. Method 2 has always the highest thermal resistance at the beginning of the TEG and decreases towards the end.

The differences in the results of the optimization methods shrink with a smaller gas temperature gradient from the entry to the exit of the TEG. This may be caused by higher mass flows or a shorter TEG. Vice versa, the differences in the results increase at lower mass flows or a longer TEG design. In the limiting case, i.e., no gas temperature gradient along the TEG, all three methods yield the same result; hence in this case all segments in the TEG have equal boundary conditions and therefore the optimization methods have the same optimization goal.

## Summary

The measurements of two different modules made of the same material but different aspect ratio of the legs integrated in a demonstrator TEG have highlighted the crucial impact of the thermal resistance on the electrical power generation. An adaptation and optimization of the module heat resistances to the heat exchanger is therefore essential.

Simulations show that individual optimization of module heat resistances is not necessary, but the optimum TEG power output performance can almost be achieved, if all modules have the same heat resistance, i.e., the same design. This result is equally important and encouraging. A cost-effective mass production of TEGs is easier if a single module design is used.

Under the considered boundary conditions the simulation has also revealed that a power optimization of every single module is less beneficial and comes at the expense of the overall TEG power output. Instead, the module heat resistance should be optimized with respect to the total TEG power output.

## References

1. Steinberg P, Briesemann S, Goßlau D (2009) Thermoelectrics goes automotive, Der Fahrzeugmotor als Energielieferant für Wärmenutzungskonzepte. IAV, Renningen
2. Glatz W, Muntwyler S, Hierold C (2006) Optimization and fabrication of thick flexible polymer based micro thermoelectric generator. *Sens Actuators A* 132:337–345
3. Beckert W, Dannowski M, Wagner L. Symposium Thermoelektrik Dresden. Simulationswerkzeuge zur Unterstützung der Integration thermo-elektrischer Generatoren in bestehende Systeme
4. Roy G, Matagne E, Jacques PJ (2013) A global design approach for large-scale thermoelectric energy harvesting systems. *J Electron Mater* 42(7):1781–1788
5. Rowe DM (2006) Thermoelectrics handbook “general principles and basic considerations”. Taylor & Francis Group, New York, pp 11–114
6. Lasdon LS, Waren AD, Jain A, Ratner M (1978) Design and testing of a generalized reduced gradient code for nonlinear programming. *ACM Trans Math Softw* 4:34–50



# Chapter 15

## Assessment of Thermoelectric Power Generation for Hybrid Electric Vehicles Based on Tracked Data

M. Morschel, B. Hesse, G. Bastian, and D. Schramm

**Abstract** Many factors, like shortage of oil or environmental pollution, lead to the need for a new and highly efficient engine generation in passenger vehicles. Plug-in hybrid electric vehicles (PHEVs) are a promising approach. Most car manufacturers therefore offer at least one hybrid vehicle. Even in these highly efficient vehicles, there is still an amount of waste heat of the combustion engine which is not used.

The idea proposed here is to integrate a thermoelectric generator (TEG) into the exhaust gas system of a PHEV. In comparison to internal combustion engine vehicles (ICEVs), the combustion temperature throughout a typical drive of a PHEV shows a distinct different characteristic (temperature gradient) and therefore other materials can be used. Due to the fact that the combustion engine is only used temporarily, the electric yield might be lower. On the other hand, the load is more constant and uniform, which affects the thermomechanical stress positively. Lower stress inside the module leads to a higher durability and lower deformation guarantees a good thermal contact to both the heat source and the heat sink.

In the present study tracked drive data of a PHEV are used to evaluate the capability of a TEG integrated in the exhaust gas system of a hybrid electric vehicle. Additionally, a FEM-simulation of the stress under realistic load is carried out. The stress as well as the overall energy output of the TEG is then compared to its potential using a conventional vehicle.

**Keywords** Thermoelectric generator • Plug-in hybrid electric vehicle • Thermomechanical stress • Efficiency

---

M. Morschel (✉) • G. Bastian  
Faculty of Technology and Bionics, Rhein-Waal University of Applied Sciences,  
Marie-Curie-Straße 1, 47533 Kleve, Germany  
e-mail: [marlis.morschel@hswr.eu](mailto:marlis.morschel@hswr.eu)

B. Hesse • D. Schramm  
University of Duisburg-Essen, Lotharstraße 1, Duisburg 47057, Germany

## Introduction

The idea of integrating a thermoelectric generator into the exhaust gas system of an internal combustion engine vehicle (ICEV) is not new and is investigated by different car manufacturers and research institutions. Looking ahead, the ICEVs will indeed be only one possible solution for individual mobility. With regard to energy resources, climate change, and ecological damage, a change in the automotive industry is inevitable. Following the trend, plug-in hybrid electric vehicles (PHEV) represent the next generation of cars. The combination of an electric motor and a combustion engine enables the range of modern vehicles and the enhanced efficiency of electric power trains at the same time. This reduces the exhaust emissions and the fuel consumption to a minimum.

Since introducing a TEG to the exhaust gas system of a vehicle aims at enhancing the overall efficiency at the first place, a combination of PHEVs and TEGs appears to be a logic step and one promising field of application.

Furthermore, the generated electrical energy can be easily stored and extends the range of the PHEV. Since the voltage used in PHEV power-trains differs from the usually used 14 V in vehicles, this high voltage storage could also be used for the TEG, which potentially enables more efficient ways of interconnection. Previous studies [1, 2] already superficially investigated the potential of the combination of hybrid electric vehicles (HEVs) and TEGs.

In this contribution the assessment is carried out considering a realistic load.

## Modeling and Simulation

For initial estimations of the potential, the modeling and simulation of the combination of a PHEV and a TEG is a reasonable tool. The capability is investigated and feasibility problems can be detected early.

### *Simulation of Exhaust Gas System*

The potential of using TEGs in a vehicle is set by the driving behavior (drive cycle). To provide the simulation with realistic inputs, the first step is logging driving data of ordinary trips. This data comprise the position, the velocity, and the acceleration. Afterwards, the data is put in a MATLAB-Simulink simulation. The detailed development of the used simulation model is explained in previous work [3]. It includes a longitudinal dynamics model with a virtual driver. Furthermore, the driving resistances, the dynamics, and the power train are considered. Concerning the power train besides the ICEV model, a PHEV model is available as described in the following reference [4].

Regarding the thermoelectric part, all practice-oriented parameters are calculated. They include the efficiency, the heat flows, and the electrical output of several

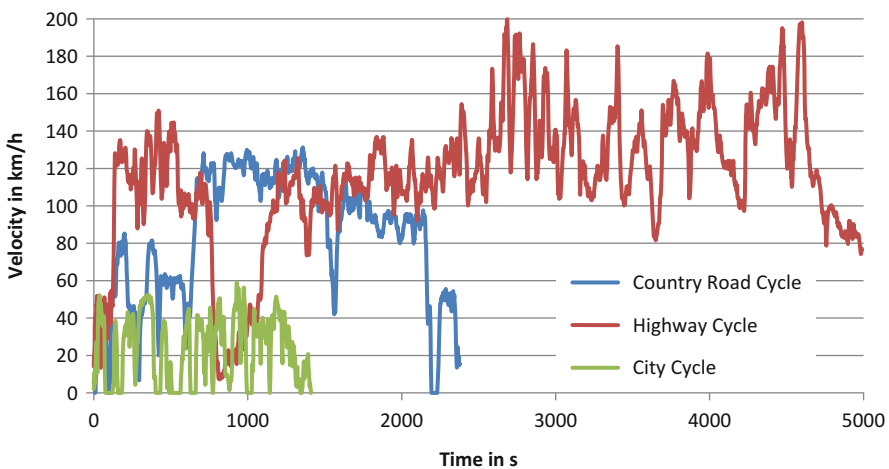
TEGs. Both the Peltier effect and the joule heating are considered. By means of the output data a statement concerning the efficiency of the combination PHEV/TEG can be made.

### *Simulation of Stress Under Realistic Load*

To simulate a realistic load, the temperature of the exhaust gas system before the TEG and the temperature of the cooling circuit are read out of the MATLAB simulation. The underlying logged driving data represent a realistic trip, and therefore it can be investigated how the TEG behaves under real-life conditions in an ICEV and a PHEV. The temperatures serve as input parameters for an Abaqus simulation. In contrast to the MATLAB simulation of several TEGs, in Abaqus just one TEG is analyzed. A coupled temperature-displacement analysis is carried out to investigate the temperature-induced deformation and stresses.

### **Investigated Trips**

The assessment of thermoelectric power generation is investigated concerning different driving cycles. The data of three different drives is tracked and used to analyze the potential of the combination of a PHEV and a TEG. By applying the different loads it is examined if one specific drive is particularly suitable for that combination. A city drive, a country road cycle, and a highway cycle represent the basis of the simulations. Figure 15.1 shows the velocity over time for the three cycles.



**Fig. 15.1** Development of velocity for different cycles

## Results

The results of the three cycles are presented. The influences of the different cycles on the generated power and the temperature difference are presented.

### *City Cycle*

The city cycle is a good example for a short drive within a city. The driven distance as well as the duration are short compared to the other cycles. The velocity characteristics are distinct for urban drives. The low velocities combined with frequent accelerations and decelerations are typical for cities. Numerous studies show that electric power trains have various advantages during these drives in terms of efficiency, air pollution, or noise. The PHEV is designed to use the electric motor within cities. That means that the ICE is not used as long as the battery provides enough energy to drive the vehicle. Typical city cycles are only driven electrically and the use of a TEG is excluded since there is almost no waste heat to be used. The simulations performed clearly emphasize this, and the city cycle doesn't need to be discussed any further in terms of using a TEG in a PHEV.

### *Country Road and Highway Cycle*

Country road and highway cycles are longer and dictated by higher vehicle velocities. This means that the combustion engine of the PHEV will be used for a considerable percentage of the drives. The engine then provides the needed heat for the TEG.

Since the heat source (combustion engine) for the TEG does not offer constant temperatures, the electric output of the TEG varies over on cycle. Figure 15.2 illustrates the relative frequency for different output power levels.

The illustrated values for the electrical power are the result of a large number of modules. Under real conditions, only a smaller amount of modules would be integrated so that the overall power of the TEG would be reduced. The chosen TEGs are standard modules, made of BiTe and PbTe.

It is interesting to notice that the TEG provides more energy during a highway drive in a PHEV than in an ICEV. Carefully looking at the operation strategy of the combustion engine of a PHEV compared to the one in an ICEV, becomes clear why the TEG has higher outputs in the PHEV. In fact, while the engine of an ICEV is directly coupled to the vehicle velocity and the needed drive torque, the operational point of the one in a PHEV can be chosen more freely. This is used to operate the engine in a PHEV more efficiently at constant operation points, if possible.

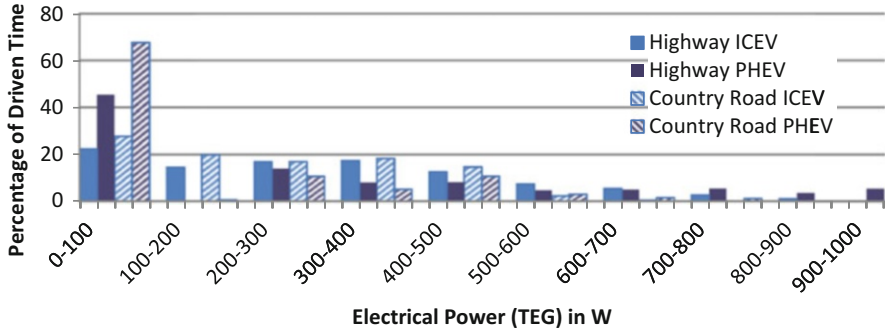


Fig. 15.2 Distribution of Electrical Power output TEG

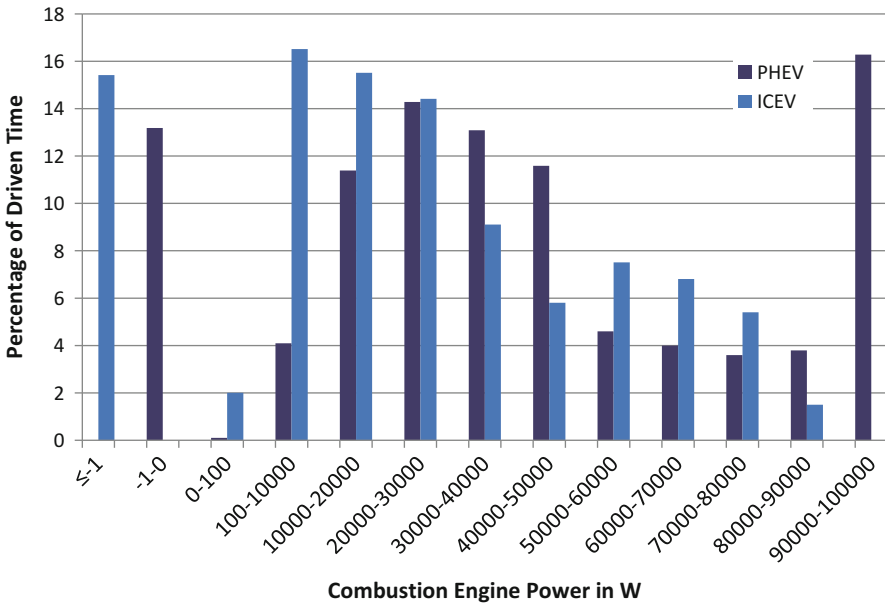
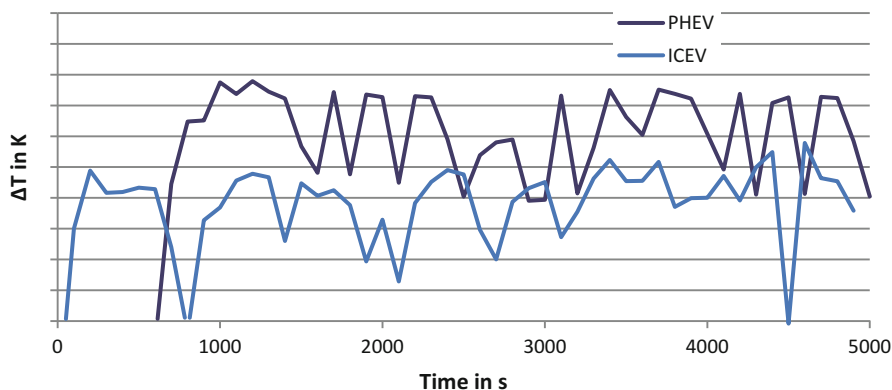


Fig. 15.3 Distribution of combustion engine power in a highway cycle

Fluctuations within the needed drive torque are compensated by the electric power train. Excessive electric energy is stored in the battery. Figure 15.3 illustrates the relative frequency for different combustion engine power levels for both the PHEV and the ICEV in a highway cycle.

The combustion engine of the PHEV is operated at the point of its maximum output power as often as possible. At the same time, the combustion engine of the PHEV is completely switched off at a considerable percentage of times. Compared to the points of operation of the ICEV engine, this leads to higher temperatures differences ( $\Delta T$ ) over the cycle (Fig. 15.4).



**Fig. 15.4** Distribution of temperature difference in the highway cycle used in this contribution

An ABAQUS simulation of a TEG module performed with the calculated temperature differences indicates that the deformations and the stress in the cycles do not show distinct significant differences between ICEV and PHEV. The mechanical properties of a TEG designed for the use in an ICEV would therefore meet also the requirements in a PHEV.

## Conclusions

The variety of available power trains will increase over the next few years. One promising technique is the PHEV. This contribution surveys the use of TEGs in a PHEV to enhance the overall efficiency.

Since the combustion engine in a PHEV is decoupled from the driven wheels, the combustion engine is operated very differently compared to ICEVs. Regarding a TEG and the use of waste heat, this leads to the necessity to analyze the driven cycles in combination with the operation strategy of the PHEV.

The simulations clearly show that a TEG is of no use within a city cycle, since the combustion engine in a PHEV will most probably not be used for these short range drives. For long drives however the operation strategy of the PHEV power train offers an enhanced potential of using TEGs. The operation of the combustion engine at constant high power leads to constant and high temperature differences to be used by the TEG.

Unfortunately, PHEVs are not primarily designed for long distance trips. The basic idea is to use them for short to mid-range trips which unveils the strength of these vehicles in terms of overall efficiency. However, surveys show that PHEVs are actually used for a considerable amount of highway drives too. To judge upon the potential TEGs have in PHEVs, the presented methods have to be supplemented by a careful analysis of real daily use.

**Acknowledgements** This work was partly supported by the German Ministry of Science and Education (BMBF).

## References

1. Yang J (2005) Potential applications of thermoelectric waste heat recovery in the automotive industry. Proceedings of the 24th international conference on thermoelectrics, SC, USA; ISBN 0-7803-9552-2:170–174
2. Kim S-K et al (2011) Thermoelectric power generation system for future hybrid vehicles using hot exhaust gas. *J Electron Mater* 40(5):783–787
3. Tatarinov D et al (2013) Modeling of a thermoelectric generator for thermal energy regeneration in automobiles. *J Electron Mater* 42(7):2274–2281
4. Koppers M, Hesse B, Hiesgen G, Schramm D (2012) Potentiale von Klimatisierungssystemen für Traktionsbatterien von Batterie- und Plug-In- Hybridfahrzeugen im Winterbetrieb. 8. VDI-Tagung Innovative Fahrzeugantriebe, Dresden, Germany

# Chapter 16

## Thermoelectric Generator for Low Temperature Applications

M. Follmer, B. Steiner, and D. Knospe

**Abstract** This paper describes the development of a thermoelectric generator for low temperature applications and focuses on the conceptual design, mathematical modeling as well as simulation of thermoelectric generators for the exhaust system of diesel-powered commercial vehicles. Two design studies have been investigated intensively within the last years. The first design study is based on common bismuth telluride (BiTe) thermoelectric modules, and the second one is characterized by axial cascaded sheets with radial located thermoelectric material (BiTe) and an integrated heat exchanger for hot exhaust gas and cold coolant water. This offers the advantage of a very high degree of integration and a compact design with the possibility to increase the electric power by adding or removing additional sheets. Functional prototypes of the two design studies have been realized and verified at an engine test bench. Comprehensive measurements showed the challenges of this trendsetting technology and potential for further optimization.

**Keywords** Thermoelectric generator • Exhaust system • Diesel-powered commercial vehicle • Design studies

---

M. Follmer (✉) • B. Steiner • D. Knospe  
Magna Powertrain - Engineering Center Steyr GmbH & Co KG,  
Steyrer Straße 32, St. Valentin 4300, Austria  
e-mail: [martin.follmer@ecs.steyr.com](mailto:martin.follmer@ecs.steyr.com)



## Introduction

### *Magna Powertrain: Engineering Center Steyr*

The Engineering Center Steyr (ECS) is the commercial vehicle competence center of Magna Powertrain and worldwide well recognized for engineering services and low volume production. Several future technologies, which will help to make commercial vehicles more environment-friendly and more efficient, are investigated at ECS.

### *Thermoelectric Generator for Low Temperature Applications*

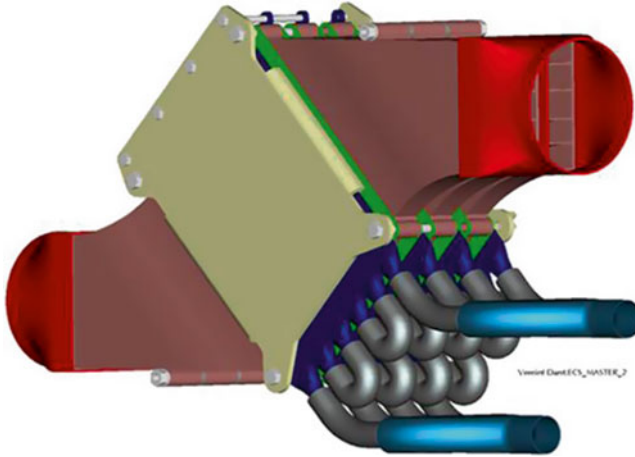
Based on the Seebeck-effect, thermoelectric generators (TEG) enable the conversion of unused exhaust gas heat energy into useful electrical energy. The generated electrical energy can be fed into the vehicles' board-net and leads to lower utilization of the alternator and consequently to a reduction of fuel consumption and exhaust emissions. Thus TEG-systems allow to reduce the CO<sub>2</sub>-emissions of vehicles and to meet the ever increasing demands of future exhaust emission standards. Due to their enormous mileages per year and nearly constant operating points, long-haul trucks represent a promising application area of this technology. A major challenge of this application is the low exhaust gas temperature of modern (Euro VI) diesel engines. In combination with the standard cooling equipment of commercial vehicles, the temperature difference available at the thermoelectric module remains rather low.

## Thermoelectric Activities

During a multiyear program, funded by the FFG (Austrian Research Promotion Agency), thermoelectric waste heat recovery for commercial vehicles has been investigated intensely at ECS. Different concepts of thermoelectric generators for diesel-powered commercial vehicles have been studied with the help of mathematical models, virtual simulations, and physical simulations (experiments) at the engine test bench. Two concepts, which are particularly promising, have been investigated in detail within the last few years: (1) Z-design and (2) plate design.

### *First Prototype: Z-Design*

The Z-design (Fig. 16.1) basically consists of commercially available thermoelectric modules using bismuth telluride (BiTe). The modules are clamped between the hot exhaust gas side and the cold coolant water side. The hot exhaust gas side (three pieces)



**Fig. 16.1** Z-design

is made of steel channels with an integrated heat exchanging structure that improves the convective heat transfer between the hot exhaust gas and the metal surface.

Further, baffle plates are implemented in order to distribute the fluid as homogeneously as possible. The coolant water flows through meander channels. Hot exhaust gas flow and cold coolant water flow have been optimized with the in-house software KULI and with CFD methods.

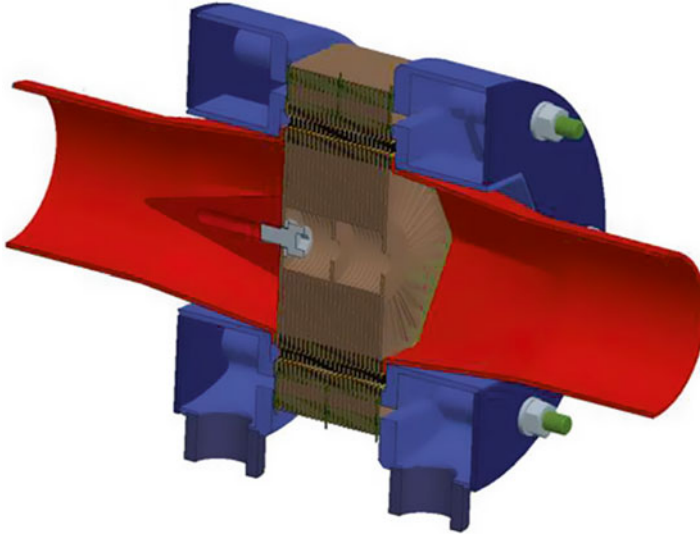
### ***Second Prototype: Plate Design***

The plate design (Fig. 16.2) is characterized by a very compact arrangement as well as integrated exhaust gas and coolant water channels. Thermoelectric material (also BiTe) is mounted on the outer side of a plate. Through the buildup of individual plates arranged one behind the other, a simple and inexpensive concept has been developed due to a high proportion of identical parts.

Furthermore, the thermoelectric generator is easily adaptable by adding or removing individual plates. The plates can be formed, for example, circular, oval, square, rectangular, or polygonal and/or curved.

### ***Virtual Simulations***

In an early design phase, the heat exchangers for hot exhaust gas and cold coolant water have been pre-dimensioned by analytical equations in order to get a qualitative and quantitative perspective of main dimensions, weight and power output. With the help of extensive CFD simulations, the two design studies have been



**Fig. 16.2** Plate design (study of the functional prototype)

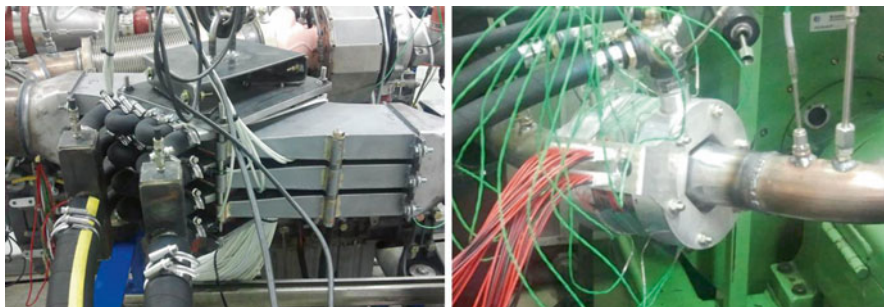
optimized. The exhaust gas pressure drop was minimized and the exhaust gas flow was as homogenous as possible within the device in order to ensure the best possible efficiency. The performed intensive numerical simulations can be divided into the following two groups:

- 3D CFD simulations using the software ANSYS-Fluent for flow optimization of the dynamic heat transfer, the pressure drop, and the mass of the heat exchanger structure.
- 1D model (electrically coupled thermal fluid) which can be integrated into vehicle models, and allows for the investigation of the thermoelectric generator and its influence on the overall vehicle in dynamic driving cycles.

### *Physical Simulations*

Finally, prototypes of the two design studies have been realized and verified at an engine test bench at ECS. The Z-design has been realized as full prototype (Fig. 16.3, left side), whereas the plate design has only been realized as functional prototype (Fig. 16.3, right side).

Comprehensive measurements show the challenges of this trendsetting technology as well as the potential for further optimization. Table 16.1 illustrates a comparison between the Z-design and the plate design under the same boundary conditions. Due to the higher degree of integration of the thermoelectric material in the plate design, the efficiency could be increased.



**Fig. 16.3** Z-design and plate design at the engine test bench at ECS

**Table 16.1** Efficiency of Z-design and plate design

	Z-design	Plate design
Temperature difference (°C)	150	150
Heat flow through TEG (W)	10.425	263
Electric power (W)	250	8.4
Efficiency (%)	2.4	3.2

**Fig. 16.4** Full-scale system based on plate design



An extrapolation, based on the engine test bench measurements of the plate design, leads to an electrical power output of approximately 1.2 kW for a full-scale TEG-system in combination with a modern Euro VI diesel engine. Before building the prototype of the full-scale system (Fig. 16.4), the design should be optimized regarding heat transfer and weight.

## Conclusion

The results of these tests demonstrate the potential of this technology for the use of the waste heat in the exhaust gas. The investigated systems are currently in prototype stage and therefore further efficiency improvements can be expected. Also comprehensive research activities are necessary to reach further improvements of the thermoelectric material within the next few years, especially for the relevant temperature range for diesel engines. The materials must withstand the loads in automotive applications and have an industry-typical long-term stability. The commercial success of this technology also depends on the successful industrialization of the manufacturing process of the used thermoelectric modules. Considering all these factors, a serial application of TEG-technology for commercial vehicles appears unrealistic before 2020.

**Acknowledgement** This work was funded by the FFG (Austrian Research Promotion Agency).

# Chapter 17

## Waste Heat Recovery in Steelworks Using a Thermoelectric Generator

T. Kuroki, K. Kabeya, K. Makino, H. Kaibe, H. Hachiuma,  
and A. Fujibayashi

**Abstract** In Japan the integrated steel industry has largely lowered its energy use for the past several decades by investing in energy efficient processes and facilities, and has kept the highest energy efficiency in the world. However, in view of energy security, the steelmaking industry is strongly required to develop new technologies to save more energy. Waste heat recovery can be one of the key technologies to meet this requirement.

Thermoelectric generation is one of the most effective technologies to recover waste heat, such as the radiant heat from steel products which has not been efficiently used, because it can convert heat directly into electric power.

A thermoelectric generation system was installed in the butt welded pipe mill at East Japan Works (Keihin District) of JFE Steel Corporation in May 2011. In this system, a thermoelectric generation unit consists of 16 Bismuth-Telluride thermoelectric genera-

---

T. Kuroki (✉)

Steel Research Laboratory, Environmental Process Research Department, JFE Steel Corporation,  
1-1 Minamiwataridacho, Kawasaki-ku, Kawasaki, Kanagawa 210-0855, Japan  
e-mail: [ta-kuroki@jfe-steel.co.jp](mailto:ta-kuroki@jfe-steel.co.jp)

K. Kabeya

Corporate Planning Department, JFE Steel Corporation,  
2-2-3 Uchisaiwaicho, Chiyoda-ku, Tokyo, 100-0011, Japan

K. Makino • H. Kaibe • H. Hachiuma

Thermo Generation Business Development Division, KELK Ltd.,  
3-25-1 Shinomiya, Hiratsuka, Kanagawa 254-8543, Japan

A. Fujibayashi

Steel Research Laboratory, JFE Steel Corporation,  
1-1, Minamiwataridacho, Kawasaki-ku, Kawasaki, Kanagawa 210-0855, Japan

Steel Research Laboratory, Environmental Process Research Department, JFE Steel Corporation,  
1-1 Minamiwataridacho, Kawasaki-ku, Kawasaki, Kanagawa 210-0855, Japan

tion modules. Each module can generate 24 W when the hot-side temperature is 553 K and the cold-side temperature is 303 K. These 16 thermoelectric generation modules are separated into four groups of four modules connected in series, and each group is connected in parallel. A commercial battery charger for off-grid photovoltaic systems was used as a maximum power point tracking (MPPT) control unit, and the output of 16 thermoelectric generation modules was used to charge storage batteries and supply power to LED lamps through the MPPT controller.

This paper describes the performance and durability of the thermoelectric generation system which has been investigated under operating conditions in butt welded pipe mill.

**Keywords** Thermoelectric generation • Waste heat • Heat recovery • Radiant heat • Thermoelectric generation system • Butt welded pipe

## Introduction

The integrated steel industry in Japan has significantly reduced its energy use for the past several decades by investing in energy efficient processes and facilities, and has kept the highest energy efficiency in the world. However the steelmaking industry is strongly required to develop new technologies for further energy conservation in view of energy security, high and volatile energy prices, and climate change. One of the key technologies to achieve the requirement is waste heat recovery. Figure 17.1 shows the waste heat for various processes of steelworks [1]. We have been investing in many energy efficient processes and facilities. However, a large amount of heat still remains wasted. For waste heat such as radiant heat from steel products which has not been efficiently used, thermoelectric generation is one of the most effective technologies to recover it, because thermoelectric generation can convert heat directly into electric power using the Seebeck effect. This environmentally friendly technology is expected to have an important role for energy conservation, waste heat recovery and CO<sub>2</sub> reduction. Thermoelectric generation has many advantages such as no mechanical moving parts, compact, no CO<sub>2</sub> emissions and long lifetime. This paper describes the thermoelectric generation system which was installed at East Japan Works of JFE Steel Corporation, using waste radiant heat from the butt welded pipe.

## Thermoelectric Generation System at Steelworks

### *Thermoelectric Generation Module*

Figure 17.2 shows a Bismuth-Telluride thermoelectric generation module (TEG module), which is made from a number of n-type and p-type thermoelectric elements [2]. It has high conversion efficiency and is a high-powered commercial thermoelectric

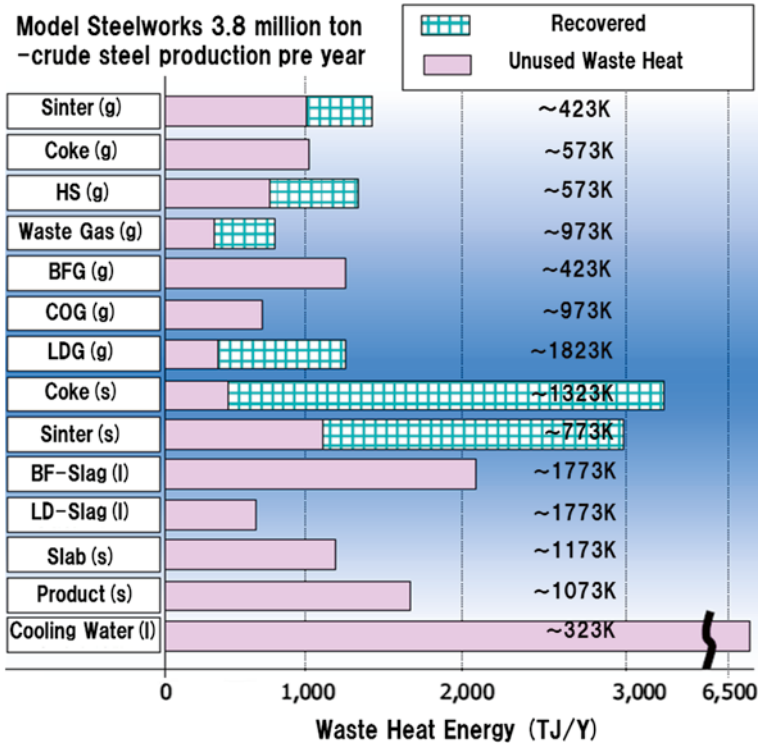


Fig. 17.1 Waste heat energy in the various processes in steelworks [1]

generator. The size of TEG module is 50 mm×50 mm×4.2 mm. Its maximum output power is 24 W, with a maximum conversion efficiency of 7.2 %, when the hot-side temperature is 553 K and the cold-side temperature is 303 K respectively [3]. The output  $P$  can be obtained from the external load  $r$  connected to the TEG module.  $P$  brings the maximum output  $P_{gmax}$  in impedance matching when  $R_i=r$ .

### Thermoelectric Generation Unit

Figure 17.3 shows an illustration of a partial cross section of the thermoelectric generation unit (TEG unit). The TEG unit consists of 16 TEG modules. These thermoelectric generation modules are separated into four groups of four thermoelectric generation modules connected in series, and each group is connected in parallel. The TEG modules were connected to the MPPT control unit to achieve maximum power at any temperature conditions. The output of 16 thermoelectric generation modules is used to charge storage batteries and supply power to LED lamps through the MPPT controller. Each TEG module is sandwiched between the heat collection plate and the water cooled plate by a spring structure, meaning that almost constant



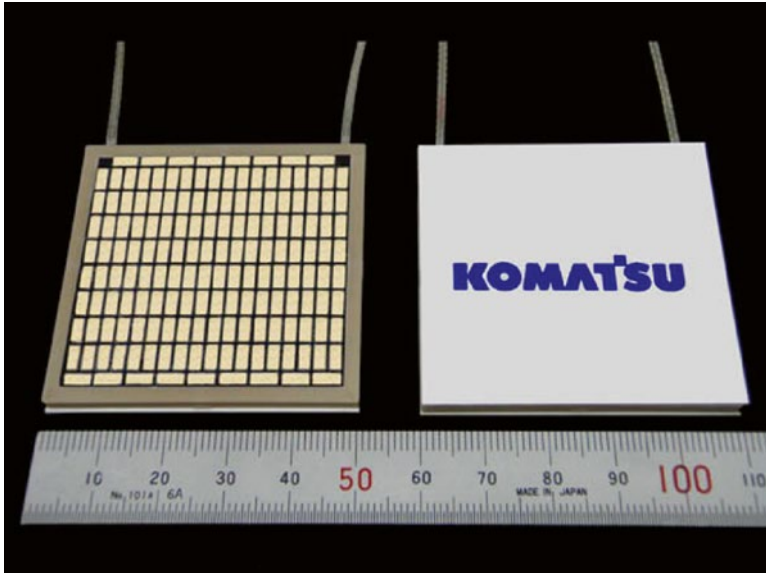


Fig. 17.2 Bi-Te thermoelectric generation module [2]

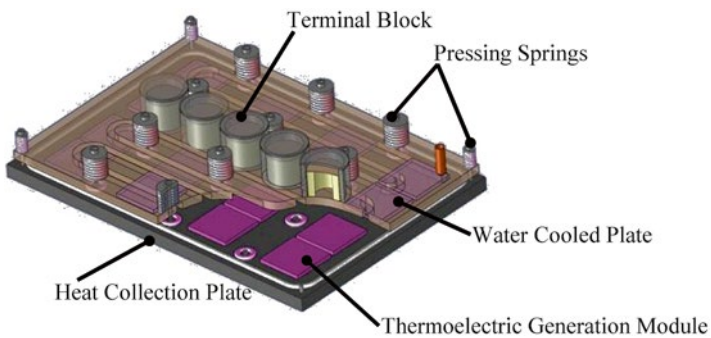
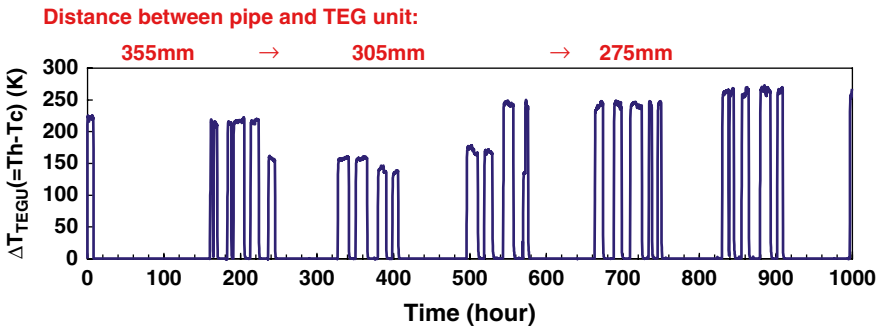
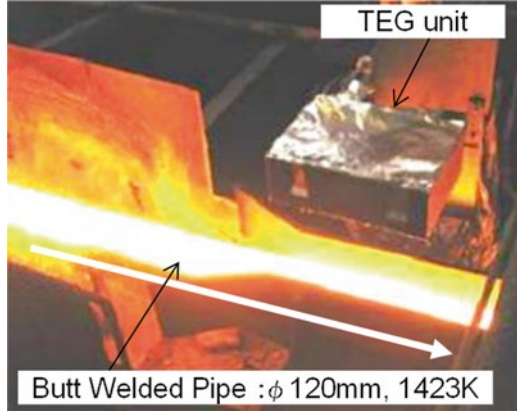


Fig. 17.3 Thermoelectric generation unit [3]

pressure is applied to the modules, even if a temperature difference is generated. The pressure is set at 1 MPa, with a cooling water flow rate of 10 l/min. The size of the heat collection plate is about 400 mm  $\times$  280 mm. Copper is used for the heat collection plate. The surface treatment of the heat collection plate is an electroless nickel plating (black) [3]. The temperature of heat collection plate  $T_h$  and water cooled plate  $T_c$  were measured by thermocouples. Figure 17.4 shows the thermoelectric generation unit installed in the JFE's butt welded pipe mill. The heat collection plate of the TEG units was heated by radiant heat from the butt welded pipe.

**Fig. 17.4** Thermoelectric generation unit installed to the JFE's butt welded pipe mill



**Fig. 17.5** One of the examples of the verification test data

### Verification Tests

JFE started verification tests to generate electric power by using radiant heat from butt welded pipes in 2011. The performance of the TEG unit had been investigated under various operating conditions in steelworks. Figure 17.5 shows the results of the measured temperature difference  $\Delta T_{TEGU}(=T_h - T_c)$ . Here,  $\Delta T_{TEGU}$  is the temperature difference of the heat collection plate ( $T_h$ ) and the water cooled plate ( $T_c$ ) of the thermoelectric generation unit.

When the welded pipe mill is under operation, the TEG unit is warmed up by radiant heat inducing a temperature difference, and the power output is generated by TEG unit.

The Eqs. (17.1) and (17.2) are the basic equation of thermoelectric generation:

$$Q_a = \alpha_c T_{hj} I - \frac{1}{2} r_c I^2 + K_c \Delta T_j \tag{17.1}$$

$$Q_d = \alpha_e T_{cj} I + \frac{1}{2} r_e I^2 + K_e \Delta T_j \quad (17.2)$$

where the heat  $Q_a$  is supplied by the thermal source at the hot surface,  $Q_d$  is the heat flowing out at cold surface,  $\alpha_e$  is the Seebeck coefficient,  $r_e$  is the internal electrical resistance,  $K_e$  is the thermal conductance,  $I$  represents the electric current [4],  $\Delta T_j (= T_{hj} - T_{cj})$  is the temperature difference of thermoelectric element,  $T_{hj}$  is the hot side temperature, and  $T_{cj}$  is the cold side temperature. These equations are derived from the heat equation subject to the Peltier effect and Joule heating with boundary conditions of the hot side temperature and the cold side temperature.

The power generation output  $P_g$  is given by Eq. (17.3):

$$P_g = Q_a - Q_d = (\alpha_e \Delta T_j - r_e I) I = R_L I^2 \quad (17.3)$$

where  $R_L$  is the external electric resistance.

Also, the maximum generation output  $P_{gmax}$  is given by Eq. (17.4).

$$P_{gmax} = \frac{1}{4} \frac{(\alpha_e \Delta T_j)^2}{r_e} \quad (17.4)$$

In order to obtain high power generation output, a large temperature difference  $\Delta T_j$  is required. On the other hand,  $T_{hj}$  must be under the maximum tolerance temperature. Therefore, it is very important to simulate  $T_{hj}$  for various conditions. In this system, the heat input  $Q_a$  is mainly the radiant heat from the pipe. The heat input  $Q_a$  is expressed by Eq. (17.5):

$$Q_a = \varepsilon \cdot F \cdot \sigma \cdot A (T_s^4 - T_h^4) + h \cdot A \cdot \Delta T \quad (17.5)$$

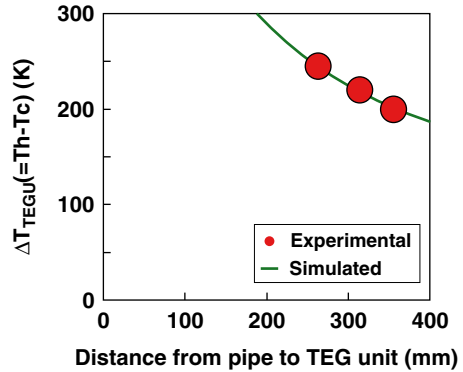
where  $\varepsilon$  is the emissivity,  $\sigma$  is Stefan-Boltzmann constant,  $F$  is the view factor,  $T_s$  is pipe temperature,  $T_h$  is the hot side temperature of the thermoelectric generation unit, and  $h$  is heat transfer coefficient.

The view factor  $F$  is a function of the distance from the pipe to the TEG unit and it is inversely proportional to the distance. Therefore, the heat input  $Q_a$  becomes larger as the TEG unit approaches the pipe. With a larger heat input, the heat collection plate temperature rises and the temperature difference  $\Delta T_{TEGU}$  increases.

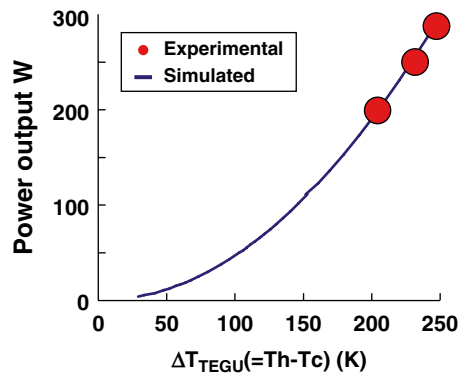
Using the thermal resistance of TEG unit and Eqs. (17.1)–(17.5), the relationship between  $\Delta T_{TEGU}$  and the distance from the pipe to the TEG unit is numerically investigated. The result is shown in Fig. 17.6. The experimental results are compatible with the simulation results.

Figure 17.7 shows the power output of TEGS units as a function of  $\Delta T_{TEGU}$ . The measurements of the power output of the TEG units seem to confirm the simulated output. The TEG output increases with  $\Delta T_{TEGU}$  and the thermoelectric generation system output is about 250 W when the  $\Delta T_{TEGU}$  is 250 K.

**Fig. 17.6** Relationship between the distance from the pipe to TEG unit and the temperature difference  $\Delta T_{\text{TEGU}}$



**Fig. 17.7** Electric power output of TEG units as a function of  $\Delta T_{\text{TEGU}}$



## Conclusion

A thermoelectric generation unit was tested in the butt welded pipe mill at the East Japan Works in the Keihin District of JFE Steel Corporation to recover waste heat. The thermoelectric generation unit which has 16 thermoelectric generation modules provides about 250 W when the temperature difference between the heat collection plate  $T_h$  and water cooled plate  $T_c$  at the thermoelectric generation unit is 250 K. The resulting electric output is a good fit between the simulation and the experimental data.

## References

1. Kabeya K (2012) Symposium on technology of the waste heat energy (AIST), No. 2, p 67
2. KELK Ltd. (2009) <http://www.kelk.co.jp/english/news/120419.html>. Accessed 12 Sept 2013
3. Kaibe H, Kajihara T, Fujimoto S, Makino K, Hachiuma H (2011) Recovery of plant waste heat by a thermoelectric generation system. *Komatsu Tech Rep* 57(164):26–30
4. Uemura K, Nishida I (1988) *Netsudenhandoutai to Sono Ouyou* (a thermoelectric semiconductor and the application). Nikkan Kogyo Shinbunsha, Tokyo, pp 26–33

# Chapter 18

## Thermoelectric Generator Power Converter System Configurations: A Review

E.A. Man, E. Schaltz, and L. Rosendahl

**Abstract** In a Thermoelectric Generator (TEG) system, the Thermoelectric (TE) modules can be connected in series, parallel, or a combination of both. Independent of the module connection, the power production of the TEG changes with the temperature gradient applied at its input. In consequence, the system requires a power conditioning circuit to deliver a stable and maximized output to the load. The solution is to integrate a DC–DC converter between the TEG and the load. Furthermore, a suitable control strategy is necessary to make the TEG operate at its maximum power point (MPP). The maximum power point tracking (MPPT) technique is widely used for TEG systems. The aim of this paper is to create a survey over the existing state-of-the-art TEG system configurations for TE energy harvesting. Depending on the application specifications, a suitable TEG system topology can be designed with the purpose of improving the power production of the overall system. The overall TEG system configurations are presented step by step. First, the possible connections of the TE modules in a TEG system are analyzed. Afterwards, the typical converter configurations used in TEG systems are discussed and options are addressed with the purpose of improving the efficiency. A discussion about the role and benefits of the MPPT depending on the TE modules connection is given. Finally, the potential of the possible TEG system configurations classified by their TEG connection is discussed and compared. The study highlights that a complete system design approach is necessary to obtain high efficiency of the TEG system.

**Keywords** DC–DC converter • Thermoelectric (TE) • Thermoelectric applications • Thermoelectric generator (TEG) • Thermoelectric generator system

---

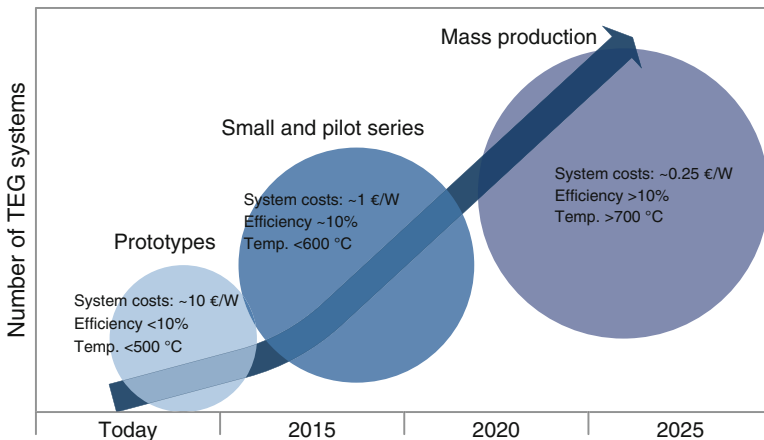
E.A. Man (✉) • E. Schaltz • L. Rosendahl  
Department of Energy Technology, Aalborg University, Aalborg 9220, Denmark  
e-mail: [eam@et.aau.dk](mailto:eam@et.aau.dk)

## Introduction

Over the last years, Thermoelectric (TE) energy harvesting has been regarded as a promising renewable technology due to the potential of the Thermoelectric Generator (TEG) to successfully produce electrical energy when exposed to a wide range of temperature difference. A TE module presents the advantages of having small size, light weight, and low maintenance. In addition, it has the ability to operate in harsh environmental conditions, it presents high reliability compared to other technologies due to the lack of moving parts, and it allows for a silent operation [1, 2]. At the moment, high production costs and low efficiency (<10 %) issues limit the expansion of the market for TE technology. However, improvements are expected in the next years, as soon as costs decrease and efficiency improves [3]. Although the concept presented in [3] and Fig. 18.1 refers to the automotive industry, the low efficiency issue covers all the TEG systems independent of applications. However, for small applications, thermoelectric harvesting can become very competitive because TE modules are simple, compact, and scalable [4, 5].

TEGs have been used in a wide range of applications [6–18], from ultra-low microwatts power systems [19] to large-scale multi-kilowatts applications [20, 21].

In waste heat recovery applications, TE modules are combined with heating systems to produce electrical energy from the dissipated heat. For this type of generation, a significant amount of research has been conducted with the objective of enhancing the performance of the system. The majority focus on improving the performance of the TE materials [22–30] and the design of the TE module [31–37], but some studies aim to find the optimum operating temperature values [7], the positioning of the modules in a system [38], or other parameters that may maximize the power production [7, 39–41].



**Fig. 18.1** Market requirements roadmap for TEG systems [3]

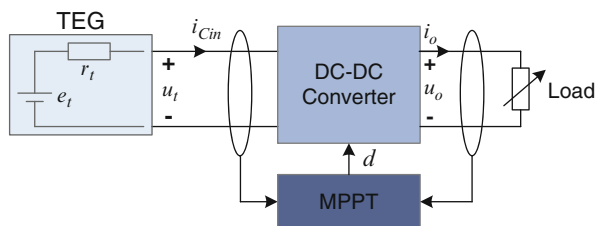
TE modules can be integrated in systems as a cogenerating source of electrical energy. In this way, an extra amount of power can be produced by the TEGs in addition to the existing generation systems. Sark [42] and Kings et al. [43] present photovoltaic-thermoelectric (PV-TE) hybrid modules as being a good way to improve the power generation of the system. The combination of TE and PV increases the renewable production of the overall system and offers better energy security. The hybrid module system studied in [42] was developed for roof-top application and the one from [43] proposes to add the PV-TE to electric vehicles. The results presented in both studies are only based on simulations and experimental validations are necessary and considered for future work. Chen et al. [44] present, in the introduction of the study, several application examples where TEGs are integrated as a cogeneration source into thermal energy systems.

Nevertheless, TEGs can be integrated in self-powering systems to generate energy for the electrical components. Application studies for TE self-powered heating systems can be found in [11, 45, 46]. TEGs can be used as temperature sensors or power supply in self-powered sensing systems, such as wrist watches, pacemakers, or other medical equipment, even in applications with difficult or no access, placed in remote locations with no grid connection, aircrafts, etc. [47–57].

This paper presents the state of the art of the general DC–DC converter system configurations for TE energy harvesting, highlighting the potential of each topology. This approach has the purpose of giving a better understanding about the key issues of the classical DC–DC converter system topologies in the form of a general presentation and relevant reference citations to offer the readers a start when considering improving the TE technology, mainly from the power electronic point of view.

## TEG System Configurations

The design of a TEG system is dependent on the application specifications. This process includes finding the optimum number of TE modules and their interconnection to form the TEG, a suitable DC–DC converter to process and deliver the electric energy from the TEG to the load and a control circuit to enhance the power production of the overall system [58]. The general configuration of the TEG system is presented in Fig. 18.2.



**Fig. 18.2** General schematic of the TEG system

The output voltage of the TEG varies according to the temperature difference input; therefore a power conditioning system is necessary to stabilize the power delivered to the load as well as to extract the maximum power from the TEG. A DC–DC converter has the ability to provide power conditioning [12]. Typically, a DC–DC converter with step-up capabilities is integrated in the TEG system due to the low output voltage produced by the TE modules. However, the additional step-down feature may be necessary too.

Each TEG system requires also a suitable control method to achieve maximum power transfer from the source to the load for any temperature difference input [59]. The MPPT is a widely used control technique in PVs due to its potential to make the PV system function at its maximum power capability for various irradiation values. PV and TEG systems have different characteristics [60, 61], but the MPPT control algorithms applied in PV applications can be used for TEG systems [12, 62–67].

Additionally, an Energy Storage Device (ESD) can be integrated into the system as the power generated by the TEGs is fluctuating. ESDs can increase the peak cover capability of the system by generating the extra power necessary when there is a mismatch between generation and load demand. Usually, such a device is either a (super-) capacitor or a battery [68].

A DC–AC inverter can be placed in the system to convert the maximum harvested DC power from the TEG into AC to deliver to the loads. However, the present review focuses only on the DC–DC TEG system configurations.

## ***TEG Module Connections***

In a TEG system, the TE modules can be connected in different combinations to form the TEG: in series, in parallel, or a combination of both.

The TE modules are series-connected when a high voltage and a low current are desired from the output of the TEG. However, the drawback of connecting many modules in series is the increase in the total electrical resistance of the TEG which affects the reliability of the generator [69]. The general schematic of the TEG system with the series-connected TE modules is presented in Fig. 18.3.

There are two ways to parallel connect the TE modules into the TEG system: (1) TE modules connected in parallel to form the TEG (Fig. 18.4) and afterwards connected to a single DC–DC converter and (2) each TE module connected to one DC–DC converter in a parallel configuration (Fig. 18.5).

Liang et al. [70] studied the performance of the system which included the TEG formed by parallel-connected TE modules (Fig. 18.4). The research was based on the analytical model developed using theoretical analysis and calculations and validated with experimental tests. Under ideal conditions, the open-circuit voltage of the parallel-connected TEG is the same voltage as that of one module, but the internal resistance is smaller, and the value is dependent on the number of the parallel-connected modules. The parameters that influence the output of this type of system configuration are the contact resistance and the thermal contact resistance.



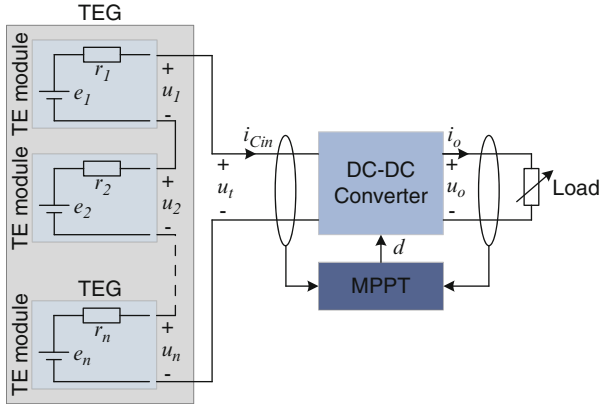


Fig. 18.3 General schematic of the series-connected TEG system

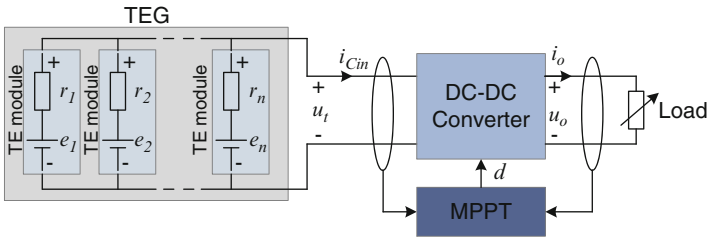
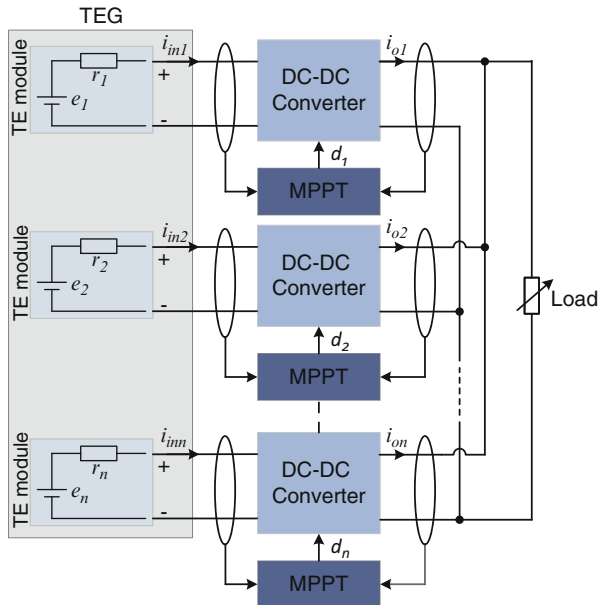
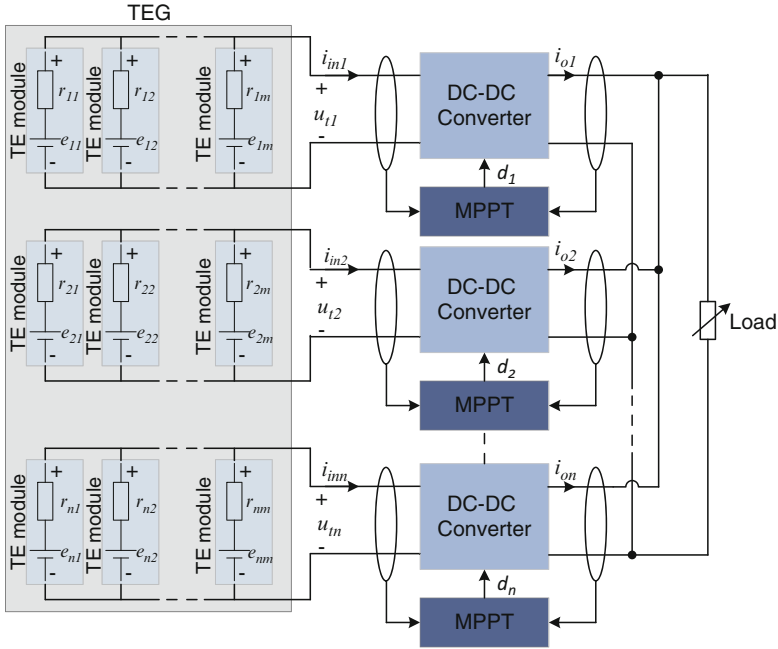


Fig. 18.4 General schematic of the TEG system with paralleled TE modules

Fig. 18.5 General schematic of the parallel-connected TEG system





**Fig. 18.6** General schematic of the series-parallel-connected TEG system

The increase of contact resistance has the same effect as the internal resistance of the TEG and may lead to decreased current and power output respectively. The thermal contact resistance affects the temperature difference input which also leads to reduced power output of the system.

The parallel configuration where each TE module is connected to one converter is seldom used for TEG applications. This is because it is not practical to connect one converter to each TE module due to the low voltage generation per module and the high converter costs for the overall system [71].

To increase the potential of this configuration, more TE modules are added in series and the arrays connected in parallel, making it more attractive for TEG applications. The series connection can achieve the necessary load voltage and by further connecting the strings in parallel, the required output power can be obtained [60]. Another advantage of this configuration is the fact that the internal resistance of the TEG will be lower compared to the series connection. For these reasons, the series-parallel connection of the TE modules can become very competitive especially in large-scale TEG application, when compared to the series-connected TE modules topology. The general schematic of the TEG system with the series-parallel-connected TE modules is presented in Fig. 18.6.

## ***Power Conditioning for TEG Systems***

A DC–DC converter is necessary to stabilize the power delivered to the loads due to the fluctuating nature of the power produced by the TEGs. Depending on the voltage harvested from the TEG and the application specifications, the DC–DC converter needs to have step-up and/or step-down characteristics. Other features required from the converter are wide input voltage range, high voltage conversion ratio, low current ripple, and high efficiency dependent on desired volume and weight. The wide input voltage range feature is necessary because the voltage generated by the TEGs varies widely and dynamically dependent on the external factors. The conversion ratio of the converters is altered by several circuit imperfections such as parasitic and switching components. Switch commutation times limit the maximum switching frequency, the duty cycle ratio, and therefore the voltage gain of the converters. The high-frequency switch signals from DC–DC converter may influence the operation of the TE module and the high ripple currents may affect the efficiency of the maximum power point tracking (MPPT). For this reason, a DC–DC converter with low input current ripple is desired for TEG power conditioning. The value of the current ripple should lie in the range of 10–20 % of the DC component to avoid peak currents [72]. The current ripple is inversely proportional to the inductor value which means that the current ripple can be reduced by increasing the inductance. However, this leads to an increase in the total weight, volume and cost of the converter.

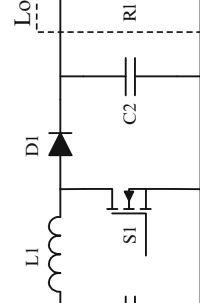

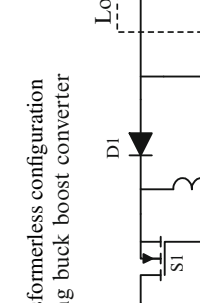
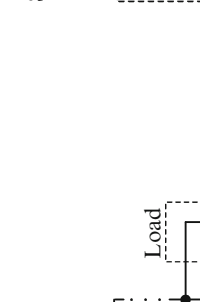
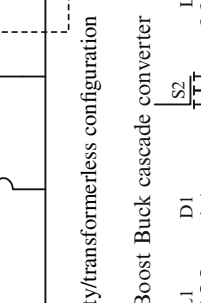
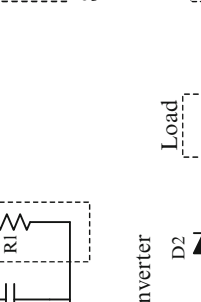
In addition, several transformerless DC–DC converter configurations have been proposed for TEG applications with series- and series-parallel-connected TE modules, such as the SEPIC converter, the Ćuk converter, the classic buck, boost, non-inverting buck-boost or their corresponding interleaved and cascaded topologies. In TEG applications when high voltage conversion ratios are required, the transformer-based DC–DC converter configurations are used, such as forward, flyback, push-pull converters etc.

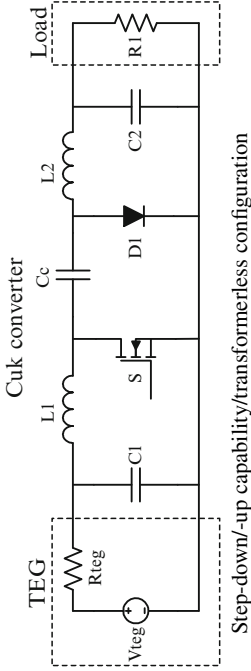
There exists several ways to categorize the DC–DC converters. Table 18.1 summarizes the most common converters used in TEG application classified by their step-up/step-down capabilities and whether they include a transformer in their configuration.

The buck converter has only the ability of stepping down the voltage generated by the generator and it is usually used in TEG systems when the TE modules are in series connection [73]. For this reason, its use is narrowed down to low and ultra-low power applications [74, 75]. The same can be said about the forward converter which also has only the step-down capability. The high step-down voltage conversion ratio and the nonpulsating output current features make the forward converter suited for applications related to high output currents.

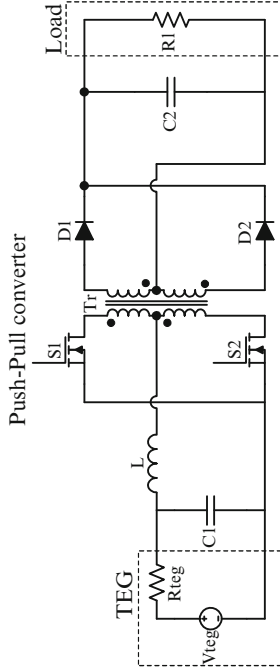
The step-up converters for TEG applications are used when the generator outputs low voltage and high current. One of the mostly used step-up DC–DC converters for TEG applications is the boost converter. It is easy to control and efficient, but the high current input can increase the current stress and conduction losses which trans-

**Table 18.1** Classification of DC–DC converters for TEG systems

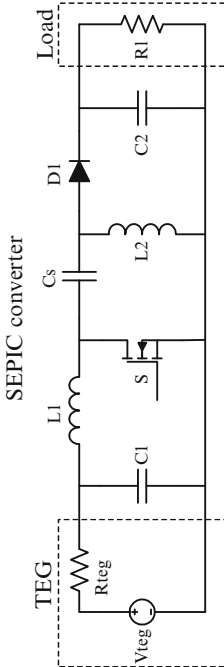
<p style="text-align: center;">Buck converter</p>  <p style="text-align: center;">Step-down capability/transformerless configuration</p>	<p style="text-align: center;">Boost converter</p>  <p style="text-align: center;">Step-up capability/transformerless configuration</p>
<p style="text-align: center;">Interleaved Boost converter</p>  <p style="text-align: center;">Step-down/-up capability/transformerless configuration</p>	<p style="text-align: center;">Step-up capability/transformerless configuration Inverting buck boost converter</p>  <p style="text-align: center;">Step-down/-up capability/transformerless configuration</p>
<p style="text-align: center;">Step-up capability/transformerless configuration Non-inverting buck boost converter</p>  <p style="text-align: center;">Step-down/-up capability/transformerless configuration</p>	<p style="text-align: center;">Boost Buck cascade converter</p>  <p style="text-align: center;">Step-down/-up capability/transformerless configuration</p>



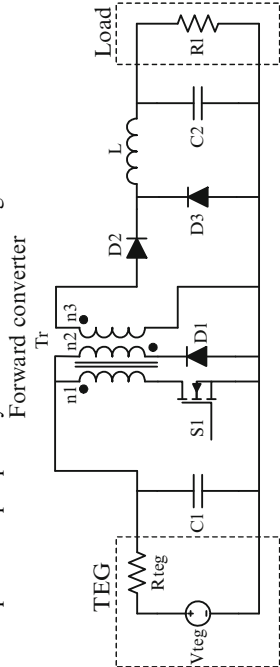
Step-down/up capability/transformerless configuration



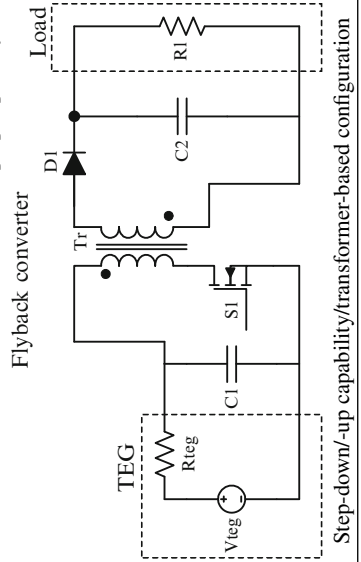
Step-up capability/transformer-based configuration



Step-down/up capability/transformerless configuration



Step-down capability/transformer-based configuration



Step-down/up capability/transformer-based configuration

late to a decrease in the efficiency. One option to reduce the input current ripple is to operate the converter in Continuous Conduction Mode (CCM). This method requires a large value of the input inductance which increases the weight and the volume of the converter [67]. To limit the value of the inductance, the boost converter can be operated in Discontinuous Conduction Mode (DCM) for low-power applications [76]. To substantially reduce the input current ripple and the current stress, the interleaved boost configuration can be chosen [58]. Both boost and interleaved boost topologies present the drawback of having limited voltage gains. Due to its transformer-based configuration, the push-pull converter is capable of high level conversion and therefore suited for medium and high TEG power applications [77]. Studies conclude that the interleaved boost configuration is often used as step-up topology for TEG systems with series and series-parallel-connected TE modules [58, 66, 74, 78].

The step-up/-down DC–DC converters proposed for TE conversion are buck-boost, its corresponding cascaded and interleaved configuration, SEPIC, Ćuk, and flyback converters.

To achieve high voltage gains, the flyback converter can be used. This type of transformer-based DC–DC step-down/-up converter has been used in small and medium power applications. It presents the drawback of poor efficiency and high switched voltage spikes due to the leakage inductance [79]. The other basic step-up/-down converter configurations suffer from high components stress and therefore are not favorable for high power applications [72].

Both inverting and non-inverting buck-boost configurations have been used in TEG applications for battery charging. One way to increase the efficiency of the non-inverting configuration is to replace the diodes with more efficient MOSFETs [80–82]. Nagayoshi et al. [80] reported 96.7 % conversion efficiency for this synchronous topology included in a 100 W TEG application for a battery load system. For the inverting buck-boost configuration, the operation in DCM proves to be more advantageous especially in low-power applications because the value of the inductance can be minimized. This leads to lower losses and decrease in the volume of the converter [68, 83].

The boost-cascaded-with-buck topology has been applied in several TEG systems [64, 65, 84]. Due to the input and output inductors, this converter has a continuous input and output current. To overcome the power density and cost problems arisen by the necessity of the large filter inductors, the converter configuration can be modified to a coupled inductor one. This configuration has proven to meet the requirements for battery charging applications. In addition, the diodes can be replaced by MOSFETs for efficiency enhancement. Wu et al. [84] reached a peak efficiency of 99 % for their 500 W prototype. It is also possible to adopt the interleaved technique to the boost-buck cascade topology to reduce the input current ripple and therefore the device current stress and increase the efficiency with the drawbacks of increasing the hardware costs and the control complexity [12]. Kim and Lai [65] reported that such a configuration with three-phase interleaving technique can achieve efficiency in a 95 % range.

The SEPIC converter is considered suitable especially for battery charging TEG applications since it has low-ripple input current and wide-range output voltage. On the other hand, compared to the buck-boost topology, the SEPIC converter presents lower efficiency because it utilizes two inductors [83].

The Ćuk converter has the additional advantage of low input and output current ripple compared to the SEPIC converter, but with the drawback of inverting the output voltage. Due to the nonpulsating nature of the converter input and output current, the TEG can operate with minimal disturbance [12, 17].

Zhang et al. [85] proposes the parallel connection of the DC–DC converter in the TEG system for automotive applications. In this way, instead of processing all the power generated by the TEG, the converter only partially balances the power between the TEG and the load. The study shows that this parallel configuration provides dual DC bus and high system efficiency with the drawback of complicated hardware and complex control due to the use of a bidirectional DC–DC converter. In addition, the authors discovered a low efficiency when the system operates in pure battery discharging mode. This means that the TEG provides small or no power output and the battery is discharging. The solution proposed is to avoid this operating mode by turning off the converter and connecting the battery directly to the load.

Andersson [74] presents the switching networks as alternative to DC–DC converters with MPPT for TEG automotive applications. The study shows that a higher efficiency can be obtained for the TEG system when using the proposed switching networks. This is because fewer switches and no capacitors or inductors are used compared to the DC–DC converters and therefore the costs for the power conditioning system can be decreased. However, this concept is relatively new and it should be further investigated.

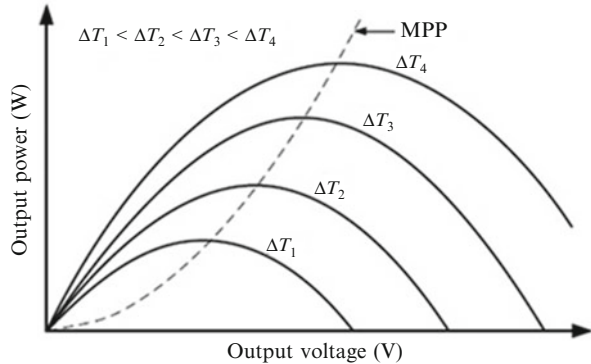
### ***MPPT for TEG Systems***

A TEG system requires also a suitable control method to achieve maximum power transfer from the source to the load for any temperature difference input. The MPPT is a widely used control technique in PV applications due to its potential to make the PV system function at their maximum power capability for various irradiation values. PV and TEG systems have different characteristics, but the MPPT control algorithms applied in PV applications can be used for TEG systems. The most used control methods are the perturb and observe (P&O), incremental conductance (INC) and the fractional open/short-circuit voltage/current (Frac.  $V_{oc}/I_{sc}$ ) [86].

In Fig. 18.7 the temperature gradients  $\Delta T_1$ ,  $\Delta T_2$ ,  $\Delta T_3$  and  $\Delta T_4$  represent some general samples to point out the dependency of the TEG voltage ( $V$ ) on the temperature difference input.

It can be seen that an increase in the temperature gradient results in an increase in the open circuit output voltage as well as in the maximum output power of the module. The output power reaches its maximum value when the load resistance is equal to the TEG internal resistance and the output voltage is half of the open circuit

**Fig. 18.7** Power/Voltage (P/V) characteristics of TEG modules for different temperature gradients [67]



voltage of the TEG. An MPPT control is necessary to perform the impedance match in order to extract the maximum power output [67].

In the series-connected TEG, each module operates at the common current and when the temperature difference input varies, it causes a deviation from the optimum operating current. The MPPT is performed at stack level; hence not all the modules work at their maximum power point (MPP). Another disadvantage of this configuration that can be mentioned is the lack of robustness as, in case one of the modules is damaged, the generator output will shut down.

In the parallel-connected TEG, the modules operate at the same output voltage and when the temperature difference input varies, it causes a deviation from the optimum operating voltage. In this case, the connection of one DC–DC converter to each module allows an individual MPPT control which means they operate at their MPP.

The series-parallel connection of the TEG also allows for an individual MPPT control for each string. The configuration presents the advantage of individual MPPT over the series connection and the increased power delivered to the load over the parallel configuration.

Vadstrup et al. [81] concluded in their research that an increase in the power output of the TEG system for the given application is possible if the MPPT is performed at module level instead of stack level for both series and parallel connection.

In case of damage, both parallel and series-parallel topologies present high robustness because only the related string will stop outputting power.

## Discussions

Despite the current TE efficiencies are in the range of 5–10 %, this is no longer regarded as an important issue when considering the benefits of energy saving, with available no-cost waste heat sources, and emission reduction offered by the TE technology. Due to the low efficiency issues, the TE society focuses more on



low-power applications where a TEG system can be built with good efficiency, low costs, and good reliability.

The TE modules that form the TEG can be coupled in series to achieve a high output voltage with low current, in parallel to obtain a low output voltage with high current or in series-parallel for a compromise between voltage and current values. The series connection is preferred in low-power applications where a small number of TE modules are connected without increasing too much the internal resistance. To overcome the drawback of the high internal resistance, the series-parallel connection of many modules is usually preferred for large-scale applications [79]. The modules are connected in series to acquire the necessary load voltage and afterwards, the strings are connected in parallel to obtain the necessary output power.

The TEG is composed by connecting several TE modules that may experience mismatch in the temperature difference input. Under these circumstances, some of the modules will fail to operate at their MPP leading to a power loss in the TEG system. To overcome this drawback, a DC–DC converter with MPPT control is inserted between the TEG and the load [60].

In order to harvest the maximum power from the TEG, an impedance matching between the generator and the load is necessary. This is regarded as the basic concept when designing a TEG system. The impedance matching task can be performed by a DC–DC converter as it can control its input conductance and therefore the virtual load conductance by means of changing the voltage conversion ratio. Under these conditions, the TEG maintains its operation in MPPT.

Transformer-based DC–DC converter topologies are attractive when isolation between the source and the load or a high voltage conversion is necessary. However, this translates also to additional costs and losses.

Studies show that the most attractive choices for power conditioning in a wide range of TEG applications are buck, boost, buck-boost converters, and their corresponding interleaved configurations. The choice is based primarily on their ability to successfully track the MPP of the TEG and therefore reducing the power loss in the systems. In addition, the converters require less components compared to other topologies; they are easy to control and present high efficiency [68]. The interleaved configurations present the additional benefit of low current ripple. Transformerless converters are also used in high power applications where weight and size are the key issues. Table 18.2 summarizes the key properties and parameters of the discussed transformerless converter topologies.

An important issue which needs to be regarded when designing the TEG system is the high input current ripple which can cause early failure. To increase the reliability of the system, the input current ripple needs to be reduced. This can be achieved by (1) adding a capacitor at the input of the converters, (2) increasing the switching frequency, (3) using the interleaved converter configurations, or (4) increasing the value of the input inductor, but also the weight and volume of the converter.

When a higher voltage is desired from the TEG, regardless of the modules connection, an advantageous alternative is to increase the temperature difference input instead of the number of the modules. By increasing the temperature difference

**Table 18.2** Comparison of key properties and parameters of the transformerless converters used for TEG applications [87]

	Buck	Boost	Buck-boost	Non-inv. buck-boost	Ćuk	SEPIC
#Semiconductors	2	2	2	4	2	2
#Capacitors	2	2	2	2	3	3
#Inductors	1	1	1	1	2	2
Inverted output	No	No	Yes	No	Yes	No
Continuous output current	CCM	No	No	CCM (buck mode)	Yes	No
Continuous input current	No	CCM	No	CCM (boost mode)	Yes	Yes

input, the series-parallel-connected TEG system can reach the output power that a parallel-connected TEG could generate.

It can be synthesized that the series-parallel-connected TEG is most practical from the point of view of costs, MPPT effect, robustness, and reliability [88].

## References

- Hsu C, Huang G, Chu H, Yu B, Yao D (2011) *J Appl Energ* 88(4):1291–1297
- Gould CA, Shammass NYA, Grainger S, Taylor I (2008) MIEL
- Observatory NANO (2011) Briefing no. 17 – thermoelectricity for energy harvesting. [Internet]. <http://bwcv.es/observatorynano/observatorynano-delivered-briefings>
- Snyder JF (2008) *Interface* 17(3):54–56
- Eisenhut C, Bitschi A (2006) *ICT*
- Riffat SB, Ma X (2003) *J Appl Therm Eng* 23(8):913–935
- Gou X, Xiao H, Yang S (2010) *J Appl Energ* 87(10):3131–3136
- Niu X, Yu J, Wang S (2009) *J Power Sources* 188(2):621–626
- Yang J (2005) *ICT*
- Ota T, Fujita K, Tokura S, Uematsu K (2006) *ICT*
- Qiu K, Hayden ACS (2008) *J Power Sources* 180(2):884–889
- Zhang X, Chau KT, Chan CC (2008) *J Asian Electric Vehicle* 6(2):1119–1124
- Martins J, Brito FP, Goncalves LM, Antunes J (2011) SAE Technical Paper
- Hussain Q, Brigham D, Maranville C (2009) SAE. *Int J Engines* 2(1)
- Saqr KM, Mansour MK, Musa MN (2008) *Int J Automot Tech* 9(2):155–160
- Talom HL, Beyene A (2009) *J Appl Therm Eng* 29(2–3):439–444
- Yu C, Chau KT (2009) *J Energ Convers Manage* 50(6):1506–1512
- Chau KT, Chan CC (2007) *Proc IEEE* 95(4):821–835
- Lu C, Park SP, Raghunathan V, Roy K (2010) ISLPED 2010
- Anatychuk LI, Rozver YY, Velichuk DD (2011) *J Electron Mater* 40(5):1206–1208
- Fisher MD, Kastovich JC, Moreland C, Corry TM (1962) *J Adv Ener Conv* 2:275–279
- Weidenkaff A, Robert R, Aguirre M, Bocher L, Lippert T, Canulescu S (2008) *J Renew Energ* 33(2):342–347
- Ohtaki M, Araki K, Yamamoto K (2009) *J Electron Mater* 38(7):1234–1238
- Vineis CJ, Shakouri A, Majumdar A, Kanatzidis MG (2010) *J Adv Mater* 22(36):3970–3980
- He J, Liu Y, Funahashi R (2011) *J Mater Res* 26(15):1762–1772
- Boukai AI, Bunimovich Y, Tahir-Kheli J, Yu JK, Goddard WA, Heath JR (2008) *Nature* 451:168–171
- Poudel B, Hao Q, Ma Y, Lan Y, Minnich A, Yu B et al (2008) *Science* 320(5876):634–638

28. Hochbaum AI, Chen R, Delgado RD, Liang W, Garnett EC, Najarian M et al (2008) *Nature* 451:163–167
29. Heremans JP, Jovovic V, Toberer ES, Saramat A, Kurosaki K, Charoenphakdee A et al (2008) *Science* 321(5888):554–557
30. Casati G, a-Monasterio CM, Prosen T (2008) *Phys Rev Lett* 101(016601–1):016601–016604
31. Crane DT, Bell LE (2006) *ICT*
32. D'Angelo J, Case ED, Matchanov N, Wu CI, Hogan TP, Barnard J et al (2011) *J Electron Mater* 40(10):2051–2062
33. Crane DT, Kossakovski D, Bell LE (2009) *J Electron Mater* 38(7):1382–1386
34. Saber HH, El-Genk MS (2002) *ICT*
35. Anatyshuk LI, Vikhor LN, Ludchak IY, Termena IS (2010) *J Thermoelectricity* 1
36. Zeng G, Bahk JH, Bowers JE, Lu H, Zide JMO, Gossard AC et al (2008) *J Electron Mater* 37(12):1786–1792
37. Rowe DM (ed.) (2006) *Thermoelectrics handbook – macro to nano*. CRC Press Taylor & Francis Group
38. Hsiao YY, Chang WC, Chen SL (2010) *J Energy* 35(3):1447–1454
39. Kumar S, Heister SD, Xu X, Salvador JR, Meisner GP (2013) *J Electron Mater* 42(6):944–955
40. Heng X, Xiaolong G, Chen Y (2008) *ICSC*
41. Casano G, Piva S (2012) *J Phys Conf* 395:012156(1)
42. van Sark WGJHM (2011) *J Appl Energ* 88(8):2785–2790
43. Kings Krishna Nagaraja Singh R., Manivannan A (2013) *Int J Eng Res* 3(2):975–979
44. Chen M, Lund H, Rosendahl LA, Condra TJ (2010) *J Appl Energ* 87(4):1231–1238
45. Qiu K, Hayden ACS (2006) *ICT*
46. Qiu K, Hayden ACS (2010) *J Electron Mater* 40(5):606–610
47. Yang Y, Lin ZH, Hou T, Zhang F, Wang ZL (2012) *J Nano Res* 5(12):888–895
48. Leonov V, Torfs T, Fiorini P, Van Hoof C (2007) *J Sensors* 7(5):650–657
49. Torfs T, Leonov V, Vullers RJM (2007) *J Sens Transducers* 80(6):1230–1238
50. Leonov V (2011) *J Renew Energ* 1
51. Van Bavel M, Leonov V, Yazicioglu RF, Torfs T, Hoof C, Posthuma NE et al (2008) *J Sens Transducers* 94(7):103–115
52. Leonov V, Van Hoof C, Vullers RJM (2009) *J Sens Transducers* 107(8):165–176
53. O'Callaghan J (2011) A breakthrough technology uses temperature differentials to power sensor-driven building automation systems. *J Sensors* [Internet]. <http://www.sensorsmag.com/networking-communications/energy-harvesting/thermoelectric-energy-harvesting-8708>
54. Bottner H, Nurus J, Schubert A, Volkert F (2007) *ICT*
55. Samson D, Otterpohl T, Kluge M, Schmid U, Becker T (2010) *J Electron Mater* 39(9):2092–2095
56. Samson D, Kluge M, Fuss T, Schmid U, Becker T (2012) *J Electron Mater* 41(6):1134–1137
57. Champier D, Favarel C, Bédécarrats JP, Kousksou T, Rozis JF (2013) *J Electron Mater* 42(7):1888–1899
58. Gao J, Sun K, Ni L, Chen M, Kang Z, Zhang L et al (2012) *J Electron Mater* 41(6):1043–1050
59. Lihua C, Dong C, Yi H, Peng FZ (2008) *PESC*
60. Nagayoshi H, Kajikawa T (2006) *ICT*
61. Singh GK (2013) *J Energy* 53:1–13
62. Nagayoshi H, Kajikawa T, Sugiyama T (2002) *ICT*
63. Nagayoshi H, Tokumisu K, Kajikawa T (2007) *ICT*
64. Kim R-y, Lai J-S (2008) *APEC*
65. Kim R-y, Lai JS (2008) *IEEE T Power Electr* 23(5):2310–2318
66. Kim R-y, Lai J-S, B Y, A K (2009) *IEEE T Ind Electron* 56(9):3709–3716
67. Ni L-x, Sun K, Zhang L, Xing Y, Chen M, Rosendahl L (2011) *ICEMS*
68. Win KK, Dasgupta S, Panda SK (2011) *ICPE & ECCE*

69. Cao D, Peng FZ (2010) ECCE
70. Liang G, Zhou J, Huang X (2011) *J Appl Energ* 88(12):5193–5199
71. Wu H, Sun K, Min C, Xing Y (2013) *J Electron Mater*
72. Erickson RW, Maksimovic D (eds.) (2001) *Fundamentals of power electronics*, 2nd edn. Kluwer Academic Publishers, pp15–22
73. Kadirvel K, Carpenter J, Lum-Shue-Chan B, Texas Instruments (2012) power-management functions for energy harvesting. *EE Times Design*
74. Andersson B (2012) A comparison of different connection techniques for thermoelectric generators in vehicle waste heat recovery, Dissertation
75. Texas Instruments, Inventor (2012 Revised 2013) Programmable output voltage ultra-low power buck converter with up to 50 mA/200 mA output current – TPS62736/TPS62737 datasheet
76. Doms I, Merken, Van Hoof C (2007)
77. Li M, Xu S, Chen Q, Zheng LR (2011) *J Electron Mater* 40(5):1136–1143
78. Kim J, Kim C (2013) *IEEE T Power Electr* 28(8):3827–3833
79. Ni L-x, Sun K, Wu H-f, Chen Z, Xing Y (2012) *ISIE*
80. Nagayoshi H, Nakabayashi T, Maiwa H, Kajikawa T (2011) *J Electron Mater* 40(5):657–662
81. Vadstrup C, Schaltz E, Chen M (2013) *J Electron Mater* (in press)
82. Phillip N, Maganga O, Burnham KJ, Ellis MA, Robinson S, Dunn J et al (2013) *J Electron Mater* 42(7):1900–1906
83. Phillip N, Maganga O, Burnham KJ, Dunn J, Rouaud C, Ellis MA et al (2012) *EFEA*
84. Wu H, Sun K, Zhang J, Xing Y (2013) *J Electron Mater* 42(7):1737–1744
85. Zhang X, Chan CC, Li W (2011) *ICEMS*
86. Laird I, Lu DD (2013) *IEEE T Power Electr* 28(7):3147–3157
87. Wens M, Steyaert M (2011) Design and implementation of fully-integrated inductive DC–DC converters in standard CMOS. Springer, pp 27–121
88. Kaibe H, Kajihara T, Fujimoto S, Makino K, Hachiumata H (2011) *Komatsu technical report* 57(164)

# Chapter 19

## Transient Thermal Response of Heat Sinks and Its Implication on Power Control Strategies

N. Youn, Y.P. Kim, and D. Wee

**Abstract** Thermoelectric generation has relatively low efficiency and power output compared with other types of energy production. Therefore, it is necessary to optimize the operating conditions of the thermoelectric system in the applied research phase. In this study, we aim to suggest the optimal operating conditions and develop a strategy to obtain maximum power output in a thermoelectric generator. First, we develop a theoretical framework for optimal control of operating voltage to get the maximum power output. Then, to maintain the optimal conditions, the temperature variation of the heat sink, which is controlled by current and voltage in the circuit, will be discussed by modeling the heat transfer of a heat sink under real-world conditions. Because of the importance of voltage control, we suggest the optimal voltage control strategy.

**Keywords** Thermoelectrics • Constant voltage algorithm • Open-circuit voltage algorithm • Optimization • Transient response • Power control strategy

### Introduction

In thermoelectric generation, it is critical to properly maintain optimal operating conditions in order to obtain the maximum power output. In a recent study [1], it was suggested that a method of optimization that controls the operating voltage to half of the “steady-state” open-circuit voltage should be a simple but effective strategy for maintaining the optimal conditions. The reason behind this is not that the optimal conditions correspond to the impedance-matching condition [2, 3], but that the typical V-I curves of thermoelectric generators can be approximated by linear relations.

---

N. Youn • Y.P. Kim • D. Wee (✉)  
Department of Environmental Science and Engineering, Ewha Womans University,  
Seoul 120-750, Republic of Korea  
e-mail: [dhwee@ewha.ac.kr](mailto:dhwee@ewha.ac.kr)

The steady-state open-circuit voltage, which is the reference for the optimum voltage, is a function of the thermal conditions of the system, which is subject to changes during its operation. In cases where a large variation in the thermal conditions is expected, it becomes necessary to regularly measure the steady-state open-circuit voltage to estimate the optimum voltage. However, since thermal inertia in the system exists, the voltage does not converge to the steady-state open-circuit voltage immediately after the current is cut off. The transient response due to the variation of the temperature inside the system should also be considered. In order to measure the steady-state open-circuit voltage that is required for estimating the optimum voltage, one typically needs to wait for this transient response to decay. When the convergence towards the steady state is too slow, too frequent and/or too long interruptions of the operation required for the measurement may affect the overall performance of the system.

In this study, we investigate the amount of time required for the heat sink to reach its thermal steady state from the instant the current is cut off. Since a typical heat sink in a thermoelectric system has relatively high thermal resistance, its thermal inertia may become the limiting factor that dominates the transient behavior of the entire system. Both analytic and numerical estimates of the time scale of the transient response are provided. Based on these estimates, we make a recommendation on power control strategies for thermoelectric generation systems.

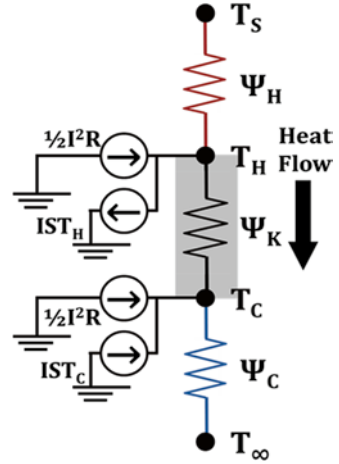
## **Numerical Analysis of a Transient Heat Transfer in a Typical Heat Sink**

First, we estimate the heat flux from the thermoelectric module to the heat sink in typical conditions. The information obtained here will be used to specify the boundary conditions in the numerical simulation of heat transfer in the heat sink. A schematic illustration of the thermal network of interest is given in Fig. 19.1.

The situation we are interested in can be described as follows. The thermoelectric generator must be operating at maximum power for most of its operational history, and hence the steady-state temperature distribution corresponding to the maximum-power condition will be the initial condition given to the heat sink. Then, the circuit suddenly breaks at  $t=t_0$ , in order to measure the open-circuit voltage. However, the heat sink and the thermoelectric module have a certain thermal inertia, and the temperature distribution over the heat sink and the thermoelectric module will not immediately change into the steady-state distribution corresponding to the open-circuit condition. Rather, as time goes on, the temperature distribution gradually approaches the steady-state distribution. Only after this transient behavior sufficiently dies out and the temperature distribution reaches a state close to the corresponding steady state one can read the accurate open-circuit voltage.

In this process, the thermal inertia of the heat sink is the most important parameter, since the largest temperature change in the system is associated with the heat sink, due to its poor thermal conductance. Additionally, in many cases the heat sink is physically the largest part of the generator, which makes its thermal inertia large

**Fig. 19.1** Schematic illustration of the thermal network representing a typical thermoelectric module [1, 3]



enough to dominate the overall transient behavior of the system. Only when the temperature distribution in the heat sink is close enough to the steady-state temperature distribution one can measure the steady-state open-circuit voltage correctly.

Since the heat sink is of paramount importance in this process, we need to analyze the transient heat transfer in it, and the thermal boundary condition at the interface with the thermoelectric module must be given by a pre-specified heat flux into the heat sink. Since we consider the transient behavior between two states (the maximum-power condition and the open-circuit condition), the heat flux for each of these two states must be estimated.

From the thermal network, the governing equations can be written as follows:

$$\dot{Q}_H = \frac{T_s - T_H}{\Psi_H} = IST_H + \frac{T_H - T_C}{\Psi_K} - \frac{1}{2} I^2 R, \tag{19.1}$$

$$\dot{Q}_C = \frac{T_C - T_\infty}{\Psi_H} = IST_C + \frac{T_H - T_C}{\Psi_K} + \frac{1}{2} I^2 R. \tag{19.2}$$

From these two equations, we obtain  $T_H$  and  $T_C$  as functions of  $I$ , which can be used to evaluate  $Q_C$ . The short-circuit current,  $I_{sc}^*$ , is approximated by:

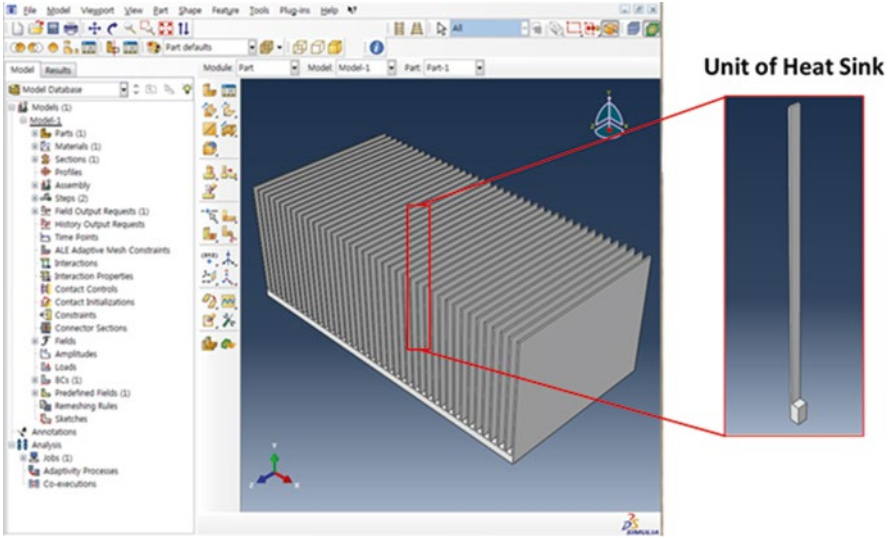
$$I_{sc}^* = \frac{S(T_s - T_\infty)}{S^2(T_s \Psi_C + T_\infty \Psi_H) + R(\Psi_C + \Psi_K + \Psi_H) \Psi_K^{-1}}. \tag{19.3}$$

As shown in a previous study [1], the maximum-power condition corresponds approximately to  $I = I_{sc}^*/2$ , while the open-circuit condition corresponds to  $I = 0$ .

We estimate the heat flux for a case where  $T_s = 354 \text{ K}$ ,  $T_\infty = 297 \text{ K}$ ,  $\Psi_H = 3.15 \text{ K W}^{-1}$ ,  $\Psi_C = 32.67 \text{ K W}^{-1}$ ,  $\Psi_K = (0.305 \text{ W/K})^{-1}$ ,  $R = 4.47 \Omega$ , and  $S = 3.60 \times 10^{-4} \times 127 \text{ V K}^{-1}$ , which can be considered a practical representative condition (Case I in [1]). The results are summarized in Table 19.1. The dimensions of the thermoelectric module ( $L \times W \times H$ ) are  $3 \text{ cm} \times 3 \text{ cm} \times 3 \text{ mm}$ .

**Table 19.1** Estimated heat losses to the heat sink for a practical representative condition

Parameters	Maximum power condition	Open-circuit condition
$I$ (A)	0.01640	0
$T_H$ (K)	349.334	349.408
$T_C$ (K)	345.334	344.628
$dT = T_H - T_C$ (K)	3.9996	4.7798
$Q_c$ (W)	1.4795	1.4579
$q_c''$ (W/m <sup>2</sup> )	1,644	1,620



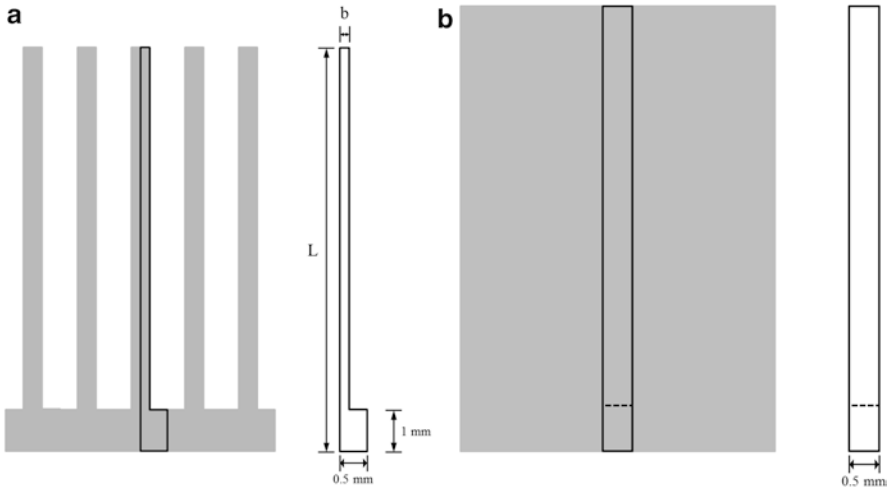
**Fig. 19.2** Computational domain of the analysis of transient heat transfer

Based on the estimated heat losses, the simulation of the heat transfer of the thermoelectric system was carried out by using Abaqus/CAE version 6.10 [4]. We assume that the main component of the heat sink is composed of planar fins. For simplicity, the numerical analysis is only performed on half of a single fin, not the entire heat sink (Figs. 19.2 and 19.3).

The material properties, the operating conditions, and the geometry of the heat sink are similar to the values reported in a previous study [5]. The length of a fin (between its bottom and its tip) is  $L$  and the thickness of the fin is  $b$ . The heat sink is made out of a metal whose density, thermal conductivity and specific heat are denoted as  $\rho$ ,  $k$ , and  $c_p$ , respectively.

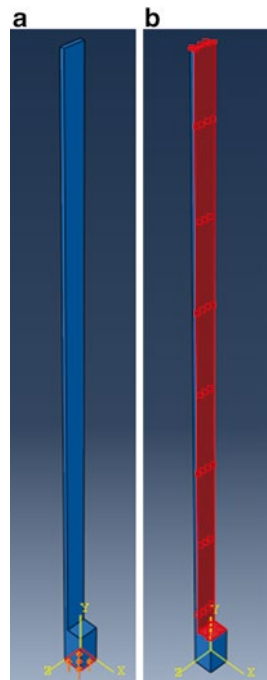
The boundary conditions are set as follows. The bottom surface marked in Fig. 19.4a is in contact with the module, receiving a heat flux from the module of  $1,620 \text{ W m}^{-2}$  in the maximum-power condition and  $1,644 \text{ W m}^{-2}$  in the open-circuit condition. The marked surface in Fig. 19.4b releases heat through a convective heat transfer process specified by the heat transfer coefficient ( $h$ ) and the ambient temperature  $297 \text{ K}$ . Numerical parameters are summarized in Table 19.2. By matching the thermal resistance of the model to  $\Psi_C$ ,  $h$  is found to be equal to  $1.17686 \text{ W K}^{-1} \text{ m}^{-2}$ .





**Fig. 19.3** Planar cut view with  $L$ ,  $b$ , and variables describing dimensions of parts of the single fin

**Fig. 19.4** Selected surfaces of the fin for specifying boundary conditions



The numerical simulation is composed of two computational steps, as shown in Table 19.3.

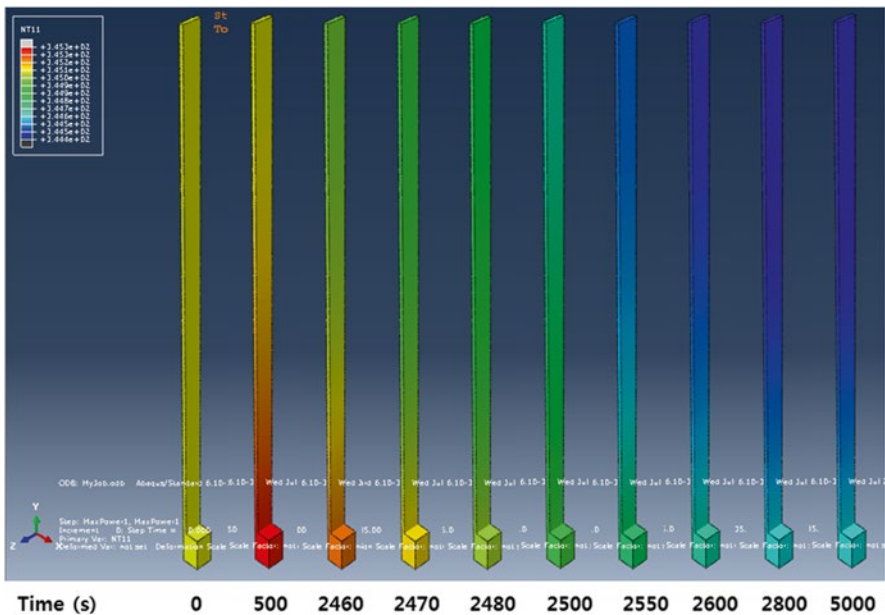
The variation of temperature distribution over time (0–5,000 seconds) is shown in Fig. 19.5. Figure 19.6 shows the evolution of the temperature at the center of the

**Table 19.2** Properties of the heat sink

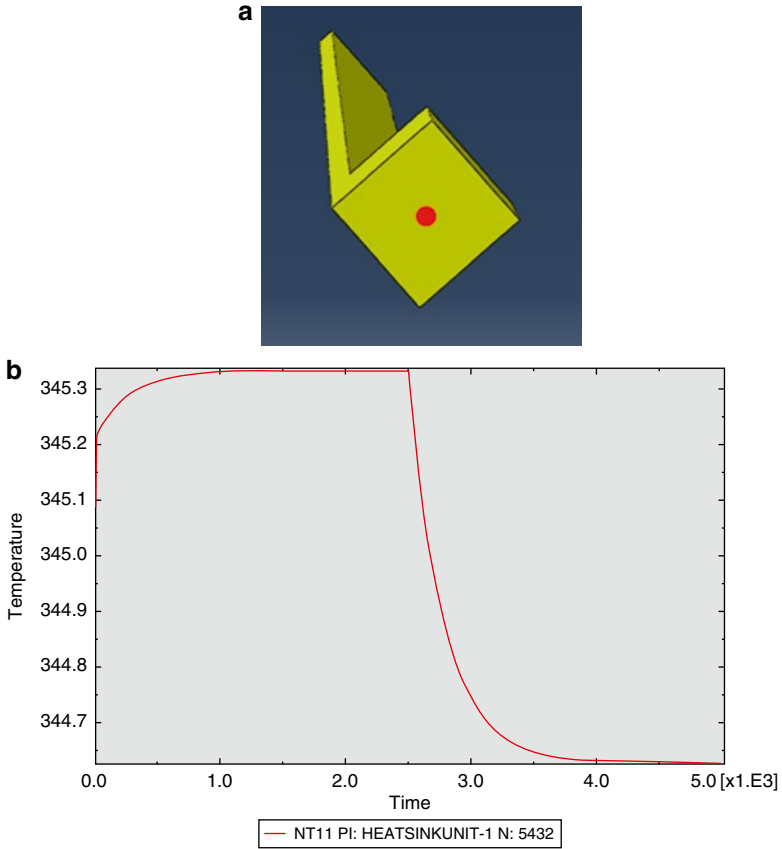
Density ( $\rho$ )	2,700 kg m <sup>-3</sup>
Thermal conductivity ( $k$ )	237 W m <sup>-1</sup> K <sup>-1</sup>
Specific heat ( $c_p$ )	904 J kg <sup>-1</sup> K <sup>-1</sup>
Initial temperature ( $T$ )	345.087 K
Ambient temperature ( $T_\infty$ )	297 K
Heat transfer coefficient ( $h$ )	1.17686 WK <sup>-1</sup> m <sup>-2</sup>
Length of fin ( $L$ )	15 mm
Thickness of fin ( $b$ )	0.1 mm

**Table 19.3** Computational steps used in the numerical simulation

Step	Time (s)	Condition			
		Initial material temperature ( $T$ )	Ambient temperature ( $T_\infty$ )	Convective heat transfer coefficient ( $h$ )	Heat flux at the bottom surface ( $q_c''$ )
Maximum power condition	$t_0 = 1 - 2,500$	345.087 K	297 K	1.17686 Wm <sup>-2</sup> K <sup>-1</sup>	1,644 W m <sup>-2</sup>
Open-circuit condition	$t_0 = 2,500 - 5,000$				1,622 W m <sup>-2</sup>



**Fig. 19.5** Evolution of the temperature field in the heat sink



**Fig. 19.6** Evolution of the temperature at the center of the bottom surface ( $T_C$ )

bottom surface, which is equal to  $T_C$ . It shows that the transient behavior dies out at a relatively slow rate, and that the time required to reach the steady state may be of the order of  $10^2$ – $10^3$  s.

## Discussion

In order to understand the results of our numerical simulation, the lumped capacitance method is applied [6]. The essence of the lumped capacitance method is to assume that the temperature field inside a solid object is spatially uniform at any instant during the transient process and hence that temperature gradients within the solid are negligible. The transient temperature response is determined by formulating an overall energy balance in the system. This balance must relate the rate of heat loss at the surface to the rate of change in the internal energy.

The main component of the heat sink is composed of planar fins. First, we consider the longitudinal, internal heat transfer through the fin. From the given data, the thermal diffusivity ( $\alpha$ ) is given by

$$\alpha = \frac{k}{\rho c_p} \approx 9.7 \times 10^{-5} \text{ m}^2 \text{ s}^{-1}. \quad (19.4)$$

The time scale of the internal heat transfer ( $\tau_{\text{int}}$ ) can be estimated by

$$\tau_{\text{int}} = \frac{L^2}{\alpha} \approx 2.32 \text{ s}, \quad (19.5)$$

from which we conclude that the transient response of the longitudinal internal heat transfer through the fin reaches its steady-state response within a few seconds. This is a reasonably fast response.

On the other hand, we must also consider the heat transfer in the transverse direction, that is in the direction of the fin thickness. Since the heat transfer in this direction also involves the convective heat transfer between the surface of the fin and the environment, we need to evaluate the corresponding Biot number (Bi):

$$\text{Bi} = \frac{hb}{k} = 4.97 \times 10^{-7} \ll 1. \quad (19.6)$$

Since the resulting Biot number is indeed small, the lumped capacitance model can be applied. This model is certainly the simplest and most convenient method that can be used to solve transient conduction problems. In this case, the governing equation becomes

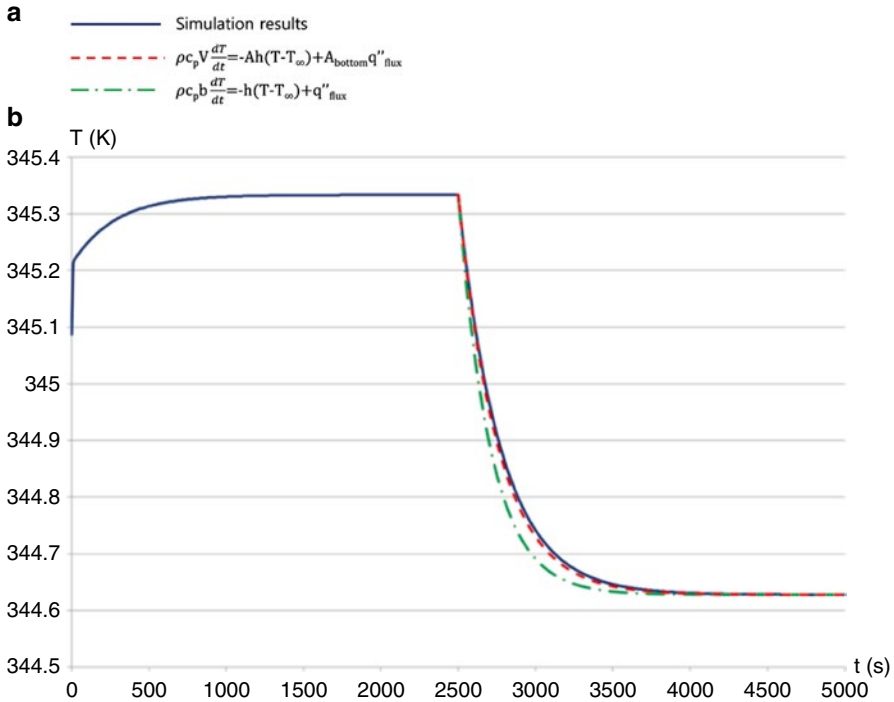
$$\rho c_p b \frac{dT}{dt} = -h(T - T_\infty) + q''_{\text{flux}}. \quad (19.7)$$

Since  $\frac{dT}{dt} \approx \frac{T - T_\infty}{\tau_{\text{ext}}}$ , the time scale of the transverse heat transfer ( $\tau_{\text{ext}}$ ) can be estimated by:

$$\tau_{\text{ext}} = \frac{\rho c_p b}{h} \approx 207.4 \text{ s}. \quad (19.8)$$

For the heat transfer process in the transverse direction, dominated by that external to the fin, the subscript, " $\tau_{\text{ext}}$ ," is given. This estimate clearly shows that the time scale of the transient response may be of the order of several hundred seconds. A more precise estimate can be obtained by considering the following version of the lumped capacitance equation:

$$\rho c_p V \frac{dT}{dt} = -Ah(T - T_\infty) + A_{\text{bottom}} q''_{\text{flux}}. \quad (19.9)$$



**Fig. 19.7** Comparison of simulation results and the lumped capacitance models

where  $V$  is the volume of the heat sink,  $A$  is the convective surface area, and  $A_{\text{bottom}}$  is the area of the bottom surface. The lumped capacitance models (Eqs. (19.7) and (19.9)) match the numerically obtained transient behavior well, while Eq. 19.9 clearly shows a superior match (Fig. 19.7).

Since  $\tau_{\text{ext}}$  is of the order of several hundred seconds, it is expected that the transient response of this transverse, external heat transfer survives for at least several minutes. As we mentioned earlier, too frequent and/or too long interruptions of the operation required for the measurement may negatively affect the overall performance of the system. If a significant and rapid temporal change in the thermal condition is expected, the performance degradation may become very pronounced. In summary, the open-circuit voltage control method may not be suitable in cases where the conditions of thermal reservoirs and the characteristics of the heat transfer between the generator and the reservoirs are rapidly changing, compared to the transient thermal response of the heat sink, the time scale of which can be estimated by the lumped capacitance method.

## References

1. Youn N, Lee H, Wee D, Gomez M, Reid R, Ohara B (2013) Achieving maximum power in thermoelectric generation with simple power electronics. *J Electron Mater* 43(6):1597–1602
2. McCarty R (2012) Thermoelectric power generator design for maximum power: its all about ZT. *J Electron Mater* 42(7):1504–1508
3. Yazawa K, Shakouri A (2012) Optimization of power and efficiency of thermoelectric devices with asymmetric thermal contacts. *J Appl Phys* 111:024509
4. Hibbit D, Karlsson B, Sorensen P (2007) *ABAQUS/Theory Manual Version 6.7*. Hibbitt, Karlsson & Sorensen, Inc., Providence, RI
5. Wang C, Hung C, Chen W (2012) Design of heat sink for improving the performance of thermoelectric generator using two-stage optimization. *Energy* 39:236–245
6. Incropera FP, Dewitt DP, Bergman TL, Lavine AS (2012) *Principles of heat and mass transfer*. John Wiley & Sons, New York, NY, pp 280–297, Chapter 5

## Chapter 20

# Feasibility Study on Screen Printing as a Fabrication Technique for Low-Cost Thermoelectric Devices

I.A. Dimitriadou, A. Fulham, M.C. Robbins, K. Simpson, R.A. Dorey, P. Jones, S. Bernadet, J. Laroche, S. Piles Guillem, C. Potyrala, and J. Wood

**Abstract** Conventional fabrication techniques for thermoelectric devices at present are expensive, time consuming, have low yield of material and come with a high failure rate for the devices. The proposed fabrication technology, screen printing of thermoelectric devices, offers a low-cost, flexible and quick manufacturing solution with a high yield of material which would help boost the market for miniature thin-film thermoelectric devices of high-voltage outputs, which can be utilised in numerous applications (e.g. energy harvesting, aerospace and automotive applications) where current devices are too expensive to be commercially attractive. The materials used for the prototype screen-printed devices were n-type  $\text{Bi}_2\text{Te}_3$  and p-type  $\text{Sb}_2\text{Te}_3$  thermoelectric materials, silver for the electrical contacts and glass and aluminium oxide as substrate materials. Five discrete stages were described and well defined as part of the ink formulation and screen-printing process: powder synthesis, material characterisation, the formulating stage, screen printing and finally heat treatment. A mathematical model was developed for the estimation of the electrical performance of screen-printed devices. Tests of screen-printed single-semiconductor pair samples proved that the fabrication technique proposed is promising, by demonstrating a power output of  $16 \mu\text{W}$  and a voltage output of  $2.1 \text{ mV}$  for the single p-n junction at a  $\Delta T$  of  $20 \text{ }^\circ\text{C}$  across it, which compares well to existing systems in terms of voltage. The feasibility study has helped to not only define a promising fabrication method for thermoelectric devices but also identify the main challenges associated with it and

---

I.A. Dimitriadou (✉) • A. Fulham • M.C. Robbins • K. Simpson  
European Thermodynamics Limited, 8 Priors Business Park,  
Wistow Road, Kibworth, LE0 8RX, Leicester, UK  
e-mail: [ismini@etdyn.com](mailto:ismini@etdyn.com)

R.A. Dorey  
University of Surrey, Guildford, Surrey, UK

P. Jones • S. Bernadet • J. Laroche • S.P. Guillem • C. Potyrala • J. Wood  
School of Applied Sciences, Cranfield University, Building 70, Cranfield  
MK43 0AL, Bedfordshire, UK

realise that in many energy-harvesting applications the  $ZT$  of a thermoelectric device may not be as important as the thermal stability and longevity of it.

**Keywords** Screen-printing • Thermoelectric devices • Ink formulation • Energy harvesting

## Introduction

Thermoelectric generators (TEGs) are solid-state systems of n- and p-type semiconductor materials sandwiched between two electrically insulating but thermally conductive ceramic plates. The n-type and p-type materials are connected electrically in series and thermally in parallel. When a temperature difference is applied across a thermoelectric generator, the generator can convert it into electrical energy [1].

Many energy generation, energy conversion and other industrial processes are associated with great amount of losses mostly in the form of waste heat. Thermoelectric generators operating under the Seebeck effect can exploit this waste heat otherwise lost to the environment and convert it into useful electrical power. An example of an application where TEGs could be widely used is the automotive industry, where the waste heat from the exhaust gases could be converted into electricity by using thermoelectric devices and then fed back into the alternator of the car contributing in fuel economy [2].

The aforementioned valuable capability of TEGs to convert waste heat into electricity offers the potential for them to be used in numerous applications, especially in an energy saving-driven economy. However, their market is limited by their high cost associated with the fact that these devices are currently fabricated by hand (pick-and-place technique), a method which involves great use of resources, high labour cost as well as a high device failure rate [3].

This study investigated the potential of minimising the manufacturing cost of TEGs by using screen printing, a low-cost, automated and reliable fabrication method [4].

## Preparation of Prototype Devices

There are five main stages involved in the preparation of screen-printed thermoelectric devices: powder synthesis, material characterisation, ink formulation, screen printing and heat treatment of the printed materials. Each one of the five stages previously mentioned was optimised through experimental trials as part of the project.

The following materials were chosen for the first prototype devices: n-type  $\text{Bi}_2\text{Te}_3$  and p-type  $\text{Sb}_2\text{Te}_3$  thermoelectric materials, silver for the electrical contacts and glass and aluminium oxide as substrate materials. Both the thermoelectric materials and the silver contacts were screen-printed onto the selected substrates.

The synthesised powders for the thermoelectric materials showed purity of 71 % for antimony telluride (detection of oxygen content) and approximately 100 % for bismuth telluride, while the powder for silver was 100 % pure.



**Table 20.1** Screen-printed thermoelectric materials

Parameter	Antimony telluride	Bismuth telluride
Grain size range	50–100 nm	150–250 nm
Purity	70 %	Close to 100 %
Temperature stability	Less than 450 °C	Less than 350 °C
Best sintering temperature-time	450 °C—30 min	350 °C—more than 30 min

Summary table of main findings

Ink formulation trials led to the optimisation of the ink composition for the best printing results as follows: 57 wt% of nanopowder, 47 wt% of solvent and 2 wt% of binder. The aforementioned mixture is ball milled for approximately 12 h and then mixed together to form the ink.

A DEK 245 screen printer was used for the fabrication of the prototype devices. The optimum squeegee speed was found to be 13 cm/s. The results for different printing conditions showed that for a given squeegee speed, the best results were obtained for low values of the squeegee pressure over the screen-printing mask [5].

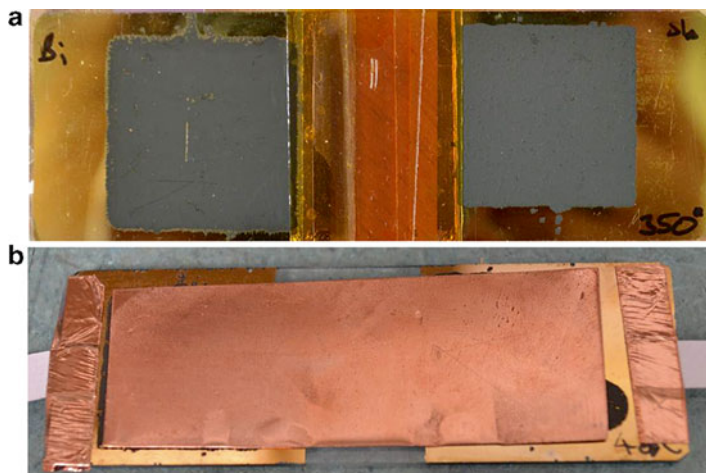
Films of 15  $\mu\text{m}$  thick thermoelectric material and silver contacts were deposited on glass and ceramic substrates. The deposited films showed good homogeneity, sufficient density and no visible flaws.

After screen-printing, the films were dried in order to remove the solvent and the binder and make the screen-printed materials denser. The density of the printed thermoelectric materials is crucial, because it determines their thermoelectric properties [6].

Sintering of the printed materials was carried out at different temperatures (250, 350 and 450 °C) for a fixed amount of time (30 min). At lower temperatures, samples for both thermoelectric materials showed no bonding between particles, while at higher temperatures, where good bonding of particles could be achieved, oxidation occurred. Time variations were the next stage at certain temperatures. A compromise between time and temperature for the sintering process was needed in order to obtain good bonding and composition for the powders of the thermoelectric materials. For antimony telluride the best sintering time-temperature combination was found to be 30 min at 450 °C, while for bismuth telluride the best combination was more than 30 min of sintering at 350 °C (Table 20.1).

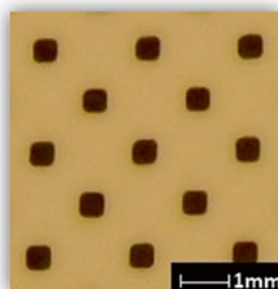
## Results and Discussion

Two single-semiconductor pair samples were produced, using bismuth telluride for the n-type material and antimony telluride for the p-type (Fig. 20.1a). Both devices were printed onto a glass substrate coated with a conductive gold film. The thickness of the thermoelectric materials printed onto the glass substrate was 15  $\mu\text{m}$  and the surface area of each thermoelement was 2 cm  $\times$  2 cm. One of the samples was sintered at 400 °C for 20 min and the other at 350 °C for 20 min under a nitrogen



**Fig. 20.1** Screen-printed thermoelectric couple of n-type  $\text{Bi}_2\text{Te}_3$  and p-type  $\text{Sb}_2\text{Te}_3$  (a) sintered at  $350^\circ\text{C}$  for 20 min and (b) sintered at  $400^\circ\text{C}$  for 20 min with a copper contact on top

**Fig. 20.2** Array of n- and p-type screen-printed thermoelectric materials demonstrating a feature size  $<1\text{ mm}$



atmosphere. The density of the printed material achieved for the two samples was approximately 70–75 %. Other sample devices produced for demonstration purposes rather than testing include two samples of screen-printed  $\text{Sb}_2\text{Te}_3$  and  $\text{Bi}_2\text{Te}_3$  thermoelectric couples on silver electrodes printed onto alumina substrates, three samples of screen printed silver electrodes (two on alumina substrates and one on a glass substrate) as well as arrays of n-type and p-type thermoelectric material printed on an aluminium oxide substrate that show the smallest feature size achieved (Fig. 20.2).

The two single-semiconductor pair samples have been tested for performance evaluation of screen-printed thermoelectric devices. For establishing the electrical contacts between the n-type and p-type pellets for each sample, a copper strip was used (Fig. 20.1b). Simple resistance measurements for the samples demonstrated that electrical connectivity at room temperature has been achieved (Table 20.2). A test rig developed for testing thick film and commercial thermoelectric devices was used in order to test the electrical performance of the screen-printed devices at

**Table 20.2** Electrical resistance measurements for the two single-thermoelectric pair samples at room temperature

Sample	Resistance (k $\Omega$ )
Sintered at 400 °C for 20 min	130–150
Sintered at 350 °C for 20 min	5–10

**Table 20.3** Electrical performance data for the single-thermoelectric pair sample sintered at 400 °C for 20 min

$T_H$ (°C)	$T_C$ (°C)	$dT$ (°C)	$P_{out}$ ( $\mu$ W)	$V_{out}$ (mV)
44.2	24.1	20	16.16	2.09

elevated hot-side temperatures. It should be noted that a 1 mm thick ceramic plate was added at the top of the copper electrode for electrical insulation between the device and the test rig.

Between the two samples tested at same conditions, the pair that was sintered at 400 °C for 20 min showed better electrical performance. For a hot-side temperature ( $T_H$ ) of 44 °C and a cold-side temperature ( $T_C$ ) of 24 °C (temperatures measured on the glass substrate and the ceramic plate, respectively), the voltage output ( $V_{out}$ ) of the sample sintered at 400 °C was 2.1 mV and the power output ( $P_{out}$ ) approximately 16.2  $\mu$ W (Table 20.3). It should be made clear that the actual temperature drop on the thermoelectric material itself was less than 5 °C and most of the temperature drop between the hot side and the cold side occurred on the glass and ceramic layers.

## Conclusions

The project's aim was to prove that screen printing can be a promising alternative fabrication method for low-cost thermoelectric devices. Five main stages were identified for the screen-printing process: powder synthesis, material characterisation, the formulating stage, screen printing and finally heat treatment.

The synthesis of the bismuth telluride and silver nanopowders was successful and resulted in pure samples, while the synthesis of the antimony telluride nanopowders needs to be improved as the samples were only 70 % pure.

The best ink composition for screen printing was found to be 51 wt% of powder, 47 wt% of solvent and 2 wt% of binder.

The most challenging task was the sintering of the printed materials. At high temperatures the material would degrade and oxidation would occur, while at lower temperatures the particle bonding was insufficient. The density achieved for the thermoelectric materials within the project was 70–75 %. More work is required in order to optimise the sintering process including sintering under alternative atmospheres or vacuum to prevent oxidation.

Testing of sample devices showed that electrical connectivity was achieved between the n-type and p-type thermoelements and that the voltage outputs of a single p-n junction compare well with voltage outputs of other existing technologies. The power output however is still quite poor and further work is required in order to minimise the electrical resistance of the thermoelements.

Except for the identification of the challenging tasks/issues associated with the proposed technology, which could be the initiating point for new research projects, the study helped us realise that in many energy-harvesting applications the ZT of a thermoelectric device may not be as important as the thermal stability and longevity of it. Hence, research related to thermoelectric energy harvesting should not focus on high ZT values, but should investigate thermoelectric materials with particularly high Seebeck values, which may mean looking at materials that in the past have been discarded (due to having a low figure-of-merit value). Fabricating and providing pellets of thermoelectric materials with high Seebeck coefficients mean that for the same temperature differences, there is the potential of making devices with higher voltage outputs and lower number of thermoelectric pellets—compared to devices utilising thermoelectric materials with lower Seebeck values but higher ZT—or even weight-optimised devices for lightweight applications such as space, aerospace and automotive. The last point is based on the fact that higher voltage outputs work better with electronics, such as DC/DC converters and MPPT microcontrollers.

**Acknowledgements** This work was supported by the Technology Strategy Board in the UK.

## References

1. Rowe DM (2006) General principles and basic considerations. In: Rowe DM (ed) *Thermoelectrics handbook: macro to nano*. Taylor & Francis, Boca Raton, pp 1-1-1-3
2. Min G (2010) Thermoelectric energy harvesting (chapter 5). In: Beeby S, White N (eds) *Energy harvesting for autonomous systems*. Northwood; pp. 135-139
3. Amatya R, Ram RJ (2010) Solar thermoelectric generator for micropower applications. *J Electron Mater* 39(9):1735-1740
4. Navone C, Soulier M, Plissonnier M, Seiler AL (2010) Development of (Bi, Sb)<sub>2</sub>(Te, Se)<sub>3</sub>-based thermoelectric modules by screen-printing process. *J Electron Mater* 39(9):1755-1759
5. Yin W, Lee D-H, Choi J, Park C, Cho SM (2008) Screen printing of silver nanoparticle suspensions for metal interconnects. *Korean J Chem Eng* 25(6):1358-1361
6. Phair JW (2008) Rheological analysis of concentrated zirconia pastes with ethyl cellulose for screen printing SOFC electrolyte films. *J Am Ceram Soc* 91(7):2130-2137

# Chapter 21

## Improving Thermoelectric Cooling by Light Emission

G. Min

**Abstract** Conventional approach to improve the cooling performance of a thermoelectric refrigerator is to increase its coefficient of performance (COP), which in turn requires to improve the figure of merit of thermoelectric materials. However, it has been recognised that improving the heat dissipation from the hot side of a thermoelectric refrigerator can indirectly improve its cooling performance. In this chapter, we show that the cooling performance of a real-world thermoelectric cooling system can be significantly improved by enhancing energy dissipation through light emission.

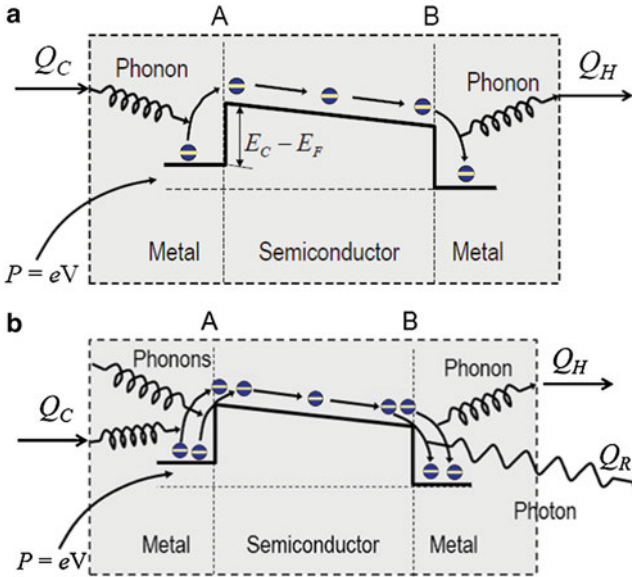
**Keywords** Thermoelectric • Thermoelectric cooling • Electronic refrigeration

Thermoelectric refrigeration, which employs electrons as the working fluid, is an environmentally friendly solid-state cooling technology [1–4]. It has the advantage of simplicity, high reliability, silent operation and total scalability. However, it suffers from the drawback of low coefficient of performance (COP) compared with conventional mechanical systems. A low COP system usually requires more input power and dissipates more heat from its hot side. Consequently, improving the COP has been a key challenge in the development of thermoelectric cooling technology. A well-known and probably most effective way to improve the COP of a thermoelectric device is to search for high ZT materials [5–8]. Over the past 50 years, tremendous efforts have been made in this aspect with only marginal improvement (Note that a significant improvement in ZT has been reported several years ago, but it has not yet been confirmed.). Understandably, the lack of success in this aspect has inspired the search for alternative approaches. It is well recognised that in many applications, particularly small-scale cooling of electronics, the problem associated

---

G. Min (✉)

School of Engineering, Cardiff University, Queen's Buildings,  
Newport Road, Cardiff CF24 3AA, UK  
e-mail: [min@cf.ac.uk](mailto:min@cf.ac.uk)



**Fig. 21.1** Schematic energy band diagram of thermoelectric cooling process. (a) Conventional thermoelectric process, in which thermal energy is absorbed at junction *A* and transported to junction *B*, and effectively heat is pumped from *A* to *B*. (b) Novel thermoelectric process, in which the thermal energy absorbed at junction *A* is transported to junction *B* where a portion of the energy is dissipated through light emission, resulting in a less increase of lattice temperature

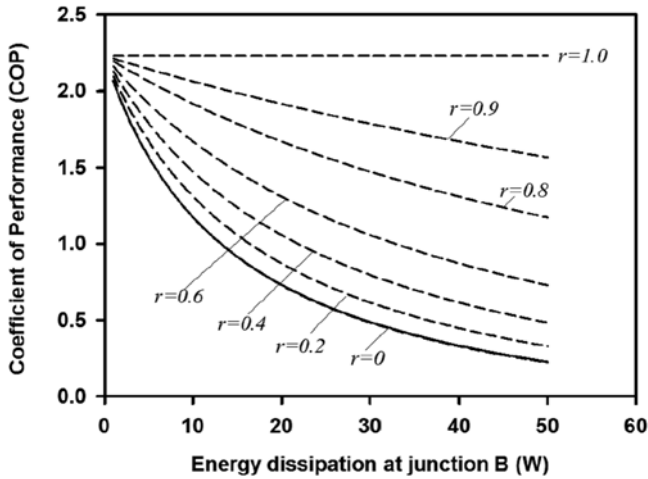
with heat dissipation is often a more difficult challenge than that to reduce power consumption. Recently, we proposed to improve the heat dissipation from the thermoelectric device with assistance from light emission [9]. The objective of this work is to demonstrate the effectiveness of this proposed approach.

Figure 21.1a shows a schematic energy band diagram of a thermoelectric process at junctions *A* and *B*. The electrons absorb energy from phonons of the crystal lattice at junction *A* and carry the absorbed energy to junction *B*, where the energy is dissipated back to the crystal lattice as phonons. As a result, junction *A* becomes cold, which will absorb heat from the ambient, and junction *B* becomes hot, which will dissipate heat to the ambient. At a steady state, the rate of thermal energy absorption at junction *A* from the ambient,  $Q_C$ , is related to the electrical power supplied to the thermoelectric device,  $P$ , and the rate of the energy dissipation to the ambient at junction *B*,  $Q_H$ , by

$$Q_H = Q_C + P \tag{21.1}$$

The COP of a thermoelectric refrigerator is defined as  $\eta = Q_C/P$ . The maximum COP, which is obtained corresponding to an optimal electrical current, is given by

$$\eta_{\max} = \frac{T_C}{T_H - T_C} \times \frac{\sqrt{1 + Z\bar{T}} - T_H / T_C}{\sqrt{1 + Z\bar{T}} + 1} \tag{21.2}$$



**Fig. 21.2** The COP of a thermoelectric system as a function of the energy dissipation at junction  $B$  for a given heat exchanger.  $r$  is the ratio of the energy dissipated via light emission to the total energy dissipated ( $r=0$  represents the energy being dissipated by conduction only;  $r=1$  represents the energy being dissipated by radiation only)

where  $T_H$  and  $T_C$ , are the temperatures at hot and cold junctions, respectively.  $Z\bar{T}$  is the dimensionless thermoelectric figure of merit, and  $\bar{T}$  is the average temperature between  $T_H$  and  $T_C$ . At first glance, Eq. (21.2) appears to indicate that the COP of a thermoelectric device does not depend on  $Q_H$ . This may be valid in the ideal case where the temperatures can be maintained without any effort. In practice, a heat exchanger must be employed in contact with the hot side of the thermoelectric device to facilitate effective heat transfer. Consequently, the effectiveness of the heat exchanger has a significant effect on the overall COP of the thermoelectric system.

Figure 21.2 shows the COP of a thermoelectric device as a function of the energy to be dissipated at junction  $B$  for a given heat exchanger. The data was calculated by assuming that the required cooling temperature at junction  $A$  is  $0\text{ }^\circ\text{C}$  (i.e.,  $T_C=273\text{ K}$ ), the ambient temperature is  $20\text{ }^\circ\text{C}$  (i.e.,  $T_A=293\text{ K}$ ), and thermoelectric figure of merit  $Z=3.0\times 10^{-3}\text{K}^{-3}$ . A typical value of  $1.1\text{ K/W}$  is used for the thermal resistance of the heat exchanger, which represents a typical commercial heat sink of  $150\text{ mm}\times 150\text{ mm}\times 30\text{ mm}$  in size and dissipating thermal energy to the ambient by natural convection. The hot-side temperature of thermoelectric device is determined using  $T_H=1.1\times Q_H+293$ . The solid line in Fig. 21.2 represents the COP of a typical thermoelectric process, in which the energy at hot junction  $B$  is dissipated to the ambient by conduction via a heat exchanger. It can be seen that the COP of this thermoelectric cooling system decreases significantly with increasing heat dissipation power. The COP is 2.20 when the heat dissipation is 1 W, while it is only 0.22 if the heat dissipation increases to 50 W. This is due to a significant increase in  $T_H$  when heat flow through the heat exchanger is increased. Clearly,  $Q_H$  has an

indirect influence on the COP of a practical thermoelectric system. Although the COP may increase if a fan or a water circulation is used, this will lead to an increase in complexity of the system and additional power consumption to drive the fan or pump the water.

A possible approach to minimise  $T_H$  is to reduce the heat flow through the heat exchanger. In order to maintain the same cooling power  $Q_C$ , the same level of  $Q_H$  will be produced. However, it is possible to reduce the heat flow through the heat exchanger by channelling heat dissipation from junction  $B$  through two paths: conduction and radiation. Unlike in the usual thermoelectric process, the total energy dissipation  $Q_H$  consists of radiation  $Q_R = rQ_H$  and conduction  $Q_C = (1 - r)Q_H$  (where  $r$  is the ratio of the portion of energy dissipated by radiation,  $Q_R$ , to the total energy to be dissipated at junction  $B$ ,  $Q_H$ ). As shown in Fig. 21.1b, when an electron jumps to a lower energy level, the energy difference can produce either a phonon or a photon. The structure of a thermoelectric device does not normally encourage the generation of photons. Consequently, the energy difference converts into the lattice heat, which has to be dissipated through a heat exchanger. In principle, it is possible to design junction  $B$  of a thermoelectric device in a similar structure to that of a light emission diode, so that a portion of energy transported to junction  $B$  can be converted into light or infrared emission. Since the light or the infrared radiation can leave the thermoelectric material without the need for a heat exchanger, the heat flow through the heat exchanger can be reduced. In this case,  $T_H$  can be determined using  $T_H = 1.1 \times (1 - r)Q_H + 293$ .

The effect of photoemission on the COP of a thermoelectric system is shown by the dashed lines in Fig. 21.2. It can be seen that a reduction in the COP due to a large  $Q_H$  is less significant if a portion of the energy at junction  $B$  is converted into light or infrared radiation. The improvement is more significant for a large  $r$ . For example, with heat dissipation by conduction alone, the COP of the system reduces from 2.20 to 0.22 when  $Q_H$  increases from 1 to 50 W. However, if 80 % of the energy at junction  $B$  can be dissipated through radiation, the COP of the system will reduce to 1.17, which represents an improvement by a factor of 5. Clearly, heat dissipation through radiation can minimise COP reduction.

Although the structures of current thermoelectric devices do not encourage light emission, it is possible to design a hybrid structure consisting of thermoelectric cooling at one junction and light emitting at another, which could lead to a realisation of the “internal-cooling” laser [10–12] and light emission-assisted thermoelectric cooling [9]. The device structures and conditions that can facilitate light emission in a hybrid system were discussed. In addition, it was found that there exists a tipping point, at which thermoelectric cooling without hot junction can be realised [9]. This leads to the possibility of a novel device—CoolLED—to produce light and cooling.

In summary, the COP calculated using Eq. (21.2) represents the best-case scenario that can only be achieved by assuming an infinitely large heat transfer from thermoelectric device to the ambient. In the real world, these predicted values may be approached by using a heat sink that is significantly larger than the thermoelectric device or by employing a complex liquid heat exchanger, both of which would



seriously offset the advantages of thermoelectric devices. In reality, we have to employ a practical heat exchanger, which will have limited capability. Under such circumstances, the COP of a thermoelectric cooling system will decrease when increasing the cooling power required. The results of calculations obtained from this work demonstrate that the COP reduction due to large heat dissipation can be minimised by employing a thermoelectric device that can dissipate energy through light emission.

**Acknowledgements** The author wishes to acknowledge financial support from the ThermoMag Project, which is co-funded by the European Commission in the 7th Framework Programme (contract NMP4-SL-2011-263207), by the European Space Agency and by the individual partner organisations.

## References

1. Ioffe AF (1957) Semiconductor thermoelements and thermoelectric cooling. Infosearch, London
2. Rowe DM, Bhandari CM (1983) Modern thermoelectrics. Holt, Rinehart and Winston, London
3. Goldsmid JH (1986) Electronic refrigeration. Pion, London
4. Rowe DM (1996) CRC handbook of thermoelectrics. CRC, London
5. Mahan G (1998) Good thermoelectrics. *Solid State Phys* 51:81
6. Min G, Rowe DM (1999) Proceedings of 5th European workshop on thermoelectrics, Pardubice, Czech, 20–21 Sept 1999, p. 81
7. Mahan G, Sales B, Sharp J (1997) Thermoelectric Materials: New Approaches to an Old Problem. *Physics Today* 50(3):42–47
8. Tritt T (2000) Recent trend in thermoelectric material research (part 3), vol 70, *Semiconductor and semimetals*. Academic, New York, NY
9. Min G, Rowe DM (2007) Conditions for observing the thermo-electro-photo cooling effect. *IET Sci Meas Technol* 1(6):329
10. Dousmanis GC, Mueller CW, Nelson H, Petzinger KG (1964) Evidence of Refrigerating Action by Means of Photon Emission in Semiconductor Diodes. *Phys Rev* 133(1A):A316
11. Mal'shukov AG, Chao KA (2001) Opto-thermionic refrigeration in semiconductor heterostructures. *Phys Rev Lett* 86(24):5570
12. Pipe KP, Ram RJ, Shakouri A (2002) Internal Cooling in a Semiconductor Laser Diode. *IEEE Photon Technol Lett* 14(4):453

# Chapter 22

## Simulation of Power Management Electronics and Energy Storage Unit for MEMS Thermoelectric Generator

L. Janak, Z. Hadas, Z. Ancik, and P. Kopecek

**Abstract** This chapter deals with a simulation modelling of the complex energy-harvesting unit based on MEMS thermoelectric generator. This chapter is mainly focused into the first steps in a development process—analysis of demands given on the aircraft-specific thermoelectric harvesting unit, choice of energy storage elements, conceptual architecture of power electronics and simulation of various operating states based on the typical operating envelope. The whole simulation modelling process is implemented in MATLAB/Simulink Simscape. Commercially available thermoelectric modules produced by Nextreme Thermal Solutions, Inc. are used as the sources of energy. The raw power output coming out of each of these modules is in the range of tens of milliwatts. Special attention is paid to the choice of energy storage unit. Designs using supercapacitors and batteries as the electric energy storage elements are considered and evaluated. Several architectures of electronics are examined through the simulation modelling. The presented model represents an important step in the process of a mechatronic design of the complex aircraft-specific thermoelectric energy-harvesting unit.

**Keywords** Thermoelectricity • Thermoelectric generators • MEMS • Power management • Simscape • Simulink • MATLAB

---

L. Janak (✉) • Z. Hadas  
Faculty of Mechanical Engineering, Brno University  
of Technology, Technicka 2, 616 69 Brno, Czech Republic  
e-mail: [ludek.janak@gmail.com](mailto:ludek.janak@gmail.com)

Z. Ancik • P. Kopecek  
UNIS, a.s., Mechatronic & Embedded Systems,  
Jundrovska 33, 624 00 Brno, Czech Republic

## Introduction

Power management electronics plays a very important role in any energy-harvesting system. Harvested electric energy on the output terminals of an energy-harvesting module must be tailored for the use with a supplied device, and the use of an energy storage element is commonly required due to discontinuities in the flow of harvested energy. The power management electronics of energy-harvesting systems has to operate around the maximal harvesting point, known as the maximum power point tracking (MPPT). This feature is necessary due to the varying conditions in the used energy-harvesting system. In the case of thermoelectric generators (TEGs), the varying conditions are represented by the changes in an internal resistance of thermoelectric module [1].

The main aim of our work is the development of a thermoelectric energy-harvesting system for critical applications (e.g. aeronautics).

Application of TEGs as the energy-harvesting systems in aerospace applications is quite a new theme which has not yet been discussed too often apart from few examples [2–6]. Only a functional sample of aircraft-specific TEG was made by EADS [2]. The possible application of TEGs in aircraft-specific field is their use for powering the autonomous sensor nodes (ASN) for structural health monitoring (SHM) and powering the wireless sensors in general [4, 5]. In comparison with other energy-harvesting technologies, the main advantages for the use of TEGs in aviation are no movable parts which represent low demands on maintenance. The important point is also the presence of ideal conditions for thermal energy harvesting onboard—natural heat gradient on the surface of an aircraft. Other sources of heat gradient—engine, engine exhaust and heat from passengers—could also be taken into account.

The main obstacles in the aircraft-specific field are, of course, airworthiness and certification processes. But also in this field some progress is made. It is notable that the above-described TEG system built by EADS was successfully tested according to EUROCAE DO-160E avionic test regulations. Random vibration test and thermal cycling test in the temperature range of  $-65\text{ }^{\circ}\text{C}$  to  $125\text{ }^{\circ}\text{C}$  were carried out. The functioning of this energy harvester was also verified during test flight [3].

Our work aims at two main fields which are suitable for the application of thermoelectric energy harvesters. The first prospective application is a power supply for monitoring and diagnostic wireless sensor units. The further opportunity for using an autonomous energy source consists of a backup source for several applications. Our ideas are described in detail in the next chapter—Application Analyses.

## Application Analyses

Our simulation modelling analyses are focused on two cases: the fully autonomous wireless sensor system powered by TEG and the TEG implemented as a backup power source. The first case study shown in Fig. 22.1 represents the fully autonomous sensor system with wireless data transfer. This system may be physically interpreted as SHM solution or sensor of any various physical units (temperature, etc.).

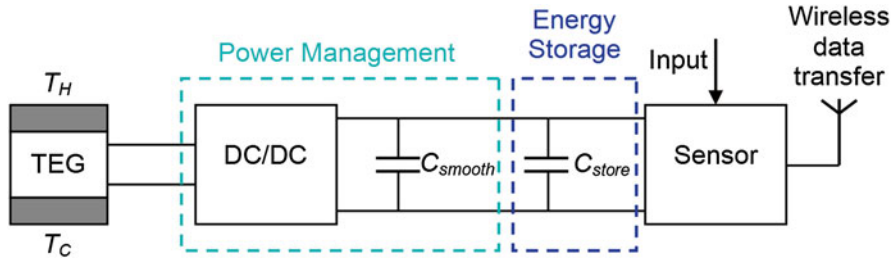


Fig. 22.1 Thermoelectric generator as a power source for the wireless sensor system

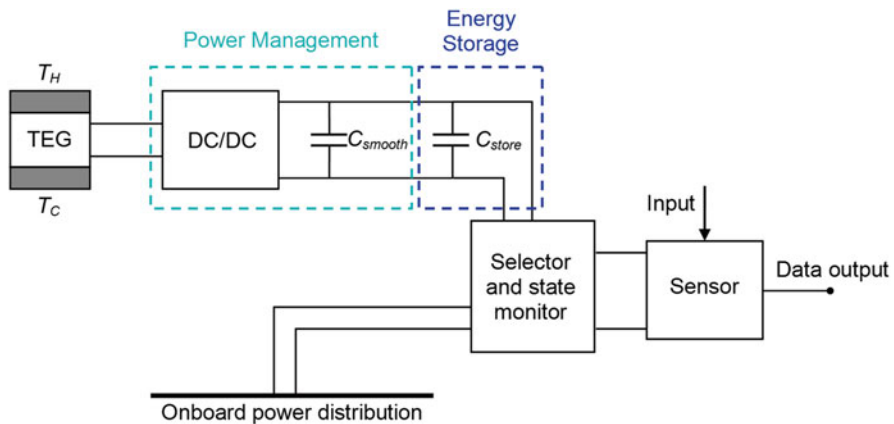


Fig. 22.2 Thermoelectric generator as a backup power source for sensor unit

The whole system consists of: TEG, power management electronics, energy storage unit, sensor with physical input and circuitry for wireless data transfer.

The power management is usually implemented as the integrated circuit (IC) based on boost, buck/boost or SEPIC DC/DC converter architecture. The power management usually includes a small capacitor to avoid output current ripples. This  $C_{smooth}$  capacitor is commonly chosen in the microfarads range. The energy storage unit (labelled as  $C_{store}$ ) is practically being realized with supercapacitors and thin-film or multiple-chemistry batteries. Architectures incorporating multiple types of the energy storage elements are also the subject of recent studies [6]. Data acquired by the sensor from its physical input are transmitted using wireless data transfer (e.g. ZigBee).

The second case is an implementation of backup power source into the onboard power distribution system of an aircraft. Topology of this application is similar to the above-mentioned case. The main difference could be observed in the selector and state monitor. This block is continuously monitors the operation state of main onboard power distribution line. The sensor is powered using the TEG only in the case of failure state in the power delivery. This approach is depicted in Fig. 22.2. The powered sensor system is connected via wired connection which conveniently enables to connect the data output in the same manner.

## Model Description

The model under consideration is implemented in MATLAB/Simulink Simscape. The power management electronics and energy storage unit parts are built of the objects from Electrical folder of Foundation Library and SimElectronics folder. The MEMS thermoelectric generator model is taken over the dynamic Simscape model previously published in [7, 8].

Input parameters to the previously built TEG model include thermal parameters (thermal masses and specific heats of module elements), electric parameters (internal resistance), geometry and thermoelectric parameters (Seebeck coefficient, number of thermocouples) of a TEG module. The boundary conditions for the simulation initialization are the temperatures of the hot and cold sides ( $T_H, T_C$ ).

Novel parts of the model—power management electronics and energy storage unit—are implemented using a grey-box modelling approach. The power management electronics equivalent circuit is based on an ideal boost converter. This converter is represented by voltage-controlled voltage source (*DC/DC converter*) with additional series of internal resistance  $R_{out DC/DC}$ . The converter is operated on the maximum power point mode (with matched impedance) which is ensured by the input voltage sensing on the matched load  $R_{in DC/DC}$ . The power electronics model is further formed of smoothing capacitor ( $C_{smooth}$ ) and *Voltage-Controlled Switch* representing the output undervoltage protection. Energy is accumulated in the  $C_{store}$  block designated to supercapacitor and thin-film or chemical battery. The powered sensor application is substituted by the *Variable Load* (variable resistor). The model topology in MATLAB Simulink Simscape is shown in Fig. 22.3.

The abovementioned approach represents a very rough idea of the nowadays commercially achievable energy-harvesting ICs. DC/DC converter is recently being physically realized as a buck, boost, buck/boost or SEPIC (single-ended primary-inductor converter) converter with MPPT. The selection of converter architecture is strictly dependant on the raw power output from a TEG module. The serial/serial-parallel/parallel combination of the fundamental MEMS TEG modules has to be

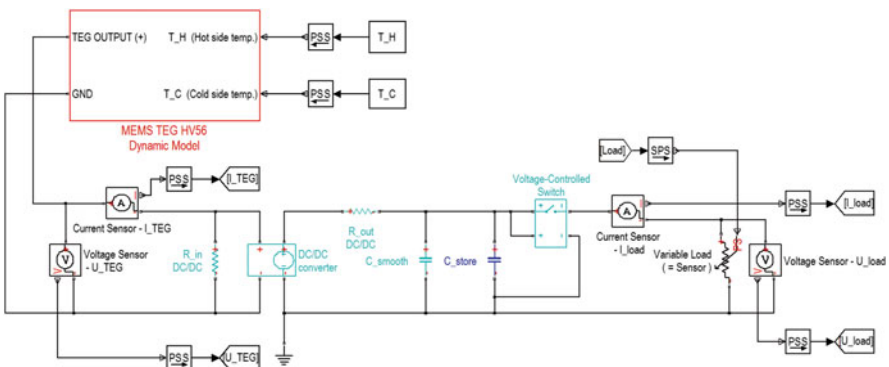
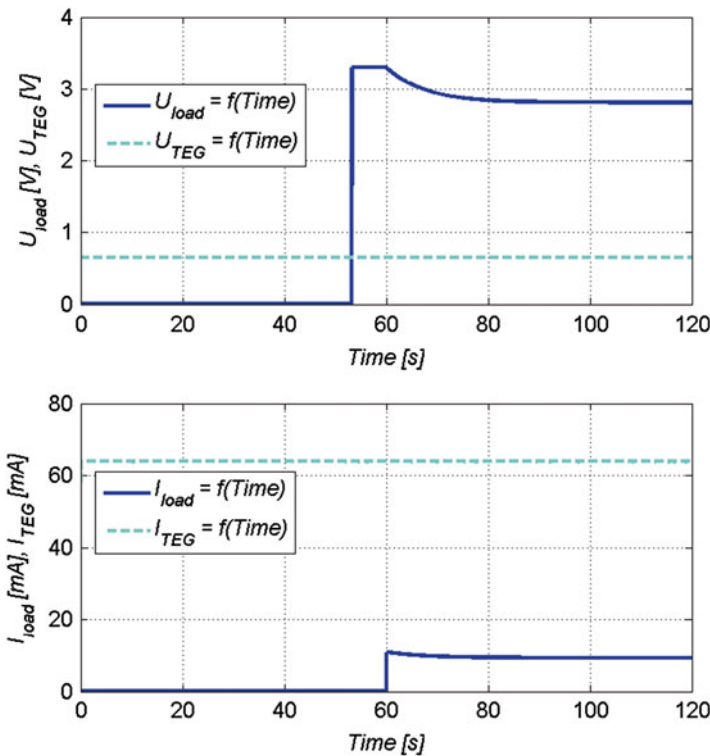


Fig. 22.3 Implementation of the power electronics and energy storage unit model in Simscape

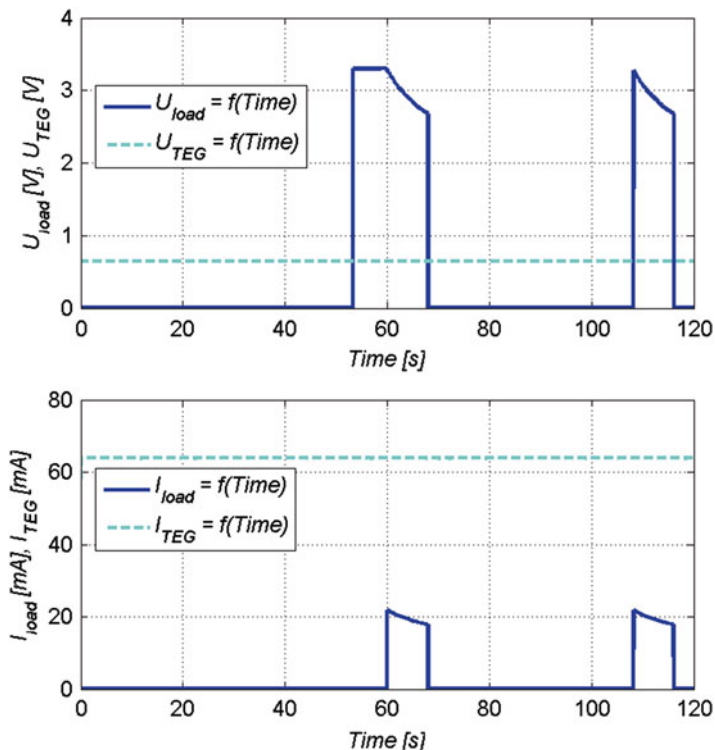
taken into account concurrently with the power electronics architecture. This approach enables the formation of a synergistic effect in the thermoelectric energy-harvesting system.

### Simulation Results

Simulations of the abovementioned model were firstly performed with the single MEMS TEG Nextreme HV56 [9]. The set temperature difference was 50 °C while the temperatures of hot and cold sides were 75 ( $T_H$ ) and 25 °C ( $T_C$ ) respectively. The voltage gain of the boost converter was set to obtain the output voltage of 3.3 V which is currently mostly used in microprocessor systems. The  $C_{store}$  was considered as the supercapacitor with capacity of 1 F. Voltages and currents on the input terminals of DC/DC converter and on the powered application (load) resulting from the simulations are depicted in Figs. 22.4 and 22.5.



**Fig. 22.4** Results—in  $Time=60$  s was applied an electric load of 300  $\Omega$ , which represents the current consumption of 10 mA. Plotted values include the  $U_{load}$  (voltage on load),  $U_{TEG}$  (voltage on the output terminals of TEG),  $I_{load}$  (current through the load) and  $I_{TEG}$  (current intake to the DC/DC converter)



**Fig. 22.5** Results—in  $Time = 60$  s was applied an electric load of  $150 \Omega$ , which represents the current consumption of 20 mA. Plotted values include the  $U_{load}$  (voltage on load),  $U_{TEG}$  (voltage on the output terminals of TEG),  $I_{load}$  (current through the load) and  $I_{TEG}$  (current intake to the DC/DC converter)

Figure 22.4 shows the situation when the load is turned on using step function after 60 s of operation. The applied electric load of  $300 \Omega$  represents the current consumption of 10 mA at the voltage of 3.3 V.

Figure 22.5 shows the situation when the load is turned on using step function after 60 s of operation. The applied electric load of  $150 \Omega$  represents the current consumption of 20 mA at the voltage of 3.3 V. The power delivery in this state is discontinuous. The storage capacitor has the satisfactory voltage over the 25 % duty cycle.

## Conclusion

Typical operating states of TEG with power conditioning electronics and energy storage unit were examined through the simulation modelling. Despite the fact that presented simulation model contains only a very rough description of the final circuitry, useful data were obtained.

Based on the achieved results, it was decided to continue with the development of an energy storage unit based on supercapacitors. The unit made of supercapacitors is mainly considered for the use with TEG backup solution (Fig. 22.2). By the simulation results (Figs. 22.4 and 22.5) it was proven that the power delivery of tens of milliamps on the voltage of 3.3 V is achievable for time periods of seconds to tens of seconds. Several parallel/serial/serial-parallel combinations of MEMS TEG modules will be considered for the prototype of backup TEG unit.

Thin-film batteries and other miniaturized batteries with modern chemistries are of interest for the highly integrated autonomous wireless sensors with ultralow power (ULP) electronics.

The power electronics stage for the single MEMS TEG module will be designed using boost architecture accordingly to our step-up converter simulation model. The SEPIC architecture may be considered for the application with multiple-parallel/serial/serial-parallel combinations of MEMS TEGs. These configurations provide higher output voltages. ICs integrating the needed boost or SEPIC functions are nowadays commercially achievable through the worldwide electronic component retailers.

Bottlenecks of the Simscape simulation include the limited electrical element library. It is connected with the necessity of many assumptions and simplifications during the modelling process. The solution for the more precise simulations may be the wider implementation and support for the SPICE blocks in Simscape. From today's perspective, the only possibility to simulate the complex energy harvesting is by the use of SPICE circuit simulators.

**Acknowledgements** This work has been supported by the project “Complex Affordable Aircraft Engine Electronic Control (CAAEEC)” TA02010259 under the Technology Agency of the Czech Republic.

## References

1. Priya S, Inman DJ (2009) Energy harvesting technologies. Springer, New York, NY, pp 337–351
2. Samson D, Otterpohl T, Kluge M, Schmid U, Becker TH (2010) J Electron Mater. doi:[10.1007/s11664-009-0997-7](https://doi.org/10.1007/s11664-009-0997-7)
3. Samson D, Kluge M, Fuss T, Schmid U, Becker TH (2012) J Electron Mater. doi:[10.1007/s11664-012-1928-6](https://doi.org/10.1007/s11664-012-1928-6)
4. Featherston CA, Holford KM, Pullin R, Lees J, Eaton M, Pearson M (2013) Proc SPIE. doi:[10.1117/12.2018401](https://doi.org/10.1117/12.2018401)
5. Becker TH, Kluge M, Schalk J, Tiplady K, Paget CH, Hilleringmann U, Otterpohl T (2009) IEEE Sens J. doi:[10.1109/JSEN.2009.2028775](https://doi.org/10.1109/JSEN.2009.2028775)
6. Thangaraj K, Elefsiniotis A, Aslam S, Becker TH, Schmid U, Lees J, Featherston CA, Pullin R (2013) Proc SPIE. doi:[10.1117/12.2017691](https://doi.org/10.1117/12.2017691)
7. Janak L, Ancik Z, Hadas Z (2013) Mechatronics 2013. doi:[10.1007/978-3-319-02294-9\\_34](https://doi.org/10.1007/978-3-319-02294-9_34)
8. Ancik Z, Vlach R, Janak L, Kopecek P, Hadas Z (2013) Proc SPIE. doi:[10.1117/12.2017134](https://doi.org/10.1117/12.2017134)
9. Nextreme HV56 Datasheet. [http://www.nextreme.com/media/pdf/techspecs/Nextreme\\_eTEG\\_HV56\\_Data\\_Sheet.pdf](http://www.nextreme.com/media/pdf/techspecs/Nextreme_eTEG_HV56_Data_Sheet.pdf). Accessed 27 Oct, 2013



# Chapter 23

## Experimental Validation of a Multiphysics Model for the Optimization of Thermoelectric Generators

C. Favarel, J.P. Bedecarrats, T. Kousksou, and D. Champier

**Abstract** Energy harvesting from waste heat is an important goal. Exhaust gases and combustion gases are typical sources of waste heat that can be converted into electricity by the proper use of thermoelectric generators (TEG). A multiphysics computer model which simulates performances of the whole thermoelectric (TE) systems has been developed with Matlab®. By using a combined genetic/Newton-Raphson algorithm applied to this model, the produced electrical power is maximized optimizing both the occupancy rate and the currents for different operating points of TEG (hot gas temperature and airflow rate).

To validate both the code and the optimization, an experimental loop was designed including a hot gas source, a cold fluid sink and a TEG composed of a hot fin exchanger, tubular cold exchangers and a flexible number of thermoelectric modules have been designed. Two designs have been tested: one with the hot exchanger partially covered by TE modules and the other with the hot exchanger completely covered. Open-circuit voltage measurements on the TEG have been carried out first. Specific MPPT (maximum power point tracker) DC/DC converters developed by the laboratory have also allowed us to complete the study of the TEG with a generator loading a battery. The comparison between experimental results and the model will be presented. The influence of the occupancy rate is studied by varying both the airflow rate and the hot inlet gas temperature. This experiment shows the interest in optimizing the occupancy rate to maximize the produced electrical power.

---

C. Favarel (✉) • J.P. Bedecarrats  
Laboratoire de Thermique, Energétique et Procédés,  
Université Pau & Pays Adour, LaTEP – EA 1932, ENSGTI,  
Rue Jules ferry, BP 7511, PAU 64075, France  
e-mail: [camille.favarel@univ-pau.fr](mailto:camille.favarel@univ-pau.fr)

T. Kousksou • D. Champier  
Laboratoire des Sciences de l'Ingénieur Appliquées à la  
Mécanique et au Génie Electrique (SIAME), Université Pau & Pays Adour,  
Hélioparc 2, avenue du Président Angot, 64053 Pau Cedex, France

**Keywords** Numerical simulation • Occupancy rate • Power generation • Thermoelectric generator • Experimental validation

## Introduction

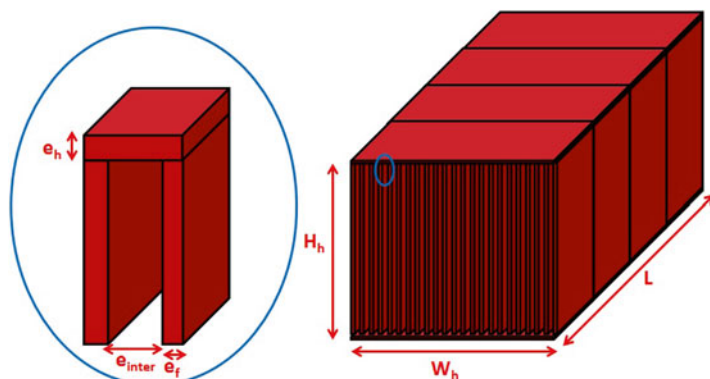
Thermal losses are everywhere [1–3], so there is a major interest in TEG modelling in order to determine whether it is appropriate or not to install a TEG. Moreover, the optimization of TEGs is facilitated by estimating the electrical production of a TEG.

On a previous paper [4], a numerical model was described highlighting the interest of optimizing a new parameter called the occupancy rate  $\tau$ . The aim of the proposed experiment is to compare the first experimental results with the model and to show the principal trends. The influence of the occupancy rate is studied using two different designs with the same exchanger but with different quantities of TE modules.

## Description of the Experimental System

### *Elements of the TEG*

The TEG is composed of thermoelectric modules sandwiched between a hot fin exchanger and a cold heat exchanger. The hot side heat exchanger (Fig. 23.1) collects and transfers the thermal power from the hot gas stream through the thermoelectric modules. It is built with an assembly of fins (thickness  $e_f$ ) separated by a space  $e_{inter}$ . The thickness of the base of the exchanger is  $e_h$ . The global dimensions of the exchanger are given in Table 23.1. It is made of aluminium 6063. Hot gas (air)



**Fig. 23.1** Geometry of the heat exchanger

**Table 23.1** Dimensions of the heat exchanger

Dimension	Symbol	Value
Height	$H_h$	0.118 m
Length	$L$	0.294 m
Width	$W_h$	0.125 m
Fin thickness	$e_f$	1.56 mm
Thickness of the exchanger walls	$e_h$	0.01 m
Distance between adjacent fins	$e_{inter}$	0.004 m

**Fig. 23.2** Photograph of the experimental TEG

circulates inside this tube. The cold heat exchanger is tubular with an inner diameter of  $D_c$  and a thickness of  $e_c$ . Thermoelectric modules available on the market [5] are used and their thermoelectric properties have been previously characterized. The whole system is divided into four slices in the direction of the hot heat flux as shown in Fig. 23.1. Each slice has one or two modules on each side connected electrically in series. A picture of the experimental TEG is shown in Fig. 23.2.

### ***TEG Designs***

Two designs of the TEG, represented in Fig. 23.3, have been tested, one with the hot exchanger partially covered and the other with the hot exchanger almost completely covered. The occupancy rate  $\tau$  is defined for each slice as the ratio of the area

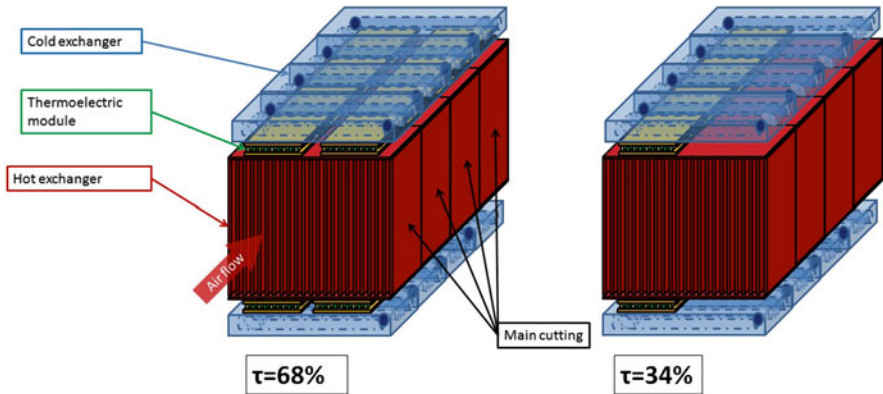


Fig. 23.3 Illustrations of two TEG designs with covered areas of 68 and 34 %

occupied by the TE modules (Si) on the area of a slice of the heat exchanger ( $SH = W_h \times L/4$ ). For the partially covered design,  $\tau = 34\%$  and for the almost completely covered,  $\tau = 68\%$ .

For each design a series of experiments at different operating points have been performed. A series at low hot inlet temperature and another at high hot inlet temperature of the gas have been done. In each series, three airflows have been tested: low (from 40 to 55 m<sup>3</sup>/h), intermediate (from 75 to 90 m<sup>3</sup>/h) and high (over 120 m<sup>3</sup>/h).

The open voltages generated by the modules were measured in a first experiment, and the output power produced by the TEG was measured in a second experiment. For the last experiment, specific DC/DC converters with MPPT (maximum power point tracking) have been developed in order to maximize in real time the electrical power extractable from the modules. These converters adapt the electrical power of the TEG for a lead-acid battery of 12 V 12 Ah.

## Results and Discussion

First of all, the temperature profile along the exchanger for an airflow rate of about 124 m<sup>3</sup>/h and a hot inlet temperature of 200 °C is represented. The chosen design is the partially covered one ( $\tau = 34\%$ ).

The curves plotted in Fig. 23.4 represent the different temperature profile of the model, where  $T_H$  and  $T_C$  are, respectively, the hot gas and cold fluid temperatures,  $T_{H,wall}$  and  $T_{C,wall}$  are, respectively, the hot and cold temperatures of the exchangers just before the module's ceramic, and  $T_{H,mod}$  and  $T_{C,mod}$  are, respectively, the hot and cold temperatures of the TE material inside the module. The first red dotted line represents the hot air temperature profile in the divergent at the inlet of the TEG. The second red dotted line represents the hot air temperature profile in the convergent at the outlet. For these two dotted lines the distance on the  $z$ -axis is not respected.

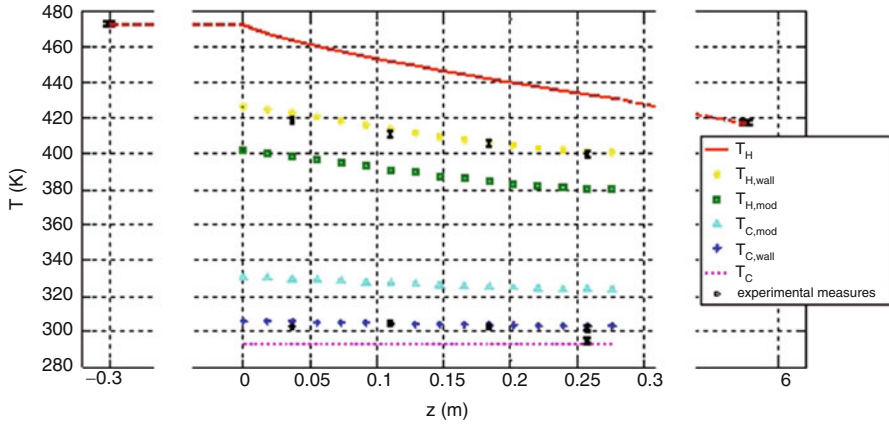


Fig. 23.4 Temperature profiles at different positions in the TEG along the flow direction

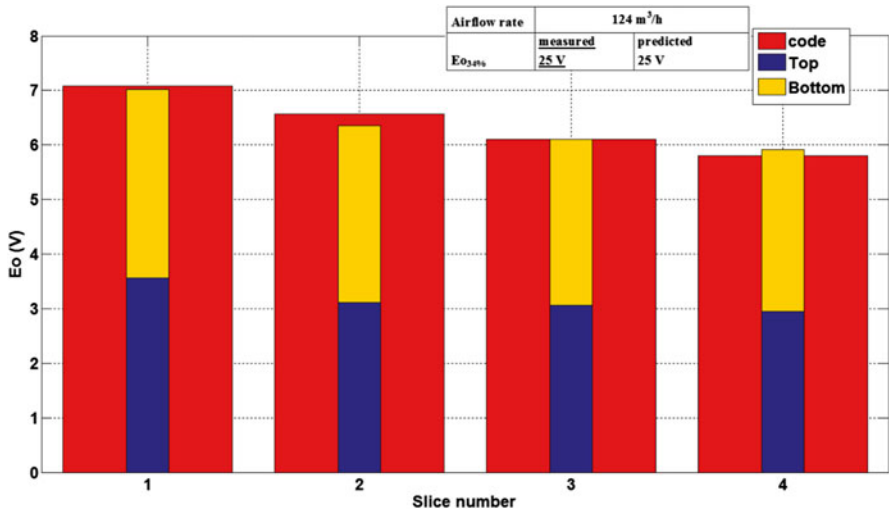


Fig. 23.5 Open-circuit voltages for different sections of the TEGs

The experimental points are represented by crosses with its error bars of  $\pm 1.5$  °C. For wall temperature each experimental point is the average of the wall temperatures measured at the module level. The temperature of the hot gas was also measured at the inlet and at the outlet of the hot heat exchanger. The temperature of the cold fluid was set to 20 °C for the inlet and was measured for the outlet. The hot inlet gas temperature is an input parameter of the model. Firstly, we can notice that the hot outlet temperature prediction is very accurate. All the other predicted temperatures are in agreement with the experimental ones.

Figure 23.5 shows the open voltage for this experiment. The red value is the code prediction whereas the stacked values represent the open-circuit voltage measured

**Table 23.2** Measured and predicted open-circuit voltages for different airflow rates

Airflow rate	41 m <sup>3</sup> /h		78 m <sup>3</sup> /h		140 m <sup>3</sup> /h	
	<u>Measured</u> (V)	Predicted (V)	<u>Measured</u> (V)	Predicted (V)	<u>Measured</u> (V)	Predicted (V)
Eo <sub>34 %</sub>	<u>17</u>	20	<u>23</u>	24	<u>27</u>	26
Eo <sub>68 %</sub>	<u>21</u>	28	<u>32</u>	37	<u>41</u>	42

**Table 23.3** Measured and predicted powers for the two TEG designs

	<u>Measured</u> (W)	Predicted (W)
Pe <sub>34 %</sub>	<u>17</u>	19
Pe <sub>68 %</sub>	<u>17</u>	16

for each single module located by the slice number, top or bottom. Again the predicted data by the model match quite well with the experimental ones for this operating point.

Table 23.2 presents both the experimental and numerical results at the different operating points. The bold underlined values are related to the experiment whereas the others are given by the code. The open voltages of the experiment and the code are both presented. It must be underlined that it is not relevant to compare directly the open voltages for making conclusions on the electrical power. Trying to calculate the power output from these open voltage measurements would be a mistake because the effects of the current in the temperature distribution are neglected.

At high airflow rate, the predictions of the open voltage match very well with the measurement. At intermediate airflow rate only the open voltage of the 34 % design is well predicted whereas for the 68 % design the model is a little optimistic. At low airflow rate the prediction are too high, so the correlation used to calculate the heat transfer coefficient needs to be refined particularly at low airflow rate where the heat exchanges are low.

The first results with load are presented in Table 23.3. The airflow rate was 59 m<sup>3</sup>/h and the hot inlet temperature was 197 °C.

We can notice that the two values of power are the same. Nevertheless, one is obtained with half the modules. This shows the economical interest of the optimization. Regarding the code prediction, we can say that it is quite accurate with a slightly better prediction for the  $\tau = 34$  % design.

## Conclusion

The purpose of these first experiments is to investigate the influence of operating parameters on the electrical generation with TE modules and to make a first comparison with a multiphysics model.

Two designs have been tested for different operating points. We show that the numerical model is accurate enough to predict the trends, but it needs to be

improved to determine the real value of the electrical power produced and the real temperature profile.

It is necessary to improve the occupation of the modules because covering completely the heat exchanger surface with TE modules is not always the best solution.

**Acknowledgements** This work was carried out within the framework of a project whose objective is to study the feasibility of producing electricity with thermoelectric modules in various applications. It is funded in part by the Regional Council of Aquitaine and the General Council of Aquitaine (France).

## References

1. Francioso L, De Pascali C, Farella I, Martucci C, Cretì P, Siciliano P, Perrone A (2011) Flexible thermoelectric generator for ambient assisted living wearable biometric sensors. *J Power Sources* 196(6):3239–3243
2. Zheng XF, Yan YY, Simpson K (2013) A potential candidate for the sustainable and reliable domestic energy generation—Thermoelectric cogeneration system. *Appl Therm Eng* 53(2): 305–311
3. Champier D, Bédécarrats JP, Kousksou T, Rivaletto M, Strub F, Pigolet P (2011) Study of a TE (thermoelectric) generator incorporated in a multifunction wood stove. *Energy* 36(3): 1518–1526
4. Favarel C, Bedecarrats JP, Kousksou T, Champier D (2012) The influence of operating parameters and occupancy rate of thermoelectric modules on the electricity generation. ECOS 2012 congress, Perugia, Italy, 26 Jun 2012
5. Technical data sheet: Thermonamic products. Available at <http://www.thermonamic.com/TEHP1-12656-0.3-English.pdf>. Accessed 18 Dec 2013

# Chapter 24

## Electrical and Configuration Characterization of Thermoelectric Generator Modules

M.A. Ashari, A.A. Abd. Rahman, and S. Sulaiman

**Abstract** Many electrical appliances and machinery emit wasted heat during their nominal functions. From heavy machinery to laptops and personal desktop computers, a significant amount of heat is dissipated during operation and even more during processing times. Thermoelectric generators (TEGs) can convert this waste heat into electricity. In order to be able to harvest energy efficiently, the need to understand the behavior of current existing thermoelectric modules is essential as it is for the implementation or application of a TEG in various scenarios. This paper describes the electrical characteristics of a typical TEG module that has undergone a series of parameter settings using an in-house and cheap solution jig. The jig evaluation was done to understand the configuration and parameters needed for the TEG module to perform at its best during applications. To obtain optimum performance from the TEG module, it is important to address several key points and identify the cause that will affect the module performance. Once the characteristic of the TEG module is analyzed and understood, it allows the design of the integration circuit to be more appropriate. Therefore this will allow a more sustainable and feasible platform of the Wireless Sensor Network when a TEG module is integrated inside the systems. The TEG module that was used in the experiments is from Hi-Z Technology Inc., model HZ-2. Among all of the Hi-Z Technology modules, this model produces the highest possible output with the lowest  $\Delta T$ .

**Keywords** Energy harvester • Thermal equilibrium • Thermoelectric generator module • Wireless sensor networks

---

Author contributed equally with all other contributors.

M.A. Ashari (✉) • A.A.A. Rahman • S. Sulaiman  
Department of Micro-Energy & Green Technology, MIMOS Bhd., Kuala Lumpur, Malaysia  
e-mail: [asri.ashari@mimos.my](mailto:asri.ashari@mimos.my); [airul@mimos.my](mailto:airul@mimos.my)



## Introduction

Green energy harvesting (power harvesting or energy scavenging) is a process in which energy is derived from external energy sources (such as solar power, thermal energy, wind energy, salinity gradients, and kinetic energy), captured, and stored into usable electrical energy. Nevertheless, the scope of green technology consists of using renewable energy without negative impacts on human involvements. By using green technology, the energy will be harvested and stored without the usage of hazardous materials that are either poisonous or pollute the environment. The existing green technology can provide enough power for small power consumption devices for WSN (Wireless Sensor Network) applications. For example, when using this technology the sensor node is targeted to be able to survive with very minimal maintenance with no requirement to change battery or energy storing part when integrated with any of the green technology devices such as thermoelectric or solar panels.

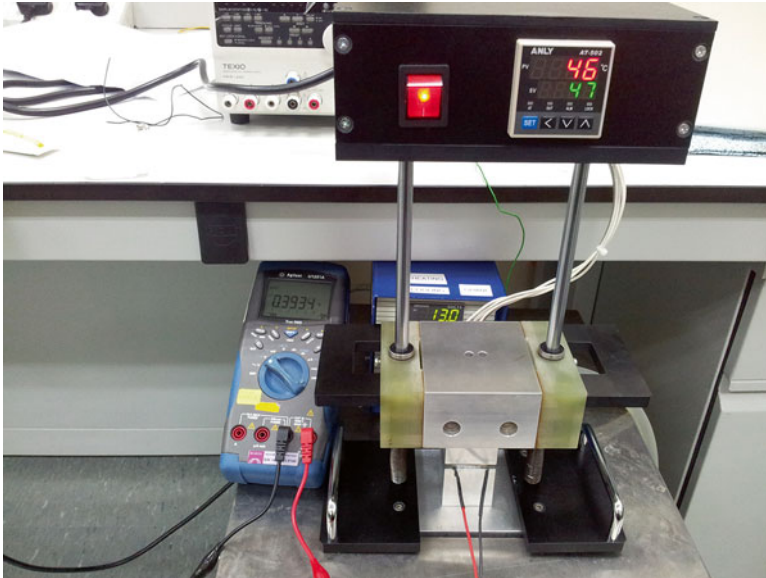
A thermoelectric based micro-power generator becomes an available energy supply to electronic devices that consume electrical power in the ranges of micro-watt ( $\mu\text{W}$ ). On the other hand, it was reported that waste heat available in ambient is one of the main sources of energy harvesting and that this can be converted to electrical energy to power up the electronic circuitry [1].

Newer technology is arising whereby a thermoelectric semiconductor-based module is able to generate electricity by experiencing a significant amount of temperature difference on the opposite surface of a P-N junction semiconductor. Recent advancements of semiconductor material technology have made highly efficient thermoelectric energy harvesting a practical reality [2]. The TEG module generates relatively small power density output in comparison to other technology modules of similar size like, for example, solar panels. This paper studies the behavior of TEG modules analysing both single and multiple units connected in series or parallel to help understanding the characteristic behavior of these modules during application.

The HZ-2 module investigated here consists of 97 thermocouples arranged electrically in series and thermally in parallel. The thermocouples consist of "Hot Pressed," bismuth telluride-based semiconductors to give the highest efficiency at generally applicable waste heat temperatures as well as high strength capable of enduring rugged applications [3]. In order to obtain satisfactory performance, it is observed that certain details must be taken care of during testing and measurements of the modules. Understanding both the setup of the jig and the best method to test the module will ultimately assist in designing a more efficient apparatus.

## Apparatus for Characterization

The interface between the module and the heat source and the interface between the module and the heat sink are very critical components of any thermoelectric system [2]. The TEG module needs to be compressively loaded between the heat source and

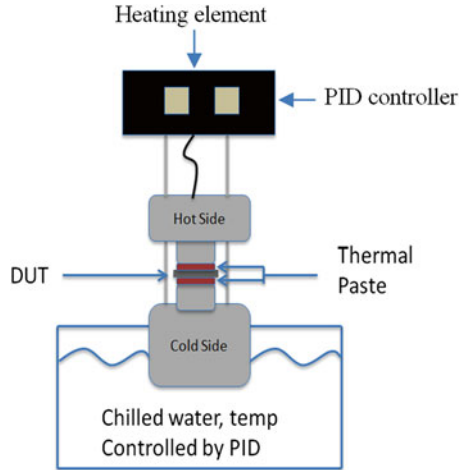


**Fig. 24.1** Apparatus used to characterize TEG module using PID controller with water bath and heating element

the heat sink. This is to ensure uniform load over the surface of the module for optimum power performance and to maximize the heat transfer across the interface [4]. Figure 24.1 illustrates a low-cost thermoelectric module characterization apparatus. It consists of a PID (Proportional-Integral-Derivative) controller connected to a heating element. The DUT (device under test) is compressively loaded in between the two aluminum blocks, with a layer of thermal paste for evenly distributed thermal conductivity between the aluminum block and the DUT. The upper block is connected to a heating element, which is controlled by the PID controller. The user can monitor and control the temperature of the upper block in order to generate the intended “hot side” temperature.

The “cold side” is generated by dipping the aluminum block of the apparatus’ lower part into a water bath as shown in Fig. 24.2 with the temperature setting being controlled by the water bath’s PID controller. Two PID controllers are used in this test set up: one for the “hot side” and one for the “cold side” (i.e., water bath). The “thermal interface” blocks are the two smaller aluminum blocks that are in contact with the DUT. These blocks are interchangeable by the user who wishes to evaluate a single/smaller module or many/larger modules simultaneously, whichever fits the desired configuration.

**Fig. 24.2** Diagram of the TEG module characterization apparatus



## Precautions and Suggested Method

The handling of this apparatus would require certain precautions in its setting up steps in order to maintain its accuracy within the desired limits. The apparatus is acknowledged for lack of vacuum in its area of experimentation. The humidity in the air also affects temperature consistency. Therefore, a vacuum chamber is planned to be installed for temperature stabilization at the cold-side area in order to avoid temperature interference and fluctuations during measurement. Precaution steps needed to be taken care of when using this apparatus are the following:

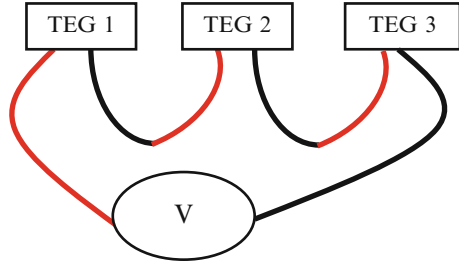
1. Use thermal insulator paste. This ensures proper contact between the aluminum block and DUT for even thermal conductivity by filling the voids in the interface that are caused by irregular surfaces. At microscopic level the surface of both materials is not totally flat.
2. Apply strong compressive load between the DUT, with the upper “hot-side” aluminum block and lower “cold-side” aluminum block. Strong contact will ensure uniform load and better thermal conductance.
3. It takes approximately 10–15 min to stabilize the temperature once the intended temperatures are reached.

## Test, Results, and Measurements

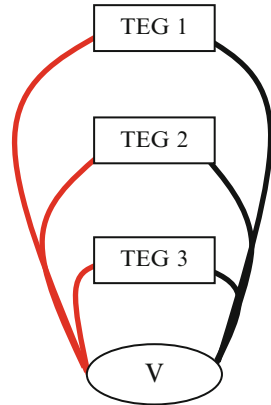
Thermoelectric elements generate power when temperature gradient is available. The thermoelectric module contains thermoelectric material that makes use of the Seebeck effect to produce electricity:

$$V_{\text{Open Circuit Voltage}} = (\alpha_{\text{pn}}) \times (T_{\text{H}} - T_{\text{C}}) \quad (24.1)$$

**Fig. 24.3** Three TEG modules connected in series configuration



**Fig. 24.4** Three TEG modules connected in parallel configuration



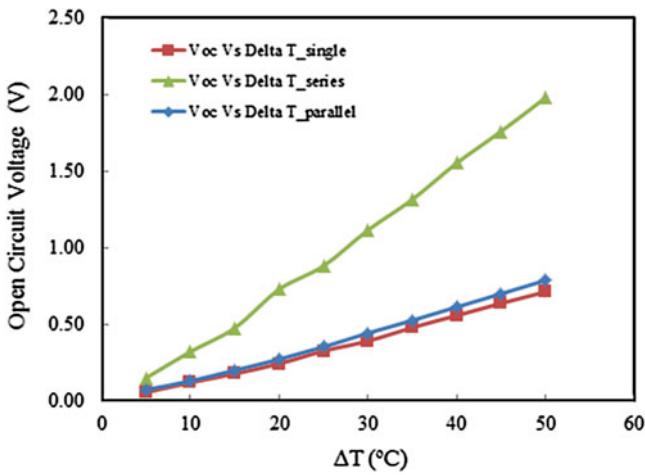
- $\alpha_{pn}$  = Seebeck coefficient of thermoelectric element.
- $T_H$  = Temperature at hot junction of thermoelectric element.
- $T_C$  = Temperature at cold junction of thermoelectric element.

Maximum power is at half of the open-circuit voltage. A larger temperature difference will produce higher voltage. High voltage will result in higher maximum power and higher current at match load. When different temperature is applied between the top and bottom surfaces of the thermoelectric module, the module will generate a certain amount of electrical voltage output. The characterization of this output will enable users to design integration circuits which ultimately enable the energy harvesting at its most optimum rate.

The recorded parameters were based on the intended application of the TEG module, i.e., integrate to a WSN mote and harvest energy from ambient versus water surface. The temperature gradient was measured up to 50°, with 5° increment. After reaching the intended temperature, its stabilization must be reached first before taking any measurement. The output of the module can be measured using a voltmeter or a data logger. There are a few configurations that are taken into account to understand more of the nature of the Bi<sub>2</sub>Te<sub>3</sub> based thermoelectric generator modules. Data tabulation Voc, Isc and total power output for temperature gradient of 5 until 50 °C for single TEG module, three TEG modules in series configuration (Fig. 24.3), and three TEG modules in parallel configuration (Fig. 24.4) are shown in Table 24.1.

**Table 24.1** Voltage and current produced by the three thermoelectric modules connected in series and parallel configuration

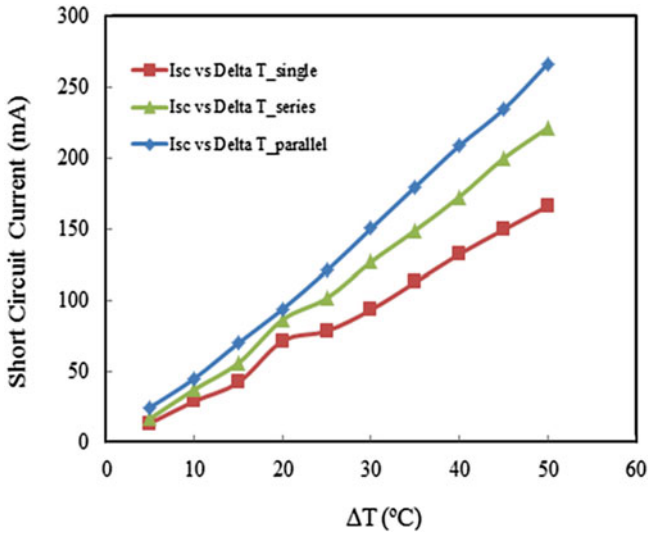
Hot side (°C)	Cold side (°C)	$\Delta T$	Single		Series		Parallel	
			Voc	Isc (mA)	Voc	Isc (mA)	Voc	Isc (mA)
30	25	5	0.056	13.3	0.1499	16.7	0.0738	24.50
30	20	10	0.1197	28.8	0.3217	37.1	0.1303	44.80
30	15	15	0.1773	42.2	0.4766	55.8	0.2004	69.80
30	10	20	0.243	71.23	0.7287	86.26	0.2724	93.70
35	10	25	0.3261	78.3	0.8818	101.3	0.3530	120.60
40	10	30	0.3913	93.22	1.1153	126.7	0.4430	150.06
45	10	35	0.4793	112.5	1.3154	148.74	0.5260	179.40
50	10	40	0.5579	132.1	1.553	172.42	0.6130	208.44
55	10	45	0.6376	149.2	1.7603	199.4	0.6995	234.00
60	10	50	0.712	165.8	1.9802	220.94	0.7869	266.20



**Fig. 24.5** Open-circuit voltage versus delta T of 5 until 50 °C for single TEG module, three TEG modules in series configuration, and three TEG modules in parallel configuration

First part of the experiment was to measure the output of a single TEG module. The TEG was inserted into the apparatus with the precautions taken and the reading was recorded with the lowest degree of voltage reading output fluctuation.

The results observed from testing show that output voltage is generated linearly with temperature differences between hot and cold surfaces. Based on the data taken in Table 24.1 and plotted in Figs. 24.5 and 24.6, connecting the modules in series will produce the highest open circuit voltage output compared to parallel configuration. The data also show that, as the temperature gradient increases, the open circuit voltage and the short-circuit current increase proportionally.



**Fig. 24.6** Short-circuit current versus delta T of 5 until 50 °C for single TEG module, three TEG modules in series configuration, and three TEG modules in parallel configuration

## Conclusion

This paper shows the electrical behavior of TEG modules when used singularly, in series configuration, and in parallel configuration. This paper also describes the best methods, apparatus, and precaution steps taken during data acquisition of the results.

## References

1. Jin X, Chengkuo L, Hanhua F (2010) Design, fabrication and characterization of CMOS MEMS-based thermoelectric power generators. *J Microelectromech Syst* 19(2):317–324
2. Vining C (2001) Semiconductors are cool. *Nature* 413:577–578
3. Hi-Z Technology Inc. Available at <http://www.hi-z.com/hz2.php>
4. Leavitt FA, Elsner NB, Bass JC (1996) Use, application and testing of the HZ-14 thermoelectric module. 15th international conference on thermoelectrics. pp. 378–382. <http://www.hi-z.com/uploads/2/3/0/9/23090410/hz-2.pdf>

# Chapter 25

## Modelica<sup>®</sup> Library for Dynamic Simulation of Thermoelectric Generators

M. Nesarajah, L. Exel, and G. Frey

**Abstract** The contribution presents a new modeling library for the dynamic simulation of thermoelectric generators (TEG) in 1D spatial resolution. The core of the library is a model of the thermoelectric legs (TEL), which has already been published by the authors. In the submitted work, this model is expanded to an overall Modelica<sup>®</sup> library for complete TEGs. The library is open source and can be extended. It is also usable by end users without deeper knowledge through a graphical user interface (GUI). The use of the library is illustrated by the example of an electronic thermostat valve powered by a TEG.

**Keywords** Thermoelectric generators • Modelica library • Simulation • Modeling

### Introduction

The presented TEG library is implemented in the open modeling language Modelica [1], which is a component-oriented modeling language. It allows a structure-preserving way of modeling complex physical systems by direct use of ordinary differential equations (ODE) and differential algebraic equations (DAE). A further advantage is the reusability of components, supported by graphical model diagrams on distinct hierarchical levels.

The library assumes that each side of the TEG has a uniform temperature resulting in a one-dimensional modeling. The dynamics of the TEG is modeled thermally transient, electrically static (no electrical capacities are considered), and electronically static (charge displacement without delay). The following section gives an

---

M. Nesarajah (✉) • L. Exel • G. Frey  
Chair of Automation, Saarland University, Saarbrücken, 66123, Germany  
e-mail: [marco.nesarajah@aut.uni-saarland.de](mailto:marco.nesarajah@aut.uni-saarland.de); [lukas.exel@aut.uni-saarland.de](mailto:lukas.exel@aut.uni-saarland.de);  
[georg.frey@aut.uni-saarland.de](mailto:georg.frey@aut.uni-saarland.de)

outline of the library, the section “Implementation and Modeling Details” discusses some implementation details, and finally the section “Simulation Example” illustrates the use of the library via a small example.

### Library Overview

The structure of the library is given in Fig. 25.1 (right). The top-level model of a complete TEG (TEG\_Module, Fig. 25.1) uses further models from four sub-packages. It reflects the concept of component-oriented modeling, whereas the model of connected TELs (CTEL) is in the center, surrounded by ceramic plates. The library contains several more or less detailed models of CTEs in the sub-package INNER\_TEG. All CTEL models are derived from one base class (CTEL\_base). This base class defines the connectors of the components (see Fig. 25.1). By means of this modeling concept, the user of the library can select the appropriate CTEL model used by the TEG\_Module easily. The simple model CTEL\_1D\_static neglects the dynamic thermal behavior of the TELs and uses an average leg temperature for the calculation of the thermoelectric voltage. More complex models (e.g., the CTEL\_1D\_dyn\_seq) consider the dynamic thermal behavior and use a spatial discretization to model the electrical and thermal behavior more accurately. A model which includes the electrical and thermal effects of the bonds connecting the TELs is also available. The parameters of the CTEL models (e.g., the length of the TELs) the number of thermocouples or the TE material, are adjustable via a GUI. The corresponding material data is loaded from data records provided in the sub-package THERMOELECTRIC\_MATERIAL\_DATA. Data for p- and n-doped Bi<sub>2</sub>Te<sub>3</sub> and PbTe are available. These data records contain temperature-dependent

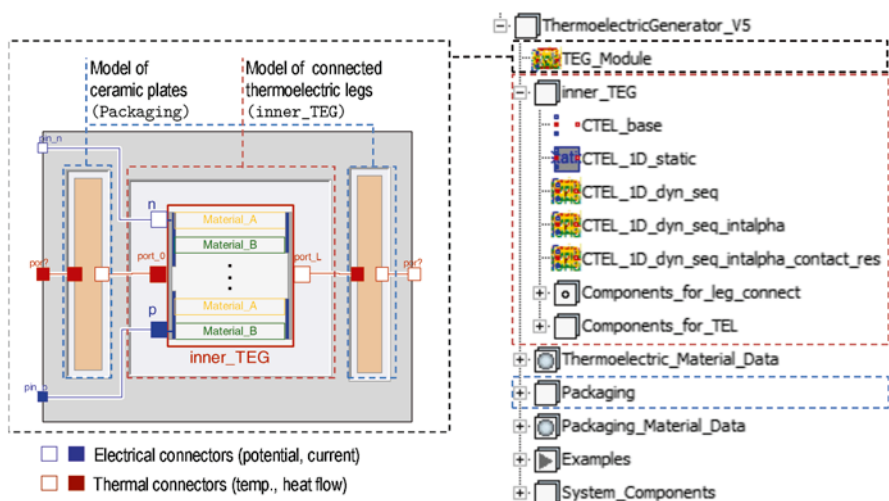


Fig. 25.1 Top-level diagram of TEG\_Module (left) and library structure (right)



material parameters like the specific heat capacity and Seebeck coefficient, which are considered by the CTEL models. If required and if material data is available, new materials can be added easily to the library. The package PACKAGING contains several models of the surrounding ceramic plates. Some of these models use the material data given in PACKAGING\_MATERIAL\_DATA. The package EXAMPLE contains some simulation examples, e.g. the one given in section “Simulation Example”. SYSTEM\_COMPONENTS comprises components like heat sinks, which are not required for the TEG but useful for system modeling.

## Implementation and Modeling Details

**TE legs:** All TEL models are based on the partial differential equations (PDE) for their thermal (25.1) and electrical (25.2) behaviors<sup>1</sup>

$$\underbrace{c \rho \frac{\partial T}{\partial t} A dx}_{\text{derivative of internal energy}} = - \underbrace{\frac{\partial}{\partial x} \left( -\lambda \frac{\partial T}{\partial x} \right) A dx}_{\substack{:= d\dot{Q}_c \\ \text{heat absorption} \\ \text{due to conduction}}} - \underbrace{I \alpha \frac{\partial T}{\partial x} dx}_{\substack{:= d\dot{Q}_T \\ \text{heat absorption} \\ \text{due to Thomson effect}}} + \underbrace{I^2 \frac{r}{A} dx}_{\substack{:= d\dot{Q}_J \\ \text{Joule heat} \\ \text{production}}} \tag{25.1}$$

$$dU = \alpha \left( -\frac{\partial T}{\partial x} \right) dx - I \frac{r}{A} dx \tag{25.2}$$

with:

---

$\alpha$ : Seebeck coefficient,	$\lambda$ : thermal conductivity,	$r$ : electrical resistivity,
$\rho$ : mass density,	$x$ : position,	$t$ : time,
$c$ : specific heat capacity,	$T$ : temperature,	$A$ : cross section area,
$U$ : voltage drop,	$I$ : electrical current.	

---

Since Modelica® only supports ODE and no PDE, the derivatives with respect to  $x$  are approximated by finite differences. To achieve  $dx \rightarrow 0$ , the model of the TE material is discretized in a one-dimensional manner like proposed among others in [3].

**Leg connectors:** The thermal and electrical behaviors of the bonds connecting the TELs are considered in the model CTEL\_1D\_dyn\_seq\_intalpha\_contact\_res. The electrical behavior is described by the line resistance—determined by material and geometrical parameters—and the contact resistance. The value for the contact resistance is based on [4] and is a changeable parameter in the model.

---

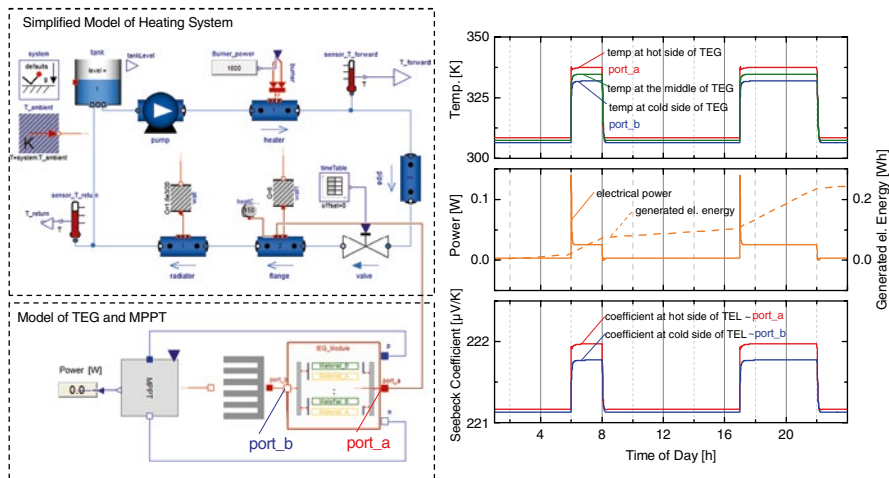
<sup>1</sup>The different TEL models result from neglecting, e.g., the derivative of the internal energy and further implementation details. For a detailed model description, see [2].

**Packaging:** The model for the heat transfer of the surrounding ceramic plates is changeable. There is the option to use a model for an ideal heat transfer, without any storage and thermal resistance, as well as a model following the one-dimensional heat equation involving thermal conduction and a heat capacity. For the calculation, material and geometric parameters of the TEG are used.

### Simulation Example

As a simulation example, an energy harvesting solution for the energy supply of an electronic thermostat on a radiator is chosen (Fig. 25.2). Whereas the heating system is modeled out of components given by the Modelica® Standard Library, the presented library is used to model the TEG system. In the simulation setup, the hot side of the TEG is connected to a heating flange and the cold side to a simple heat sink. The parameters of the TEG with 199 thermocouples come from a manufacturer’s data sheet. Due to the temperature-dependent, fluctuating internal resistance of the TEG, it is connected to a maximum power point tracker (MPPT) to reach the maximally possible output power. There is no limitation in the simulation time, so short-term and long-term simulations are possible. The simulation results are also shown in Fig. 25.2. The TEG temperatures, the electrical output power, the generated electrical energy, and the temperature-dependent Seebeck coefficient are plotted under the assumption of active heating in the morning and in the evening. In the given simulation scenario, the generated electrical energy would be enough to cover the energy consumption by an electronic thermostat valve.

Furthermore, the application of the library for a real test bench was done in [5].



**Fig. 25.2** Left: Modelica®/Dymola® diagram of a heating unit (taken from the Modelica Fluid library) with integration of a TEG model to simulate energy harvesting for an electronic thermostat valve. Right: simulation results for whole day simulation

## Conclusions

In this paper, a modeling library for the dynamic simulation of TEGs was presented. The characteristics were described and the effectiveness of the library was shown with the help of a simulation example.

The Modelica® library is available on request at the Chair of Automation of the Saarland University.

## References

1. Website of the Modelica Association. <http://www.modelica.org>
2. Felgner F, Exel L, Nesarajah M, Frey G (2014) Component-oriented modeling of thermoelectric devices for energy system design. *IEEE Trans Ind Electron* 61(3):1301–1310
3. Tiller M (2001) *Introduction to physical modeling with Modelica*. Kluwer Academic Publishers, Boston
4. Goldsmid HJ (2010) *Introduction to thermoelectricity*. Springer, New York, pp 174–176
5. Nesarajah M, Frey G (2014) Object-oriented Modeling of an Energy Harvesting System Based on Thermoelectric Generators. In: A. Y. Oral et al. (Eds.): *International Congress on Energy Efficiency and Energy Related Materials (ENEFM2013)*, Springer Proceedings in Physics 155. Springer International Publishing, pp. 211–216

# Chapter 26

## Modeling and Design of Tubular Thermoelectric Generator Used for Waste Heat Recovery

H. Tjoa, B. Plochmann, and G. Fischerauer

**Abstract** In many energy conversion processes, thermal energy is released to the environment; that is, it remains unused. With the aid of thermoelectric generators (TEGs), a part of this energy can be converted into electrical energy. The efficiency of the process can be increased and the CO<sub>2</sub> emissions are therefore reduced. In this contribution, the simulation and the design of a new concept of thermoelectric generator are discussed. The TEG is built ribbonlike and is wrapped around an electrically insulated tube, which is heated by waste heat from the inside and cooled by water from the outside. A numerical model is developed to theoretically study this concept. The goal is to understand the characteristics of the TEG and with it achieve a performance-optimized TEG design. In order to achieve the optimal design, parameter studies were carried out with the numerical model, which should help to determine the performance of the TEG. Geometrical dimensions, thermal resistance, and electrical resistance in the components are taken into account to accurately model the modules. The convective heat transport was taken into consideration in the study of the heat transfer as it plays a major role in the later application. Furthermore, the temperatures and the heat flows are also studied as small changes of these can often have a direct impact on the system.

**Keywords** Thermoelectric generator • Simulation • Finite element method • Design • Modeling • Waste heat recovery

---

H. Tjoa (✉) • G. Fischerauer  
University of Bayreuth, ZET, Chair of Metrology and Control Engineering,  
Bayreuth, Germany  
e-mail: [mrt@uni-bayreuth.de](mailto:mrt@uni-bayreuth.de)

B. Plochmann  
University of Bayreuth, ZET, Chair of Functional Materials, Bayreuth, Germany

## Introduction

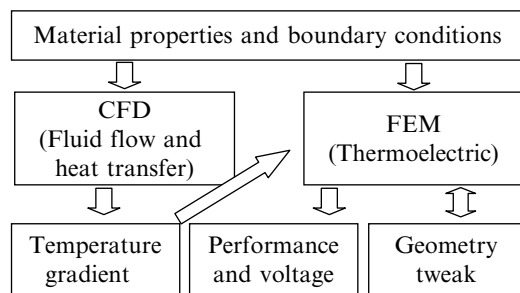
Thermal energy is produced as a by-product in many energy-conversion processes. This energy is often unused and released directly to the environment. With a thermoelectric generator (TEG), a portion of this energy can be converted into electrical energy.

There are different ways to integrate a TEG in a system. As a promising concept for a TEG system we propose a design in which a ribbonlike flexible TEG is wrapped around an electrically insulated tube (the TEG materials can, for example, be an n-type and a p-type semiconductor). The tube will be heated by waste heat and cooled by water. To analyze this concept, a combination of computational fluid dynamics (CFD) analysis and finite element method (FEM) was used. With this method, both the gas flow and the temperature distribution can be studied, and thus the electrical performance of the TEG can be predicted.

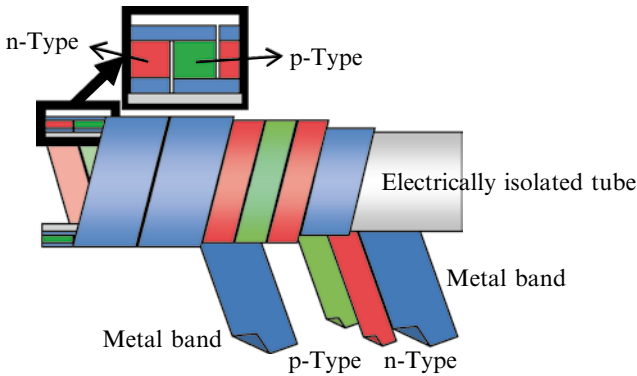
In the design of the planned TEG, different challenges need to be addressed. To ensure a high temperature difference over the TEG and a high usable output voltage, the heat transfer from the environment to the TEG surfaces must be as good as possible. Furthermore, the TEG should have a small internal resistance to reduce the electrical losses. These two parameters are directly influenced by the TEG geometry. In the following, we describe our attempt to find optimal design parameters by simulation. The goal of the simulation is a performance-optimized TEG system.

## Model Setup

We have based our analysis on CFD and FEM simulations. The program platform used was Ansys as the suitability of this code to model conventional TEGs has already been demonstrated in various works [1–4]. The analysis process is depicted in Fig. 26.1. The solution of the CFD analysis yields the temperature distribution in the tube which will be used as boundary conditions in the thermoelectric analysis by FEM simulation. This two-step process takes the fluid flow and heat transfer into account, therefore providing realistic results for the TEG output.

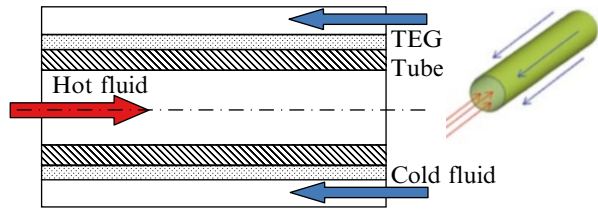


**Fig. 26.1** Modeling approach



**Fig. 26.2** Geometry of the proposed TEG

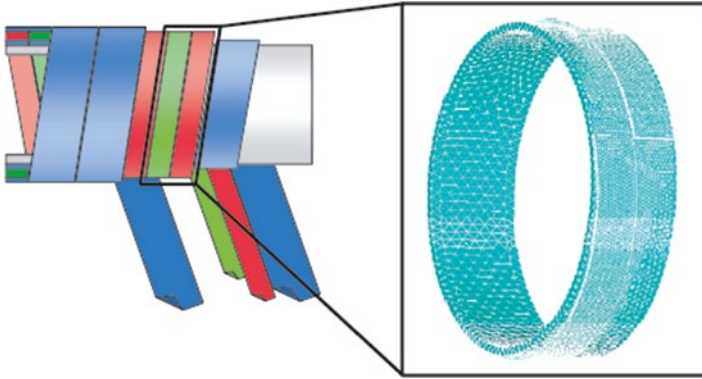
**Fig. 26.3** Sectional view of model geometry with the TEG wrapped around a tube



The components and arrangement of the planned TEG are depicted in Fig. 26.2. It consists of flexible thermoelectric materials that are wrapped around an electrically insulated tube. The thermoelectric legs are contacted electrically by a flexible metal band. To isolate the thermocouple from one another a longitudinal cut along the surface is needed.

Figure 26.3 shows the sectional view of the model for the TEG in operating condition. It consists of two fluid flows that are separated by the TEG-wrapped tube wall. To determine the temperature difference between the two sides of the TEG, the heat transfer needs to be investigated. The convective heat transport was taken into account in the investigation since, in most cases, heat transfer in the fluid flows is influenced by convection, which is affected by properties of the flow (flow velocity, Reynolds number, Prandtl number, etc.). A 3-D model was created using Ansys Fluent to simulate the behavior of the TEG.

The equations used in the thermal-electric analysis in Ansys include all governing equations and also consider relevant effects such as Seebeck, Peltier, Joule heating, and Thompson. The model of the thermoelectric legs and the electrical contacts uses a free mesh with tetrahedral elements (Solid227), which are typically used for thermal-electric analysis [4]. To reduce the number of finite-element nodes and the calculation time, only one thermocouple is modeled as unit cell of the geometry under consideration (in other words, the geometry was considered to be infinitely periodic along the tube axis; Fig. 26.4). The result of the simulation of a single thermocouple can then be extrapolated analytically to the number of thermocouples in a module.



**Fig. 26.4** Modeling of one thermocouple in Ansys

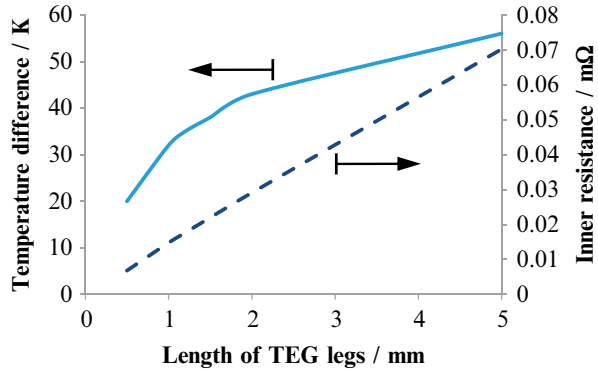
The geometry was modeled with Ansys Designmodeler and then exported to Ansys apdl as an Ansys neutral file. The geometry was meshed and the boundary conditions were defined in Ansys apdl. Since only one thermocouple is modeled, the mean temperature in the tube wall was used as the boundary condition instead of the temperature distribution. Surface effects such as thermal radiation were neglected as the tube is surrounded by water. The temperature dependence of the material is also neglected because the simulation is intended for low temperatures (80 °C at most).

## Parameter Studies

To discuss a first design test, we assume that the flexible TEG is made of materials with Seebeck coefficients of, respectively, 200  $\mu\text{V/K}$  (p-type leg) and  $-200 \mu\text{V/K}$  (n-type leg), with a thermal conductivity of 2 W/m K, and an electrical conductivity of  $10^5 \text{ S/m}$ . The flexible thermoelectric legs are connected electrically by copper band, and the TEG module is assumed to be load matched. With these material parameters, we can determine the optimal design parameters. Of particular importance are the tube diameter and the TEG foil thickness, as they directly affect the temperature drop over the TEG and the internal resistance. Results of variations in these parameters are presented in the following. The simulation is carried out with a hot-side temperature of 80 °C and a cold-side temperature of 10 °C. We assume that both fluids have a good heat transfer coefficient.

The simulated relation between the temperature drop over the TEG and the TEG thickness on the one hand and that between the internal resistance and the TEG thickness on the other hand is plotted in Fig. 26.5. By increasing the thickness of the TEG foil, both the internal resistance and the temperature drop increase. The former is equivalent to the electric resistance of the foil material, and can be calculated analytically from the material resistivity, the foil thickness, and the cross-sectional area of the foil. The temperature difference was obtained through the CFD analysis.

**Fig. 26.5** Temperature difference between the two TEG surfaces and internal resistance for different resistance for different values of TEG foil thickness (leg length)



**Fig. 26.6** Power output as a function of TEG foil thickness (leg length). Tube dimensions: Inner diameter 80 mm and wall thickness 2 mm

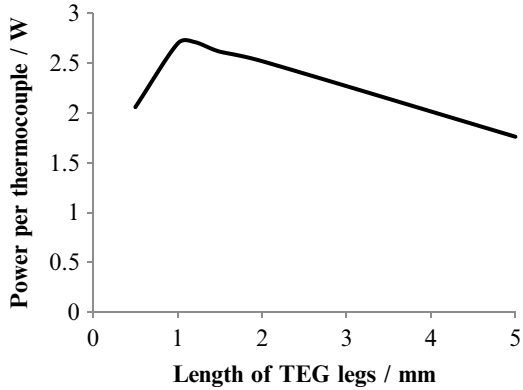
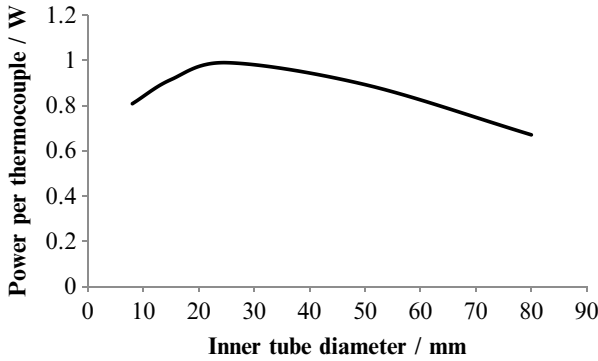
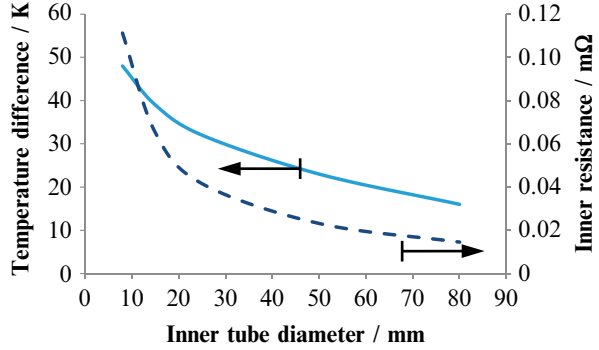


Figure 26.6 presents the theoretically achievable performance of the TEG in load-matching condition as a function of the foil thickness. The maximum power occurs at around 1 mm. A close look at the curve indicates that the maximum power reduces significantly with increasing foil thickness. At 10 mm thickness, the power reduces to around one-third of the maximum power as the internal resistance increases. The high output power of the single thermocouple is due to the small internal resistance and the large values of the electrical conductivity and the Seebeck coefficient assumed for the TEG material, which results in a high electric current.

In addition to the TEG thickness, the tube diameter is also studied. The size of the tube diameter determines the length of the TEG foil wrapped around the tube as well as the flow characteristics in the tube (laminar or turbulent). In our parameter study, we only considered standard DIN size tubes. It is assumed that the flow rate is constant. The results are plotted in Figs. 26.7 and 26.8. It is evident that both the internal resistance and the temperature difference decrease as a result of the reduction in flow velocity as the tube gets bigger. The looked-for optimum occurs at around 25 mm tube diameter.



**Fig. 26.7** Temperature difference between the two TEG surfaces and inner resistance for different tube diameters



**Fig. 26.8** Investigation of optimal tube diameter. TEG foil dimensions: Thickness 1 mm, width 5 mm

### Comparison with Analytical Model

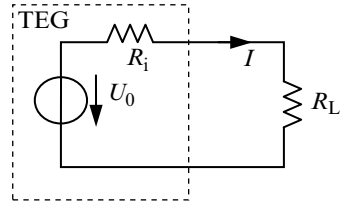
To corroborate the numerical results, they were compared with the results of an analytical model based on known basic equations. For this calculation, the geometry parameters of the proposed TEG will be converted to those of an equivalent standard TEG as the known equations are intended for standard TEGs.

The model for the TEG circuit is depicted in Fig. 26.9. The TEG is represented as a simple voltage source with an inner resistance (equivalent Helmholtz/Thévenin source) and is connected to a load resistance to get output power. Hence, the inner resistance and the output power of the circuit at load-matching conditions are determined by

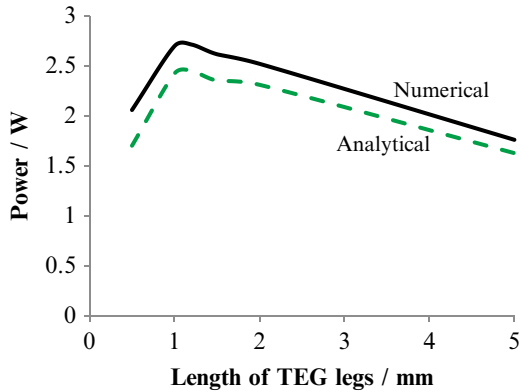
$$R_i = \frac{\rho \ell}{A}, \tag{26.1}$$

$$P_{out} = \frac{\left( (k_p - k_n) \Delta T \right)^2}{4R_i}. \tag{26.2}$$

**Fig. 26.9** Equivalent electric circuit of the TEG module



**Fig. 26.10** Comparison numerical vs. analytical calculation



Here,  $\rho$ ,  $\ell$ , and  $A$  are the electric resistivity, the length, and the cross-sectional area of the thermocouple legs, respectively.  $k_p$  and  $k_n$  denote the Seebeck coefficients of the p-type and the n-type thermoelectric, and  $\Delta T$  is the temperature drop over the TEG.

The results of the numerical simulation are compared with those from the analytical calculation in Fig. 26.10. The two curves are in good agreement as far as the functional dependence is concerned. As to the absolute power level, a constant offset is observed. This may be an indication of the fact that the model assumptions and the approximations involved in both the simple analytical model and the numerical model are consistent with each other. The constant difference between the two curves visible in Fig. 26.10 is thought to be mainly due to the Thomson effect and the Peltier effect which are taken into account in the numerical model, but not in the simplified analytical model.

## Conclusion

The proposed concept of TEG with a novel geometry was analyzed and modeled. We developed a CFD model for the fluid flow system and a steady-state FEM model for the TEG. The models solved the temperature and electric potential equations and accounted for all thermoelectric effects. The models were used to investigate

the characteristics of the novel TEG and to determine the optimal design parameters through parameter studies.

The design optimum can be determined by the aid of the numerical models. The output power is quite sensitive to the foil thickness and the inner tube diameter, as these change both the inner resistance and the temperature difference between the two TEG surfaces. The output power of the example TEG presented reaches a maximum at 1 mm foil thickness and 25 mm inner tube diameter.

**Acknowledgement** We gratefully acknowledge the support of the German Federal Ministry of Education and Research with its funding of the Project Thermo-Oxid-Power (contract number 03x3553C).

## References

1. Zhang Y, D' Angelo J, Wang X, Yang J (2012) Multi-physics modeling of thermoelectric generators for waste heat recovery applications, DEER Conference, Michigan
2. Wang CC, Hung CI, Chen WH (2012) Design of heat sink for improving the performance of thermoelectric generator using two-stage optimization. *Energy* 39:236–245
3. Fraisse G, Ramousse J, Sgorlon D, Goupil C (2013) Comparison of different modeling approaches for thermoelectric elements. *Energy Convers Manag* 65:351–356
4. Antonova EE, Looman DC (2005) Finite elements for thermoelectric device analysis in ANSYS. International conference on thermoelectrics, Cannonsburg

# Index

## A

Alumina (Al<sub>2</sub>O<sub>3</sub>), 84–86, 180  
Anodized aluminum (Al), 83–87

## B

Butt welded pipe, 144, 146, 147, 149

## C

Characterization, 21, 31, 50, 53–59, 178, 181, 205–211  
Constant voltage algorithm, 167  
Contact resistance ( $R_c$ ), 54, 64, 72, 75–76, 79, 81, 102, 103, 106–108, 154, 156, 215  
Costs, 20, 44, 45, 50, 51, 84–86, 92, 118, 127, 152, 156, 157, 160–164, 177–182, 207

## D

DC–DC converter, 153, 154, 157, 158, 160–163  
Design, 12, 17, 46, 62, 112, 118, 119, 123, 126, 127, 132, 134, 138–141, 152, 153, 163, 186, 195, 198–200, 202, 206, 209, 219–226  
studies, 139, 140  
Diesel-powered commercial vehicle, 138

## E

Efficiency, 141, 142, 157, 160  
Electrical properties, 42, 79  
Electronic refrigeration, 183, 184  
Energy harvester/harvesting, 54, 152–154, 163, 182, 190, 192, 193, 206, 209, 216  
Eutectic, 4, 5, 45–48

Exhaust system, 118, 125, 126, 130–131, 138–140  
Experimental validation, 153, 197–203

## F

Figure of merit, 2, 16–17, 30, 44, 50, 54, 62, 63, 65, 69, 113, 182, 185  
Finite element method (FEM), 85, 99–108, 220, 225

## G

Grain boundaries, 5, 9, 13, 17, 30, 42

## H

Harman method, 61–69  
Heat recovery, 20, 72, 117–127, 138, 143–149, 152, 219–226  
Higher manganese silicides (HMS), 44, 47–49, 90, 91, 93, 103

## I

Ink formulation, 178, 179

## J

Joining material, 71–81

## M

MATLAB, 130, 131, 192  
Measurement device, 54, 58, 59  
Measuring error, 54, 59  
Mechanical processing, 20, 24, 26, 45

MEMS, 189–195  
 Metal silicides, 43–51  
 Modelica library, 213–217  
 Modeling, 130–131, 213–216, 219–226

**N**  
 Nanosilver/nano-Ag, 71–81  
 Nanostructuring, 2, 30, 43–51  
 Numerical simulation, 140, 168, 171–173, 225

**O**  
 Occupancy rate ( $\tau$ ), 198, 199  
 Open-circuit voltage algorithm, 167–170, 172  
 Optimization, 12, 13, 26, 44, 50, 64, 99–108, 123–127, 140, 167, 197–203

**P**  
 Plug-in hybrid electric vehicle (PHEV), 130–134  
 Porcupine diagram, 61–69  
 Power  
   control strategy, 167–175  
   generation, 2, 50, 51, 72, 123, 125, 127, 129–134, 148, 153, 178  
   management, 189–195  
 Processing, 2, 9, 17, 23, 24, 26, 30, 33, 34, 39, 45, 72, 74, 92, 161  
 Production modification, 44

**R**  
 Radiant heat, 144, 146–148  
 Rapid solidification, 2, 31–34, 45

**S**  
 Screen-printing, 73, 177–182  
 Shear force, 76, 78, 79, 81  
 Simscape, 192, 195  
 Simulation, 85, 86, 101, 103, 127, 130–132, 134, 138–140, 148, 149, 153, 168, 170–173, 175, 189–195, 213–217, 220–222, 225  
 Simulink, 130, 192  
 Sintering, 11–13, 17, 20, 21, 25, 26, 37–42, 45, 49, 50, 72–77, 80, 179, 181  
 Skutterudite, 2, 4, 72, 90  
 Sodium cobalt oxide, 37–42

Solid solutions, 11  
 Solid state reaction (SSR) synthesis, 38–42  
 Space applications, 72, 111, 112, 190  
 Structural changes, 12, 42  
 Structural disorder, 12, 16  
 Substrate, 44, 45, 47, 72, 73, 75–78, 80, 81, 83–87, 178–181

**T**  
 Tellurides, 84, 119, 138, 144, 178, 179, 181, 206  
 Thermal equilibrium, 205  
 Thermal resistance, 84, 86, 118–121, 123–127, 148, 168, 170, 185, 216  
 Thermoelectric (TE)  
   applications, 2, 9, 30, 38, 44, 84, 90, 152, 153, 156, 157, 160–164  
   cooling, 183–187  
   devices, 20, 30, 61–69, 90, 100, 101, 110, 177–187  
   generator system/module, 20, 71–81, 91, 97, 102, 103, 108, 118, 119, 121, 129–134, 138, 142, 168, 169, 190, 198, 199, 205–211  
   materials, 16, 20, 30, 38, 44, 47, 49, 50, 53–59, 68, 90, 93, 101, 112, 118, 119, 124, 139, 140, 142, 178–182, 186, 208, 221  
   oxide, 37–42  
 Thermoelectric generator (TEG), 54, 83–87, 101–103, 106–107, 109–115, 117–127, 130, 137–149, 151–164, 167, 168, 178, 189–195, 197–203, 213–217, 219–226  
 Thermomechanical stress, 131, 134  
 Transient response, 168, 174, 175

**W**  
 Waste heat, 30, 54, 118, 124, 132, 134, 142, 145, 162, 178, 206, 220  
   recovery, 72, 117–127, 138, 143–149, 152, 219–226  
 Wireless sensor networks (WSNs), 190, 191, 206, 209

**Z**  
 Zn<sub>4</sub>Sb<sub>3</sub>, 19–26, 29–35  
 $zT$  meter, 61–69